Investigation of Aluminum-Based Plasmonic Devices for Sensing Applications in the Near-Infrared Region

THESIS

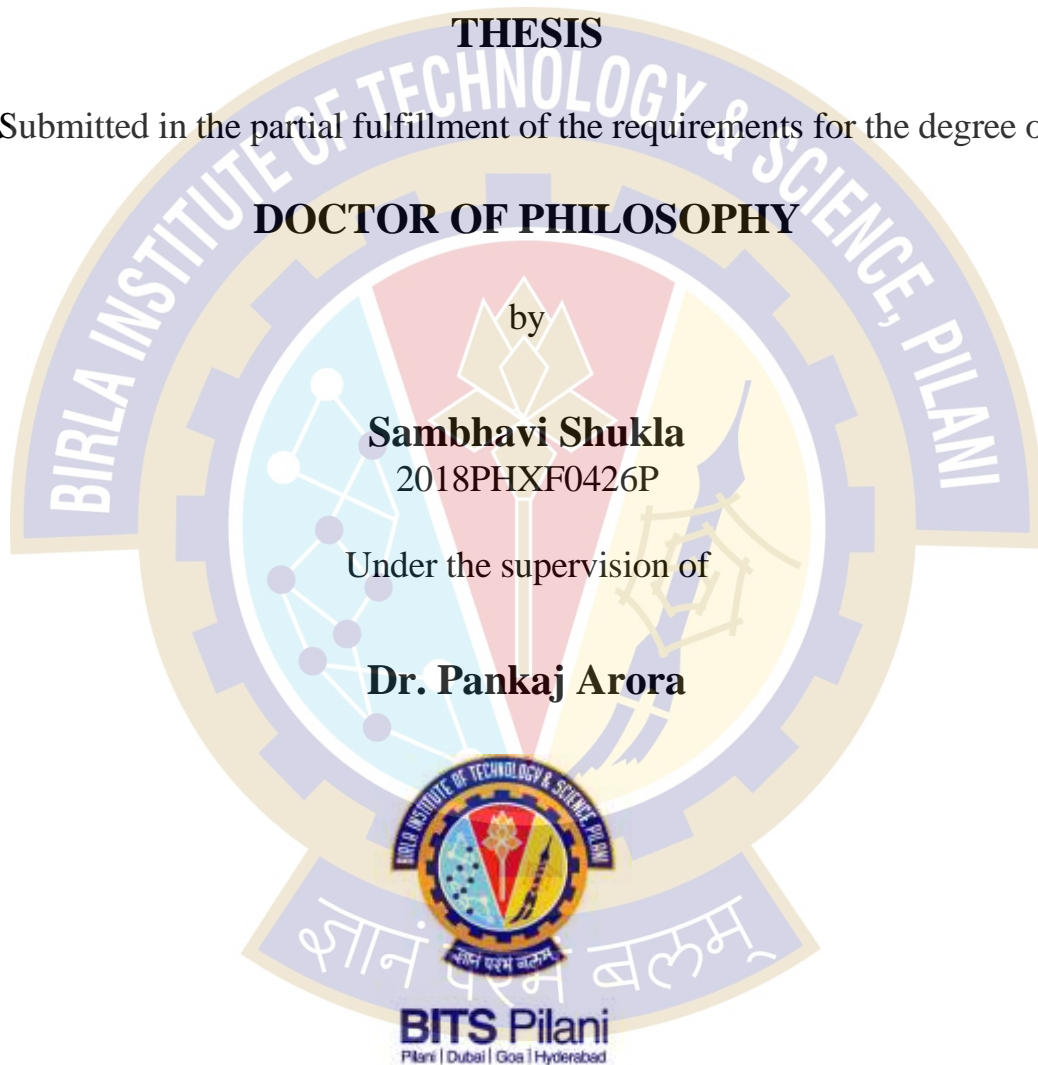Submitted in the partial fulfillment of the requirements for the degree of

DOCTOR OF PHILOSOPHY

by

Sambhavi Shukla
2018PHXF0426P

Under the supervision of

Dr. Pankaj Arora

BIRLA INSTITUTE OF TECHNOLOGY & SCIENCE

PILANI – 333031 (RAJASTHAN) INDIA

2022

BIRLA INSTITUTE OF TECHNOLOGY & SCIENCE

PILANI- 333031 (RAJASTHAN) INDIA

CERTIFICATE

This is to certify that the thesis entitled **"Investigation of Aluminum-based plasmonic devices for sensing applications in the near infra-red region"** submitted by **SAMBHAVI,** ID. No**. 2018PHXF0426P** for the award of Ph.D. of the institute embodies original work done by her under my supervision.

Signature in full of the Supervisor   _____

Name   :   **Dr. Pankaj Arora**

Designation   :   **Assistant Professor**

                    Department of Electrical and Electronics Engineering

                    BITS Pilani, Pilani campus,

                    Pilani, Rajasthan, 333031, India

Date   : _____

Dedicated

to

My Parents and My Brother

ACKNOWLEDGEMENT

With immense joy and profound gratitude, I would like to take this opportunity to express my gratitude to all the people who have helped me through this incredible journey toward the successful completion of the thesis.

First and foremost, I always profoundly obligate the unintimidated support and guidance of my Ph.D. Research supervisor **Dr. Pankaj Arora,** Assistant Professor, Department of Electrical and Electronics Engineering, Birla Institute of Technology and Science, Pilani (BITS-Pilani), Pilani Campus, Rajasthan, whose excellent knowledge, and constant inspiration helped me to complete my research work and his profound contribution in shaping up the foundation of my research career. It has been a complete honor to be his Ph.D. student since his expertise, understanding, and patience guided me continuously throughout my Ph.D. His advice, support, and constructive criticism have helped me to develop critical and scientific thinking. My involvement with him in scientific discussions has helped me to evolve my intellectual maturity. His generous and constant support and encouragement have immensely aided in polishing my scientific temperament and thus guided me throughout my journey to attaining this Ph.D. thesis. I would also like to thank him for encouraging me to attend international conferences and workshops, which gave me a golden opportunity to interact with eminent scientists and researchers working in our field of interest, which will be very helpful for my future.

I wish to express my deep sense of gratitude to my institute **Birla Institute of Technology and Science, Pilani (BITS Pilani), Pilani Campus, Rajasthan,** for providing me with an opportunity to fulfill my dream.

I sincerely thank **Prof. Souvik Bhattacharyya,** Vice-chancellor of BITS Pilani, and **Prof. Sudhir Kumar Barai,** Director of BITS Pilani, Pilani campus to pursue a Ph.D. from the institute.

I would also extend my gratitude to **Prof S. K. Verma**, Dean, Administration, BITS, Pilani, for his constant academic support and guidance about the official requirements to fulfill the Ph.D. program. I also thank Associate Dean, Academic-Graduate Studies & Research Division (AGSRD), BITS Pilani, and **Prof. Praveen Kumar AV, BITS Pilani**, Convener, Departmental Research Committee (DRC), for their timely guidance and support regarding the academic formalities throughout the thesis work.

My heartfelt thanks to the Head of Department, Department of Electrical and Electronics Engineering, BITS Pilani, for providing me with departmental support and facilities that helped me successfully complete this thesis.

This research work would not have been the same without the constructive evaluation of my Doctoral Advisory Committee (DAC) members. I convey my grateful acknowledgment and thanks to both my DAC members, **Prof. Navneet Gupta,** Department of Electrical and Electronics Engineering, and **Prof. Niladri Sarkar,** Department of Physics for the fruitful suggestions they provided during my presentations.
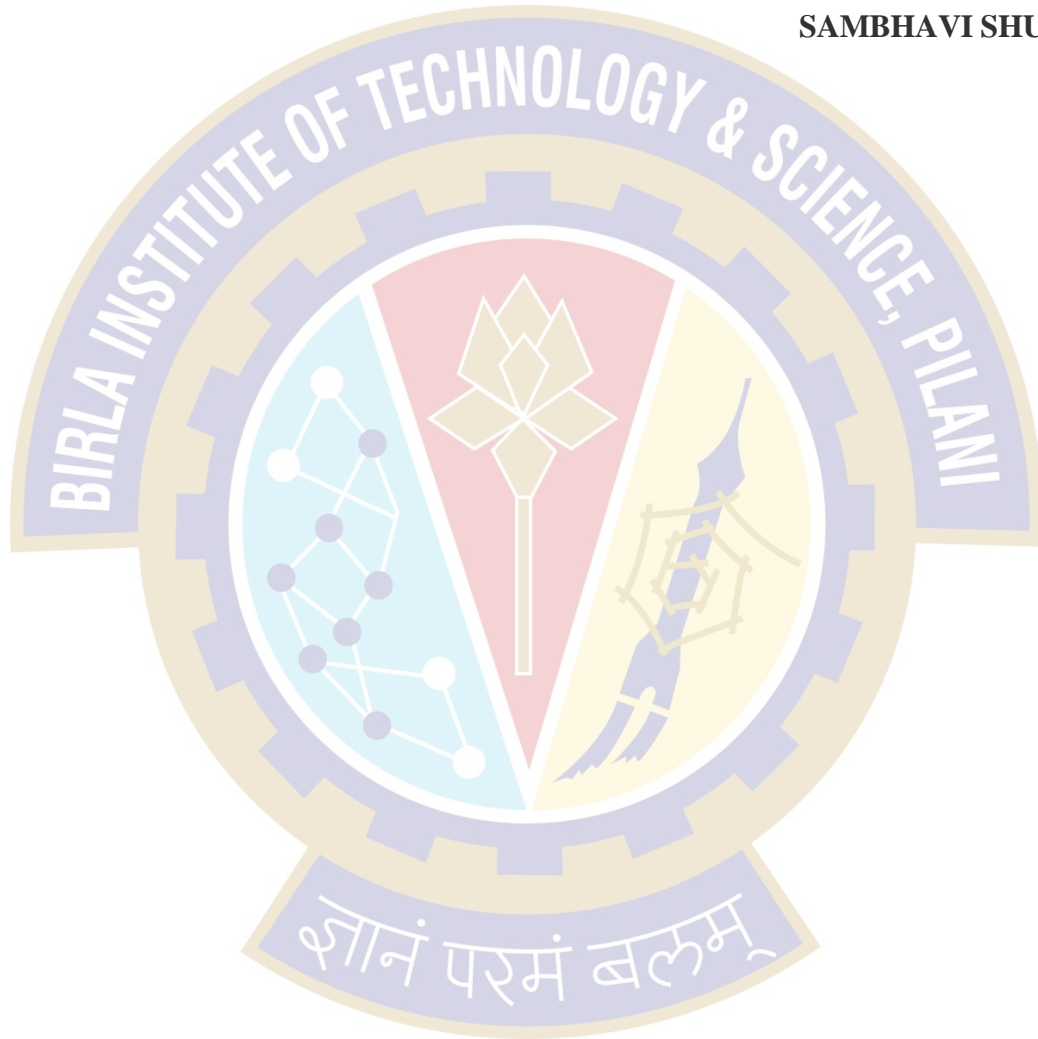
ABSTRACT

Label-free methods of sensing have become imperative in the world of biosensing mainly because they utilize intrinsic properties such as refractive index or permittivity etc. Surface Plasmon Resonance (SPR) is one such physical phenomenon that can facilitate real-time detection at the nanometer scale. The cumulative oscillation of conduction electrons at the boundary surface of the metal-dielectric interface gives rise to an entity, namely, Surface Plasmons (SPs). Such a phenomenon occurs due to the phase-matching conditions at the interface, resulting in resonance conditions. This plasmon resonance condition examines the material optical properties by monitoring the shifts in the resonant points of locations concerning corresponding variations in the concentration of the bio-sample or the refractive index of the unknown bio-sample. Thus, SPR is an investigative route for biosensing purposes in terms of high precision, fast response, lower cost, and strong resistance to temperature fluctuations. Such advantages have stimulated the use of SPR-based sensors for applications like cancer detection, food safety, enzyme detection, etc.

Therefore, this thesis focuses on investigating various SPR-based sensors with Aluminum (Al) as the plasmonic metal in the near-infrared region and analyzes the output performances in terms of higher sensitivity as well as the Figure of Merit (FOM). Two types of coupling mechanisms are utilized to excite the SPs i.e., prism-based coupling and periodic nanostructure-based coupling. Prism is employed for guiding the incident light towards the metal-analyte interface under the total internal reflection scheme. On the other hand, periodic nanostructure uses the diffraction phenomenon of light to achieve the phase-matching condition for SP excitation.

The optical characteristics of Al-based plasmonic sensors are explored for the near-infrared region using different modes of interrogation (angle and wavelength). The performance sensing parameters are studied in terms of reflection, and transmission characteristics of light that exhibit competitive results concerning gold and silver. The entire analysis is based on the near-infrared spectral regime that provides for non-invasive and non-destructive medical diagnosis. Biorecognition elements can help to enhance the sensor's performance, for which 2D nanomaterials are explored for the biofunctionalization of Al. This way, the unique optical properties provided by Graphene, MoS_2, MXene, etc. are investigated, thereby envisaging 2D nanomaterials for effective biosensing. Therefore, the ability of Al as the plasmonic metal is

extensively exploited in the NIR region, to realize it as a major key player in plasmonic-based devices.
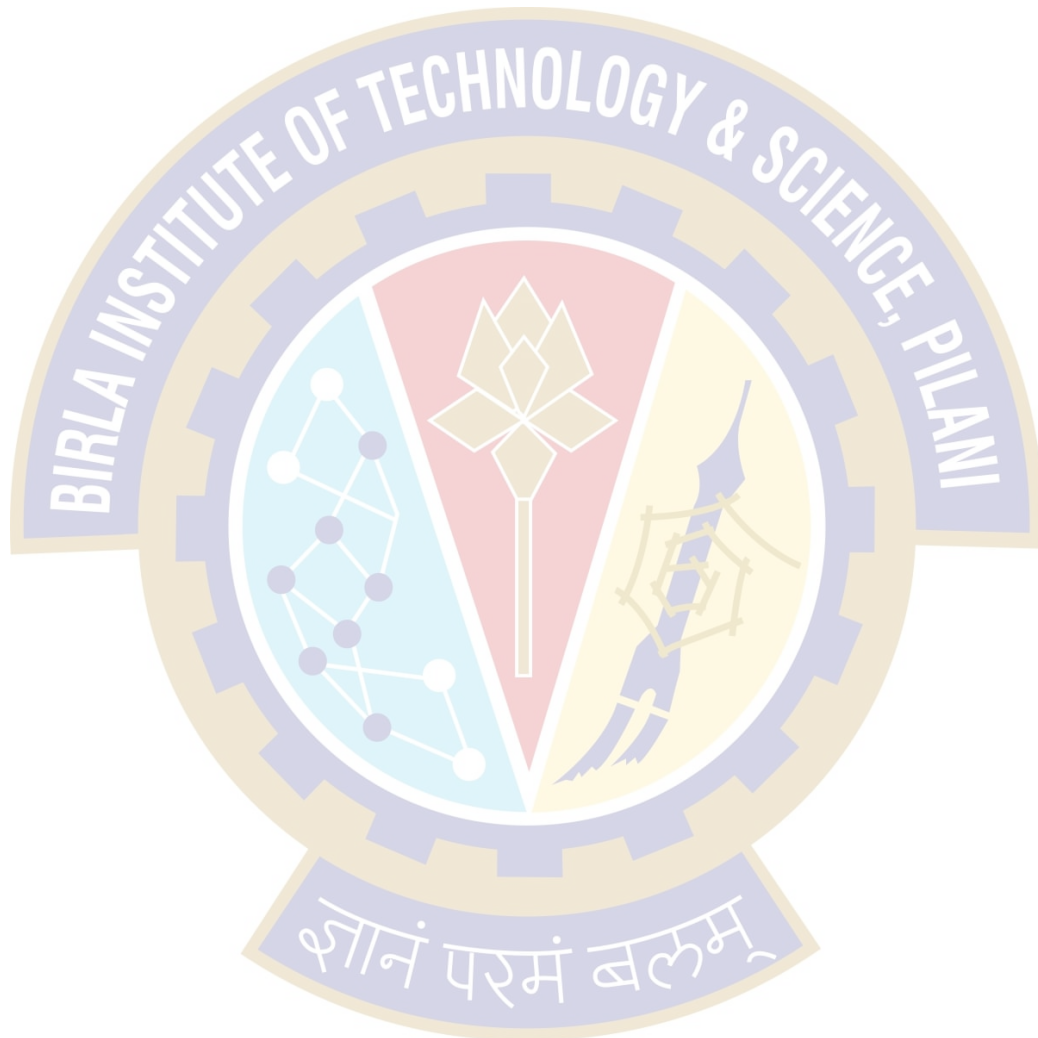
TABLE OF CONTENTS

Contents

LIST OF FIGURES

LIST OF TABLES

LIST OF ABBREVIATION

SPR	Surface Plasmon Resonance
LSPR	Localized Surface Plasmon Resonance
SP	Surface Plasmon
SPP	Surface Plasmon Polaritons
NIR	Near-Infrared Region
RCWA	Rigorous Coupled Wave Analysis
TMM	Transfer Matrix Method
FWHM	Full Width at Half Maximum
FOM	Figure of Merit
TMDC	Transition Metal Dichalcogenides
BRE	BioRecognition Element
CMOS	Complementary Metal Oxide Semiconductor
SEM	Scanning Electron Microscope
TM	Transverse Magnetic
PMMA	Poly Methyl Meth Acrylate
SERS	Surface-Enhanced Raman Scattering
NPA	Nano Pyramid Array
PVP	PolyVinyl Pyrrolidone
PVA	PolyVinyl Alcohol
PEG	PolyEthylene Glycol
NC	NanoCrystal
PCF	Plasmonic Colour Filtering
FDTD	Finite Difference Time Domain
EELS	Electron Energy Loss Spectroscopy
NSL	NanoSphere Lithography

CMS NW	Core Multishell Nano Wire
BNA	Bowtie Nano antennae array
MDM	Metal Dielectric Metal
Al NR	Aluminum Nano Ribbon
MFIEF	Magnetic Field Intensity Enhancement Factor
PBS	Phosphate Buffer Saline
BSA	Bovine Serum Albumin
ATR	Attenuated Total Reflection
ASM	Aluminum-Si-MoS$_2$
ASMG	Aluminum-Si-MoS$_2$-Gr
AM	Aluminum-MoS$_2$
AMG	Aluminum-MoS$_2$-Gr
UV	Ultra-Violet
NPs	NanoParticles
RIU	Refarctive Index Unit
OPV	Organic Photo Voltaics
QM	Quantum Mechanical
STH	Solar to Hydrogen ratio
IQE	Internal Quantum Efficiency
MIM	Metal-Insulator-Metal
WS$_2$	Tungsten disulfide
IS	Intrinsic Sensitivity
NA	Nano-Array
BTO	Barium Titanate
MIR	Mid-Infrared
FG	Fluorinated Graphene
BP	Black Phosphorus
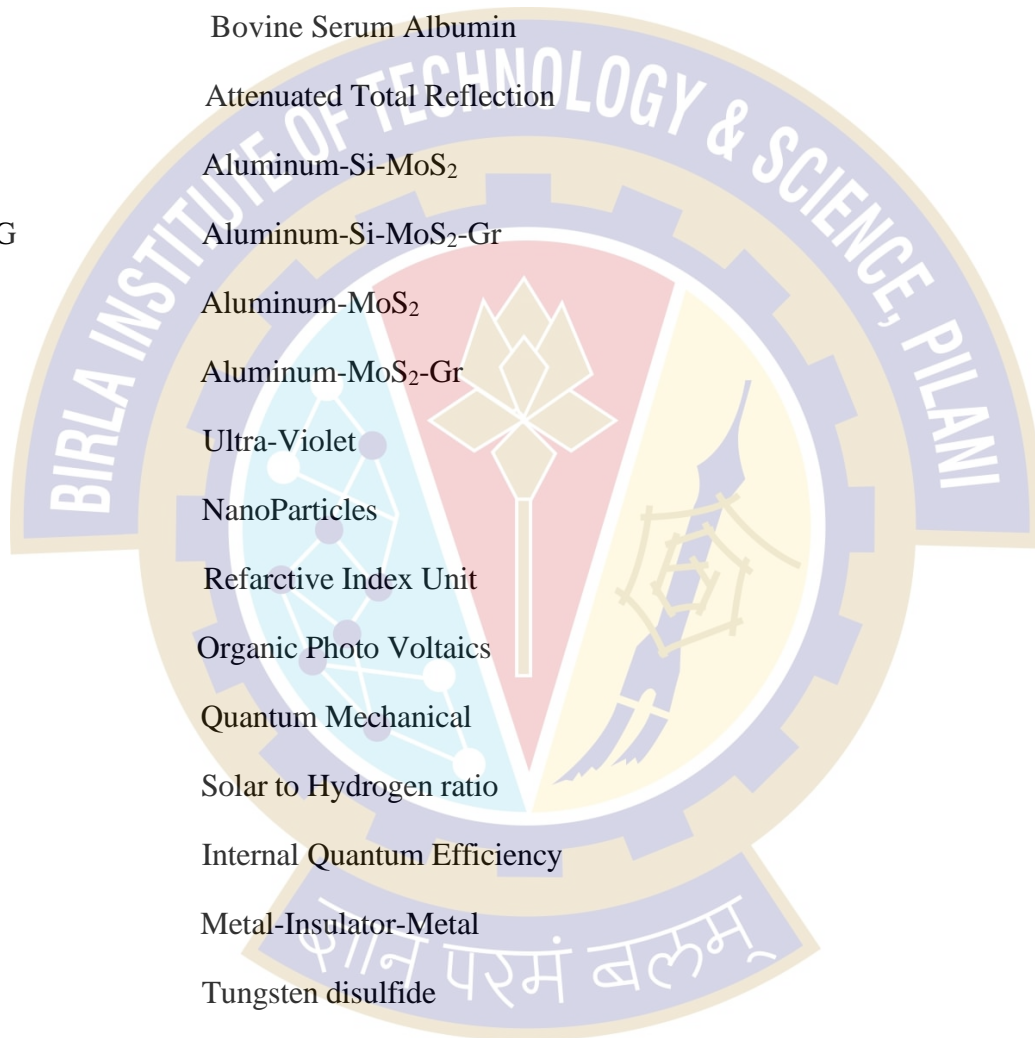
DBL   Dielectric Buffer Layer

DL   Dielectric Layer

MoS$_2$ Molybdenum disulfide

Hb Conc^n Hemoglobin Concentration

EBL   Electron Beam Lithography

QF   Quality Factor
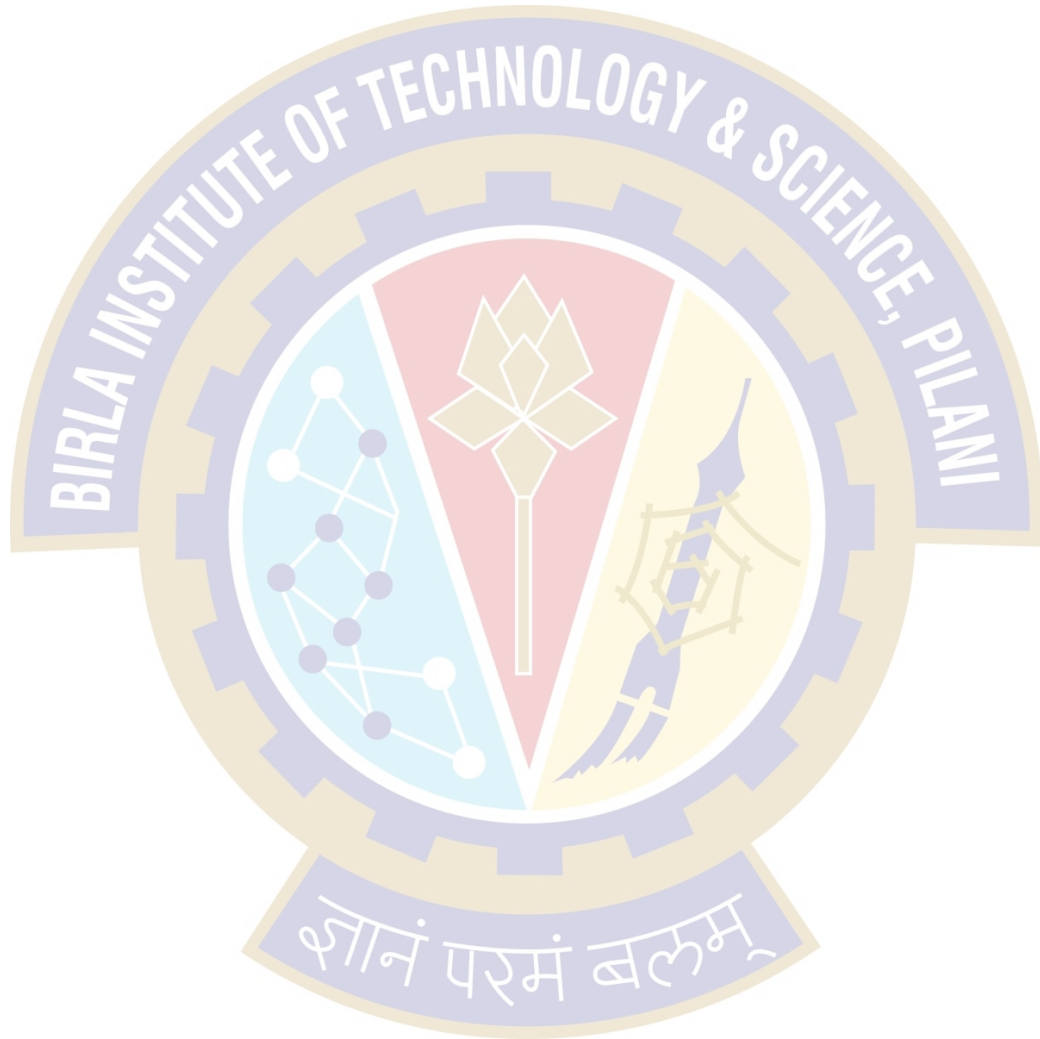
LIST OF SYMBOLS

t_m	thickness of the metal film
n_a	refractive index of the analyte
Δn_a	change in the refractive index of the analyte
$\Delta\theta_{SPP}$	change in the SPP resonance angle
t_{ns}	thickness of nanostructure
t_{buf}	thickness of buffer layer
f	fill factor
P	period of 1D nanostructure
P_x	period of 2D nanostructure along the x dimension
P_y	period of 2D nanostructure along the y dimension
w	width
S_θ	angular sensitivity
λ_{SP}	SP resonance wavelength
$\Delta \lambda_{SP}$	change in the SP resonance wavelength
λ_{SUB}	substrate mode resonance wavelength
λ_c	collision wavelength
λ_p	plasma wavelength
ω	angular frequency of incident light
r_p	reflection coefficient
ε_m	permittivity of metal
ε_d	permittivity of dielectric material
ε_o	permittivity of free space
ε_g	effective permittivity of Gr layer
σ_g	optical permittivity
m	diffraction order
n_p	refractive index of the prism

K_c wave vector of incident light

K_{SPP} wave vector of the surface plasmon

t_{Si} thickness of silicon layer

t_{Gr} thickness of graphene layer

t_{mx} thickness of MXene layer

t_{FG} thickness of fluorinated graphene layer

c_g concentration of glucose solution

t_{MoS2} thickness of MoS_2 layer

t_{BP} thickness of BP layer

t_{BTO} thickness of BTO layer

t_a thickness of analyte

n_{Si} refractive index of silicon

c_a concentration of adsorbed molecules

dn_a/dc_a adsorbed increment in the biomolecules

E_Z electric field distribution along the z dimension

$\boldsymbol{\theta}_{SP}$ SP resonance angle

Gr   Graphene
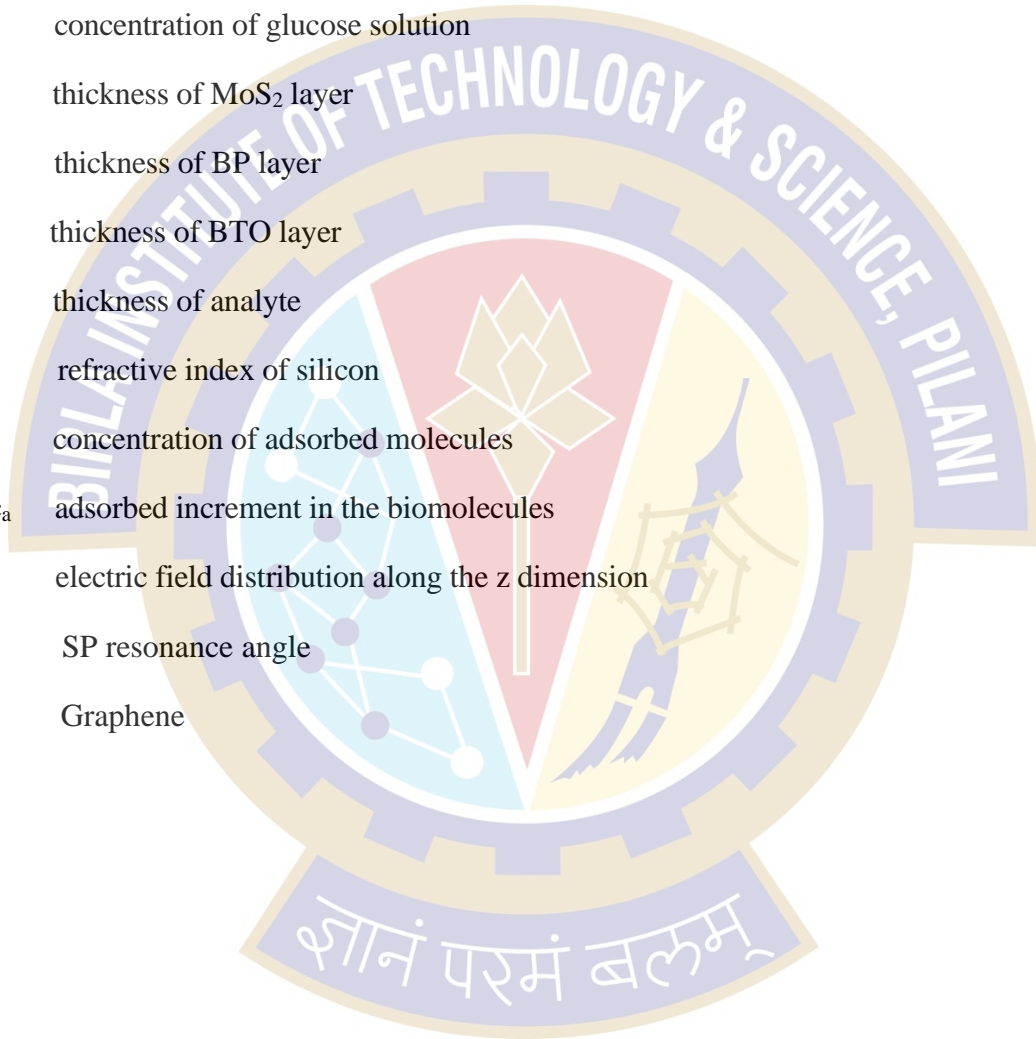
Chapter 1

Introduction

1.1 Background

In the world of nanophotonic technologies, Surface Plasmon Resonance (SPR) is one of the most successful sensing techniques that examines the electric field interaction when light is manipulated at sub-wavelength dimensions. With their early advent in the 1900s, when the Kretschmann configuration (1968) was reported, a structured approach to plasmon resonance came into being [10]. Thereafter, exhaustive research based on conventional noble metals (gold, silver) circling the visible region (400nm-700nm) came into the picture. Such impactful results brought the employability of SPR-based sensors towards applications like biological sensing [9], food safety [11], drug discovery [12], cancer detection [13], etc. Before proposing new SPR-based plasmonic devices in the NIR region, a basic understanding of the Surface Plasmon (SP) excitation is a prerogative.
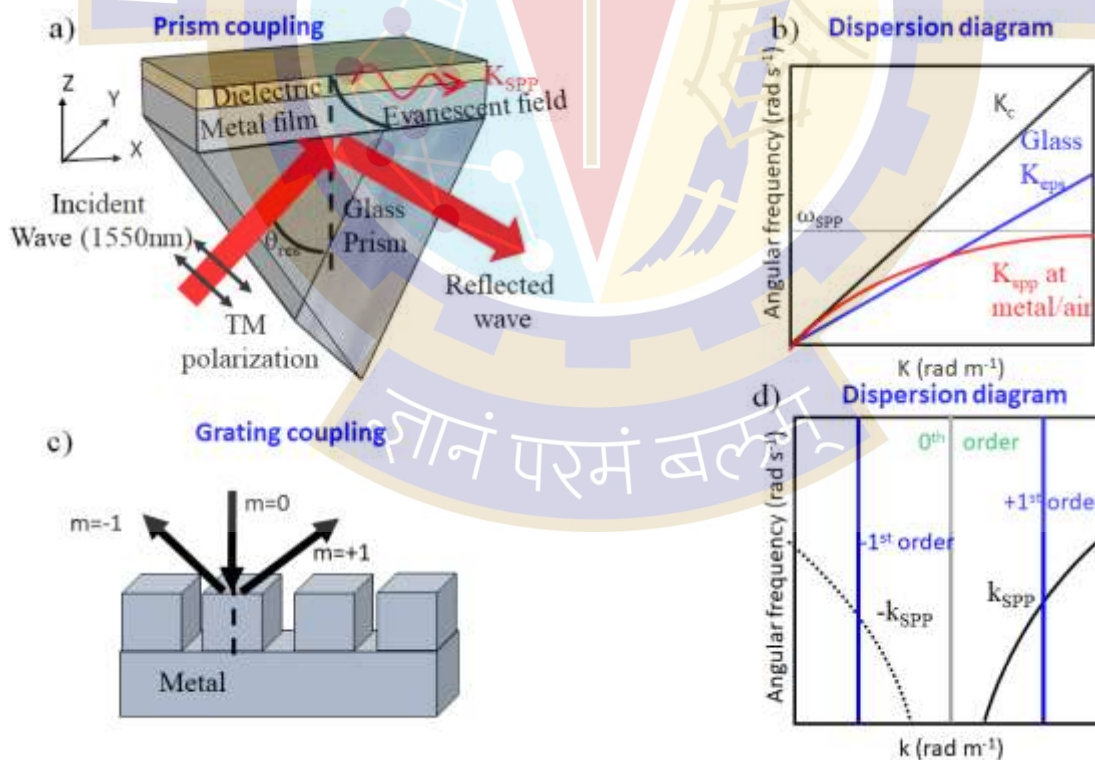
Fig. 1.1 (a) Schematic for a conventional Kretschmann configuration (b) Dispersion diagram for the prism-based coupling (c) Schematic for periodic nanostructure-based SP excitation (d) Dispersion diagram for the nanostructure-based coupling.

1

Fig. 1.1(a) represents the schematic of prism-based coupling which is known as the conventional Kretschmann configuration to initiate the SP excitation at the metal-dielectric interface. A Transverse Magnetic (TM) polarized light is incident on the metal-coated glass prism under a total internal reflection arrangement. At the phase matching condition, the evanescent field generated by incident light gets coupled to SPs at the metal-dielectric interface which can be explained with the dispersion diagram as shown in Fig. 1.1(b). The wave vector (K_{spp}) of the Surface Plasmon Polariton (SPP) can be written as given below in equation (1.1). Here, ε_m is the permittivity of the metal, ε_d is the permittivity of the dielectric material, and K_c is the wave vector for the incident light in free space respectively.

$$K_{spp} = K_c \sqrt{\frac{\varepsilon m . \varepsilon d}{\varepsilon m + \varepsilon d}} \qquad (1.1)$$

In Fig. 1.1(b), the black solid line represents the dispersion relation for incident light coming from the air (light line) and the red solid line represents the dispersion curve for SPP at the metal-dielectric interface. From Fig 1.1(b), it is clear that there is no intersection between the red and black solid lines which concludes that SPP excitation is not possible for the direct illumination of light. One solution is to use a high-index prism coated with thin metal in order to increase the momentum of incident light and achieve SPP excitation as shown in Fig. 1.1(b) where the blue solid line represents the dispersion relation for the light coming through a glass prism and meeting the red solid line at a point which is called the phase/wave vector matching condition for SPP excitation. In prism-based coupling, the wave-vector matching for SPP and incident light can be explained using equation (1.2) where θ_{res} is the SPR angle and n_p refers to the refractive index of the prism [14].

$$K_{spp} = K_c \sqrt{\frac{\varepsilon m . \varepsilon d}{\varepsilon m + \varepsilon d}} = K_c . n_p . \sin\theta_{res} \qquad (1.2)$$

Fig. 1.1(c) represents the schematic of another technique for SPP excitation at the metal-dielectric interface using periodic nanostructures. A normal incident light illuminating the patterned metal is diffracted by the periodic structure and it is possible for at least one of the diffracted orders to couple with SPPs by optimizing the parameters of periodic nanostructures. In periodic nanostructure-based coupling, the phase matching condition for SPPs excitation can be explained by equation (1.3), where m refers to the diffraction order and *P* is the period of the periodic nanostructures.

$$K_{spp} = K_c \sqrt{\frac{\varepsilon m . \varepsilon d}{\varepsilon m + \varepsilon d}} = \pm m \frac{2\pi}{P} + \frac{2\pi}{\lambda} n_p . \sin\theta \qquad (1.3)$$

2

Fig. 1.1(d) represents the dispersion diagram for the case of periodic nanostructures-based coupling where the 1st diffraction order couples to SPPs at the phase matching condition. Other types of SPP coupling mechanisms include waveguide-based SPP coupling, single nano-aperture-based SPP coupling, and periodic sub-wavelength nano-holes-based SPP coupling. In this thesis, we will be concentrating mainly on prism-based and periodic nanostructures-based coupling. After the phase matching conditions, maximum absorption takes place except at points of reflection minima or transmission maxima where the SPR occurs. These reflection or transmission characteristics are generally studied under a range of incident wavelengths or incident angles.
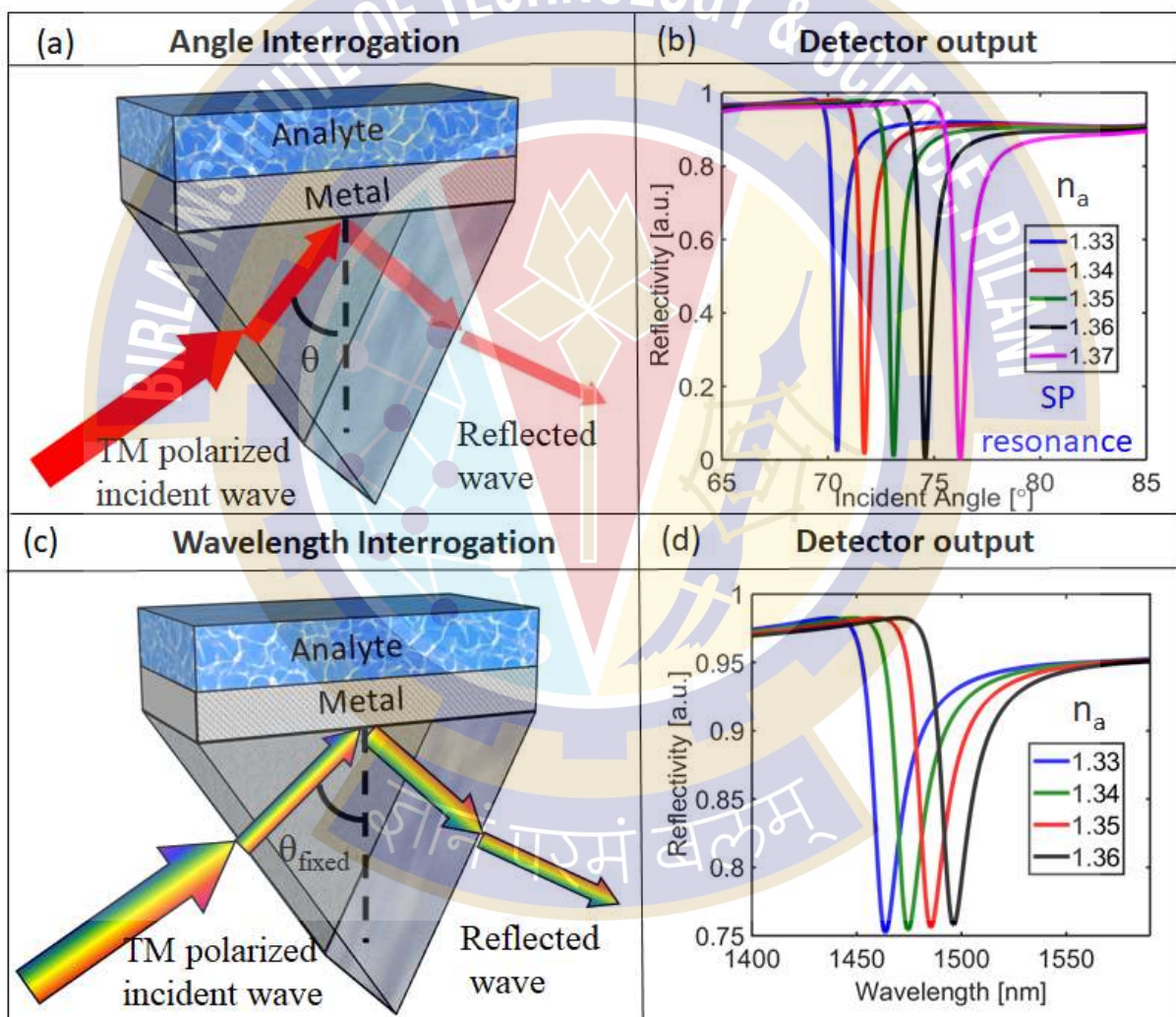
Fig. 1.2 (a) Schematic for angle interrogation (narrowband excitation) using prism-based coupling (b) Reflectivity curves with variation in the refractive index of the analyte under angle interrogation (c) Schematic for wavelength interrogation (broadband excitation) using prism-based coupling (d) Reflectivity curves with variation in the refractive index of the analyte under wavelength interrogation.

Fig. 1.2(a) shows an angle interrogation scheme (narrowband excitation) using prism-based coupling where a monochromatic light source excites SPP at the metal-analyte interface after the phase matching condition is achieved. The reflected light is captured in the detector for different angles of incidence and a sharp dip is observed in the reflectivity curve for a particular value of SPR angle as shown in Fig. 1.2(b). Such interrogation technique refers to angle interrogation (Fig. 1.2(b)) where the change in the refractive index of the analyte is measured in terms of the shift in the SPR angle. Alternative to this method is the wavelength interrogation or broadband excitation as shown in Fig. 1.2(c) which involves a spectral variation of the reflected light under a fixed angle of incidence. The resultant SPR curves are investigated as points of reflection minima under a given set of wavelength range as shown in Fig. 1.2(d) and the changes in the refractive index of the analyte are measured in terms of the shift in SPR wavelength.

For the plasmonic devices to act as a biosensor, a self-assembled monolayer is usually employed to activate the sensing surface [15]. This activation layer provides the immobilization of the ligands (biomolecules) to the target surface, thereby causing variations in the surrounding region. Of late, 2D nanomaterials have also been intensely studied to improve the sensor performance along with an additional advantage of providing oxidation stability to Aluminum (Al)-based plasmonic devices. It is well-known that 2D nanomaterials act as Biorecognition Elements (BRE) for biosensing applications [16]. However, there are limited reports on the analysis of such Transition Metal Dichalcogenides (TMDCs) over Al-based plasmonic sensors with enhanced sensitivity and Figure of Merit (FOM) in the Near-Infrared Region (NIR). In addition, biomedical sensing applications require carbon-based terminations to be accurately detected. Generally speaking, the essence of biomedical sensing is the accurate detection of carbon-based terminations of certain analytes (ssDNA, viruses, proteins) which brings forth attention toward 2D nanomaterials [17]. This mechanism modifies the confined electromagnetic field at the boundary surface of the metal-analyte interface. Moreover, there is a dearth of research on 2D nanomaterials with Al-based plasmonic devices (prism/ periodic nanostructures) in the NIR region that can justify accurate sensing with high-performance sensing parameters.
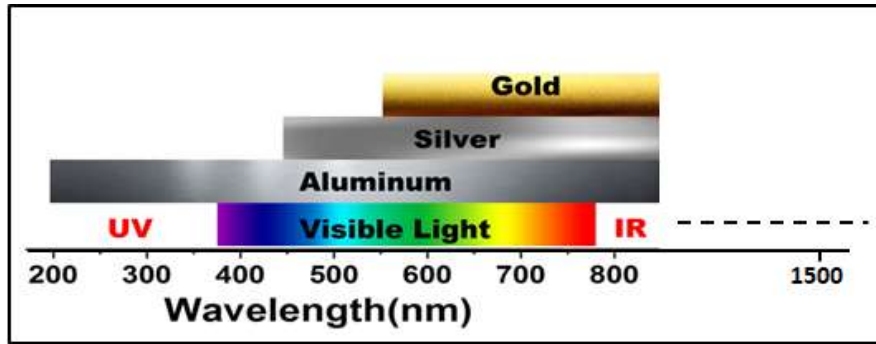
Fig. 1. 3. Schematic showing Al as the universal plasmonic metal for the entire electromagnetic spectrum taken from ref. [18].

Fig. 1.3 represents the existence of the plasmonic behavior of Al in the entire UV-Visible-NIR region [18]. Recently, a few reports on Al-based plasmonics have come to the forefront. However, most of the established work is still largely limited to the (Ultra-Violet) UV and visible part of the spectrum, despite the advantage of observing the non-destructive analysis for the NIR region [19]. Nowadays, optical fiber is the center of research for all kinds of communication and deep tissue imaging in mammals requires the probes to delve into NIR sensing [20]. Thus, to realize integrated photonics in the near-infrared region, cheaper solutions for mass production with better optical output must be made viable.

Although, tremendous research on Gold (Au) and Silver (Ag)-based SPR sensors has provided remarkable results for visible region. However, the on-chip sensors call for resources with better Complementary Metal Oxide Semiconductor (CMOS) compatibility which are also economically viable at the same time is the need of the hour. A cheap material that can respond plasmonically well over the entire electromagnetic spectrum along with a better optical output would be an ideal choice for large-scale production of SPR-based plasmonic sensing.

1.2 Motivation and Objectives

The need of the hour for high-quality plasmonic sensors is to be of lower cost, simpler fabrication techniques as well as high-performance sensing parameters that can promote the feasibility of plasmonic devices on a large scale without any photo-degeneration of bio-samples. Thus, the motivation of this work is to investigate plasmonic sensors that can address the following concerns:

1. hold economic value to favor large-scale production and compatibility towards optoelectronic devices.

2. feasible enough to work for telecommunication wavelength for easier integration to an optical fiber with self-referencing capability.

5

3. offer high-performance sensing parameters as the optical outputs in the near-infrared regime

4. exhibit robustness to follow both modes of interrogation simultaneously.

5. can cover a larger spectral range to sense a large number of analytes corresponding to different wavelength regimes.

6. can be integrated with 2D nanomaterials for enhanced sensing parameters.

7. can offer multiwavelength sensing in a single experiment.

Based on the above facts, we narrowed down our objectives to the following:

1. To investigate the Silicon-Graphene (Gr) layers over an Al-based plasmonic device for enhanced sensitivity and high adsorption in the near-infrared region.

2. To investigate 2D TMDC material (MoS_2) over Al-based plasmonic devices for both enhanced sensitivity and FOM in the near-infrared region.

3. To investigate 2D nanomaterials on Al-MXene-based plasmonic devices for enhanced robustness and higher sensing parameters in the near-infrared region.

4. To engineer a multi-layered Al-based plasmonic device with a metal-dielectric-metal configuration for enhanced resolution of the sensing device.

5. To engineer 1D and 2D Al-based periodic plasmonic nanostructures for sensing applications with self-referencing and multiwavelength sensing capabilities respectively.

6. To engineer an Al-nanostructure-based plasmonic device with enhanced sensitivity and FOM for both wavelength and angle interrogation.

1.3 Thesis Outline
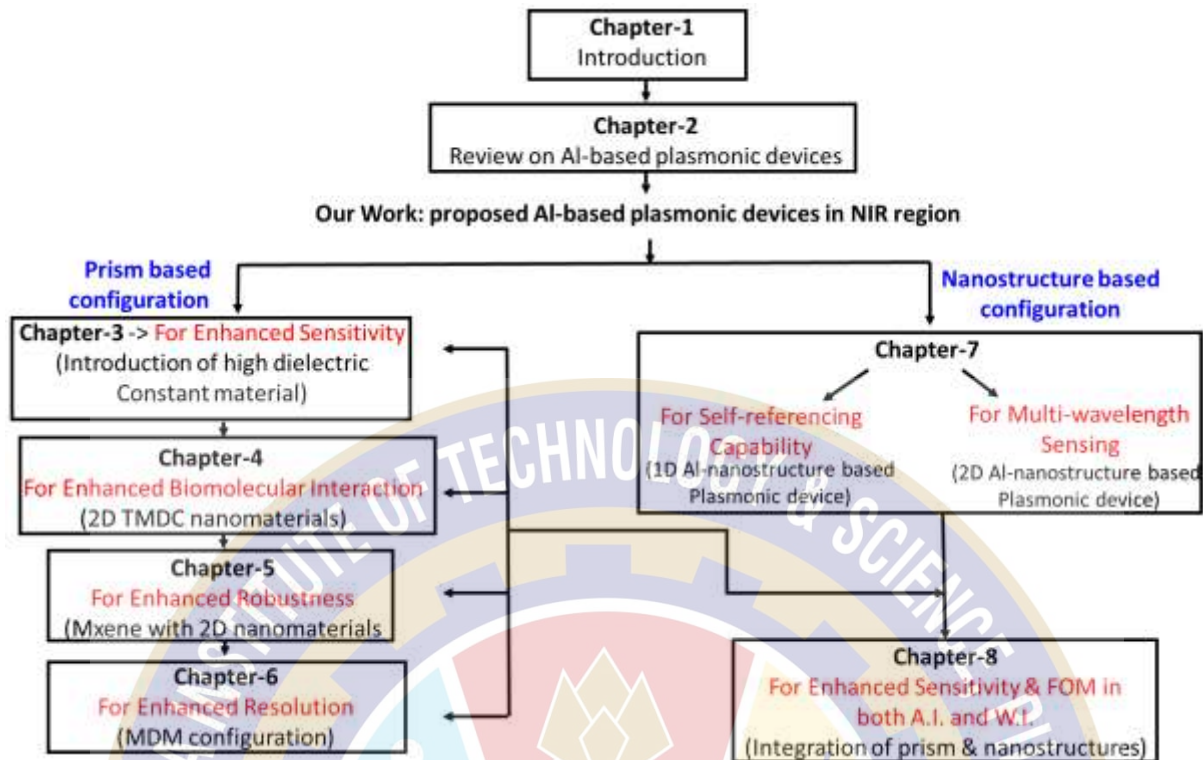
Fig. 1. 4. Flowchart for the thesis organization.

The flowchart in Fig. 1.4 explains the thesis organization into chapters as follows:

Chapter 2: This chapter presents a review of literature that discreetly elaborates on the **previously reported results and discussions in the field of Al-based plasmonic devices in the form of nanoapertures, nanofilms, and nanostructures**. A multitude of research is seen in the UV and visible part of the spectrum, **with limited reports in the NIR regime** that motivates us towards the investigation of Al-based SPR sensors in the NIR region.

Chapter 3: Angle scanning over **Si-Graphene (Gr) stacks** is utilized for prism configuration coated with thin Al film to capture the changes in the refractive index of the analyte with enhanced sensitivity. The high-index dielectric layer (Si) is employed for increasing the sensitivity while Gr is used for enhanced biomolecular interaction. At the same time, the uniqueness of the plasmonic device holds in detecting both the bulk and surface sensitivity.

Chapter 4: Moving beyond Gr, this chapter presents a comparative analysis of different combinations of **Al-MoS₂**-based plasmonic devices at 1550nm under angle interrogation. Among the proposed Al-MoS₂-based plasmonic devices, Al-Si-MoS₂-Gr and Al-MoS₂-based devices are found to be the best-suited designs for biosensing applications. While the former exhibited maximum sensitivity, the latter showed greater FOM. This chapter provides us with an interesting insight into MoS₂ material that enhances FOM due to the negligible imaginary part of the dielectric constant in the NIR region.

Chapter 5: Keeping up with the strategy of improving sensing at a minuscule level via angle interrogation, next we examine the biomolecular interaction of **Al-MXene-based** plasmonic devices in the NIR region, in the vicinity of 2D nanomaterials, which is the first of its kind in terms of sensing at longer wavelengths with underlying thin Al film as the plasmonic metal. Robust heterostructures formed with MXene provide stability in terms of oxidation as well as enhanced interaction with the biomolecules.

Chapter 6: To further uplift the performance parameters, a **multi-layered configuration** involving **metal-dielectric-metal** as the intermediate layers in Al-based plasmonic devices leading to enhanced field confinement, is used to detect changes in the different blood components. Here, barium titanate is considered as the high-index low loss dielectric material sandwiched between Al thin film for the proposed MDM configuration.

Chapter 7: After prism-based configurations, we switch to exploring the wavelength mode of interrogation for a **plasmonic device with Al-based 1D periodic nanostructures** that provide self-referencing capability in the near-infrared regime for sensing applications. To demonstrate **multi-wavelength SP sensing in two different wavelength regions, Al-based 2D periodic nanostructures** are proposed where the characteristics of analyte at different wavelengths can be extracted in a single experiment.

Chapter 8: Finally, we move on to investigating such an Al-nanostructure-based plasmonic design that can perform **both angle and wavelength interrogations** with **enhanced sensitivity and high FOM simultaneously.** This chapter integrates the entire ideology of the preceding chapters. Both prismatic and nanostructure-based arrangements are utilized in the same plasmonic device for enhanced sensing parameters.

1.4 Conclusions

This chapter provides the background for SPR-based optical sensors and subsequently defines the objectives of the proposed thesis work. The following conclusions can be drawn from this chapter:

1. The resonance phenomenon at the metal-dielectric interface is a result of phase matching condition between the incident light and the SPs, giving rise to a change in the optical properties studied in terms of reflectivity or transmittivity spectrum.

2. The incident light coupling can only be initiated by inculcating certain arrangements, such as a high index prism or periodic nanostructure to allow phase matching at the boundary surface.

3. As Al produces narrower linewidth of SPR curves and its cost-effectiveness can be a major advantage for the large-scale production of sensor devices. Therefore, investigating the plasmonic behavior of Al in the NIR region is the essence of the thesis.

4. For the biofunctionalization of the sensing surface of the plasmonic sensors, the unique properties of 2D nanomaterials such as Graphene, Molybdenum disulfide, Black Phosphorus, Fluorinated Graphene, and MXene can be exploited in order to ensure effective sensing characteristics.
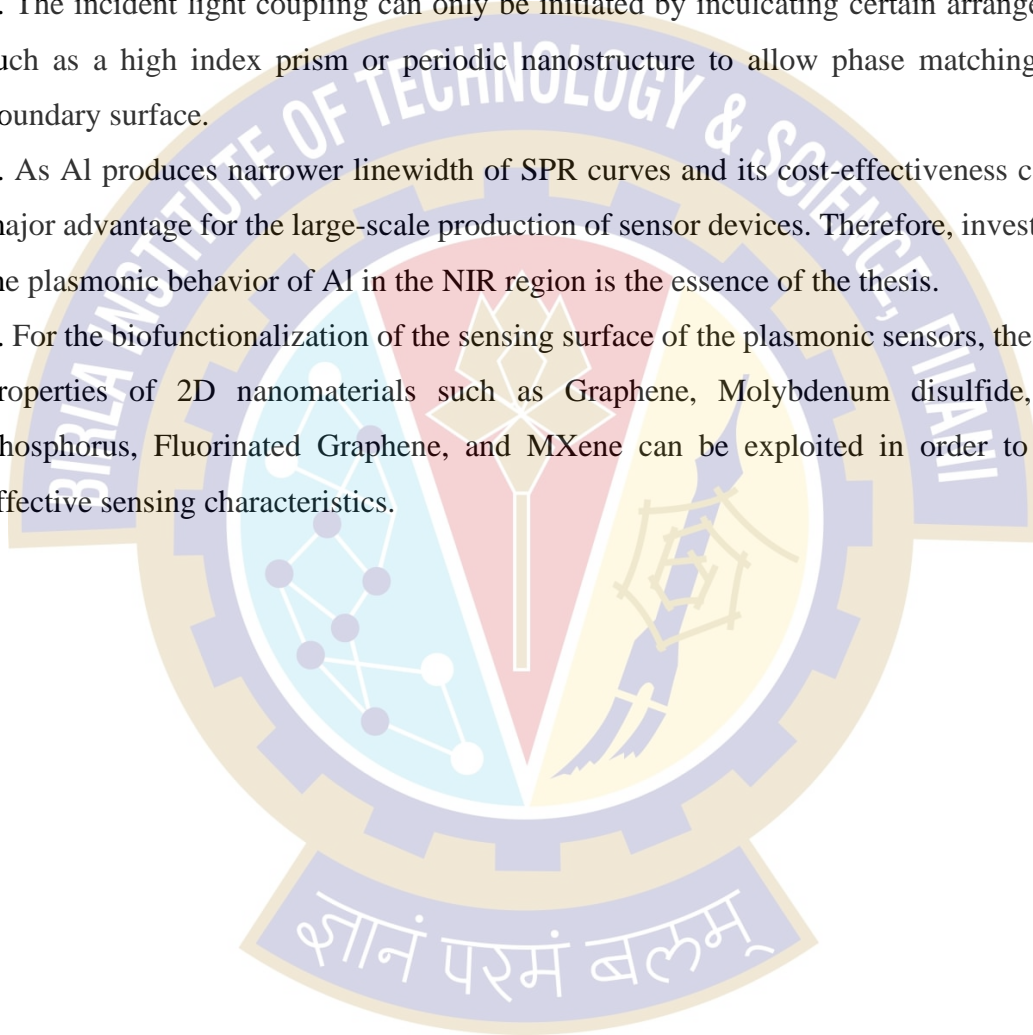
Chapter 2

Literature Review and Methodology

A deeper understanding of materials sciences has envisaged "plasmonics" to become a rigorously evolved domain in a vast field of unprecedented applications. Intense electric field confinement towards the nanoscale dimensions results in plasmon resonance at the interface of two different media. Among the plasmonic activity initiators, noble metals such as Au and Ag have been the leading contenders. No wonder, Aluminum (Al) being the first non-noble metal upon which the plasmons were evidenced, got relatively behind [21].
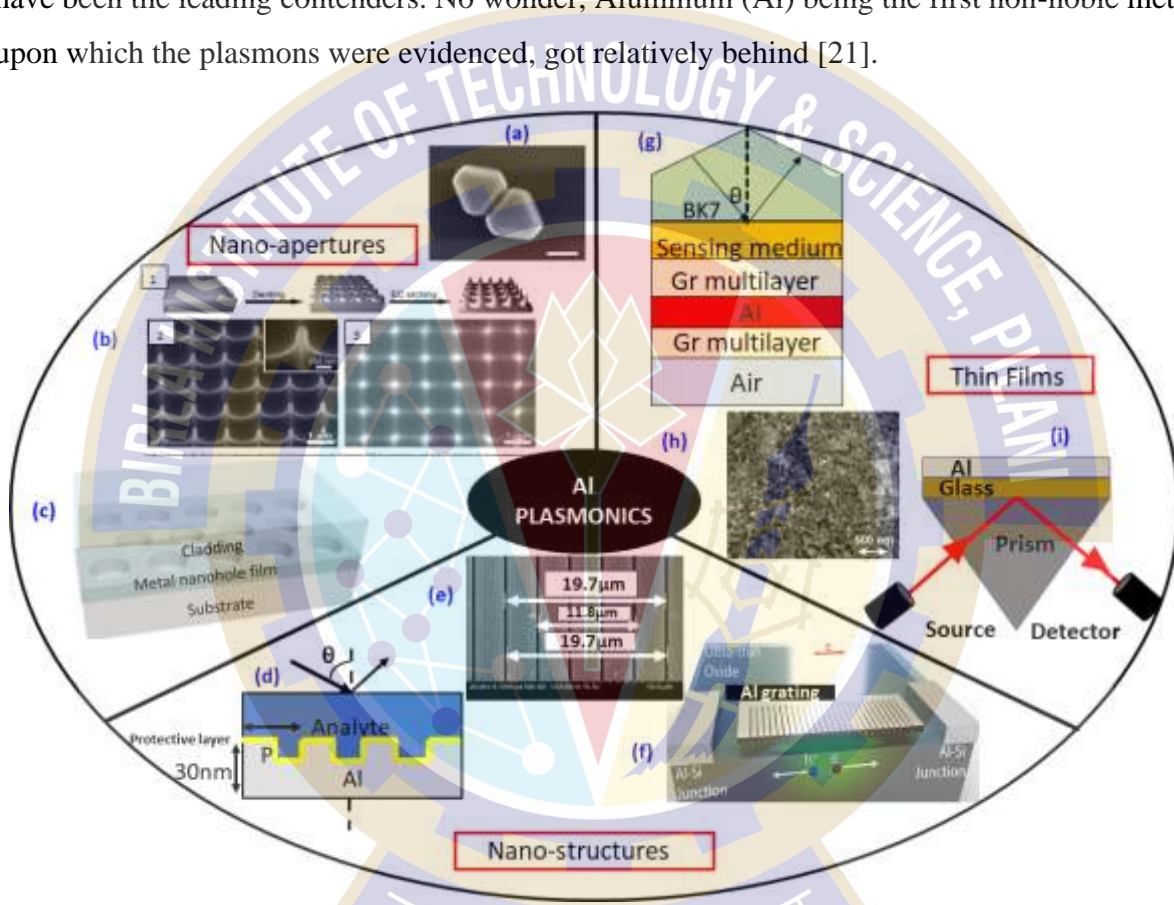
Fig. 2.1 Recent works on Al-based plasmonic devices (a) Scanning Electron Microscopy (SEM) image of Al dimer from Ref. [1] (b) Al nanopyramid array (NPA) with (1) array synthesis procedure, SEM image of (2) side view (3) top view from Ref. [2], (c) Schematic of Al ultra-thin film with a hexagonal nanohole array from Ref. [3] (d) Schematic of Al-based nanostructure covered with a protective layer from Ref. [4] (e) SEM image of Al nanostructure with the indication of measurements of periods [5] (f) Schematic of Al-Si-Al photodetector from Ref. [6] (g) Schematic of Gr-Al-Gr sandwich-like structure from Ref. [7] (h) SEM image of an annealed Al film from Ref. [8] (i) Illustration of Kretschmann configuration with Al-film from Ref. [9].

2.1 Introduction

As Al is much cheaper [22], CMOS compatible [23], providing a better optical response in terms of narrow linewidth [24] as well as stability (due to alumina formation) [25], it has returned to the research spectrum, after almost sixty years of its entry in the plasmonic domain in 1959 [21]. Al films that are deposited via thermal evaporation techniques have naturally formed nanostructures over a large area, thus being an ideal candidate for large-scale production [26]. As it is well known, a high negative real part of the permittivity of Al promises stronger plasmonic resonances [27]. The broadband nature of Al has already been evidenced before, spanning across the entire electromagnetic spectrum from UV to NIR region [28][29]. At the same time, the nonlinear optical response of Al is much greater than Au, and Ag which makes Al a suitable material for a higher-order harmonic generation [30]. Some of the works in this review suggest that structural geometry plays a prominent role in field manipulations at the nanometer scale.

Fig. 2.1 shows exemplary results with Al-based plasmonic devices in the form of nanoapertures of Al nano-dimer (scale bar =200nm) [1], Al NPA array with a two-step procedure i.e. imprinting followed by electrochemical etching as shown in figure 2.1 ((b) part) [2], hexagonal nanohole array [3], Al-nanostructure covered with protective layer to avoid oxidation [4], Al-nanostructures with indicated measurement of periods[5], photodetector comprising of 50nm thick Al periodic nanostructure array [6], and thin films with sandwich likie structure for SP excitation at 633nm [7], annealed Al film at 700°C for 10mints in forming gas [8] and Al-based Kretschmann configuration from ref [9]. Additionally, Al-based plasmonic devices have been widely implemented in the biosensing domain [9],[31].

In this chapter, we collect a wide range of various exciting results and possibilities that are arising out of Al-based tunable plasmons on the metal-dielectric interface. Al has already entered into a wealth of applications, right from on-chip plasmonic integration to point-of-care diagnosis. Here, various Al-based plasmonic devices that have been presented in the past, over the entire wavelength spectrum, are discussed. In general, when we talk about the dielectric constant (ϵ), Al exhibits a negative real part of ϵ over a broader spectrum as compared to Au and Ag exhibiting metallic nature over a larger range [32]. For various bioentities (aromatic amino acids in cells, nucleotide bases, nucleic acids) having absorption bands in the UV region [33]. Al exhibits a fairly high faraday number that refers to the ability of a material to enhance electromagnetic field in the proximity of the interface [33]. Al is the only material that facilitates a fluorescence-free background hence improving the signal-to-noise ratio for UV

and Deep UV excitations [31]. Unlike Au and Ag, the high plasma frequency of Al allows for remarkable plasmonic responses in the UV portion of the EM wave spectrum. Since Ag has interband transition around 350nm, hence Al is the most appealing material for biosensing towards higher energies i.e., the UV band. Although Gerald et al. have beautifully culminated results of Al films ascertaining the Localized Surface Plasmon Resonances (LSPRs) in the UV region, yet they are in affirmation of its extensive use in the visible and near-infrared band as well. However, the strong radiative losses in the UV band can cause a bottleneck. Meanwhile, when it comes to the visible region (400-700nm), the ability to control the Al thickness, down to the size of a few monolayers has made it the "Silicon" of superconductivity, initiating high fidelity for nanofabrication techniques [34]. With controlled fabrication under pristine conditions, pure Al nano-disks exhibit maximum light scattering capability in the visible region. Thus, admitting Al for plasmonics in the visible regime [35]. However, the work that highlights the importance of SPR measurements for biochemical variations in the living cells for the first time, clearly explains that the SPR methodology excluded in-vivo interactions when the commercial binding characteristics were studied (e.g., BIA core) in the visible region [36]. Since the NIR region corresponds to the transparent window for the majority of the living tissues, so, for non-invasive and non-destructive medical diagnostics, the NIR region becomes a region of prime importance [19]. The imaginary part of the dielectric constant for Al reduces with longer wavelengths, hence resulting in SPR curves with reduced linewidth, thus increasing resolution in the NIR region [22]. Also, the relative abundance of Al for the design of plasmonic absorbers in the solar hybrids' conversion (45% of the total solar intensity is located between 750 nm and 1.75 µm), or for inexpensive Surface-enhanced Raman Scattering (SERS) and fluorescence enhancing substrates are some of the captivating properties for the use of Al in the NIR spectral region. The indispensable advantage of CMOS compatibility enables the use of Al-based plasmonic nanostructures for silicon-integrated optoelectronic applications, such as integrated biomolecular sensing [37]. Thus, the ability of Al to be extensively exploited in all the respective spectral regions makes this plasmonic material to be universally important in the SPR sensing domain.

We have divided this review into three different forms of Al (nanoapertures, nanostructures, and thin films) based plasmonic devices that can take over the entire band of the spectrum with intense field confinement at the boundary surface. Each section enlists the results and discussions of breakthroughs in the field of Al-based plasmonic devices, depending largely on thickness, size, shape, periodicity, and the fabrication procedures involved.

2.2 Nano-apertures-based plasmonic devices

2.2.1 Ultraviolet [U.V.] band

Among the early works, Al was found to be the most effective in the UV range. Mahdavi and Blair showed that nanoapertures (diameter 70-90nm) in Al would exhibit the greatest excitation intensity enhancement (of the order of 3 as against the order of 2 in Au and Ag) for dyes under 266 nm excitation wavelength. Nevertheless, by choosing nanoparticles (size less than 10nm) of different shapes, it is possible to analyze the relative contribution of varying shapes (same volume), given that NPs exhibit high catalytic activity by UV illumination. This is due to the large surface-to-volume ratio, thus pointing towards photocatalysis application. With just 1.8% metal content, the absorption cross-section in $Al + Al_2O_3$ is comparable to Rhodium (Rh) and Gallium (Ga) spherical NP. Although, the effect of the oxide layer weakens the absorption efficiency, but the effect is less significant in the case of an increasing size of Al nanoparticles as it forms a self-terminating oxide shell [33]. Chemical synthesis of Al NP for UV plasmonics has been shown for two different families of Al NP: one with an average diameter of 2nm and the other with a diameter ranging from 10nm to 20nm. For the aforementioned families, the lowest FWHM achieved is 25nm (experimental results) which is relatively low [38]. Among the works done on higher-order modes of Al-based nanoantenna better tunability of the localized electric field is demonstrated by Graphene (Gr)-based Al Nano-Ribbon (G-AlNR). This phenomenon is more pronounced in the UV region as compared to the corresponding fundamental modes in the visible range. To comprehend the absorptivity of the proposed G-AlNR plasmonic device, parameters like the thickness of the AlNR and the vertical distance of the embedded Gr in the Al_2O_3 substrate are among the important ones. Proposed third-order G-AlNR shows sensitivity and FOM of 25nm/RIU (Refractive Index Unit) and $3RIU^{-1}$ respectively [39]. Oxide shell thickness over Al core for nanocylinder (diameter = 20nm) and nano spheres influences the peak position without any reduction in the extinction spectra cross-section. Similarly, by modulating the aspect ratio (length/diameter), SPR curves for the Al core/Al_2O_3 shell can be red-shifted. Thus, extremely short resonance wavelength and tuning of the geometrical parameters of Al nanostructures bring about multipole resonance peaks in the deep UV to blue light region. Such multipole resonance appears even when the particle size was still relatively small, which has only been witnessed in other metals at larger particle sizes [40]. On studying the reflection light scattering properties of Al nano shells, unique thickness-dependent scattering features were observed. The authors have reemphasized that Al should be

the primary plasmonic material in the wavelength range of 100 nm-315 nm. Exploiting Al nanodimers to be used as a substrate for SERS, it is seen that the Al nanosphere of radius 6 nm has the highest absorption cross-section. The optimal SERS enhancement factors are still substantial with peak $|E|^4$ values for Al and Al/Al$_2$O$_3$ being 2 x 10^9 and 1.2 x 10^7 respectively [41].

Furthermore, multipole resonances are discussed with different diameters of spherical NPs in deep-UV wavelength, due to reduced interband damping for higher-order modes. With the particle size being comparable to the respective incident wavelength, the conduction electrons resonate resulting in dipole, quadrupole, and octapole resonances. For example, at an NP diameter of 200nm, broad dipole resonance is seen, red-shifting the bands towards the NIR region. These reports once again deduce the fact that the optical characteristics can be strongly modulated by altering shape, size, and the type of metal used.

From the application point of view, as the resonant energy of LSPRs closely matches the electronic transition energy of most biomolecules, utilizing Al NPs for such platforms produce very good homogeneity and reproducibility in the UV region [42].

Comparison with Au and Ag nanoaperture-based plasmonic devices:

A significant absorption enhancement for Al NPs is predicted for Organic PhotoVoltaic (OPV) devices when compared with Au and Ag nanoparticles [43]. By observing the isotropic and anisotropic behavior of Cu, Ag, Au, and Al nanostructures in the entire electromagnetic spectrum (FDTD analysis), Al nanorods showed the highest refractive index sensitivity (shift in the LSPR wavelength v/s the change in the refractive index of the medium) of about 375.06 nm/RIU in the UV region [44]. Compared to Au and Ag, a stronger redshift and broader absorption peaks are observed with the Al NPs in the UV region which has compelled the researchers to delve into exploring Al in the sub-nano-meter range. Also, they exhibit greater localized field interaction owing to their lower imaginary dielectric constant in this regime [32]. Unlike Ag and Au nano-shells, the shorter wavelength antisymmetric peak was observed to be stronger than the longer wavelength symmetric peak for the Al counterpart. This in turn is very advantageous for applications dealing with deep UV range. By manipulating the inner core radius, inner core dielectric constant, or the oxide shell thickness, the high energy anti-symmetric peak can easily be tailored for biosensing applications [45].

2.2.2 Visible band

To blue-shift, the cross-over wavelength (a region where the solar spectrum is still intense) to the edge of the solar spectrum, the Al nano-disc is placed in an array on the surface of the Silicon (Si) diode. This arrangement substantially blueshifts the cross-over point as compared to Ag NPs on thin film solar cells, leading to enhanced photocurrent generation [46]. EELS and cathodoluminescence measurements were used to investigate 'thick' Al nano disks (when the diameter is comparable to thickness). The authors arrived at two conclusions here: At a fixed thickness of Al nano disks (15nm) and varying diameter (from 20nm to 120nm), plasmonic modes of Al nano disks can be spectrally tuned from deep UV to visible region. Also, the difference in the electron beam position corresponds to different colors, thus labeled as different modes for respective beam positions away from the nano disk center [47]. Since the relative contribution to the absorption spectrum for Al nanoparticles is majorly size-dependent. In that regard, Al nanospheres exhibited higher FOM for sensing in the shorter wavelength region, nanorods, on the other hand, showed higher FOM in the range of 250 to 450nm and nano disks showed higher absorption spectra over a larger part of visible-NIR wavelength regime [48]. The shape of the NP is another factor that affects the pattern in which the electrons are oscillating, thereby changing the corresponding resonant frequency. Thus, Al nanospheres (monomer), nanorods (dimer), and rhombus nanostructure (multimer) configurations were studied with different polarizations and interparticle spacing. The local enhancement factor (η) (ratio of the intensity of field around the object and the incident field) decreases as the dipole resonance mode (<20nm) changes to quadrupole resonance mode (>30nm). The variation in η is also seen with reduced interparticle distance due to the additive effect of the mutual interference effect. The multimer configuration is polarization insensitive which shows more hotspots for the dimer configuration. On the other hand, longitudinal plasmon coupling is much stronger than transverse coupling [49]. In the view of the fabrication, when subwavelength holes were fabricated in a triangular array instead of a square array, the wavelength interval between two SPR peaks was considerably larger thus avoiding cross-talk filtering along with reasonable transmission efficiency. As a result, a nano-hole array with a larger hole size in a thinner Al-film offers higher transmittivity but larger bandwidth [50]. At sub-nanometer dimensions, even the Quantum-Mechanical (QM) effects are likely to become notable. Stronger QM effects are expected by Al as compared to Au. Therefore, a full QM investigation on multi-concentric Al nanoshells is presented by Kulkarni et al. Among the QM effects, (for example electron tunneling) it is agreed that there is a disappearance of plasmon

15

peaks at lower energy. However, these effects are occurring at larger separations for metals with lower work functions such as Al [51]. For a clean route of hydrogen production from water, hematite as a photoanode has limited Solar to Hydrogen (STH) efficiency due to low Internal Quantum Efficiency (IQE). Instead, utilizing Si-Al-Fe$_2$O$_3$ Core Multi Shell (CMS) Nanowire (NW) structures are employed where the visible range plasmon resonances are used to enhance the field in the 50nm hematite shells. The resultant absorption enhancement in Al-based CMS NW is high with an STH efficiency of 14.5%. Although this study concentrates on a single NW and not on large-scale devices [52]. The authors have elucidated the fabrication details of Al nano rings (diameter 90nm, wall thickness 30nm) using a double patterning process. The redeposition during the etching process results in 60% Al and 40% dielectric which redshifts the observed resonance as compared to bulk Al. But the central wavelength is still tunable across the entire visible spectrum [53]. In Al nano-dome array, the incident light (532nm) manifests itself better in the SP excitation, when compared to Al nanocavities. These SP resonances are strongly dependent on the periodicity and also the few-layer-Gr that is used as a 'SERS mediator' here. As a new plasmonic material, Al@Al$_2$O$_3$ core-shell nanostructures are studied by Ziashahabi et al. Herein, the plasmonic longitudinal peak is noted for nanorods with different dimensions and different dielectric environments. It is observed that the plasmonic wavelength got red shifted on increasing thickness of Alumina as well on increasing length of nanorods with the same diameter [54]. Further in 2018, the synthesis of single crystalline Al nanorods most notably with the P-polarised light is discussed, which is spanning across the visible and UV regions of the spectrum. The optical properties of such nanorods are dominated by higher-order quadrupole and octupole modes. Already the single crystalline Al has two times lower imaginary constant than the polycrystalline Al, thereafter, longitudinal resonances can be tuned across the visible band when the rods are scaled down in overall size by a factor of 5-10 [55]. During the same time, Gillibert et al. explored the optical characteristics of periodic Al nanocylinders over a range of different diameters. The quality factor for Al nanocylinder values can reach up to 70 for wavelengths up to 500 nm. Also, based on their tunability for different areas of the visible region, they can have any of the dipolar, hexapolar, quadripolar, and Woods anomalies [56],[57]. Among other applications, the Plasmonic Color Filtering (PCF) application which was usually fulfilled by Metal Insulator Metal (MIM) stack layer configuration, utilized square arrays of Al nanorings placed over ITO-coated glass substrate, for the first time, for improved selectivity. The geometry follows a simulation study showing high tunability over a broad-spectrum range. Selectivity of PCF, is addressed by using a 40nm thick Al nano-rings array (inner radius = 20nm, outer radius =

16

55nm, ring width = 35nm for magenta/green) for realising dual-mode (additive and subtractive) color filters. As a result, high optical efficiencies (65%-70% transmission) and narrowband response (FWHM – 20nm) result in highly selective PCFs in this simulation study [58]. Later, for the first time, Al nanoring was fabricated for efficient plasmonic biosensing. In the range of 1.4 to 1.5 RIU (for chemical and industrial biosensing), the proposed sensor produces high sensitivity of 408nm/RIU and FOM of about 5.88 RIU^{-1}, which is much better than the previous Au-based nano-rings listed by the authors [37].

Comparison with Au and Ag nanoaperture-based plasmonic devices:

With a comparative analysis among different metallic nanohole films (Au, Ag, Cu, Al), Al showed a minimum FWHM of about 10nm with an obvious compromise noted in the reflectivity minima, at 600nm [59]. The Al nanosphere (radius = 6nm) exhibited an absorption efficiency (Q_{abs}) of 13.0, leaving behind Au, Ag, and Sodium. Using the size and permittivity of metal NPs as a basis for studying image reconstruction, Al has a larger range of wavelength among the metals with minimal deviation from the ideal condition of $\varepsilon = -1$, thus serving better for minimal losses incurred [60].

2.2.3 Infrared [I.R.] Band

The resonance can be tuned from 400nm to 1400nm by varying the Al nano-shell thickness when the application concerns dual broadband SPR peaks. Nanoshells (R_1 = 15nm, R_2 = 20nm, shell thickness = 0.6nm) can be preferred over nanodisks, with two distinct peaks each in the visible and NIR region. [61]. By simply varying the NP size, the plasmonic response can be varied over a broad spectral range. In the quest for exploring the core-shell nano geometry for tuning the resonance activity, Al@Gr nano spherical nanostructures were studied showing high tunability from visible to IR region (558-1448nm) with surrounding media as TiO_2 that have better extinction efficiency than Au and almost comparable to Ag [62]. Studying the Al nanoparticles of non-spherical shapes i.e. "nanocaps" has shown potential applications in the NIR region. Using the discreet dipole approximation model, the optical properties of Al nanocaps were studied, the results of which were close to the experimental ones. The experimental results show relatively broadened peaks due to higher aggregations of suspended particles [63]. In 2014, Jerome and co-workers have detailed that Al is no longer limited to UV applications and can well be explored for the next generation of nano-optics based on the near IR region. They have experimentally investigated the dissipation related to an individual nanoantenna. Here, the modes are resolved spectrally and spatially using high-resolution EELS

images of individual Al-nanoantenna. What makes these multipolar modes more distinguishing from Au, and Ag is that the high free-electron density as well as their high value of bulk plasma frequency, make the resonances well separated in energy space. A higher aspect ratio (length/width) for higher-order modes of nanoantennae would mean narrower linewidth as compared to their dipolar counterparts at the same energy level. This results in high-quality factor (energy/linewidth) due to reduced radiative as well as interband transition damping [28]. Recently in 2020, the Bowtie NanoAntenna array (BNA) with Al MIM configuration was explored by Wang et al. Here, the geometric parameters such as gap distance, period, antenna side length, antenna thickness, antenna angle, and thickness of insulating layer are tuned across the UV-Vis-NIR region. Geometrical parameters of the Al BNA array with MIM structure are optimized and these are useful in high sensitivity bio-sensing platforms with a sensitivity of 497 nm/RIU [64]. Up conversion, photoluminescence explains the emission of photons with higher energies as compared to absorbed photons, the amplification of which is 100 times with the help of Al nanocylinders. The light incident on the nanocylinders (λ=980nm) creates hot spots near the edges which alters the local electric field, hence overlapping with upconversion to facilitate optical absorption by rare earth metals. Plasmons of Al NanoPyramid Array (NPA) have been used for cancer diagnosis in the entire UV-Vis-IR wave band. The reflectivity spectrum was tuned by varying incident angles, wherein the UV-blue plasmon bands mainly existed in only two angle intervals (8-46º and 65-68°) meanwhile, visible and NIR plasmons could be found at all angles. Since CA 199 is a biomarker specific to cancer exists, therefore, apart from showing excellent selectivity, the Al NPA biosensor was used to detect changes in the concentrations of Cytochrome C and CA199 with limits of detection being 800nM and 28ng/mL respectively [2]. In 2008, the plasmonic properties of Al nanodisks were explored to support long-lived LSPR, thus giving rise to potential alternatives like plasmon-enhanced photovoltaics. Pronounced peaks are seen for the measured extinction efficiencies with a range of Al nano-disk diameter at a constant height of 20nm from visible (~300nm) to the infrared region (~2400nm) which is associated with dipolar LSPR [65]. Later, Liu et al. discussed that compared to nano disks, nanospheres, nanorods, and Al nanoholes are easier to fabricate plus useful for applications like optical nanocircuits and plasmonic nano-lasers. Considering the effect of interband transitions at around 800nm, nonlinear optical properties are studied for Al nano shells in CS_2 solution. The results show that by tuning the inner radius, interband transition-induced absorption can enhance the third-order nonlinearity of Al-CS_2 composites in the NIR region [66].

Comparison with Au and Ag nanoaperture-based plasmonic devices:

Compared to Ag, and Au NP, which are agreeably more prevalent in NP research, the lower cytotoxicity of Al NP makes it a promising candidate. Lower corrosion rates of Al as compared to Ag in aqueous solutions and higher cost of Au NP particularly in the cancer treatment area have paved the way for growing Al use in the biomedical industry [67].

2.3 Nanofilms-based plasmonic devices

2.3.1 Ultraviolet [U.V.] band

Al can equally be employed for metal-enhanced fluorescence apart from the already known application of Al being a fluorescence "quencher". A 10 nm thick Al film showed a reduced fluorescence lifetime for the system to be cycled faster in addition to fewer destructive processes occurring. This work provides the usefulness of robust Al film substrates in fluorescence-based bioassays such as DNA [68].

It is worth noting that Al epitaxial films are now been used for high-performance quantum computers requiring high-quality Al superconducting qubits. The growth of Al epitaxial films on commercially available substrates (GaAs, sapphire) has opened the window to explore Al plasmonics for real-world applications [34]. When Al thin film for far-UV and deep-UV was compared with Au-based sensor in the visible region, the former showed a six times larger SPR angle shift thus improving the sensitivity and surface measurement accuracy and reasserting the seat of Al for UV-based sensing applications [69].

Comparison with Au and Ag thin film-based plasmonic devices:

Resolution estimation (standard deviation of noise versus the sensitivity of the sensor output) of Au, Ag, Cu, and Al single-layer and double-layer SP-based sensors was performed by FOM (depending on the type of sensor modulation implemented) analysis. Using a Rigorous Coupled Wave Analysis (RCWA), the highest enhancement i.e., the ratio of intensity at the metal-analyte interface and incident wave intensity, below 0.5µm, is demonstrated by Al among above mentioned four metals, and the Al-Au bilayer combination performs best in the UV region [70].

2.3.2 Visible band

The prediction of SPR behavior on Al film was conducted using both FDTD analysis as well as Fresnel methods for the visible region. The sensitivity for Al films was 61.6 % higher than for Au films. The experiments have shown that Al is a better choice for a typical timescale of biosensing experiments (1-8hours) as the oxide layer covered acts as a protective layer without altering the shift in the spectrum [9]. As the metal deposition conditions affect the optical performance significantly, certain rules to deposit high-quality plasmonic Al films in the visible and UV regime are set out by the authors. For example, at fixed substrate temperature, the homogenous temperature of deposition must be taken care of while depositing thin film. Secondly, to control the reactive nature of Al films, faster deposition rates are more acceptable and at the same time, the best vacuum conditions must be laid out to reduce the effect of residual gases [71].

The Al-silica interface is infiltrated with nanolayers of Ga for studying linear and nonlinear plasmonics. Ga provides reversible excitation between solid and liquid phases meanwhile Al provides a high-quality interface with silica. Investigating the intensity modulation in such a nanocomposite is studied either by changing the temperature or stimulating them with a laser source [72]. Sobhani et al. concluded that the higher plasma frequency of Al causes its linewidth to be majorly dominated by the radiative losses. Utilizing such limitation, it is seen that the linewidth becomes narrower when the nanoparticles (diameter =180nm) are close to Al film (35nm) as compared to when directly sitting on the silica substrate. The possible origin of such reduced effective radiative losses is the substrate-mediated hybridization of dipolar and quadrupolar modes [73].

Concerning the interaction of Al film with 2D nanomaterials, an exhaustive analysis of the visible region is done over the years. Al thickness of 17nm is sandwiched by Gr layers from both the top and bottom side of the film, resulting in a sensitivity increment from 274/RIU at L=1 to 1483/RIU at L=40 layers of Gr. This is the case when sensitivity refers to a change in reflectance to a change in the refractive index of the media [7]. The plasmonic design of Al-MoS_2-Al was used to obtain enhanced absorption characteristics because of stronger SPR excitation. With Al as the low-cost material which displays minimum internal damping than its counterparts, the authors claim that for minimum reflectance, Al-MoS_2 is the most suitable configuration for high accuracy and detection levels. Meanwhile, the Al-perovskite-based

configuration displays maximum peak sensitivity along with the advantage of simple synthesis for long-range SPR sensors, when compared with Al-Gr and Al-MoS$_2$ [74]. The proposed epitaxial Al films for the entire visible region attain long SPP propagation lengths (5-13 µm). This film can be used as a SERS substrate at 532nm. The chemical mapping of a substrate is tested by a vertically stacked MoS$_2$ monolayer as a uniform analyte. Thus the authors claim the possibility of using Al epitaxial films as a building material in quantum computers [34].

Comparison with Au and Ag thin film-based plasmonic devices:

A high-quality factor (resonant frequency/linewidth) has been realized for Al surface lattice which is close to the theoretical limit reported by gold surface lattice, thus we can achieve comparable results to the conventional noble metals that too at a much cheaper price [75]. Thus, we can say that coupling with Al films produces not only narrower but brighter resonances relative to Au or Ag [73].

2.3.3 Infrared [I.R.] Band

When the Al layer is used over a chalcogenide prism, its performance is analyzed by Intrinsic Sensitivity (IS) (which depends more on the SPR curve rather than the SPR shifting) owing to the unique set of excitation parameters in the NIR region i.e., higher probe depth and accurate SPR dip. As a result, 400% higher sensitivity was observed when Al film was used as compared to Au only. When Al film was used over Si prism while performing angular interrogation, tolerance of +-10% in Al thickness resulted in exceptionally high sensitivity promoting ease in fabrication. Here, it is suggested that imaging sensitivity will increase with the increasing number of Gr layers, therefore, it is undertaken as the parameter for interrogation rather than the conventional sensitivity [76].

For Ultrasound sensors, the changes in refractive index are proportional to the corresponding changes in the pressure waves. The spectral dependence of the sensor is discussed to determine the wavelengths at which the highest sensitivity is obtained using Al as the plasmonic metal. This shows that the NIR region (1550nm) is the best region to operate for Al as it gives the highest sensitivity. Even the effect of oxide is lower in the NIR region which is indicated by lower uncertainty of the reflectivity constant at optimum conditions [22]. Angular interrogation has been performed for the Au-Al-based SPR sensor for high-quality factor and FOM for the detection of hemoglobin at the wavelength of 900nm. With an optimized Al thickness of 60nm, the sensitivity of about 287°/nm was achieved along with an FOM of 0.97 deg^{-1} [77].

When palladium is used for hydrogen sensing over Al thin film, the proposed structure provides an improved FWHM of 0.49° as opposed to 0.92° and 0.71° for palladium over Au and Ag respectively [78].

Comparison with Au and Ag thin film-based plasmonic devices:

Concerning disposable sensor applications, Al films can easily replace the costly Au films, also because the Al-surface oxide growth in de-ionized water does not cause major sensor degradation [79]. The properties of eight different plasmonic materials, namely, Ag, Al, Au, Cu, Mg, Ni, Pd, and Pt were studied. Herein, the third harmonic generation which is important to study the non-linear generation from plasmonic nanostructures shows that Al can withstand rather high intensity of laser while silver has the poorest photostability [80].

2.4 Periodic nanostructures-based plasmonic devices

2.4.1. Ultraviolet [U.V.] band

The possible requirements of Al to be used in the UV region are predominantly quoted in the literature. As it is known, high frequency significantly improves the scattering efficiency, along with a large set of biomolecules that absorb light in the range of 220–280 nm, so SPR from Al nanostructures can dramatically improve the label-free detection of such biomolecules.

Gerard et al. in their review paper have discussed a list of applications where Al-based plasmonics has asserted their presence with great results. For example, the authors concurred that with Al periodic nanostructures, the efficiency of native fluorescence of many biomolecules can be enhanced by many folds, which is weak otherwise. When it comes to SERS, due to surface roughness incurred with thin films, reproducible systems with size-controllable nanostructures are being explored. In the field of optoelectronics, Al nanostructures have gained attention in plasmon-enhanced deep-UV emission in multi-quantum wells with light-emitting diodes. Al nanostructure acts as a plasmonic color filter, sorting colors and providing an additional photocurrent due to local field enhancement in an Al-Si plasmonic photodetector [32]. The surface sensing capability of nanostructures is limited by a large imaginary dielectric constant and longer electromagnetic field decay length. This issue can be overcome by using Al-capped nano slits, as demonstrated by Lee et al., thereby exhibiting Fano resonances using both angle and wavelength interrogation. The experimental results were close to the calculated values where the sensing capabilities of the proposed nanostructures were verified by measuring interactions between Bovine Serum Albumin (BSA) and anti-BSA. With the changing ridge height of the nano-slits as well as deposited film

thickness, the resulting transmission spectrum keeps shifting from Wood's anomaly dominant (peak) resonance, asymmetric Fano profile (peak and dip) to SPR-dominant (dip). Using hot embossing nanoimprint lithography, the capped Al nano slits present the narrowest possible bandwidth observed with an improved FOM of about 150. With reproducible and high throughput as well as low cost, the fabrication of such highly sensitive capped nano slits can benefit real-time sensing applications [81].

Noteworthy preparation methods of Al nanostructures were presented alongside the challenges faced during the fabrication process. During Electron Beam Lithography (EBL), the fabricated Al nanostructures suffer from polycrystallinity which reduces the overall quality factor. This quality factor can be sustained by the use of Al lattice modes that can sustain strong absorption near UV, hence can be used as fluorescence enhancers for wide band-gap semiconductors. Rapid Thermal Annealing is another self-organization approach for the fabrication of Al nanostructures. However, during the dewetting process, the formation of an alumina layer may hinder the formation of well-separated particles. To avoid this, the substrate preparation method was added to reduce the adhesion of the Al layer to the substrate [82].

Comparison with Au and Ag nanostructure-based plasmonic devices:

For the Semiconductor-Insulator-Metal structure in a nano-laser, a detailed comparison between the Al and Ag-based metal films underneath ZnO nanowires is evaluated. It was observed that the Al-based SPP nanolaser offered a favorable trade-off between the waveguide confinement factor and propagation length, thus balancing the transparency gain constant for a nano laser [83].

2.4.2 Visible band

Investigating the effect of different parameters on the SPR properties, the Al nanostructures are introduced as an alternative plasmonic adjustable for the visible region. They are supposed to have better control of geometry as compared to prism-based configurations.

From the fabrication point of view, the inconsistency of field distribution in the visible region due to the in-homogenous layer depths can be rectified by manufacturing Al nanostructures lithographically. Thus, ensuring uniformity in adsorption and making it viable for deployment in the visible region [84]. The plasmonic color filtering operation is the ability to achieve full-color tuning and image switching across the entire visible spectrum as was demonstrated by a 2D periodic array of Al nanostructures ($P_x = P_y = 400nm$, thickness = 35nm) on an elastomeric

n-type Si substrate. Based on the gentle elastic modulation along the long and short axis of the nanostructure substrate, the periodicity changes, and thus the corresponding wavelength-selective scattering response is obtained, paving way for flexible photonic devices [85]. A unique color-filtering system called camouflage requires the desired image content to be as such regardless of the orientation. Here, angle insensitivity becomes a prime concern. Al-based nanostructures of 144nm (angle-independence up to 70°) periodicity have been able to establish a phenomenon. Depending on the polarization as well as the varying thickness of ZrO_2 (using the Atomic layer deposition process) covering the Al-nanostructures, the resonance can be tuned throughout the visible region [86].

Comparison with Au and Ag nanostructure-based plasmonic devices:

In 2017, Lee et al. demonstrated Fano resonance by using Al nano-slit arrays. An appreciable quality factor of about 152 (473nm /3.1nm) was reported by the system. The proposed work aims towards improving surface sensitivities of nanostructures-based Al sensors, as there is an enhanced sensitivity for Al nano-slit arrays when compared to Au nanohole arrays, hence favoring bio-interaction [81].

2.4.3 Infrared [I.R.] Band

We can say that Al as a plasmonic metal was excelling in the results but mainly concentrated in the UV-Vis region. Improved results are still being explored in the case of Al-based plasmonic nanostructures for the IR region.

The concurrent rise of Al in the plasmonic domain has directed the extension of its application for plasmonic biosensing towards the NIR range. Another aspect of employing Al nanostructures in the NIR region (λ =1500nm) has been attributed to the higher excitation power with a very low probability of destroying the nanostructure under incident laser flux. This was observed by Melentiev et al. when they considered third-order harmonic generation in Al nanostructures [87].

The SERS capability of Al nanostructures for the Vis-NIR region has been explored. Overall, a comparative analysis has been performed between smooth and discontinuous Al films. In studying SERS on fresh Al sheets with discontinuous or non-uniform Al width, the experimental results indicate the use of Al nanostructures for SERS spectra at 785nm and 532nm excitation [8]. Nan Zhao et al. have justified quite well that the Al nanostructures in the NIR region are a promising combination for future applications in biosensors. With the SERS

enhancement seen more at longer wavelengths, the paper shows a high enhancement factor of about ~1.48 x 10^5, superior reproducibility, and long-term stability. A comparison between the Al 3D hierarchical nanostructures and recently reported noble metal nanostructures in terms of the SERS enhancement factor shows that the proposed work brings forth high density and highly accessible hot spots for NIR analysis [26].

Spettel et al. have shown a shift in the reflectivity spectra for Al grating (depth=225nm, Period=2.8µm, width =1.6µm) for a wavelength range of 2-6 µm and different incident angles (25º to 85º) both experimentally and by simulations using RCWA. The discussion about the mid-infra-red sensing in plasmonics is noticed along with the importance of Al in exhibiting strong plasmonic resonance. The best plasmonic response (narrowest resonance dip) was found for Al among AuSn and TiW [27].

After Hughes et al. experimentally and theoretically proved the maximum absorption of Al at around 1.55eV [88], endless research has been towards the utilization of Al films for broadband absorption applications. Seeking a plasmonic alliance for a predefined spectrum, multiple Al nanostructures sufficiently satisfy a particularly targeted spectrum. Using the interpolation method to determine peak parameters over a range of width, period, and depth of the nanostructure, a reference library is looked up to identify the nanostructure corresponding to the peak in each of the target spectra [89].

Comparison with Au and Ag nanostructure-based plasmonic devices:

Angular interrogation is performed at 1550nm (telecommunication wavelength) for different bimetallic configurations of Al, Ag, and Au, out of which, Al achieves the sharpest reflectance (sensitivity = 245.3°/RIU) due to minimum internal damping. To get rid of chemical instability, a bi-metallic design of 27nm Al along with a protective layer of 3nm Au is chosen for sensing purposes [4].

TABLE 2.1: List of the work done so far on Al-based plasmonic devices

Geometry	Sensitivity	FOM[RIU^{-1}]	Reference
NANOAPERTURES			
Al nanosphere (5 to 80nm) Nanorod	85.4 to 266.1 nm/RIU 234 nm/ RIU for aspect ratio = 2	8 for 20nm size sphere 4.3 for aspect ratio = 2.5	[48]
Al nano disks on top of ZnO layer (diameter:80nm, thickness: 40nm)	120nm/RIU	--	[82]
Gr-Al nanoribbon	25nm/RIU	3	[39]

Nanorings (Inner rad.: 20nm Outer rad.: 65nm Ring pitch: 320 nm)	408 nm/RIU	5.88	[37]
NANO-FILMS			
Gr-MoS$_2$-Al film	190.36 °/RIU	73	[90]
Al film-Au film-Au grating (λ=900nm)	279.9 °/RIU	245.2	[77]
Al film- Au grating-Al$_2$O$_3$ filled	270.33 °/RIU	267.65	[91]
Al thin film with nanohole array	348 nm/ RIU	348	[3]
NANO-STRUCTURES			
Al-grating-based SPR sensor (λ=900nm)	189.5 °/RIU	231	[92]
Al-Al grating (λ=1500nm)	247.2 °/RIU	170.48	[4]
Al-based BNA-based MIM config.	497 nm/RIU	--	[64]

2.6 Conclusion

Unfolding the exemplary results of Al-based plasmonic devices in the entire wavelength spectrum (UV-Vis-NIR), this chapter summarises some of the major fundamental and applied research on Al as plasmonic material. When the dimensions are reduced to the nanoscale, the optical properties greatly become size-dependent. Therefore, interesting results on different forms of Al nanoapertures, nanofilms, and nanostructures based plasmonic devices are discussed for each wavelength regime. For UV-based SPR sensors, the high plasma frequency of Al, as well as the absence of interband transition in the UV portion, allows for remarkable plasmonic responses. Similarly, in the visible region, high surface sensitivity has been reported for Al nanostructure-based devices with reduced deleterious effects of the native bulk oxide. Apart from this, the NIR region provides a sharp spectral response with Al-based plasmonic devices, as has been discussed above. Thus, taking the advantage of different nano-dimensional geometries, Al has established itself well as an equal contender in the field of the plasmonic domain. By utilizing various nano-dimensional geometries, Al has successfully established itself as an equal contender in the plasmonic domain. Whether it's in the UV range to enhance the native fluorescence, the visible range for broad spectral absorption for solar cells, or the NIR wavelength range for non-destructive investigation of bio-samples

In the future, large-scale commercialization of Al-based plasmonic devices can serve as a favorable outcome due to the much-reduced cost and robustness of the device to work in the entire EM wave spectrum along with its CMOS compatibility. In conclusion, we can say that Al is the only plasmonic metal that can realize SPR response over a broad range of the spectrum (UV-Vis-NIR) by simply varying the size, shape, and environmental conditions of the surrounding medium.
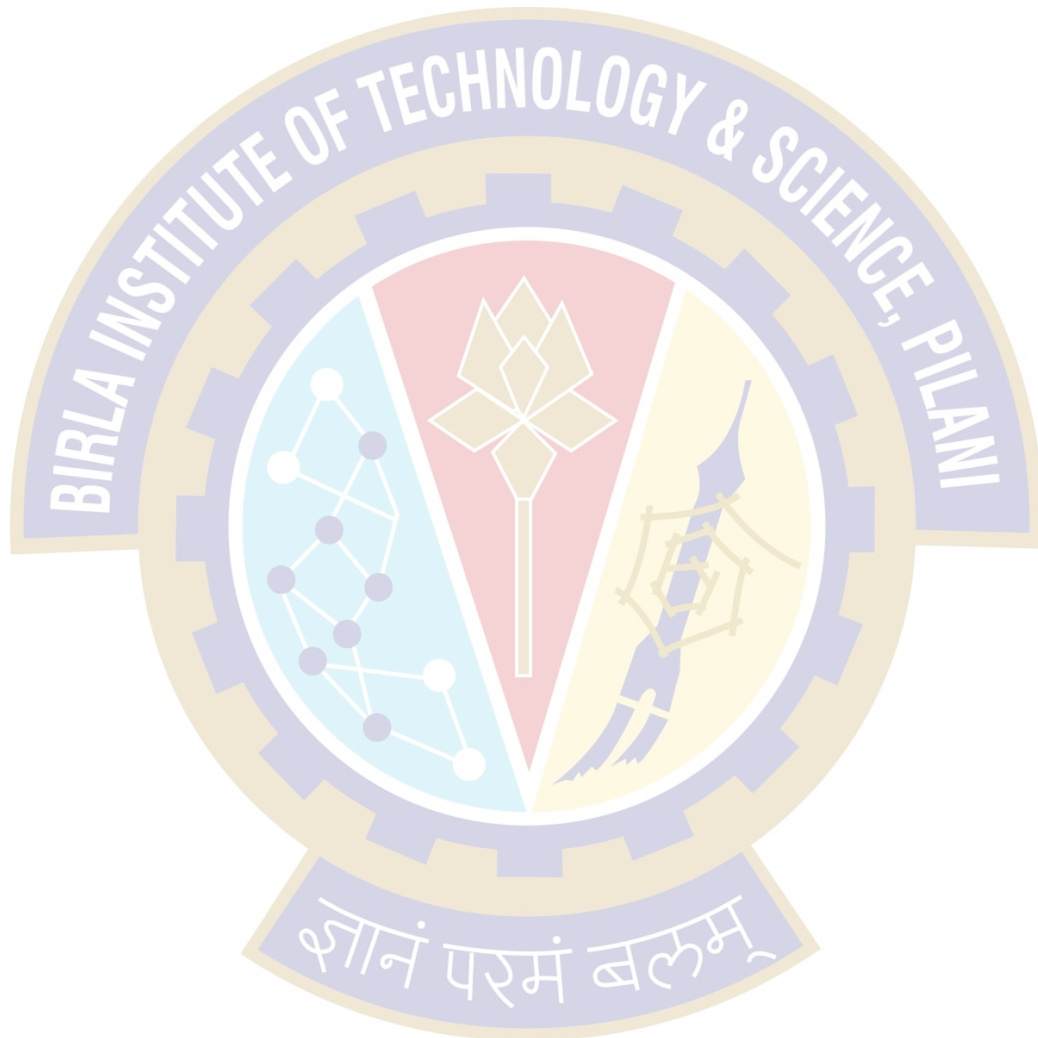
Chapter 3

Design and analysis of a multi-layered aluminum-silicon-graphene-based plasmonic device for sensing

The gist of the literature review is that most of the work has been exclusively concentrated on the nanoapertures; be it nanodisks, nanoarrays, nanocylinders, nanospheres, etc. Regarding thin films, and periodic nanostructures, substantial research is cornered around the UV and visible parts of the spectrum. Therefore, in this thesis, we have broadly investigated two classes of plasmonic sensors for the near-infrared region i.e., thin homogeneous Al film-based plasmonic sensors, and periodic Al nanostructures-based plasmonic sensors.

To begin with, we focussed on a thin film-based Kretschmann configuration in this chapter. The optimized design is investigated for biosensing in the optical communication window i.e., 1550nm. The presence of high refractive index dielectric material is an important means to achieve enhanced sensitivity over the plasmonic metal and Graphene (Gr) layer for enhanced biomolecular interaction at the interface. It has been observed previously, that combining Silicon(Si)-Gr leads to field enrichment at the metal-dielectric interface [93]. Therefore, we undertake stacks of Si-Gr layers as the dielectric material and BRE over the Al thin film-based plasmonic device respectively. Thereafter, the performance of the Si-Gr stacks-based plasmonic device is compared with the previously reported works on similar prismatic arrangements. Additionally, the effect of the chemical potential of Gr is also studied on the performance parameters. Subsequently, the proposed Al-Si-Gr-based plasmonic design is investigated for leptospirosis detection analysis.

3.1 Introduction

Attenuated Total Reflection (ATR) configuration is the conventional way of exciting the SPs using a homogeneous thin metal film coated on a glass prism to detect the refractive index changes near the sensing surface. Such a conventional ATR arrangement was modified in this chapter, where the presence of the Gr layer increased the interaction with bio-analyte by adsorbing the biomolecules due to its carbon-based ring structures and the presence of a thin Si layer helped to enhance the sensitivity of the proposed device. All the geometrical parameters of the layers over the base index prism were engineered for the maximum sensitivity towards varying concentrations of the measured analyte in the optical

communication band using the Transfer Matrix Method (TMM). The use of Al as a plasmonic metal makes the proposed device more economical and compatible with optoelectronic devices. The stacking of Si-Gr layers over the thin metal-coated glass prism led to the maximum sensitivity of 200°/RIU at the wavelength of 1550 nm. To demonstrate the proposed device as a bio-sensor, rodent urine was considered as the analyte under test to detect the changes in the varying concentration of Leptospira bacterium. Compared to the conventional gold thin film-based plasmonic biosensor, the addition of Si and Gr layers over a thin Al metal-coated glass prism offered better sensitivity and detection accuracy in the communication regime. The proposed plasmonic device opens a new window for the detection of biomolecular interactions in the optical communication band.

As per our knowledge, the Gr layer for biosensing applications has been used so far in the visible region. This is the first time, we used a combination of Si and Gr layers sandwiched between Al and analyte, to enhance the sensitivity in the optical communication band. The sensing in the optical communication band will be advantageous from a biosensing point of view as it causes minimal photodamage to the bio-samples [94], [95]. Moreover, in the communication band, the SPR sensor offered a high probe depth [96].

3.2   Design parameters of proposed device

The proposed plasmonic device is mainly a five-layer structure as shown in Fig. 3.1 (a) that included a thin layer of Al metal deposited on the top of a Calcium Fluoride (CaF$_2$, n =1.462) prism [97]. Due to better rejection of errors during mechanical setup as well as a higher threshold for laser damage, the CaF$_2$ prism was used as the material substrate. The proposed schematic had an Al layer of thickness 't$_m$' followed by the Si layer of thickness 't$_{si}$' that was terminated by a very thin sheet of Gr monolayer of thickness 't$_{gr}$'. The Gr layer was in contact with the analyte under observation. The refractive index of the analyte (water) was considered to be 1.33. The evanescent waves were produced when incident light of wavelength 1550 nm strikes the metal-dielectric interface through the prism. Distributed feedback (DFB) lasers are commonly used to emit light at a specific wavelength, such as 1550nm. Such lasers are widely used in IR regions because they provide high output power, low noise, and stable wavelength operation. This results in reduced energy transfer to the reflected light and hence leading to points of reflection minima. As the surrounding condition of the medium changes, it will be detected by the resonant angle shift of the corresponding reflection minima.

The geometrical parameters for the structure were optimized for maximum sensitivity, high signal contrast, and low Full Width at Half Maximum (FWHM) towards varied concentrations of the measured analyte corresponding to different refractive indices using the N-layer TMM technique.
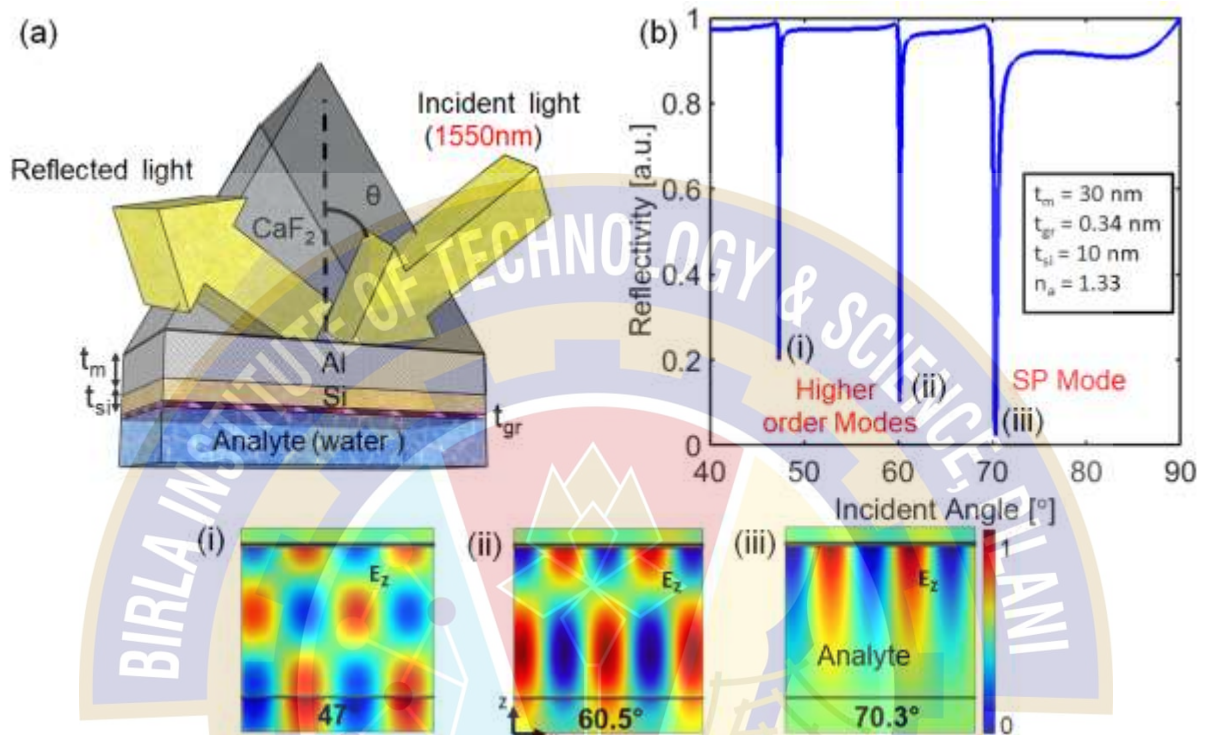
Fig. 3.1 (a) A schematic diagram for the proposed plasmonic device (not to scale) (b) Calculated reflectivity curve for the proposed multilayered Al-Si-Gr-based plasmonic device for t_m = 30 nm, t_{si} = 10 nm, t_{gr} = 0.34 nm with water as an analyte, inset (i), (ii) and (iii) represent the electric field distributions for the resonance dips corresponding to 47°, 60.5° (higher-order modes) and 70.3° (SP mode) respectively.

The effective permittivity of the Gr layer is given by equation (3.1)

$$\varepsilon_g = 1 + i\frac{\sigma_g}{\omega\varepsilon_0 d_g} \tag{3.1}$$

where σ_g and d_g are the optical conductivity and thickness of the Gr layer, ω and ε_o is the angular frequency of incident light and the vacuum permittivity respectively [98], [99]. Since the permittivity of Gr is dependent on chemical potential, the value of optical conductivity σ_g, for the wavelength of 1550 nm was calculated using the Kubo formula [112]. For efficient light absorption by Gr, the chemical potential should be less than half of the energy of (0.8eV/2) incident light [98], where the permittivity values are almost uniform. To ensure significant light absorption by Gr and to maintain a uniform dielectric constant value, the chemical potential was assumed to be 0 eV in the present work. The monolayer Gr has a

thickness (d_g) of about 0.34 nm, subsequently, for L number of layers, the thickness will be L times 0.34 nm [102]. The refractive index of Si is given by equation (3.2)

$$n_{Si} = A + A_1 . \, e^{\frac{-\lambda}{t1}} + A_2 . \, e^{\frac{-\lambda}{t2}} \qquad (3.2)$$

Where A = 3.44904, A_1=2271.88813, A_2= 3.39538, t_1= 0.058304, t_2= 0.30384 and λ is the wavelength in µm (i.e. 1.55 here) [103].

3.3 Numerical Analysis

Fig. 3.1 (b) shows the calculated reflectivity curve for the optimized parameters of metal thickness i.e., t_m = 30 nm, a Si layer thickness t_{si} of 10 nm, and monolayer Gr. For the wavelength of 1550 nm, three dips were observed in the reflectivity curve at the angles of 47°, 60.5°, and 70.3° respectively. To analyze the reason for the occurrence of these dips, the electric field distributions were calculated as shown in the inset (i)-(iii) of Fig. 3.1 respectively. The dips at the angles 47° and 60.5° are attributed to the presence of high-order waveguide/dielectric modes since the field was being guided in the analyte whereas the dip at 70.3° is due to the excitation of SP mode since the field was confined at the metal-analyte interface. Since SP mode was excited at the metal-analyte interface and was very sensitive to any change in the surrounding material, this mode has been utilized for calculating the changes in the refractive index of the analyte.
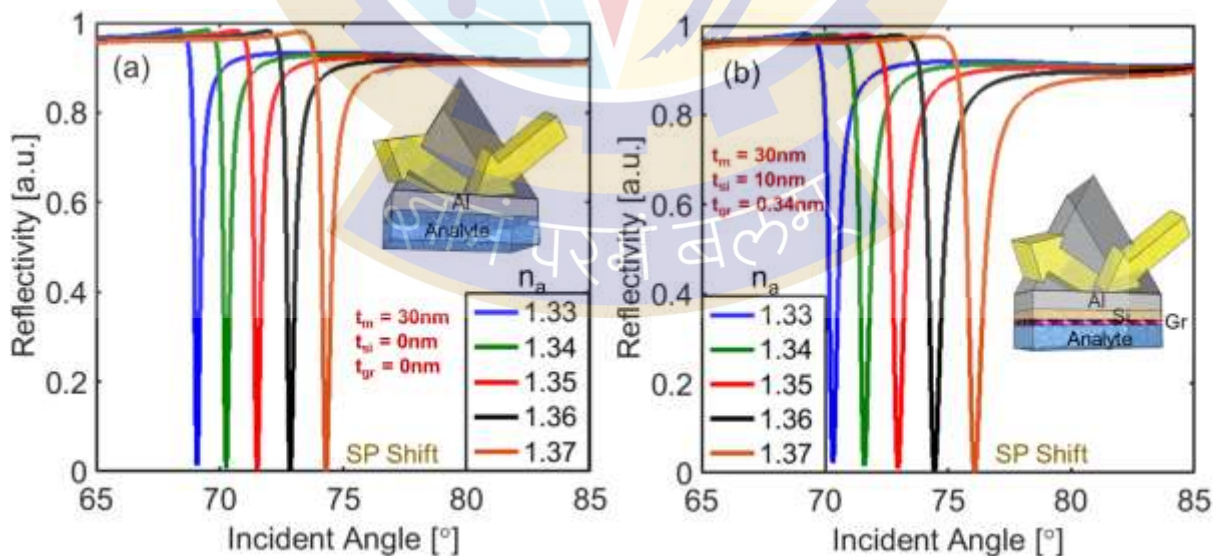
Fig. 3.2 Calculated reflectivity curves with variation in the refractive index of the analyte ranging from 1.33 to 1.37 for (a) conventional Kretschmann configuration (b) for the proposed device where the Si and Gr layers have been added to the conventional configuration.

To calculate the sensitivity of the proposed device, the analyte with the refractive index varying from 1.33 to 1.37 was considered on top of the plasmonic device, and to compare the enhancement in the sensitivity concerning the conventional Kretschmann configuration, the same analyte has been considered on the top of Al coated glass prism. Fig. 3.2(a) shows the reflectivity curves for the optimized thin Al-coated glass prism and Fig. 3.2(b) represents the reflectivity curves for the proposed plasmonic device considering the analyte of varying refractive index for both the configurations. A right shift in the position of SP mode was observed with the increase in the refractive index of the analyte for both configurations. The sensitivity calculated from the relative change in resonance angle for SP mode over the change in the refractive index came out to be 118°/RIU for the case of conventional configuration (Fig. 3.2(a)) whereas for the case of the proposed plasmonic device the sensitivity was found to be 128°/RIU (Fig. 3.2(b)).

The improvement in the sensitivity for the proposed plasmonic device was attributed to the enhancement in the magnetic field intensity at the Gr-analyte interface after the addition of Si-Gr layers between Al and analyte. Si-Gr layers not only contributed to field enrichment but also prevented the thin Al layer from oxidation [104]. Fig. 3.3(a) represents the magnetic field distribution for the proposed plasmonic device and Fig. 3.3(b) shows the comparison of the Magnetic Field Intensity Enhancement Factor (MFIEF) for both configurations. It is clear that with the addition of the Si–Gr layer in the proposed device, there is an increase in the MFIEF at the interface resulting in more interaction with the analyte and subsequently, enhancement in the sensitivity [105]–[107].
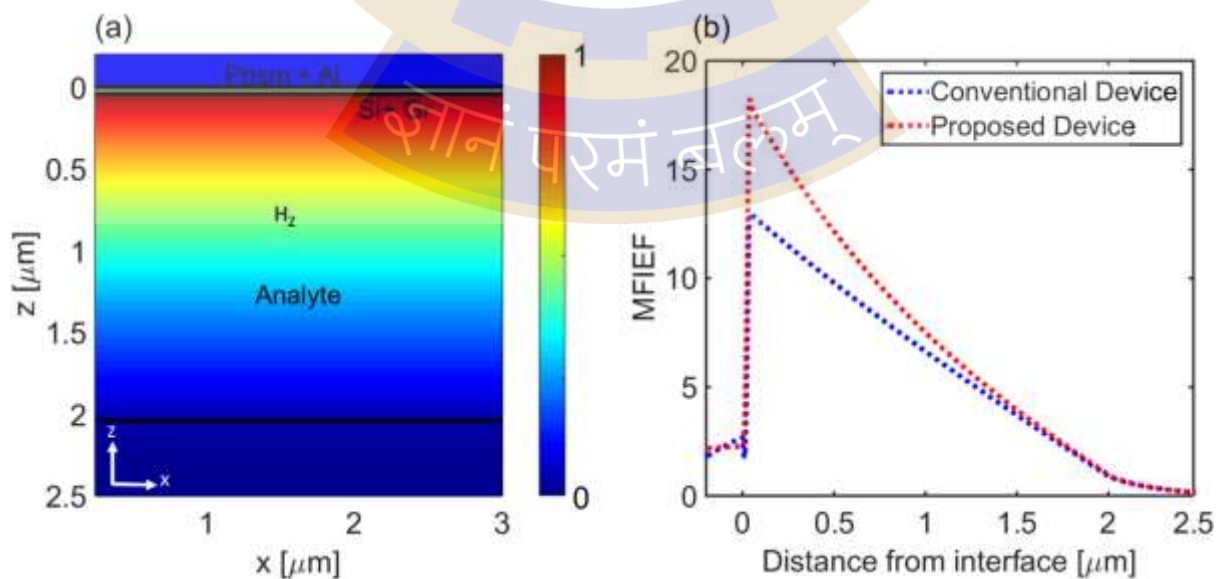
For a biosensing application, it is very important to have strong interaction between the top layer of the device and the biomolecules (analyte). The addition of the Gr layer to the existing metal-prism structure leads to a stronger interaction with the bio-molecules due to its carbon-based ring structures and the addition of the Si layer between Al and Gr, enhances the sensitivity due to the high real part of the refractive index [108], [109]. Moreover, the introduction of the Si-Gr layer produced more accurate results due to the longer propagation lengths of evanescent waves in the z-direction.
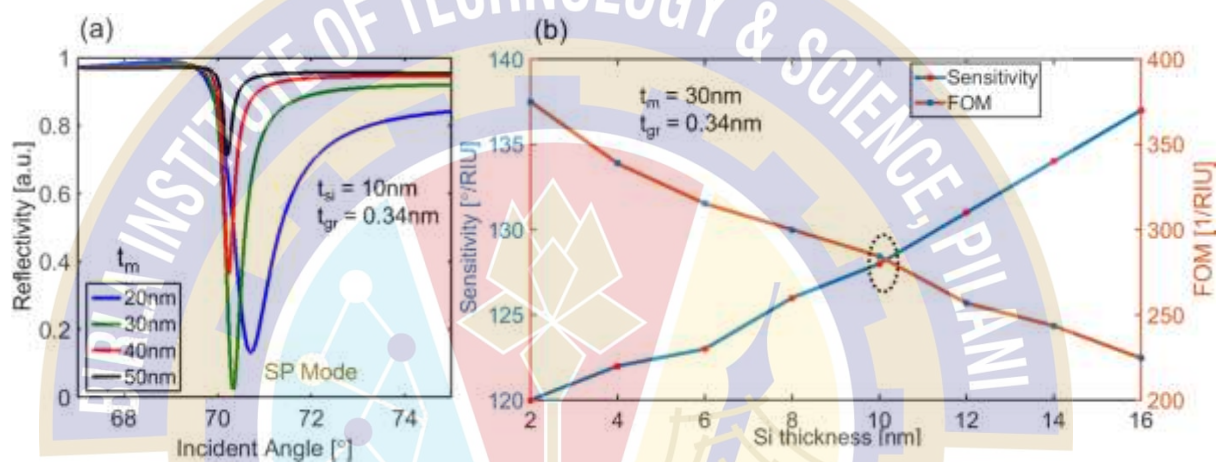
Fig. 3.4 Calculated reflectivity curves for the proposed plasmonic device (a) with t_{si} = 10nm, t_{gr} = 0.34nm and for different values of t_m (b) Variation in the sensitivity and FOM for different values of Si thickness (t_{si}) with t_m = 30 nm, and t_{gr} = 0.34 nm

For the optimization of the proposed configuration, the effect of each parameter on the sensitivity, signal contrast, and FWHM was studied by varying all the geometrical parameters of each layer at a time, keeping all others constant.

Fig. 3.4(a) shows the reflectivity curves for the proposed plasmonic device with t_{si} = 10nm, t_{gr} = 0.34nm, and for different values of t_m. In Fig. 3.4(a), when Al thickness (t_m) was varied from 20 nm to 50 nm in steps of 10 nm, t_m = 30 nm resulted in the minimum reflectivity (high signal contrast) and low FWHM, hence was taken to be the optimized value of Al metal thickness. The minimum reflectivity value of the dips indicates a stronger localized field at the interface, and low FWHM is necessary to enhance the resolution of the sensor. There was no appreciable change in the signal contrast while the sensitivity and FWHM were found to be increasing with the increase in Si layer thickness. Fig. 3.4(b), shows the variation of sensitivity, and Figure of Merit (FOM=sensitivity/FWHM) values with the increase in the thickness of the Si layer. A

thickness of 10 nm for the Si layer was chosen to be the optimum thickness required for maximum sensitivity and higher FOM offered by the plasmonic device.
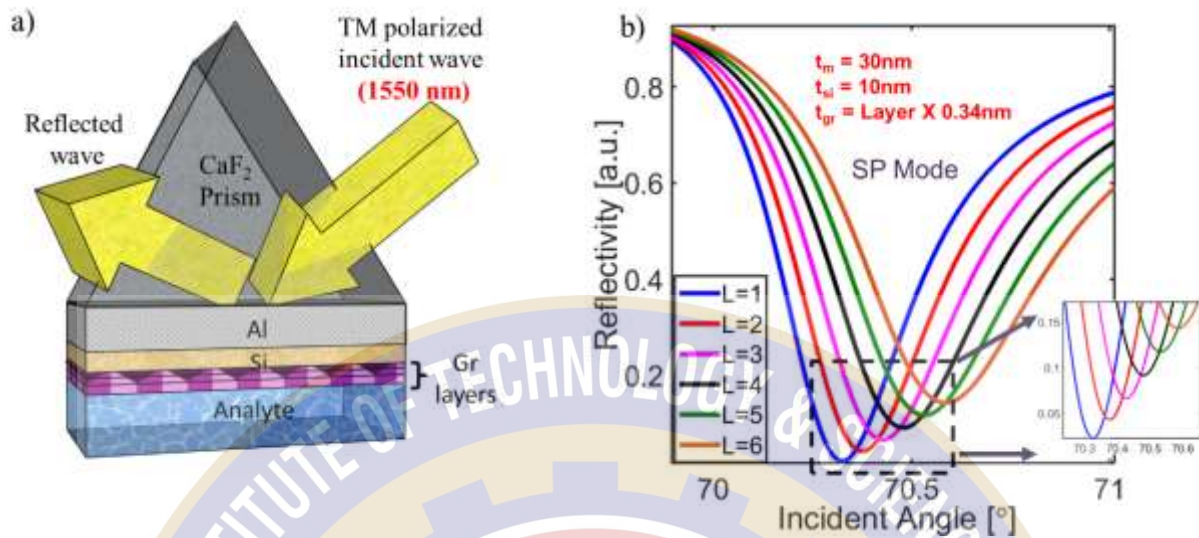
Fig. 3.5. (a) The schematic of the proposed plasmonic device with Gr multilayers (not to scale) (b) Reflectivity curves of the plasmonic device with the increase in the number of Gr layers at the wavelength of 1550 nm.

The advantage of Gr is that several Gr layers can be coated on a surface in a controlled manner due to the presence of Van der Waals forces between the two Gr layers. So, after optimizing the parameters of the proposed plasmonic device, the number of Gr layers was increased in the plasmonic device as shown in Fig. 3.5(a). Fig. 3.5(b) shows the reflectivity curves of the plasmonic device with the increase in the number of Gr layers (e.g., bilayer, tri-layer, and other multilayers). The increase in the number of Gr layers resulted in low signal contrast and a larger FWHM as shown in Fig. 3.5(b).

The sensitivity and FOM values with the increasing number of Gr layers were calculated as presented in Table 3.1. It can be inferred from the tabulated values that the sensitivity increases linearly with the number of Gr layers. However, FWHM increases more rapidly than sensitivity, which leads to the net effect of a decreasing FOM. The value of sensitivity changed from 128°/RIU to 131°/RIU whereas the FWHM value changed (due to more damping [110]) from 0.44° to 0.77° by increasing the number of layers from 1 to 8. So, one layer of Gr (monolayer) in the plasmonic device seems to be a good choice for better sensitivity and FOM. Though the use of ultra-high doping in the Gr layer can help to achieve the narrowest plasmonic dips since high doping concentration leads to higher Fermi levels, and the real and imaginary part of the refractive index of Gr is dependent on Fermi levels. Hence, the higher value of Fermi levels results in the narrowest plasmonic dips due to less damping [111]–[114].

TABLE 3.1: Comparison of performance parameters with the increase in the number of Gr layers in the proposed device

Number of graphene layers	S_θ [°/RIU]	FWHM [°]	FOM [RIU^{-1}]
1	**128**	**0.44**	**290.9**
2	129	0.48	268.75
3	129	0.50	258
4	129	0.53	243.39
5	130	0.59	220.33
6	130	0.63	206.34
7	130	0.66	196.96
8	131	0.70	187.14

Next, instead of one layer of Si and Gr in the plasmonic device, the stacking of Si-Gr layers was considered between the Al metal and the analyte as shown in Fig. 3.6 (a). The sensitivity and FOM values were calculated with the increase in the number of Si-Gr stacks in the plasmonic device as shown in Table 3.2. The value of sensitivity was found to be increasing whereas the FOM was found to be decreasing with the increase in the number of Si-Gr stacks. In this case, the sensitivity value increased from 128°/RIU to 323°/RIU whereas the FOM value decreased from 290 RIU^{-1} to 62 RIU^{-1}. For a reliable and good SPR sensor, the FWHM (SP mode linewidth) should be as small and the sensitivity should be as large as possible [94]. Usually, there is always a trade-off between FWHM and the sensitivity of the SP-based sensor. To analyze the sensor's overall performance, the values of sensitivity and FOM were plotted with the increase in the number of Si-Gr stacks as shown in Fig. 3.6 (b). The optimized value of Si-Gr stacks was found to be 3 while maintaining the trade-off between the sensitivity and FOM.
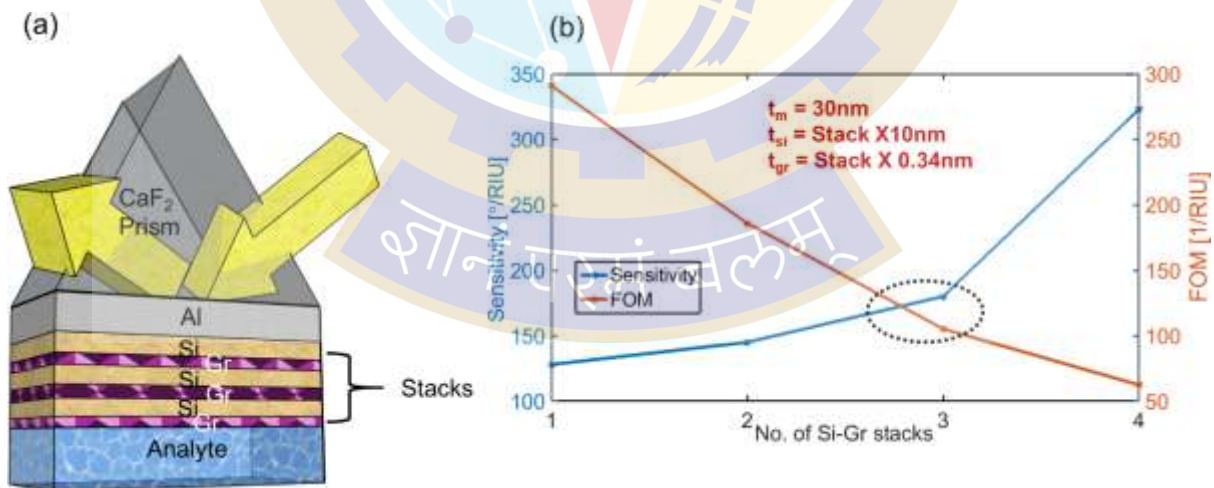
Fig. 3.6 (a) The schematic of the proposed plasmonic device with Si-Gr stacks (not to scale) (b) Variation of sensitivity and FOM with the increase in the number of Si-Gr stacks in the proposed plasmonic device.

35

TABLE 3.2: Comparison of parameters with the increase in the number of Si-Gr stacks in the proposed device

Number of Si-Gr stacks	S_0 [º/RIU]	FWHM [°]	FOM [RIU^{-1}]
1	128	0.44	290.9
2	145	0.78	185.89
3	**182**	**1.73**	**105.20**
4	323	5.18	62.35
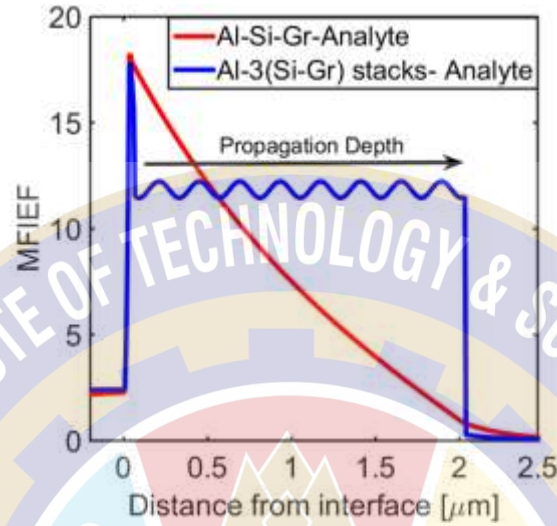
Fig. 3.7 The comparison of MFIEF with respect to the normal distance from the interface for single stack and three stack Al-Si-Gr-Analyte based plasmonic device respectively.

To know the physics behind the increase in the sensing parameters with Al-Si-Gr stacks based configuration, the absolute value of magnetic field distribution was calculated and MFIEF value was plotted with respect to distance from the interface as shown in Fig. 3.7. The field is guided for a longer distance along the interface which results in increased interaction of the field and analyte. The value of MFIEF clearly highlights the field enhancement because the addition of Si-Gr stacks creates a cavity-like periodic structure that helped to improve the sensing parameters drastically by the field enhancement with a longer propagation length at the interface.

To demonstrate the bio-sensing application with the proposed plasmonic device, rodent urine was considered as the analyte to detect the change in the concentration of Leptospira bacterium [115], [116]. A 3 nm layer of Phosphate Buffer Saline (PBS) solution (n = 1.334) was considered to activate the Gr surface of the proposed plasmonic device consisting of 3 Si-Gr stacks for better attachment of biomolecules, as shown in Fig. 3.7(a). The relative shift in the resonance angle was observed over different samples of rodent urine to their corresponding refractive indices as tabulated in Table 3.3. A linear increment in the sensitivity was noticed with increasing refractive indices of the sample. The change in the SP resonance angle (θ_{SP})

with variation in the refractive index was plotted as shown in Fig. 3.7(b). The overall sensitivity and FOM achieved were found to be 200°/RIU and 95.23 RIU^{-1} respectively.
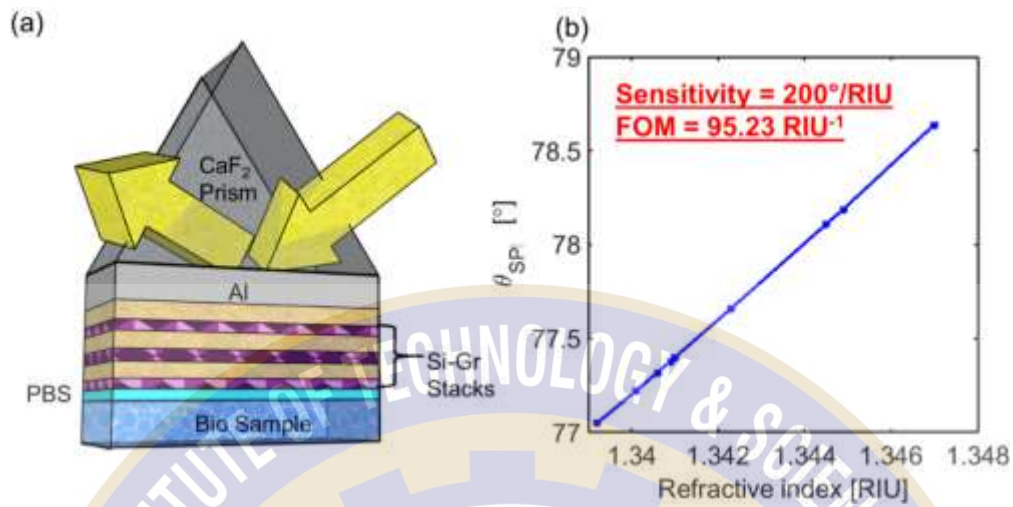
Fig. 3.8 (a) The schematic of the proposed plasmonic device with 3 Si-Gr stacks to demonstrate biosensing application (not to scale) (b) Plot for the shift in the SP resonance angle with variation in the refractive indices corresponding to different concentrations of Leptospira bacterium.

TABLE 3.3: Variation of SP resonance angle with the increase in the refractive indices corresponding to different concentrations of Leptospira bacterium

Refractive Index (Sample)	θ_{SP} [°]	$\Delta\theta_{SP}$ [°]	Δn [RIU]	S_θ [°/RIU]
1.3392	77.05	-	-	-
1.3401	77.22	0.17	0.0009	188.88
1.3406	77.32	0.10	0.0005	200.00
1.3409	77.38	0.06	0.0003	200.00
1.3410	77.40	0.02	0.0001	200.00
1.3423	77.66	0.26	0.0013	200.00
1.3445	78.11	0.45	0.0022	204.50
1.3449	78.19	0.08	0.0004	200.00
1.3470	78.64	0.45	0.0021	214.28

In SPR-based sensing, bulk sensitivity carries the weight of refractive index changes of the unknown bio-analyte introduced. Yet, it fails to acknowledge the variation in sizes of the incoming biomolecule to be captured in the vicinity of the metal surface. Since the sensitivity of SPR sensors is due to exponentially decaying evanescent fields, it is important to distinguish the surface sensitivity at the nanometric vicinity of the metal layer from the bulk sensitivity in the surrounding medium. To demonstrate the surface sensitivity of the proposed engineered device, Al_2O_3 layers with well-defined thicknesses and the refractive index were considered on the top of the device, and the reflectivity curves were calculated for different thicknesses of Al_2O_3 layers (0-20nm) as shown in Fig. 3. 9(a). The shift in the resonance angle was observed with the variation in the thickness of the Al_2O_3 layer as shown in Fig. 3.9(b). The decrease in angle shift compared to the bulk sensitivity can be explained by the distribution of the SPR

evanescent field [117]. From Fig. 3.8, it can be seen that the proposed devices are efficient for capturing the changes for biosensing applications, which involve molecular binding events (e.g., antibody/antigen detection or DNA hybridization) in a confined region close to the metal surface. The present work focused exclusively on bulk sensing while engineering the plasmonic devices followed by the demonstration of the biosensing application for Leptospira bacterium detection because the size of the bacterium is around 1-2 μm. But certainly, the proposed device can be used for both surface and bulk sensitivity.
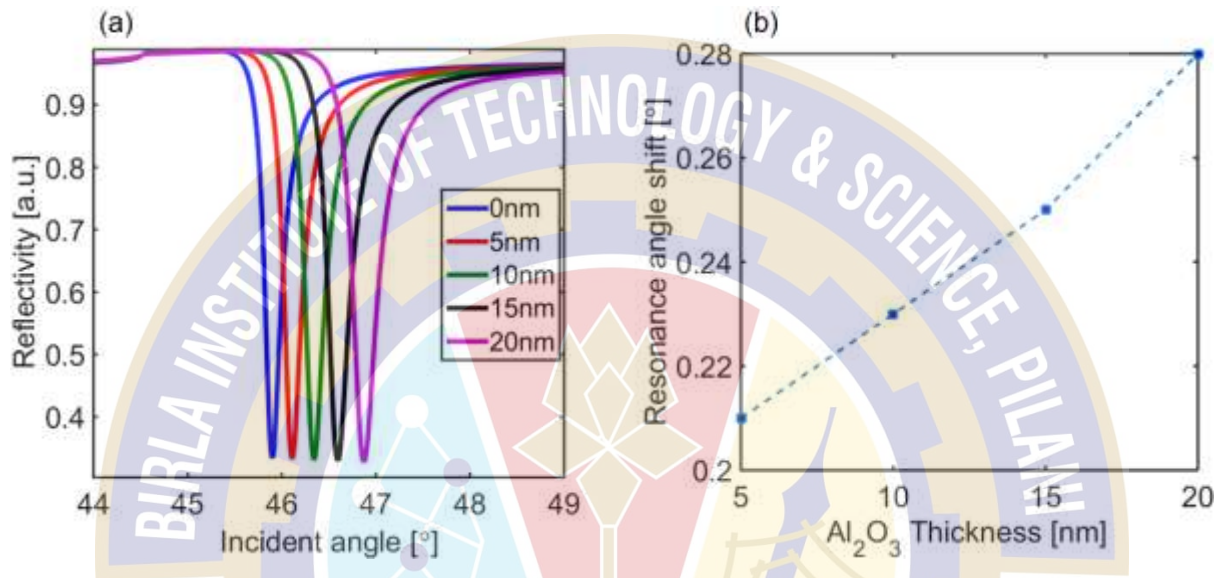
Fig. 3.9 (a) Reflectivity curves of the engineered plasmonic device with the variation in the thickness of the Al_2O_3 layer deposited on the top of the device (b) Plot for the shift in the SP resonance angle with variation in thickness of Al_2O_3 layer deposited on the top of the device.

Further, the effect of the chemical potential of the Gr layer on the performance of the engineered plasmonic device was calculated in terms of sensitivity, FWHM, and FOM as shown in Table 3.4. From Table 3.4, it was observed that there is no change in the performance parameter up to a value of chemical potential = 0.2 eV but after that, the value of FWHM was found to be decreasing due to the smaller value of the imaginary part of the refractive index.

TABLE 3.4: Effect of the chemical potential of Gr on the sensitivity, FWHM, and FOM of the proposed plasmonic device

Chemical Potential (eV)	S_θ [°/RIU]	FWHM [°]	FOM [RIU^{-1}]
0	200	2.10	95.23
0.1	200	2.10	95.23
0.15	200	2.10	95.23
0.2	200	2.10	95.23
0.25	200	2.09	95.69
0.3	200	2.09	95.69
0.35	200	2.03	98.52

Finally, the results obtained with the proposed plasmonic device were compared with the previously reported results in the literature as shown in Table 3.5. An appreciable improvement

in the sensitivity and FOM was observed with the proposed plasmonic device when compared to other work.

TABLE 3. 5: Comparison of the proposed work with previous results reported in the literature

Ref. no	Schematic	S_θ [°/RIU]	FOM [1/RIU]
[102]	Au + Gr	53.2	12.33
[118]	Au + Si + Gr	134.6	7.49
[107]	Air + Au + Gr	43.18	44.60
[119]	Au + Gr	33.98	2.78
[110]	Au + WS$_2$+ Gr	95.71	25.19
[120]	Air + Cr + Ag + Gr	68.03	9.691
Proposed work	**Al + (Si – Gr) Stacks**	**200**	**95.23**

3.4 Conclusion

A multi-layered thin Al film-based plasmonic device was proposed to capture the changes in the refractive index of the analyte in the optical communication band. A thin layer of Si and Gr was sandwiched between Al and analyte to enhance the sensitivity of the plasmonic device for bio-sensing applications. The enhancement in the sensitivity was observed for the proposed device due to the high dielectric index of the Si layer and stronger interaction between the Gr layer and analyte due to its high surface-to-volume ratio. The addition of Si-Gr stacks to the proposed device helped further to increase the sensitivity of the device. The engineered plasmonic device was used to capture the changes in the concentration of Leptospira bacterium in rodent urine and the sensitivity and FOM were found to be 200°/RIU and 95.23 RIU^{-1} respectively which are much better than the previously reported results in the literature (as shown in the table above). The proposed device proves to be much more feasible since introducing Al as a plasmonic metal makes the overall proposed design more economical and compatible with optoelectronic devices.

Chapter 4

Design and comparative analysis of aluminum-MoS₂-based plasmonic devices with enhanced sensitivity and Figure of Merit

In the previous chapter, we demonstrated the Gr layer as biosensing initiating element for Al-based plasmonic devices. Agreeably, Gr provides the increased adsorption of biomolecules on the sensing surface, leading to enhanced sensitivity but at the cost of increasing FWHM of SPR curves. Thus, 2D nanomaterials like Transition Metal Dichalcogenide (TMDC) (MoS_2, WeS_2, WS_2, etc.), have become exceedingly popular for better plasmonic sensing activity. According to recent trends, 2D nanomaterials forming multi-layered composite films are a continuous progression in research due to high electron mobility and large surface area to strengthen electric field enhancement at the interface. Molybdenum disulfide (MoS_2) often referred to as the "Beyond Graphene" material, is one of the most exclusively researched nanomaterials, among the other TMDCs. Thus, a comparative analysis is now performed, on the Al-based Kretschmann arrangement at 1550nm, for different combinations of Al-MoS_2-based plasmonic devices under angle interrogation that provided us with application-specific results. A comparative analysis is prepared for these configurations in the presence and absence of a high dielectric layer i.e., Silicon (Si).

4.1   Introduction

The property of broken Centro-symmetry [11], high fluorescence quenching ability [12], and higher optical absorption efficiency [~5%] are among some of the exquisite electrical and optical properties offered by MoS_2, giving them an extra edge over Gr. Toxicity is also a serious issue as far as the viability of cells is concerned while undergoing bio-sensing. Lower toxicity in multi-layered MoS_2 has facilitated the uptake of 2D MoS_2 into live cells for in-vivo biosensors [13]. Multi-layered MoS_2 also proves to enhance sensitivity as reported frequently in the past [14–16]. Apart from biosensors based on pure MoS_2, composites of 2D MoS_2 are also being investigated. Considering the biocompatible nature of Gr and MoS_2, researchers have studied the plasmonic activity when MoS_2 layers are stacked together with the Gr sheets [12,16,17]. MoS_2 being structurally analogous to Gr has Van der Waals forces of attraction existing between them, leading to this nanocomposite becoming an excellent platform for detection in biosensing applications. Black phosphorus/MoS_2 heterostructure has already grabbed a lot of attention [19], but the readily oxidizable nature of black

phosphorus has led to other high-index promising dielectrics like Silicon (Si) to act as replacements, hence significantly enhancing the sensitivity [20]. Nevertheless, almost all the work done on Gr/MoS$_2$ has been studied in the visible region at a wavelength of around 633 nm, while S. Chen and C. Lin have presented wavelength interrogation from the 400 nm–800 nm range [21]. In the visible region, the existence of a non-zero imaginary part of the dielectric constant for MoS$_2$ gives rise to broader SPR curves, thereby deteriorating detection accuracy as shown by Zeng et al. [22]. Browsing through the previous reports, one may end up confused as to which parameter to be held accountable for the best performance in optical sensing since both sensitivity and FOM are important parameters. Hence, there is a need to focus our research on plasmonic devices which can provide cumulative results with perfect trade-offs among all the geometrical parameters, to achieve maximum sensitivity along with FOM. Moreover, there is still a dearth of research when it comes to the performance analysis of MoS$_2$-based plasmonic devices in the higher wavelength regime, especially in the communication band.

The present study takes into account multiple Al-MoS$_2$-based Ktreschmann configurations, in the NIR region. Important performance parameters (Sensitivity and FOM) are studied for the following four engineered structures: Al-Si-MoS$_2$-Gr (ASMG), Al-MoS$_2$-Gr (AMG), Al-Si-MoS$_2$ (ASM), and Al-MoS$_2$ (AM). Such a comparative analysis yields a platform that can provide an exhaustive approach to the behavior of 2D materials in the NIR region (1550 nm). Herein, a comparison of Al-MoS$_2$-based engineered plasmonic devices is presented in the optical communication window. After the required optimization for the geometrical parameters, two (ASMG and AM) out of the four structures are selected in terms of the highest sensitivity (141°/RIU) and FOM (335.13 RIU^{-1}) to demonstrate the Single-Stranded DNA (ssDNA) sensing, from the proposed plasmonic devices. The results show that the proposed nanomaterial-based plasmonic devices prove to be much more promising configurations in the NIR regime as both the important parameters i.e., sensitivity as well FOM is sufficiently high as compared to the works in the existing literature.

4.2 Design parameters for the proposed devices
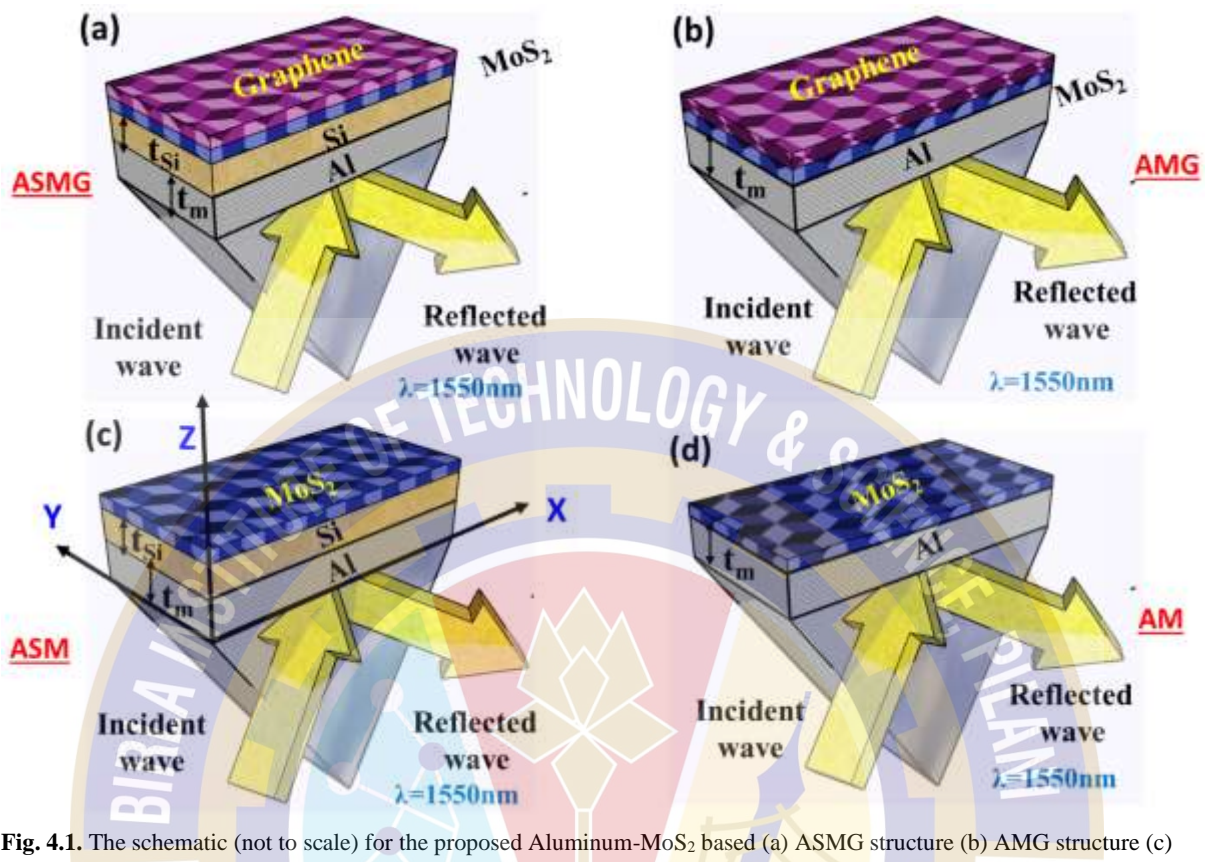
Fig. 4.1. The schematic (not to scale) for the proposed Aluminum-MoS$_2$ based (a) ASMG structure (b) AMG structure (c) ASM structure and (d) AM structure.

In all four Al-MoS$_2$-based configurations, Al was considered as the plasmonic metal layer as shown in Fig. 4.1. In our proposed structures, CaF$_2$ was chosen to be the coupling prism over which the angular interrogation was performed. On the top of the metal-prism arrangement, Si was used as a high-index dielectric for ASMG and ASM structures as shown in Fig. 4.1(a) and 1(c). Since Gr acts as the BRE layer for the external biomolecules, so it was in direct contact with the analyte, to be inserted after the MoS$_2$ layer for ASMG and AMG structures as shown in Fig. 4.1(a) and 1(b). The analyte at the top of all these four structures was considered to be water (n$_a$ = 1.33). The monolayer MoS$_2$ has a thickness of about 0.65 nm, subsequently, for L number of layers, the thickness will be L times 0.65 nm. The refractive index of MoS$_2$ at 1550nm has been extracted from ref [121]. Monochromatic p-polarized light was used to excite SPs at the metal-dielectric interface. As soon as the light energy gets coupled to the conduction-electrons inside the metal, it gives rise to a resonance condition. The TMM was employed to simulate the results for all four engineered structures. The SPR curve obtained with the corresponding points of reflection minima helps us to calculate the FWHM of the proposed device. Finally, two important parameters i.e., Sensitivity ($\delta\theta_{SP}/\delta n_a$) and

FOM were calculated, where $\delta\theta_{SP}$ is the shift in the resonant angle and δn_a is the corresponding change in the refractive index of the analyte.

4.3 Numerical Analysis

Al thickness was varied from 10 nm to 50 nm in steps of 10 nm and the points of reflection minima were noted. After taking into account the FWHM values as well, both the parameters were plotted against each other to obtain the optimum thickness for the Al layer as shown in Fig. 4.2(a). It can be seen that a thickness of 30 nm satisfies both conditions and hence was taken to be the optimized Al thickness for all the successive simulations.
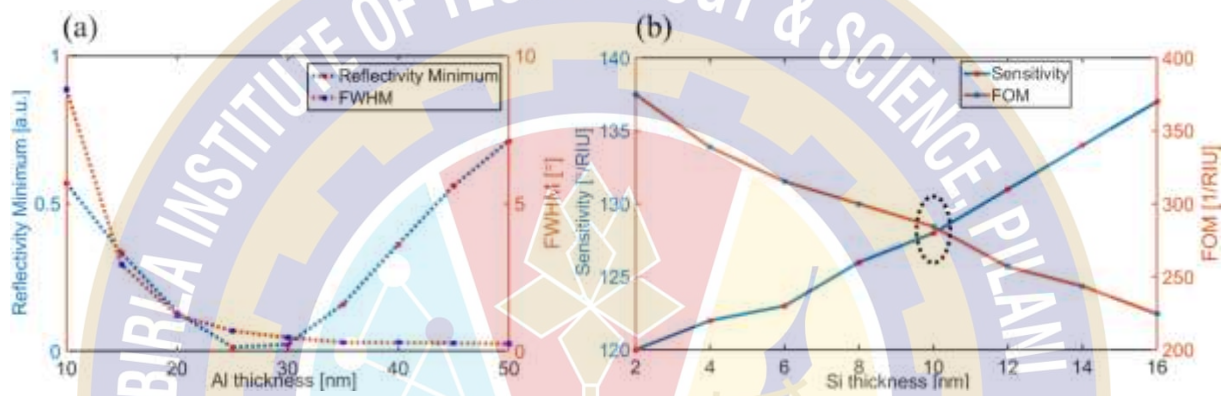
Fig. 4.2. (a) Variation in the change in the reflectivity minima and FWHM for SP curve with respect to different values of Al thickness (b) Variation in the sensitivity and FOM with respect to different values of Si thickness. The ASMG structure is considered while doing the optimization for the thickness of the Al and Si layer.

Further, to get a clearer perspective on the variation of Si layer thickness on the device performance, the sensitivity, and FOM were plotted with the increase in the thickness of the Si layer as shown in Fig. 4.2(b). From the plot, 10 nm was considered the optimized thickness of Si to achieve both high sensitivity and FOM.

After the optimization of Al and Si thickness to 30 nm and 10 nm respectively, the refractive index 'n_a' of the top layer (analyte) of all the proposed devices was changed from 1.33 to 1.34 and the reflectivity curves for all the proposed structures were calculated concerning the incident angle as shown in Fig. 4.3. The thickness for the monolayer of Gr and MoS_2 was considered to be 0.34 nm and 0.65 nm respectively. A right shift in the reflectivity curves was observed with the increase in the refractive index of the analyte. From Fig. 4.3, the sensitivity and the FOM values were calculated for each structure and tabulated in Table 4.1. It can be inferred from Table 4.1 that the addition of a 10 nm high dielectric index Si layer (e.g., ASMG and ASM structures) leads to an increase in the sensitivity from 118°/RIU to 128°/RIU while

for the case of AMG and AM structures, the higher value of FOM was obtained compared to ASMG and ASM structures.
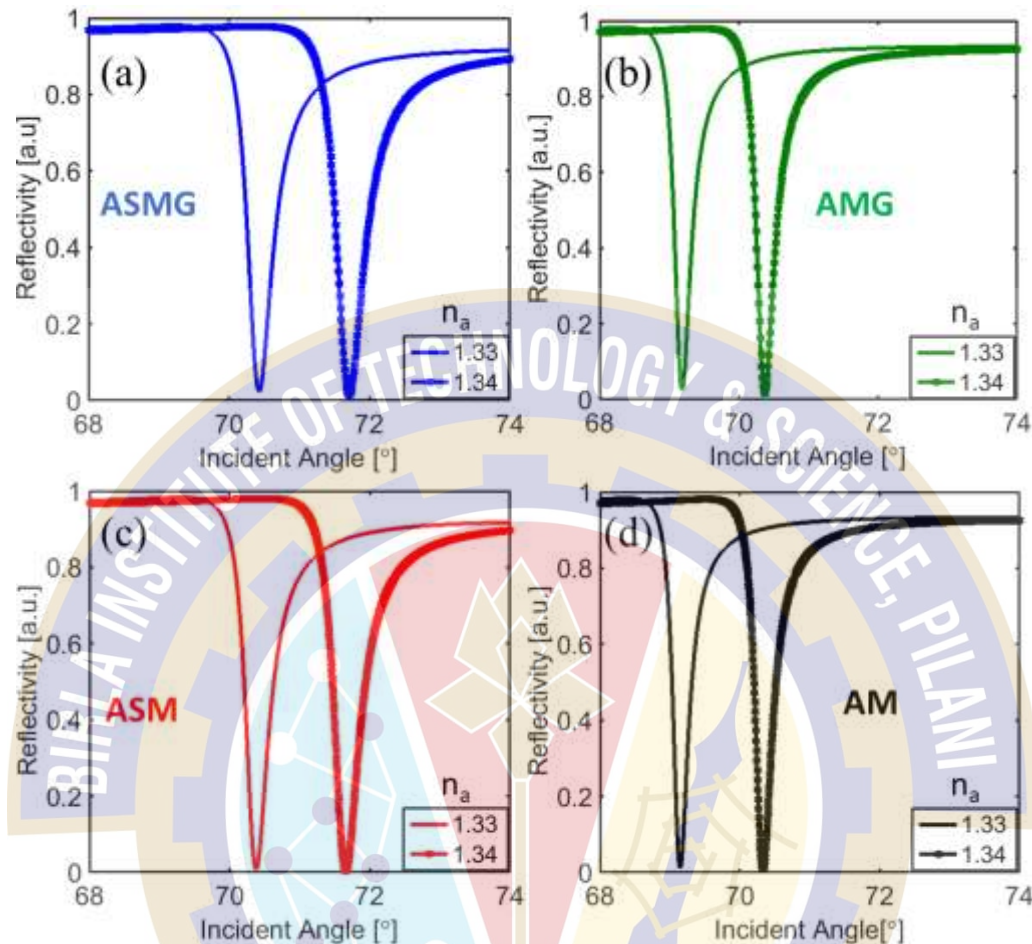
Fig. 4.3. Reflectivity curves with the variation in the refractive index of the analyte for (a) ASMG (b) AMG (c) ASM (d) AM structures respectively.

TABLE 4.1: Comparison of sensitivity and FOM for all the proposed structures

Structure	Sensitivity [°/RIU]	FOM [RIU^{-1}]
ASMG	128	278.26
AMG	118	393.33
ASM	128	304.76
AM	118	421.42

To increase both the sensitivity and FOM simultaneously for all the structures, multilayer MoS$_2$ layers were considered for the structures. The value of sensitivity, FWHM, and FOM were calculated for the different values of MoS$_2$ layers. Table 4.2 illustrates the calculated values of sensitivity, FWHM, and FOM for ASMG structure with an increase in the number of MoS$_2$ layers. It can be seen that the sensitivity increases with the increase in the number of MoS$_2$ layers but with the decrease in FOM.

TABLE 4.2: Comparison of performance parameters with an increase in the number of MoS$_2$ layers for ASMG structure

Number of MoS$_2$ Layers	Sensitivity [$^\circ$/RIU]	FWHM[$^\circ$]	FOM [RIU^{-1}]
0	128	0.44	290.9
2	129	0.47	270.46
4	131	0.50	262
6	133	0.54	246.29
8	134	0.58	231.03
10	137	0.62	220.96
12	139	0.67	207.46
13	**141**	**0.70**	**201.42**
14	143	0.71	201.40
16	146	0.78	187.17
18	149	0.85	175.29
20	153	0.93	164.51
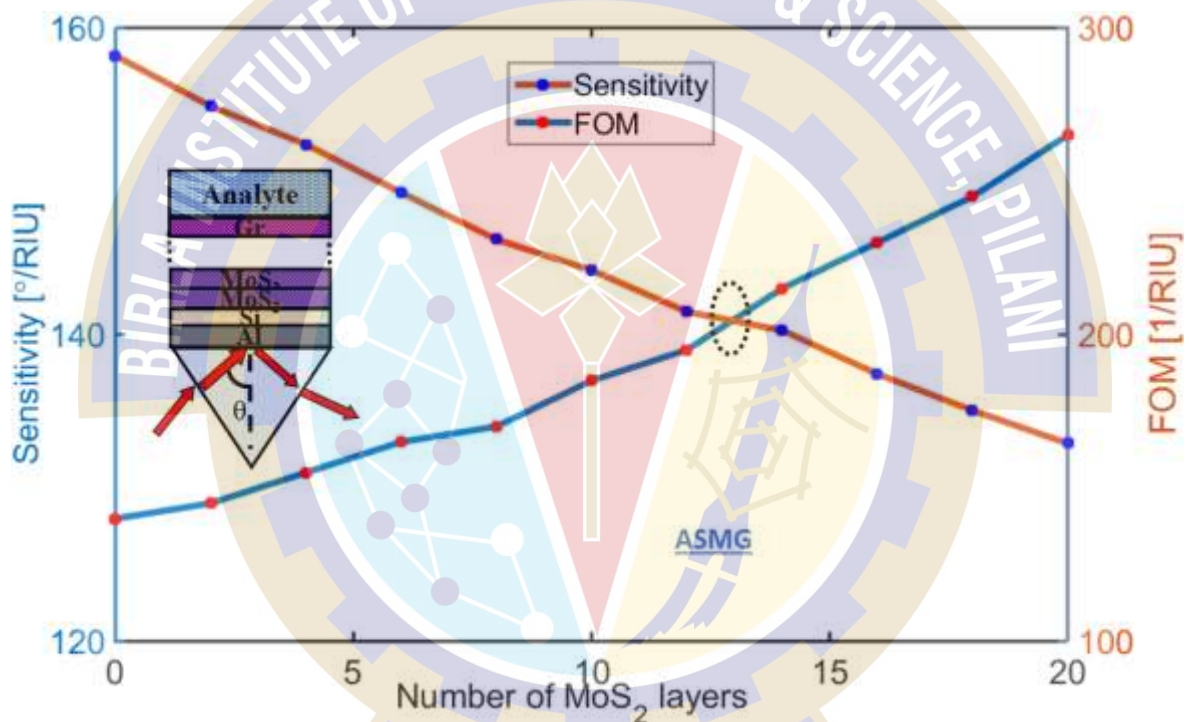
Fig. 4.4. Variation of sensitivity and FOM with the increase in the number of MoS$_2$ layers in the proposed ASMG plasmonic device.

With a slight increase in the sensitivity, FWHM increases almost two times resulting in a much lower value of FOM. Therefore, there was a need to reach a certain trade-off between the two important parameters. Plotting sensitivity and FOM with the variation in the number of MoS$_2$ layers, in Fig. 4.4, it was concluded that L = 13 number of MoS$_2$ layers would give an appreciable performance for ASMG proposed plasmonic device in the communication band.
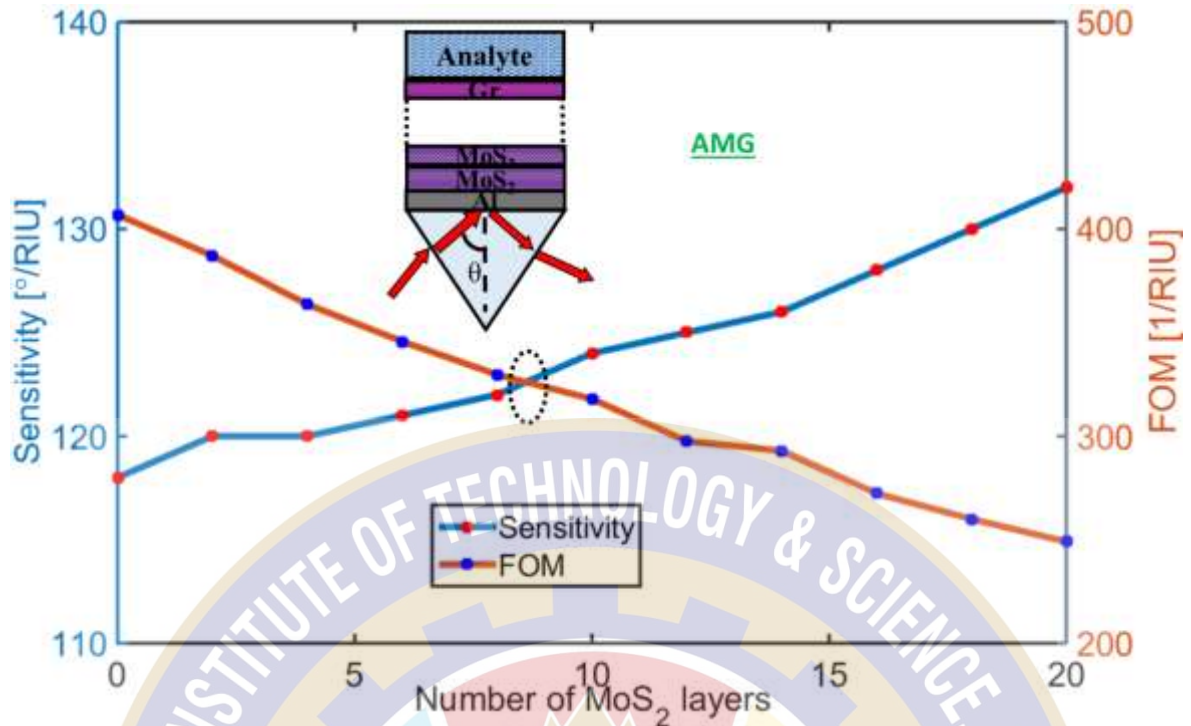
Fig. 4.5. Variation of sensitivity and FOM with the increase in the number of MoS_2 layers in the proposed AMG plasmonic device.

Similar conclusions can be drawn for the rest of the proposed structures, where the device performance was checked for an optimized number of MoS_2 layers at a compromise between both the sensitivity and FOM. The performance of the AMG structure was examined for a larger number of MoS_2 layers as shown in Fig. 4.5. The number of optimized layers comes out to be 9 and the corresponding sensitivity and FOM were calculated to be 123°/RIU and 323.68 RIU^{-1} respectively, as can be seen in Table 4.3.

TABLE 4.3: Comparison of performance parameters with an increase in the number of MoS_2 layers for AMG structure

Number of MoS2 Layers	Sensitivity [° /RIU]	FWHM [º]	FOM [RIU^{-1}]
0	118	0.29	406.89
2	120	0.31	387.09
4	120	0.33	363.63
6	121	0.35	345.71
8	122	0.37	329.72
9	**123**	**0.38**	**323.68**
10	124	0.39	317.94
12	125	0.42	297.61
14	126	0.43	293.02
16	128	0.47	272.34
18	130	0.50	260
20	132	0.53	249.05
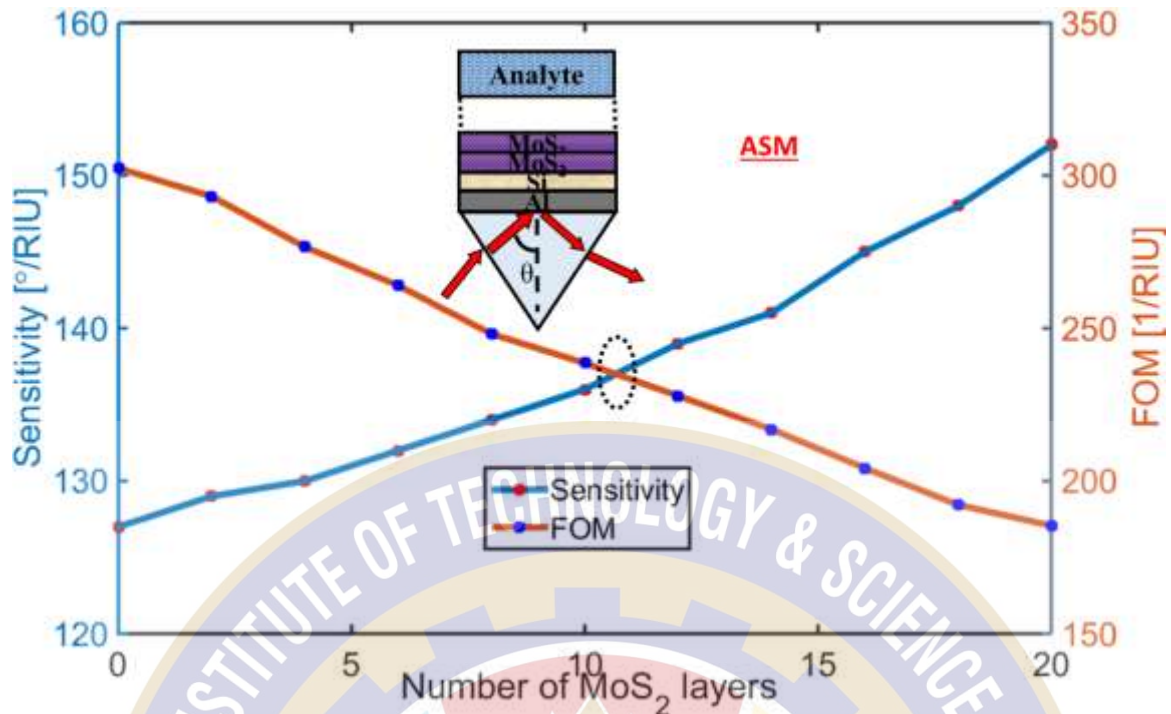
Fig. 4.6. Variation of sensitivity and FOM with the increase in the number of MoS$_2$ layers in the proposed ASM plasmonic device.

11 layers of MoS$_2$ were optimized for the ASM structure according to Fig. 6. Table 4.4 shows the performance parameters for the ASM structure having an optimized sensitivity of 137°/RIU and FOM of 232.20 RIU^{-1}.

TABLE 4.4: Comparison of performance parameters with an increase in the number of MoS$_2$ layers for ASM structure

Number of MoS$_2$ Layers	Sensitivity [°/RIU]	FWHM [°]	FOM [RIU^{-1}]
0	127	0.42	302.38
2	129	0.44	293.18
4	130	0.47	276.59
6	132	0.50	264
8	134	0.54	248.14
10	136	0.57	238.59
11	**137**	**0.59**	**232.20**
12	139	0.61	227.86
14	141	0.65	216.92
16	145	0.71	204.22
18	148	0.77	192.2
20	152	0.82	185.36
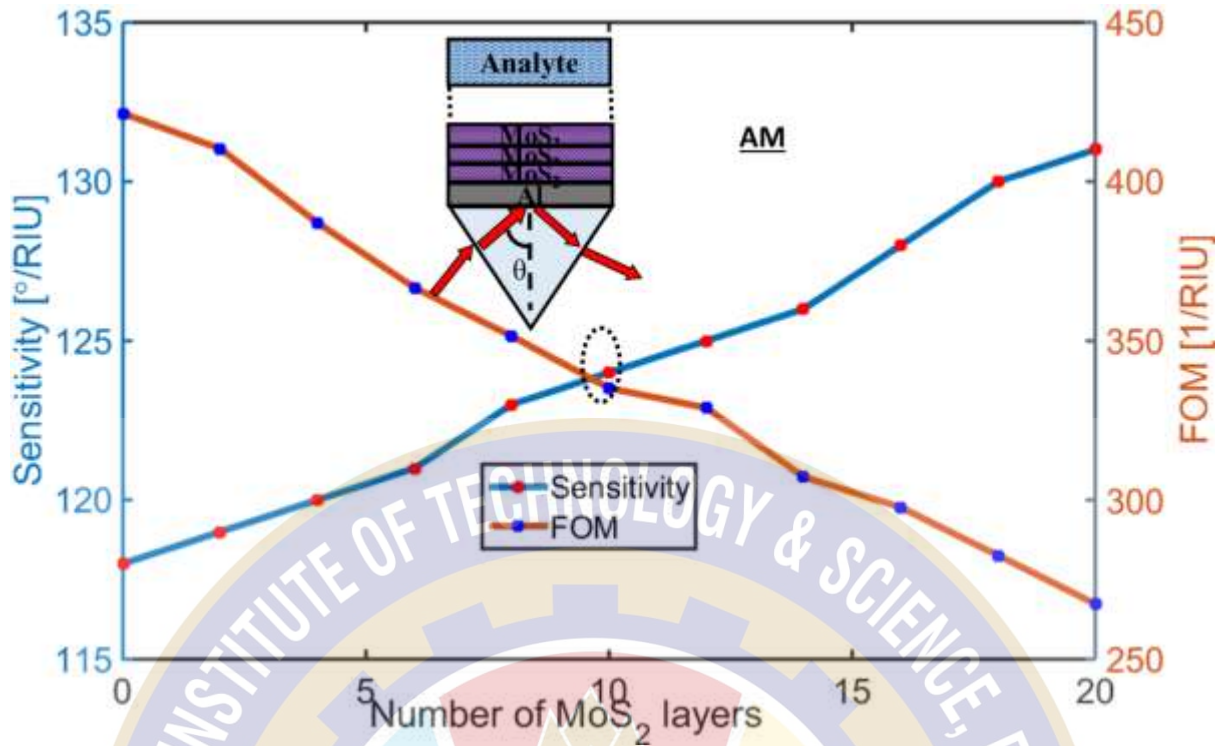
Fig. 4.7. Variation of sensitivity and FOM with the increase in the number of MoS$_2$ layers for the proposed AM plasmonic device.

Lastly, the trade-off for the AM structure was achieved at 10 MoS$_2$ layers as shown in Fig. 4.7. From Table 4.5, the optimized value of sensitivity and FOM obtained were 124°/RIU and 335.13 RIU^{-1} respectively.

TABLE 4.5: Comparison of performance parameters with an increase in the number of MoS$_2$ layers for AM structure.

Number of MoS$_2$ Layers	Sensitivity [°/RIU]	FWHM [º]	FOM[RIU^{-1}]
0	118	0.28	421.42
2	119	0.29	410.34
4	120	0.31	387.09
6	121	0.33	366.67
8	123	0.35	351.42
10	**124**	**0.37**	**335.13**
12	125	0.38	328.94
14	126	0.41	307.31
16	128	0.43	297.67
18	130	0.46	282.60
20	131	0.49	267.34

After the successive optimizations of MoS$_2$ layers for all four configurations, there arises a need to have a comparative study among the four proposed plasmonic devices. While the

sensitivity was found to be maximum for the optimized ASMG structure (141°/ RIU), the highest FOM was achieved for the AM configuration (335.13 RIU^{-1}). Fig. 4.8 shows the comparative analysis for all four engineered structures in terms of sensitivity, FWHM, and FOM with respect to increase the refractive index of the analyte. The sensitivity was found to be increasing with the increase in the refractive index of the analyte and the maximum sensitivity of 195°/RIU was achieved for the case of ASMG structure as shown in Fig. 4.8 (a). The FWHM values were also found to be increasing with the increase in the refractive index for all the structures but with the smallest increment in FWHM for the case of AM structure as shown in Fig. 4.8 (b). Fig. 4.8 (c) shows the variation in FOM with the increase in the refractive index of the analyte. A maximum value of FOM is found to be 335.13 RIU^{-1} for the case of AM structure due to low FWHM.
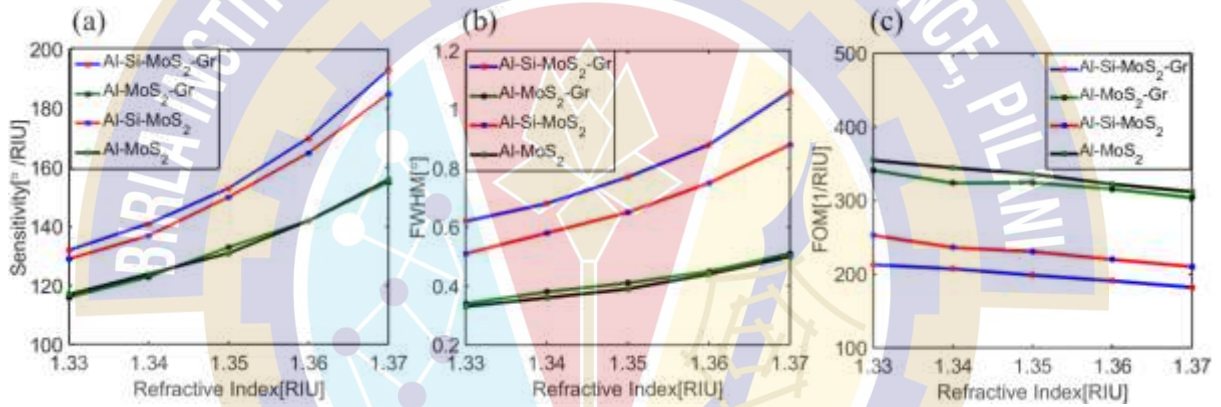
Fig. 4.8. Comparative analysis of the performance parameters for all four structures in terms of (a) Sensitivity (b) FWHM and (c) FOM with respect to increase in the refractive index of the analyte.

Fig. 4.9(a) shows the magnetic field distributions of the ASMG structure for SP mode at the wavelength of 1550 nm. It can be seen that the field is strongly confined to the metal-analyte interface. As we move away from the interface, the change in color shows the reduction in magnetic field interactions. Fig. 4.9 (b) shows the plot for MFIEF with respect to the normal distance from the interface for the proposed configurations and conventional Kretschmann configuration respectively. Indeed, the proposed configurations offered an enhancement in the Magnetic field intensity with respect to the conventional configuration due to the presence of Si/Gr/MoS$_2$ layers.
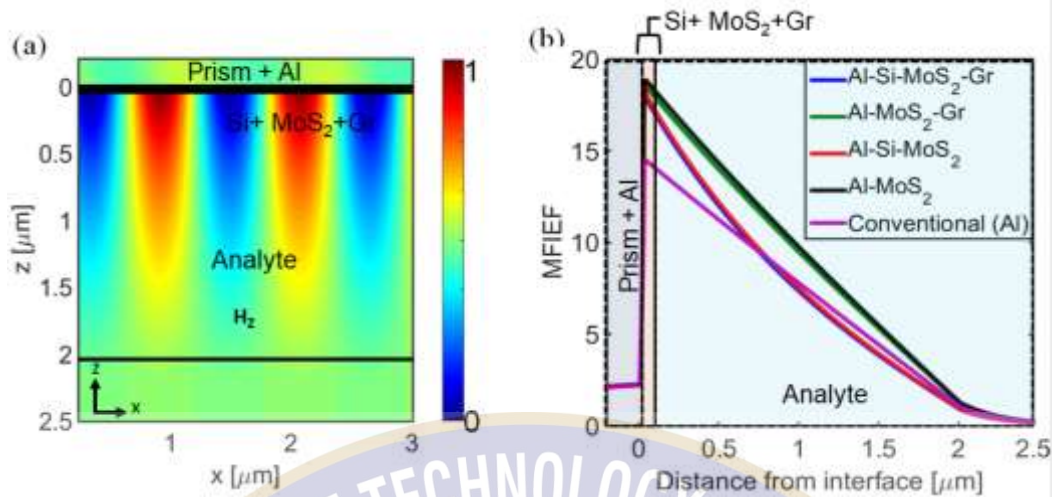
Fig. 4.9. (a) Magnetic field distribution for the ASMG structure for SP mode at the wavelength of 1550 nm (b) Comparison of Magnetic Field Intensity Enhancement Factor (MFIEF) with respect to the normal distance from the interface for the proposed configurations and conventional Kretschmann configuration respectively.

Next, the obtained results from the proposed configurations were compared with the previously reported works in terms of sensitivity and FOM. All the previous works lack in taking both the parameters, sensitivity, and FOM simultaneously into consideration during device optimization. All four proposed structures have appreciable sensitivity as well as FOM in the NIR region. Whereas the previously reported work either offered a good sensitivity but at the cost of low FOM or a high FOM but with a lesser value of the sensitivity (Table 4.6).

As SPR biosensors are already being used in numerous biosensing events so, in the last section, we demonstrated a biosensing application by detecting the minute changes in the concentration of ssDNA. The particular usage of the Gr-MoS$_2$ composite for DNA-sensing has already been put forth by Rahman et al. [29]. Gr can strongly attach the carbon-based antigen, for example, DNA, with the help of pi-stacking, whereas MoS$_2$ can adsorb the DNA with the help of van der wall forces between the basal plane of MoS$_2$ and nucleobases of DNA [20].

We presented the sensitivity analysis for ASMG and AM structures for a corresponding change in the SPR angle when a different concentration of ssDNA gets immobilized on the surface of the device. The refractive index of the sensing medium changes according to the variation in molar concentration and is expressed as [35]:

$$n_{da} = n_d + c_a.dn_a/dc_a \tag{4.1}$$

Where n_d is the refractive index of the sensing medium before the adsorption of biomolecules, c_a is the concentration of the adsorbed molecules and dn_a/dc_a is the adsorbed increment in the biomolecules. dn_a/dc_a is equal to 0.182 cm^3/gm for the case of a PBS buffer solution ($n_d =$

50

1.334) as a sensing medium. Soon after the immobilization of the adsorbate on the surface, the transfer of carriers took between e-rich ssDNA molecules and composite layers, causing a change in propagation constant. Thus, the wave-matching condition occurs at a greater SPR angle. As seen in Fig. 4.10, an increase in the ssDNA molar concentration caused a rightward shift in the resonance angle, hence demonstrating the biosensing effect. The properties like increased adsorption ability and unique optical characteristics offered by both Gr and MoS_2 as well as the inclusion of a high index Si layer were all assimilated in the proposed configurations, resulting in improved biosensing technique in the NIR region. Table 4.7 mentions the sensitivity achieved by ASMG and AM configurations when the molar concentration of the ssDNA was varied from 5 mM to 40 mM in steps of 5 mM of ssDNA sequences.

TABLE 4. 6: Comparison of performance parameters of the proposed configurations to previously reported works

Ref. no.	Schematic	S_θ [°/RIU]	FOM [RIU^{-1}]
[90]	Air-MoS_2-Al-MoS_2-Gr	215	72.5
[122]	Ag-Blue P/MoS_2	355.52	92.12
[123]	Au-MoS_2-Gr	67.79	96.84
[124]	Au-MoS_2	33.26	218.8
[125]	Au-Si-MoS_2-Gr	49.29	246.45
Our proposed work	**Al-Si-MoS_2-Gr** **Al-MoS_2-Gr** **Al-Si-MoS_2** **Al-MoS_2**	**141** **123** **137** **124**	**201.42** **323.68** **232.20** **335.13**
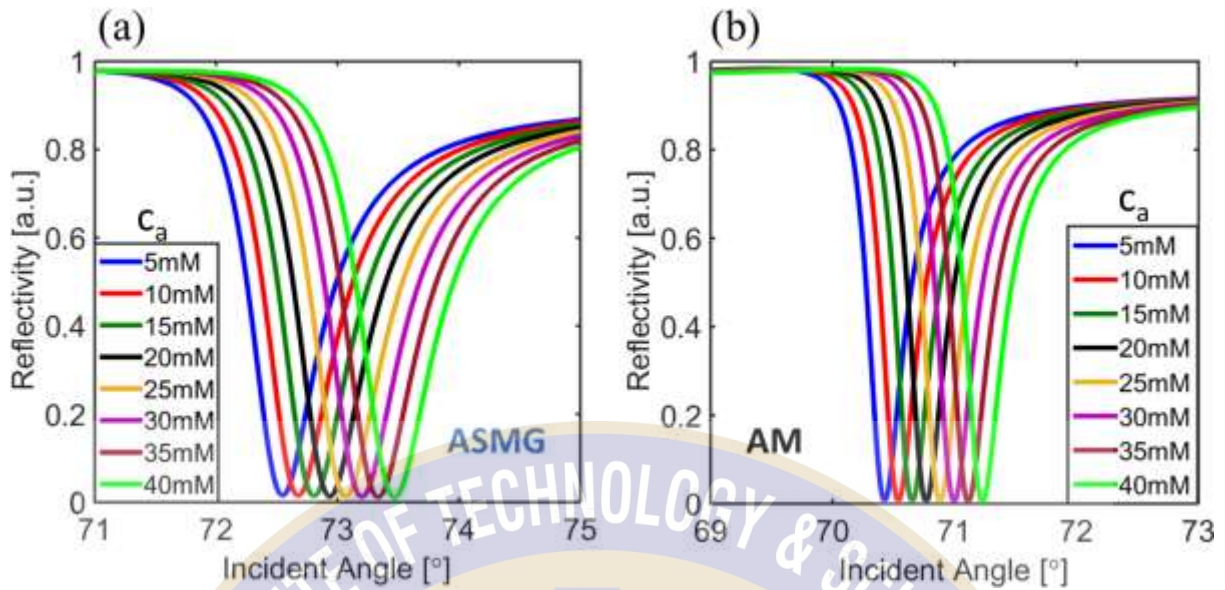
Fig. 4.10: Reflectivity Spectra with variation in ssDNA molar concentration for (a) ASMG and (b) AM configurations respectively.

TABLE 4.7: Comparison of performance parameters of the proposed ASMG and AM configurations with an increase in ssDNA concentrations

Concentration (c_a)	ASMG			AM		
	$\Delta\theta_{SP}$ [°]	Sensitivity [°/RIU]	FOM [RIU^{-1}]	$\Delta\theta_{SP}$ [°]	Sensitivity [°/RIU]	FOM [RIU^{-1}]
5 mM	0.12	**131.86**	180.63	0.13	120.87	**326.67**
10 mM	0.12	**142.85**	195.68	0.12	131.86	**347.00**
15 mM	0.13	**142.85**	190.46	0.11	120.87	**318.07**
20 mM	0.13	**142.85**	187.96	0.11	120.87	**318.07**
25 mM	0.14	**153.84**	202.42	0.12	131.86	**338.10**
30 mM	0.13	**142.85**	185.51	0.11	120.87	**309.92**
35 mM	0.13	**142.85**	183.14	0.12	131.86	**338.10**
40 mM	0.14	**153.84**	194.73	0.12	131.86	**329.65**

4.4 Conclusion

In this chapter, Al-MoS$_2$-based plasmonic devices were explored in the NIR region. The compatibility of Al among optoelectronic devices and the ability of Gr to act as a biorecognition element were examined along with the increased adsorption activity due to the presence of MoS$_2$ layers. Silicon was also used between the intermediate layers as a high-index dielectric, in turn enhancing the overall sensitivity. For better sensor performance, a trade-off was established between the sensitivity and FOM, giving the optimized number of MoS$_2$

layers for each of the proposed devices. After the required parameter optimizations, a comparative study was presented for all four proposed configurations in terms of sensitivity, FWHM, and FOM. It was found that the ASMG structure exhibited maximum sensitivity and the AM structure attained the highest FOM. Finally, the best two out of four devices were selected to demonstrate the biosensing application by capturing the changes in ssDNA concentrations. From the results, it was evident that the enhanced sensor performance in terms of both sensitivity and FOM can be achieved with the Aluminum-MoS_2 combination in the longer wavelength regime.

Chapter 5

Investigation of 2D nanomaterials on MXene (Ti$_3$C$_2$T$_X$)-based aluminum-plasmonic devices

After studying different conventional 2D nanomaterials on Al thin film for plasmonic devices, in the previous chapter, it will be interesting to study them over transition metal carbide (MXene) based materials. Since 2D nanomaterials can provide quality collaboration for MXene (Ti$_3$C$_2$T$_x$), from their functionalization to the application [126], we have undertaken Black Phosphorus (BP), Gr, MoS$_2$, and Fluorinated Graphene (FG) sheets for this purpose. These combinations with Al-Ti$_3$C$_2$T$_x$-based plasmonic devices can boost their presence in the plasmonic domain at 1550nm. Also, for the first time, this work brings into picture four such configurations (Ti$_3$C$_2$T$_x$-FG, Ti$_3$C$_2$T$_x$-MoS$_2$, Ti$_3$C$_2$T$_x$-BP, and Ti$_3$C$_2$T$_x$-Gr) for Al-based plasmonic devices with both high sensitivity as well as FOM simultaneously in the NIR region. Refractive indices corresponding to protein solutions are utilized on the proposed configurations to demonstrate the biosensing application. It is observed that with the corresponding change in the refractive index of the solution, the reflectivity curves exhibit redshift, thus suggesting possibilities for the potential application of Al-Ti$_3$C$_2$T$_x$-based plasmonic devices in the biosensing arena.

5.1   Introduction

MXene group has become a recent hotspot for SPR sensors due to its superior capacity for loading biomolecules [126]. Ti$_3$C$_2$T$_x$ is the first discovered and the most widely used MXene [127]. The negatively charged surface terminations of Ti$_3$C$_2$T$_x$ (for T$_x$ = hydroxyl (OH), fluorine (F), and oxygen (O)) are useful for sensing a wide variety of analytes [128]. Ti$_3$C$_2$T$_x$ can be obtained through a minimally intensive layer delamination method after selective etching of Al from the MAX phase (Ti$_3$AlC$_2$) [129]. Overall, the flexibility, hydrophilicity, and large surface area for improved adsorption of Ti$_3$C$_2$T$_x$ nanosheets have provided a useful platform for the ultrasensitive determination of unknown analyte samples [130][131]. Among the prism-based configurations, entire design simulations are cornered around 633m for Ti$_3$C$_2$T$_x$ in the vicinity of noble metals like Au, and Ag [132][133]. Out of the few reported works regarding Al, the Ti$_3$C$_2$T$_x$ -based fiber optic SPR sensor showed improved sensitivity of about 46.3% for Al with 12 layers of Ti$_3$C$_2$T$_x$ at a wavelength of 532nm but without any discussion about the resulting FOM [134]. Here, Ti$_3$C$_2$T$_x$ on top of Al metal protects the latter

from oxidation as well. Additionally, $Ti_3C_2T_x$ nanosheets are preferred for biosensing rather than pristine $Ti_3C_2T_x$ as the single or few-layered $Ti_3C_2T_x$ provides increased adsorption sites for the target molecules [135]. Equally popular is Graphene (Gr) for biosensing [136], which has a very close lattice match with $Ti_3C_2T_x$ resulting in Van der Waals heterostructure [131]. However, Gr inertness produces lower selectivity in adsorption; therefore, among the many derivatives of Gr, FG has become a nascent area of interest with many promising applications in the future biomedical field [137]. With almost comparable mechanical strength to Gr, FG exhibits superior optical isotropy. FG sheets implemented over the Kretschmann configuration ($Ti_3C_2T_x$ based) in the NIR region by Pandey et al. showed decent FOM, but without regard to sensitivity [138]. Additionally, when it comes to examining in-vivo biosensors for live cells, toxicity in the lowest levels is a requisite parameter. Zhang et al. have used MoS_2 over $Ti_3C_2T_x$-based SPR sensors, with a sensitivity of 246°/RIU and FOM of 34.2 RIU^{-1} at 633nm [132]. Besides, the integration of 2D MoS_2 with $Ti_3C_2T_x$ nanoparticles has resulted in enhanced photodetection [139]. However, MoS_2 in the visible region ends up with broader SPR curves resulting in a poor FOM (due to the existence of the large imaginary part of the dielectric constant). Similarly, another 2D nanomaterial namely, Black Phosphorus (BP) has been reported to exhibit better absorption and adsorption properties compared to Gr, MoS_2 as clearly highlighted by Srivastava et al. [140], except for its readily oxidizable nature, several methods for which have been reported to mitigate the same [133]. As the combination of BP- $Ti_3C_2T_x$ is found to be the most stable, the utilization of such nanocomposites with the optimal metal thickness is studied for efficient SPR sensors [133].

Nonetheless, in the visible regime, all such works dealing with $Ti_3C_2T_x$ have only focused on either of the two performance parameters, i.e., sensitivity or figure of merit. On the other hand, at 1550nm, $Ti_3C_2T_x$ has only been discussed as a plasmonic metal-like behaving material [141]. This leads us to two conclusions. Firstly, it becomes imperative to study the biomolecular interaction on Al-$Ti_3C_2T_x$-based plasmonic devices at longer wavelengths in the vicinity of 2D nanomaterials. Secondly, from the point of view of practical sensor implementation, all the performance parameters carry equal weightage. Compromising any one parameter at the cost of others doesn't meet the requirements of accurate real-time sensing. Thus, this chapter highlights the detailed analysis of all the above-discussed nanomaterials, thereby utilizing them with Al-$Ti_3C_2T_x$-based plasmonic devices in the NIR wavelength region for biosensing applications.

5.2 Design parameters for proposed devices

In all four Al-Ti$_3$C$_2$T$_x$-based configurations, Al was considered the plasmonic metal. Angular interrogation was performed for the proposed engineered plasmonic devices over CaF$_2$ (n_p = 1.426) as the coupling prism.
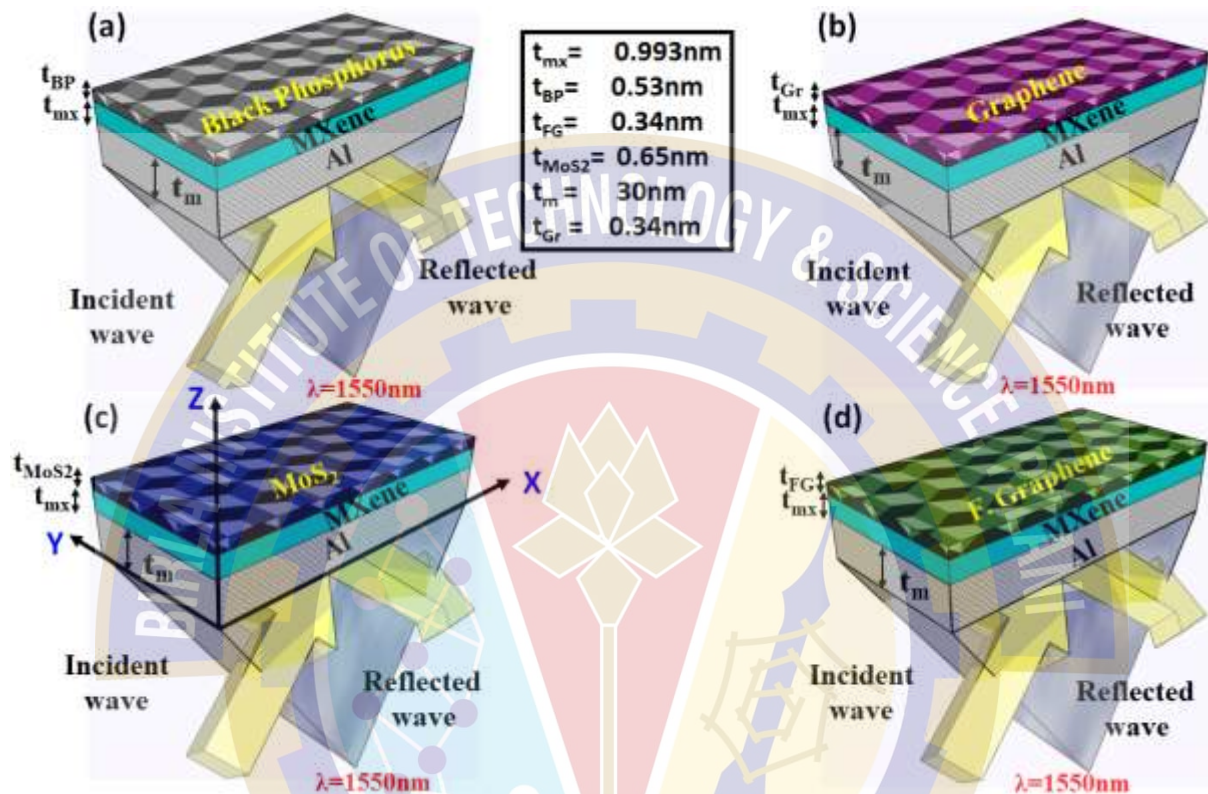
Fig. 5.1. The schematic (not to scale) for the proposed Al- MXene-based plasmonic devices with (a) Black Phosphorus (BP) (b) Graphene (Gr) (c) MoS$_2$ (d) Fluorinated Graphene (FG), under total internal reflection scheme at a wavelength of 1550nm.

Over the optimized Al-Ti$_3$C$_2$T$_x$ layer combination, different 2D nanomaterials were chosen to study the effect of the plasmonic resonance condition at the interface. The sensing medium was considered to be water (n_a =1.33). Fig. 5.1 shows the schematic representation of the proposed plasmonic configurations considering BP, Gr, MoS$_2$, and FG on the top of engineered plasmonic devices, respectively. All four configurations have shown that Al-Ti$_3$C$_2$T$_x$-based plasmonic design can achieve appreciable sensitivity and FOM simultaneously in the longer wavelength regime. Both the performance parameters (sensitivity and FOM) were satisfied, for the first time, unlike the previous works concerning Ti$_3$C$_2$T$_x$ for plasmonics [142].

The refractive index for the Gr sheet was calculated using Kubo's formula [93]. The refractive index for Ti$_3$C$_2$T$_x$ with the (OH)$_2$ terminated functional group was calculated from the work published by Berdiyorov et al. [143] as the hydroxyl functional group has been reported with

the strongest binding energy strength [144]. The refractive index for BP was calculated from the recent work published by Ross et al. [145]. The refractive indices and the corresponding thicknesses of the 2D nanomaterials used for subsequent simulations are tabulated below in Table 5.1. Finally, the two sensing parameters i.e., sensitivity and FOM were calculated for the proposed plasmonic devices.

TABLE 5.1: Refractive indices and the thicknesses of the 2D nanomaterials used in the work

2D Nanomaterials used	Thickness	Refractive index at 1550nm	The Refractive index value is taken from the Reference
$Ti_3C_2T_x$	0.993nm	$2.1095 - i1.1338$	[143]
Fluorinated Graphene	0.34nm	$2.62563 - i10^{-6}$	[138]
MoS_2	0.65nm	3.647	[146]
Black Phosphorus	0.53nm	$3.0945 - i1.58369$	[145]

5.3 Numerical Analysis

To begin with, firstly, the Al metal layer was optimized for minimum reflectivity and narrow linewidth of SP mode. Fig. 5.2(a) shows the reflection characteristics for an Al-$Ti_3C_2T_x$ (monolayer) based plasmonic device with the variation of Al metal height (t_m) from 25nm to 35nm, in steps of 5nm. At $t_m = 30$nm, the lowest reflectivity with a decent line width of SP mode was seen, which would mean a maximum transfer of energy to the conduction electrons of Al, thus exhibiting highly efficient SP excitation at the boundary surface. Thereafter, the effect of variation in the refractive index of the analyte (n_a) on an engineered Al-$Ti_3C_2T_x$-based plasmonic device was studied as shown in Fig. 5.2(b). The refractive index of the analyte 'n_a' was changed from 1.33 to 1.34. With a monolayer of $Ti_3C_2T_x$ (Fig. 5.2(b)), a sensitivity value of 119°/RIU was obtained with FOM as 340 RIU^{-1}.
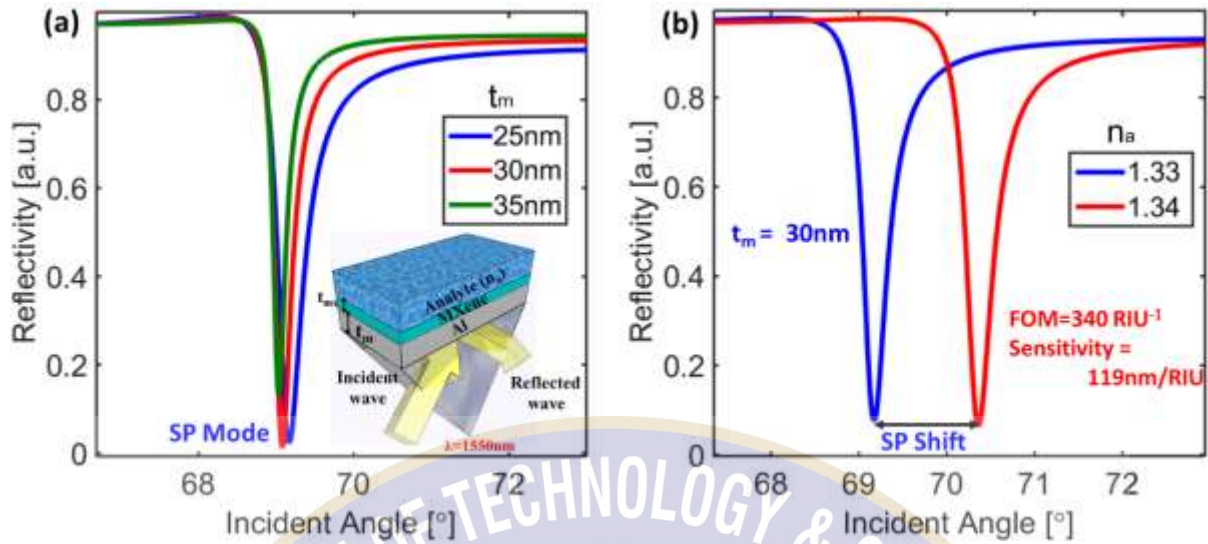
Fig. 5.2. Reflection characteristics for Al-Mxene (monolayer) based plasmonic device at the wavelength of 1550 nm (a) with variation in the Al metal height (t_m) (b) with the variation in the refractive index of analyte (n_a).

To study the effect of multilayers of $Ti_3C_2T_x$ on the plasmonic device, the reflection characteristics with the increase in the number of $Ti_3C_2T_x$ layers (L) for Al-$Ti_3C_2T_x$ based plasmonic device was calculated as shown in Fig. 5.3(a). With the increase in L, the linewidth and the reflection minima for SP curves change adversely. The linewidth of SP curves was found to be broader and the increase in the values of minimum reflectivity (R_{min}) was noticed with the increase in L. Fig. 5.3 (b) represents the variation in FOM and R_{min} with the variation in the number of $Ti_3C_2T_x$ layers. With sensitivity being almost constant, there was a drastic reduction in FOM from 340 RIU^{-1} (L=1) to 89.5 RIU^{-1} (L=11). Therefore, we can conclude that monolayer $Ti_3C_2T_x$ can suffice for subsequent simulations. Besides, many researchers also support the use of monolayer $Ti_3C_2T_x$ sheets since the flexibility gets reduced with the increasing number of $Ti_3C_2T_x$ layers along with the decline in sensing performance [147][148].
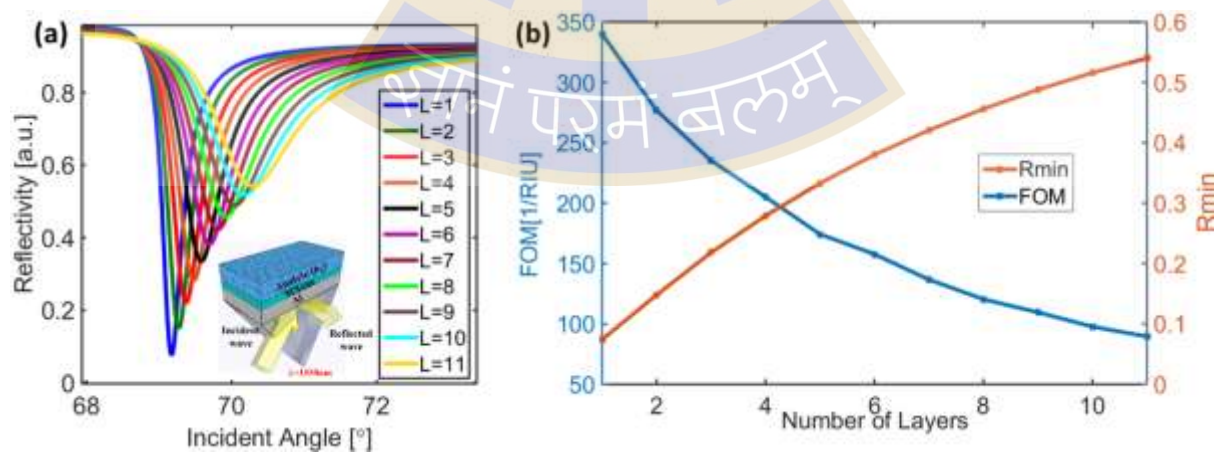
Fig. 5.3. (a) Reflection characteristics for the engineered Al-MXene-based plasmonic device with the variation in the number of MXene layers (b) The variation of FOM and R_{min} with the increase in the number of MXene layers for Al-MXene-based plasmonic device.

Since the long-term oxidation stability of $Ti_3C_2T_x$ aqueous solution is low [149], therefore assembling $Ti_3C_2T_x$ nanosheets with 2D nanomaterials can be an interesting way to resolve this issue along with better sensing performance as reported by Yoon et al. [150]. Moreover, investigating the effect of 2D nanomaterials with $Ti_3C_2T_x$ is significant because of the exceptional properties provided by $Ti_3C_2T_x$-based nanocomposites. The strong heterostructure that they form paves the way for outstanding structural integrity along with providing a shielding effect against the oxidation of $Ti_3C_2T_x$. Gr flakes can improve the mechanical robustness of $Ti_3C_2T_x$ after the formation of the 2D heterostructure. The field enhancement at the interface and increased surface adsorption are the two advantages of having heterostructure as the analyte interacting layer [151]. $Ti_3C_2T_x$-based heterostructures with MoS_2 help to fully utilize $Ti_3C_2T_x$'s unique structure by enhancing the surface reactivity plus pinning for ultrasensitive biosensors [150]. The excellent stability is obtained for $BP/Ti_3C_2T_x$ heterostructure as compared to bare $Ti_3C_2T_x$ and BP as confirmed by Li et al. experimentally [152].

So, the reflection characteristics for the proposed configurations (Fig. 5.1) with a monolayer of BP, Gr, MoS_2, and FG as the intermediate layers between $Ti_3C_2T_x$ and the analyte (sensing medium) were calculated as shown in Fig. 5.4. The refractive index of the analyte (n_a) was varied for all the proposed 4 configurations from 1.33 to 1.34 and a redshift in the SP wavelength was observed with an increase in the value of n_a as shown in Fig. 5.4. Table 5.2 compiles all the performance parameters for each of the proposed plasmonic designs. With these tabulated values, we can conclude that the $Ti_3C_2T_x$ layer which has so far been implemented only in the visible range, did not exhibit such large values of sensitivity along with FOM, which can be seen in the NIR range.
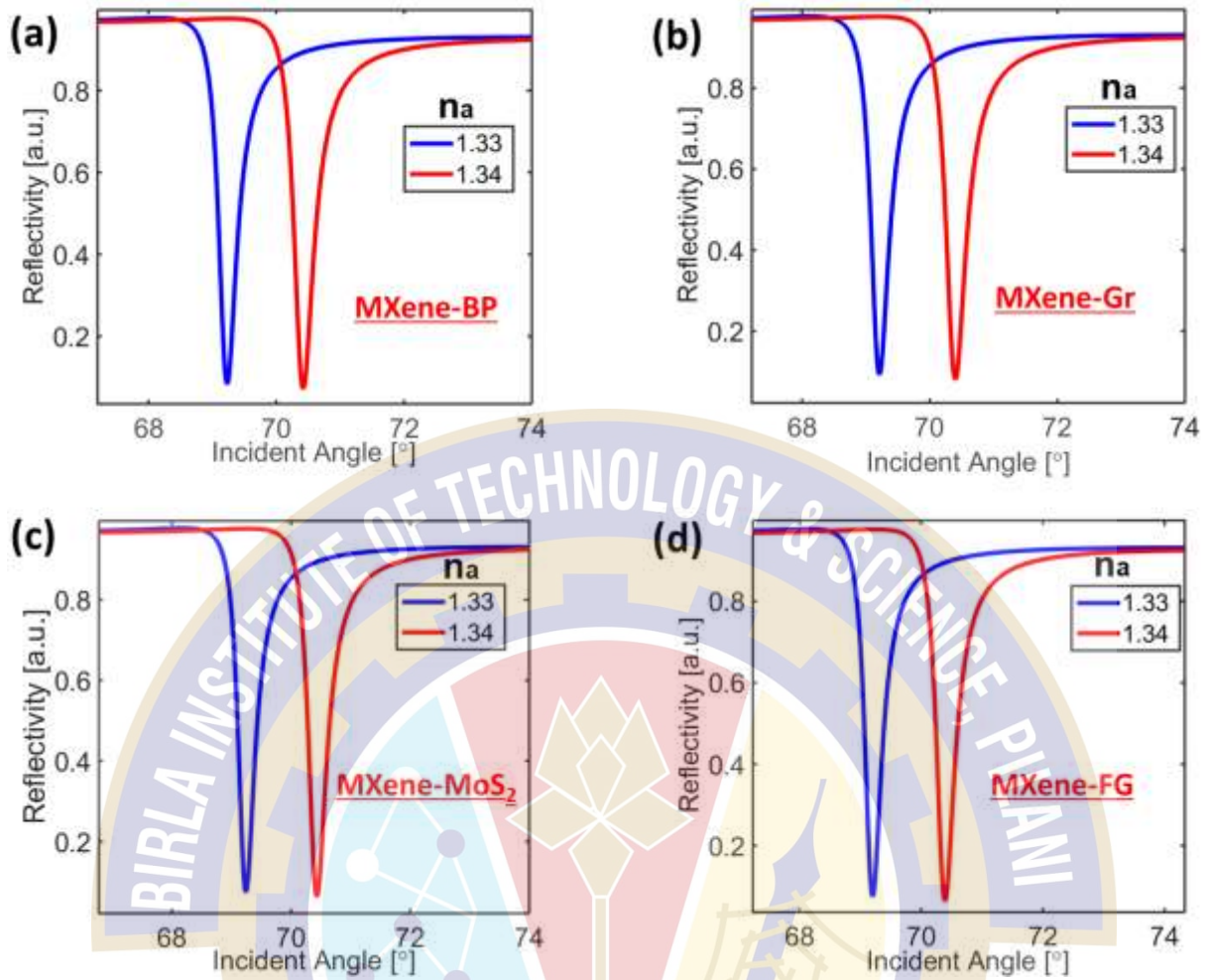
Fig. 5.4. Reflectivity curves with the variation in analyte index (n_a) exhibiting a redshift in SP mode for (a) Al- $Ti_3C_2T_x$ -BP (b) Al- $Ti_3C_2T_x$ -Gr (c) Al- $Ti_3C_2T_x$ -MoS_2 and (d) Al- $Ti_3C_2T_x$ -FG based configurations respectively.

TABLE 5.2: Comparison of performance parameters for the proposed configurations

Parameter	Al- $Ti_3C_2T_x$ - BP	Al- $Ti_3C_2T_x$ - Gr	Al- $Ti_3C_2T_x$ - MoS_2	Al- $Ti_3C_2T_x$ - FG
$S_\theta[°/RIU]$	119	119	119	119
FOM [RIU^{-1}]	330.55	330.55	330.55	340
R_{min}	0.082	0.092	0.074	0.074

After such appreciable results for all four design configurations, the multilayer effect of these 2D nanomaterials on Al-$Ti_3C_2T_x$-based configurations was evaluated with the change in the analyte index (n_a). Fig. 5.5 shows the reflection characteristics for all the proposed configurations with the increase in the number of layers of the 2D nanomaterials. We can observe the peculiarities with the varying number of layers for the aforementioned configurations. On the one hand, Gr and BP showed deteriorating R_{min} and broader SP linewidth due to a significant imaginary part of the dielectric constant (Fig.5.5 (a) & (b)). On the other hand, however, MoS_2 and FG showed almost constant reflection dips and linewidth

60

as we increase the number of layers (Fig. 5.5 (c) & (d)), due to the very small imaginary part (negligible) of the dielectric constant. Although the change in sensitivity is minute, however, the contrasting differences in the linewidth, as well as R_{min}, calls for a certain trade-off to be achieved to obtain an optimized design.
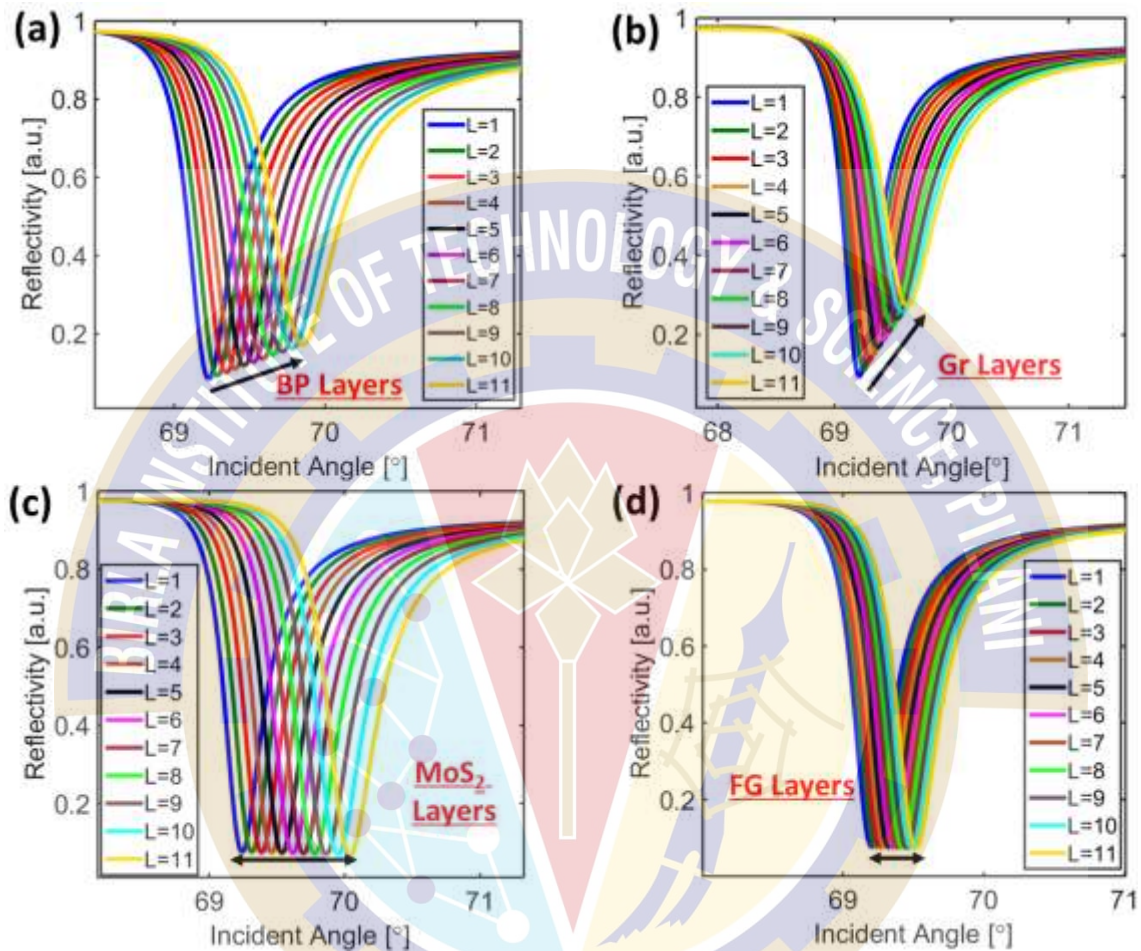
Fig.5.5. Reflectivity curves exhibiting SP mode with varying the number of layers of (a) BP (b) Gr (c) MoS_2 and (d) FG for proposed Al- $Ti_3C_2T_x$ -based plasmonic devices.

Subsequently, with the increasing number of layers, the corresponding R_{min} and FOM were calculated for each case and a perfect trade-off was achieved to get standardized results. Fig. 5.6 shows the trade-off between FOM and R_{min} for the proposed plasmonic devices using BP, Gr, MoS_2, and FG as the BRE for proposed Al-$Ti_3C_2T_x$-based devices. In the case of BP and Gr layers, the FOM was found to be decreasing, and R_{min} was found to be increasing with the increase in the number of layers (Fig. 5.6 (a) & Fig. 5.6 (b)). When the trend for the calculated values of FOM and R_{min} was observed for FG and MoS_2 mediated plasmonic devices, interestingly, there were very minor changes observed for the said parameters with increasing the number of layers (Fig. 5.6 (c) & Fig. 5.6 (d)). The proposed design employing FG has an almost constant FOM. Concurrently there is a slight variation in FOM for the Al-$Ti_3C_2T_x$-MoS_2

configuration. There is hardly any change in performance parameters within the range of 10 to 12 layers of FG or MoS_2. Thus, we can conclude that we don't need stringent control over the number of layers for Al-$Ti_3C_2T_x$-MoS_2 and Al-$Ti_3C_2T_x$-FG-based plasmonic devices since the R_{min} and FOM are hardly affected by the increase in the number of MoS_2 and FG layers. Nevertheless, in general, the characteristics of 2D nanomaterials are mostly layer-dependent, thus it is imperative to ensure the precise control of thickness or the number of layers. Characterization methods such as Raman spectroscopy and photoluminescence spectra can be employed for such analysis, as the respective intensity peaks are thickness dependent.

As for the fabrication techniques of single to few-layered nanomaterials reported in the context of MoS_2, BP, FG, and Gr, several works have shown the successful realization of 2D nanomaterials with precise control of the layer thickness by controlling the precursor parameters (reaction temperature, time, pressure, gas flow rate) during the chemical vapor deposition process [153], [154], [155].
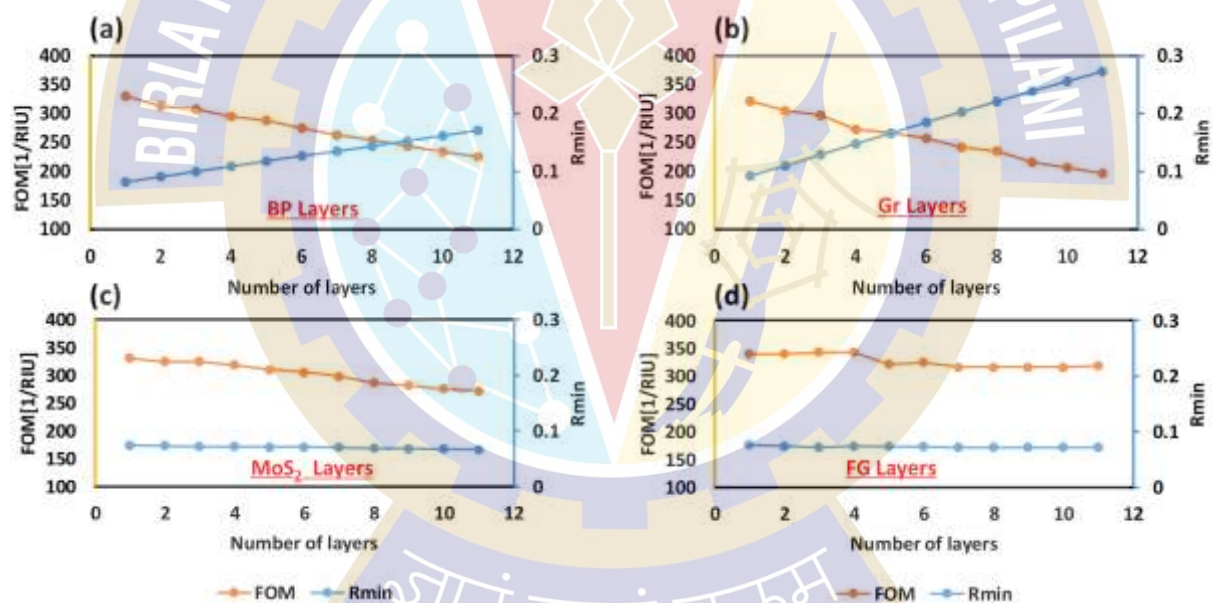
Fig.5.6. Variation in FOM and R_{min} in the proposed Al-$Ti_3C_2T_x$-based plasmonic devices for the increase in the number of layers of (a) BP (b) Gr (c) MoS_2 (d) FG respectively.

For demonstrating the biosensing application for the proposed Al-$Ti_3C_2T_x$-based configurations, we considered the detection of minute changes in the concentration of protein solution. The proposed design entailing monolayer MoS_2, and FG as the biorecognition element, were used for detecting any changes in the corresponding refractive index of the protein solution. The values of corresponding refractive indices for the protein solution were taken from the reference [156]. Fig. 5.7 shows an increment in the SP resonance angle with the

change in the refractive index of the protein solution, thus validating the real-time application of the proposed device. All the design configurations have a sensitivity of around 119º/RIU. Meanwhile, the appreciable values of FOM and the reflection minima open the window for the possibility of utilizing $Ti_3C_2T_x$-based Al plasmonic devices in the NIR region.
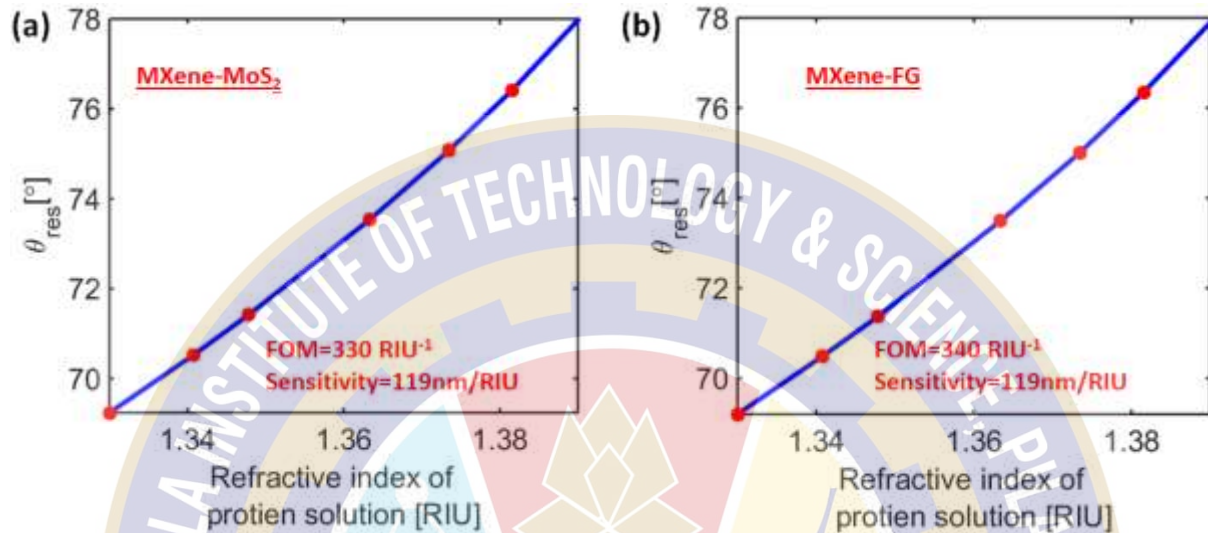
Fig. 5.7. Plot for a shift in the SPR angle (θ_{res}) with variation in the refractive indices corresponding to protein solution for (a) Al-$Ti_3C_2T_x$-MoS_2 (b) Al-$Ti_3C_2T_x$-FG based plasmonic device respectively.

Finally, Table 5.3 compiles all the work done so far on $Ti_3C_2T_x$-based plasmonic devices in the visible and NIR region. For the results reported previously, we can observe that our work has achieved a three-digit sensitivity and FOM simultaneously with the added advantage that the proposed plasmonic device holds rigidity and stability when it comes to the deposition of 2D nanomaterials as BRE elements. Such facts are unmatched by any previous works reported so far.

TABLE 5.3: Comparison of the proposed work with previous results reported in the literature

Ref. no	Schematic	S_θ [°/RIU]	FOM [1/RIU]	λ [nm]
[157]	Ag + Si+ $Ti_3C_2T_x$	231	39.83	633
[158]	Cu + Ni + BP+ $Ti_3C_2T_x$	304.47	57.8	633
[133]	Au+ $Ti_3C_2T_x$ +TMD+2D material	190.22	15.51	633
[128]	Ag + Si+ BP+ $Ti_3C_2T_x$	264	41.25	633
[132]	Au+ Ag + Si+ $Ti_3C_2T_x$	274	36.88	633
[158]	Metal+ ZnO + $Ti_3C_2T_x$	264	30.18	633
[141]	DL (Dielectric layer) + $Ti_3C_2T_x$ + Gr	52	326.74	1500
[138]	DBL (Dielectric buffer layer) + $Ti_3C_2T_x$ +FG	64	347	1550

[142]	DL+ $Ti_3C_2T_X$	26	304	1550
Proposed work	**Al + $Ti_3C_2T_X$ +MoS$_2$**	**119**	**330.55**	
	Al + $Ti_3C_2T_X$ +BP			
	Al + $Ti_3C_2T_X$ +Gr	**119**	**330.55**	**1550**
	Al +$Ti_3C_2T_X$ + FG			
		119	**330.55**	
		119	**340**	

From the fabrication aspects of the proposed plasmonic devices, the first step involves cleaning the glass prism with acetone, IPA, and DI water. After cleaning the glass prism, thin Al metal film can be deposited over the prism using the e-beam or thermal evaporation technique. MXene ($Ti_3C_2T_X$) layer can be obtained through a minimally intensive layer delamination method, after selective etching of Al from the MAX phase (Ti_3AlC_2)[129]. 2D nanomaterial such as Gr sheets can be deposited using a spray-assisted layer-by-layer process [159]. Likewise, MoS_2@MXene ($Ti_3C_2T_X$) fabrication can be performed via the hydrothermal method [160]. BP@ MXene ($Ti_3C_2T_X$) can be fabricated using an in-situ growth process via the chemical vapor transport method [161]. Correspondingly, for FG layer deposition, the spin-coating technique can be implemented [138]. In the proposed sensor, prior to each measurement, the sensing surface needs to be washed thoroughly with the solution in which the protein sample has been prepared. The common liquids/solutions used for washing the surface of the sensor after each measurement are bovine serum albumin (BSA), phosphate-buffered saline (PBS), and deionized water. The best way to carry out such experiments is to fabricate multiple microfluidic channels onto a single sensor and pass different concentrations of the sample in each of the channels to have the same reference.

5.4 Conclusion

Highlighting the versatility of Al in the NIR region for an enhanced plasmonic response, in this chapter, we investigated Al-MXene ($Ti_3C_2T_X$) based plasmonic devices employing 2D nanomaterials. The primary focus of this work was to explore the Al-based plasmonic devices with MXene ($Ti_3C_2T_X$) nanosheets, such that both the parameters, i.e., sensitivity and FOM, are taken care of. After engineering Al-MXene ($Ti_3C_2T_X$) based plasmonic design, the subsequent effect of 2D nanomaterial layers was studied for BP, Gr, MoS_2, and FG as the

intermediate layers between the Al-MXene ($Ti_3C_2T_X$) layer and the analyte. It was found that employing such nanocomposites provided us with added advantages without even degrading the performance parameters as such. The Al-MXene ($Ti_3C_2T_X$)-FG configuration was concluded as the best choice for sensing purposes, followed by the Al-MXene ($Ti_3C_2T_X$)-MoS_2 configuration. These results strengthen the potential application of MXene ($Ti_3C_2T_X$) for Al plasmonics in the NIR region. Lastly, to demonstrate biosensing application, minute changes in the concentration of the protein solution were detected using the proposed designs. The redshift in the SPR angle with the varying concentration of protein samples proved that the proposed Al-MXene ($Ti_3C_2T_X$)-based plasmonic devices are a better candidate for analysis in the NIR region with both high sensitivity and FOM.
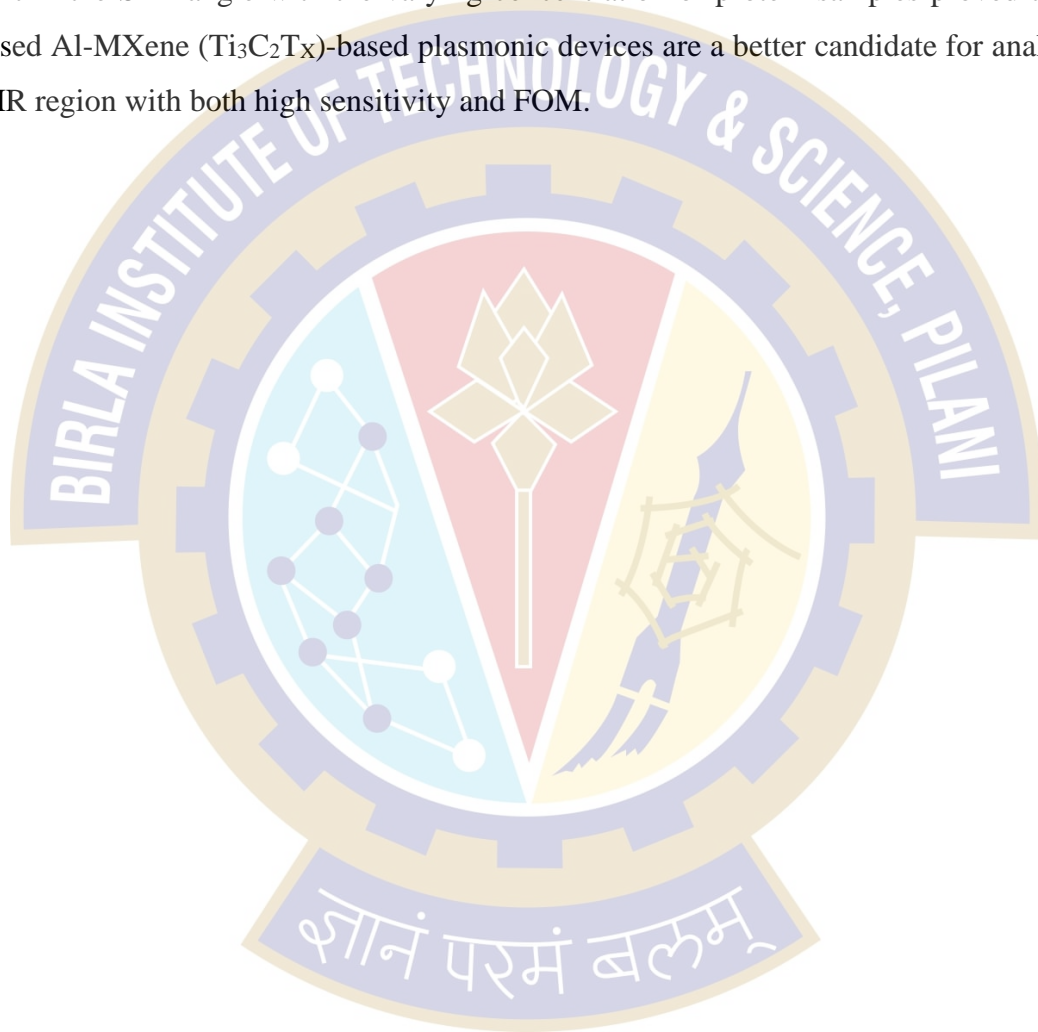
Chapter 6

Resolution enhancement using a multi-layered aluminum-based plasmonic device with metal-dielectric-metal configuration

An optimized plasmonic device always strives for higher sensitivity, as well as FOM. As observed in chapter 3, the inclusion of the dielectric layer (Si) enhances the sensitivity of the plasmonic device. In a quest to uplift the FOM further, a miniaturized design following a thin metal layer above the incumbent metal-dielectric (barium titanate) configuration is the point of discussion in this chapter. A metal-dielectric-metal (MDM) configuration is undertaken which leads to field confinement at the interface. This confined field at the nanoscale leads to increased FOM/resolution in the near-infrared region.

6.1   Introduction

The literature reports myriad combinations employing high dielectric constant materials like Silicon (Si), PMMA, and Barium Titanate (BaTiO$_3$) also known as BTO, for improved SPR sensitivity, or using different material substrates to identify the change in the position of the resonance dips [162]. Various MDM designs for field confinement [163], and 2D nanomaterials (Graphene, MoS$_2$, MXene) for increased affinity towards biomolecules [146] have also been reported over the conventional metal-analyte-based Kretschmann configuration to achieve high-performance yielding parameters. These examples point toward different combinations that bring about a rational design with improved feasibility, detection accuracy, and reduced cost for large-scale production.

So far, among the previously reported Ag-based SPR configurations, that considered the dielectric properties of BTO, sensitivity improved substantially but at the cost of compromising FOM [164][165]. Also, in Au-based sensors employing BTO, FOM was observed to be as low as 37.22 RIU-1[166]. Furthermore, several multi-layered geometries also reported enhanced sensitivity. However, FOM was largely ignored in almost all such modified Kretschmann arrangements. Among the MDM configurations utilizing BTO, Karki et al. have demonstrated an exhaustive sensitivity analysis for Au, Ag, and Copper (Cu) metal layers at 633nm with and without BTO, wherein the stability and sensitivity issues associated with the single metal layered design was reported to be overcome by a bimetallic design [167]. Many Au and Ag-

based MDM structures were also reported for better sensing performance parameters with respect to conventional single metal layer-based SPR sensor in the visible region for either angle interrogation or wavelength interrogation [168].

This brings us to a dualistic approach for the present work, i.e., considering multi-layered Al-based Kretschmann configuration firstly, over the conventional single metal design in the NIR region. Secondly, to study resolution enhancement in Al-based MDM configuration comprising BTO as the high dielectric constant material utilizing the strong field confinement at the interface.

Since utilizing an MDM configuration leads to the reduced linewidth of SPR curves, the FOM will be boosted significantly. After successive optimization of the intermediate layers, a 2D nanomaterial (MoS_2) is considered for the biofunctionalization of the Al metal. A high absorption coefficient and a narrow linewidth in the NIR region are some of the appealing properties of MoS_2. Analysis of the blood profile for the detection of the chikungunya virus is shown in the last section of this chapter to capture minute changes in the infected and normal blood components. The chikungunya virus is transmitted by the bite of infected female mosquitoes from one human body to another, especially affecting older people and people with serious health issues. The disease can severely increase morbidity and neurological manifestations as has been reported earlier [169]. Since the refractive index of blood depends on the changes in the concentration of its constituents (RBC, plasma, platelets), the normal and infected blood components can be accounted for by changes in the SPR dips due to changes in the refractive index. Finally, on comparing the results of the proposed device with the previously reported works, a significant improvement in the value of FOM in the NIR region is achieved by utilizing the MDM configuration. The proposed novel SPR sensor can very well be employed in the biomedical domain for varying levels of nanoscale detection.

6.2 Design parameters for the proposed device

Fig. 6.1(a) shows the schematic of the proposed plasmonic device using a conventional Kretschmann configuration, wherein CaF_2 glass prism was considered as the substrate and Al was considered as the plasmonic metal. The entire simulations were performed for angle interrogation at telecommunication wavelength (1550nm) employing the TMM method. Over a 30nm thick Al film (t_{m1}), BTO ($t_{BTO} = 10$nm) was deposited as a dielectric material to increase the sensitivity. Thereafter, the second film of Al ($t_{m2} = 10$nm) was deposited again to get the MDM configuration, thus intensifying field confinement. MoS_2 was used as a BRE layer for the analyte under test. The overall fabrication procedure for the proposed device is easy to

achieve. In between two metal layers of Al, BTO can be deposited using methods like Metal Organic Chemical Vapor Deposition (MOCVD) or sol-gel method, etc. There are detailed experimental reports for the deposition of BTO over Al films for the application of thin-film capacitors [170]. The refractive index for BTO was calculated from the experimental values reported by Cardona [171]. The refractive index for the MoS_2 monolayer (0.65nm) was extracted from Ref. [146]. The analyte 'n_a' was considered as water over which the change in SPR angle is observed.

6.3 Numerical Analysis

The reflection characteristics for the proposed device calculated using TMM Method are shown in Fig. 6.1 (b) where the dip in the reflectivity curve is due to the SP excitation at the interface. A redshift in the SPR curve was noticed with the increase in the analyte's refractive index from 1.33 to 1.34. To quantify the performance parameters of the proposed device, FWHM and Sensitivity (S_θ) were calculated which corresponds to the linewidth of the SPR curves and shift in SPR angle w.r.t the change in the refractive index of the analyte, respectively. Finally, considering both parameters, FOM was found to be 540.9 RIU^{-1}.
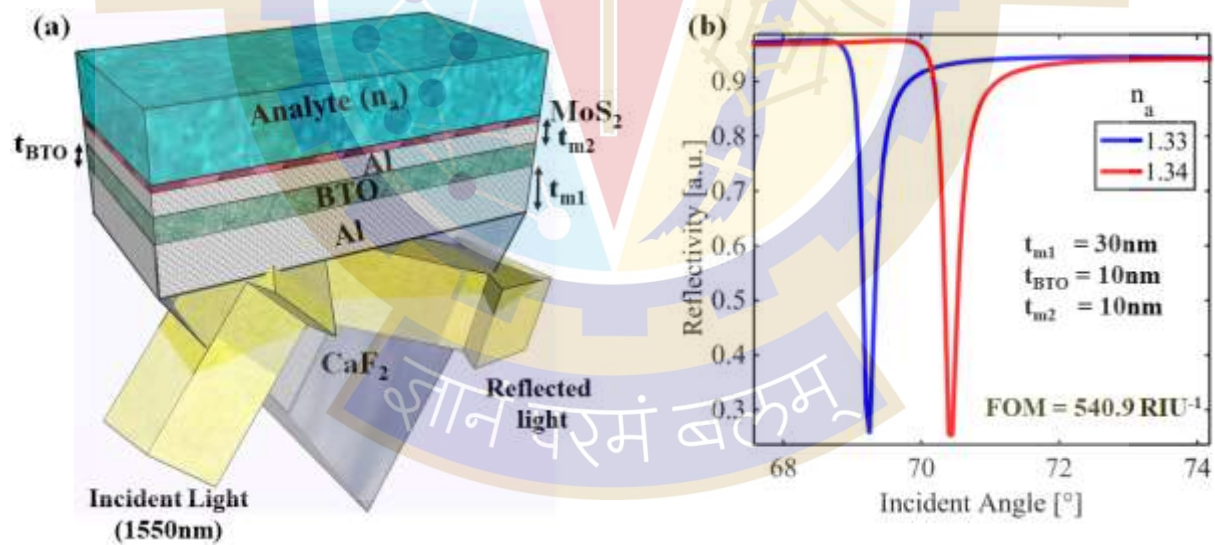
Fig. 6.1 (a) Schematic for the proposed Al-based multi-layered plasmonic device with MDM configuration (b) Reflection characteristics for the proposed device with the redshift in SP angle due to change in the refractive index of the analyte.

To get the optimized parameter for all the intermediate layers of the proposed device, several simulations were carried out considering low FWHM of SPR curves, and high signal contrast (low value of R_{min}) as decisive parameters. Firstly, a conventional Kretschmann configuration with thin Al metal (t_{m1}) coated with an analyte was considered as shown in the inset of Fig.

6.2(a), and the thickness of Al film (t_{m1}) was varied from 20nm to 40nm in steps of 10nm. The calculated reflection characteristics are shown in Fig. 6.2 (a). It was observed that the reflectivity dip corresponding to 30nm strives for efficient SP excitation due to high signal contrast (low value of R_{min}) whereas the value of t_{m1} = 20 nm and 40 nm led to poor signal contrast. Fig. 6.2 (b), shows the electric field distribution for t_{m1} = 30 nm, where the excitation of SP mode can be observed with stronger field enhancement at the interface as compared to t_{m1} = 20 nm and 40 nm (not shown here).
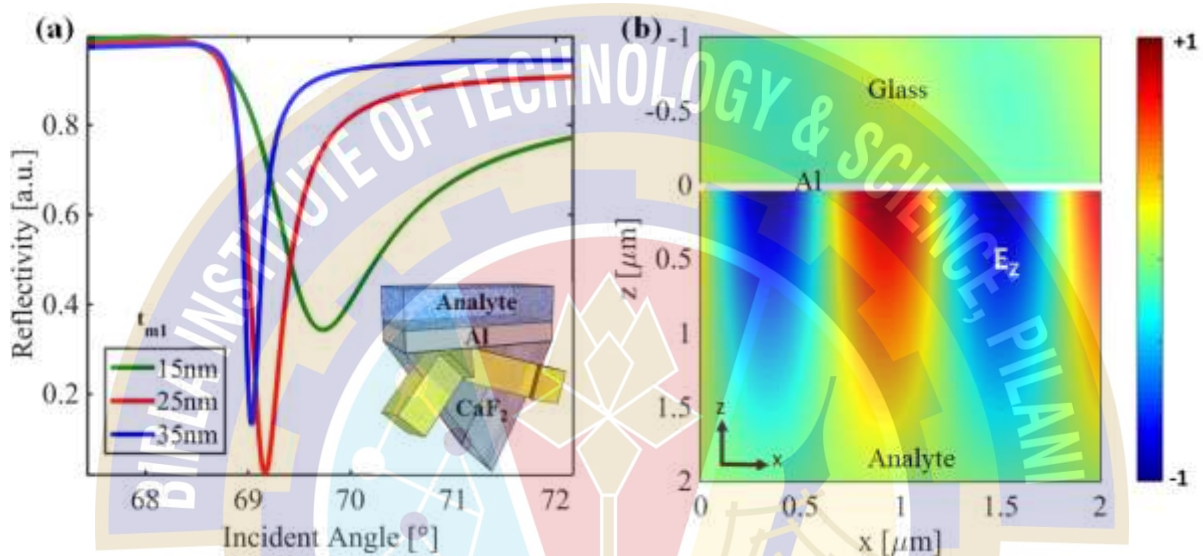
Fig. 6.2 (a) Reflection characteristics for the conventional Kretschmann configuration with the variation in the Al metal thickness (t_{m1}). The inset shows the schematic of the conventional Kretschmann configuration with a thin Al metal-analyte interface (b) Electric field distribution corresponding to the SP mode for Al metal thickness of t_{m1} = 30 nm.

Next, a high dielectric constant material 'BTO' was considered on the top of the Al thin metal layer (t_{m1} = 30nm), and reflection characteristics were calculated with the variation in the thickness of BTO material (t_{BTO}) over a range of 5nm to 15nm as shown in Fig. 6.3 (a). It can be seen that the signal contrast (value of R_{min}) is almost constant with the variation in the thickness of the BTO layer. Since the high dielectric constant of BTO leads to enhanced sensitivity, the sensitivity and FOM are chosen to be the decisive parameters to get the optimized value of t_{BTO}. To calculate the sensitivity and FWHM from SPR curves, the refractive index of the analyte was varied from 1.33 to 1.34. An increase in the redshift was observed with the changing analyte's index as we keep on increasing the BTO thickness. It was also observed that with the increase in the BTO thickness (t_{BTO}), the FWHM also increased. Therefore, a trade-off was established between sensitivity (S_θ) and FOM over a varying thickness of BTO (t_{BTO}) as shown in Fig. 6.3 (b). A value of 10 nm for the thickness of the BTO layer was found to be the optimized one for a decent value of sensitivity and FOM. The

comparison among the respective values of sensitivity and FOM with the variation in t_{BTO} can be seen subsequently in Table 6.1 below.
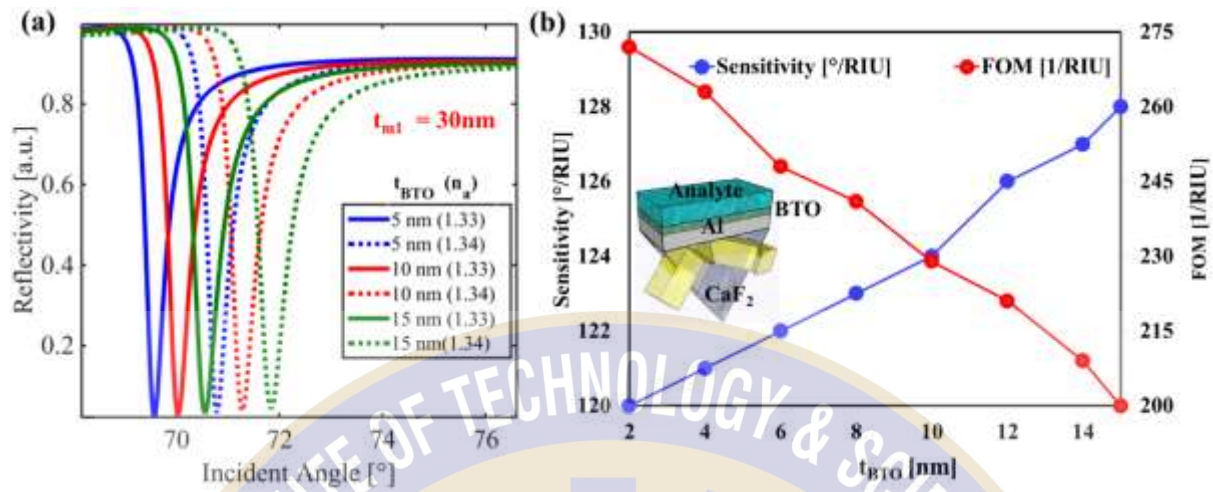
Fig. 6.3 (a) Reflection characteristics for varying thickness of BTO at 30nm of Al thin film (b) Trade-off between sensitivity and FOM for varying BTO thickness in the range of 2nm to 16nm.

TABLE 6.1: Comparison of performance parameters with an increase in thickness of BTO for 30 nm of t_{m1} layer

t_{BTO} [nm]	S_θ [°/RIU]	FWHM [°]	FOM [RIU^{-1}]	R_{min}
5	121	0.51	237.2	0.025
10	**124**	**0.54**	**229.6**	**0.028**
15	128	0.64	200	0.032

After optimizing the thicknesses of the Aluminum thin metal layer (t_{m1} = 30nm), and BTO layer (t_{BTO} =10nm), we considered another Al metal layer of thickness t_{m2} deposited on the BTO layer to achieve MDM configuration. The reflection characteristics were calculated with the variation in the thickness of the second Al metal layer (t_{m2}) over a range of 5nm to 15nm, as shown in Fig. 6.4 (a). To calculate the sensitivity and FWHM from SPR curves, the refractive index of the analyte was varied from 1.33 to 1.34. Although the sensitivity was observed to be almost constant with the increase in thickness of the second Al metal layer (t_{m2}), the FWHM was found to be decreasing, resulting in improved FOM or the resolution of the sensor. A decrease in the signal contrast (value of R_{min}) was also observed with increasing the second Al metal layer thickness (t_{m2}). To have a decent value of signal contrast and FWHM, a trade-off between the R_{min} and FWHM was established with the variation in the thickness of the second metal layer (t_{m2}) as shown in Fig. 6.4 (b). An optimized value of t_{m2} = 10 nm was noticed for a decent value of signal contrast and FWHM for the proposed MDM configuration. The comparison among the respective values of Rmin, FWHM, and FOM with the variation in t_{m2} can be seen subsequently in Table 6.2 below.
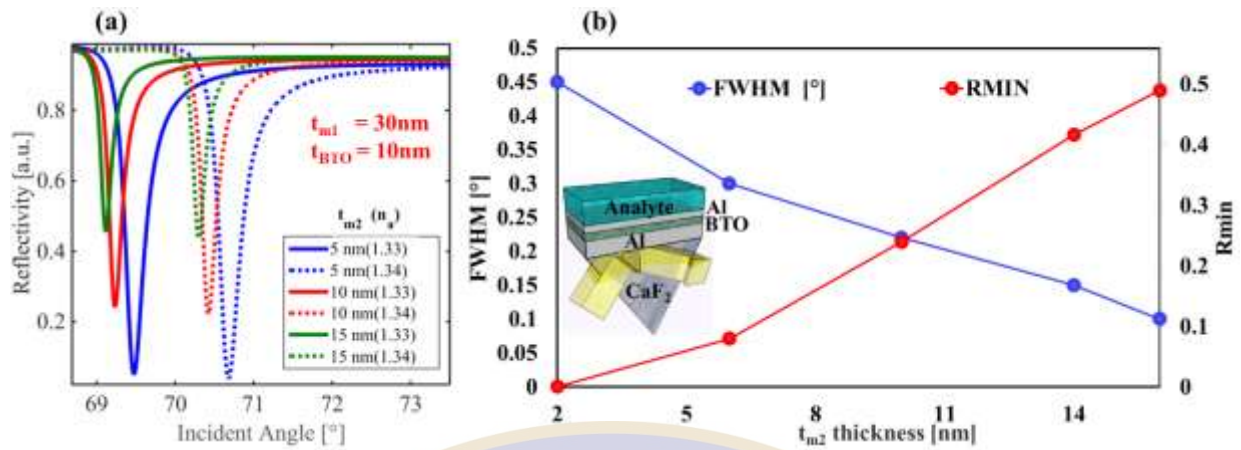
Fig. 6.4 (a) Reflection characteristics for varying thickness of t_{m2} for 30nm of first Al thin layer and 10 nm of BTO layer (b) Trade-off between sensitivity and FOM of varying t_{m2} in the range of 2nm to 16nm.

TABLE 6.2: Comparison of performance parameters with an increase in thickness of t_{m2}, for 30nm of the first Al thin layer and 10 nm of the BTO layer

t_{m2} [nm]	S_θ [°/RIU]	FWHM [°]	FOM [RIU^{-1}]	R_{min}
5	121	0.31	390.3	0.049
10	**119**	**0.22**	**540.9**	**0.24**
15	118	0.18	655.5	0.45

The reason for an increased resolution or FOM of the proposed MDM configuration-based plasmonic device can be explained with the help of calculated electric field distribution as shown in Fig. 6.5. Fig. 6.5(a) shows the electric field distribution for conventional Kretschmann configuration (glass prism + Al metal + analyte), whereas Fig. 6.5(b) shows the electric field distribution for the proposed Al-based multi-layered plasmonic device with MDM configuration respectively. An enhanced electric field observed in the vicinity of the metal-analyte interface was attributed to the SP mode excitation after the maximum energy transfer from the incident light to SPs (Fig. 6.5 (a)). Eventually, this field interaction gets more localized as soon as the t_{m2} layer was added above the BTO thin film to form an MDM configuration (Fig. 6.5 (b)). The strong field localization results in a lower FWHM of the SP curve in the case of MDM configuration [172]. Such field distribution is directly related to the penetration depth that defines the interaction length of SPs. As a result, a reduced penetration depth in the MDM configuration (a few tens of nanometers) leads to reduced FWHM and thus larger FOM concerning conventional Kretschmann plasmonic devices having a penetration depth of about hundreds of nano-meters.
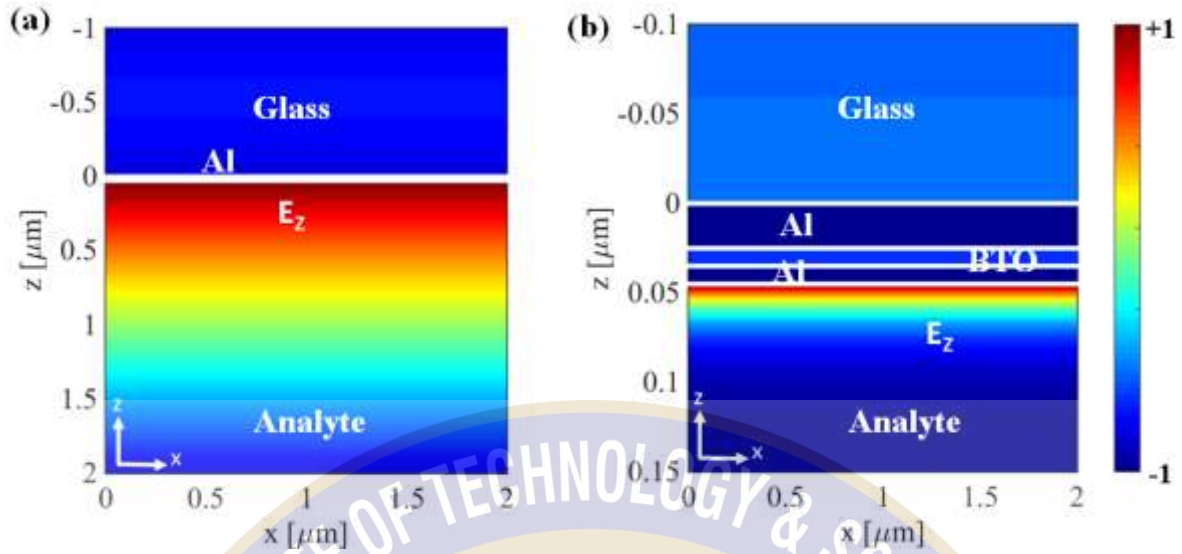
Fig. 6.5: Electric field (Ez) distributions of the SPR dip for (a) Conventional Kretschmann configuration {Glass + Al metal + Analyte} and (b) the proposed Al-based multi-layered plasmonic device with MDM configuration respectively.

Table 6.3 compares the effect of each of the intermediate layers in between the glass prism and analyte. Compared to the conventional Kretschmann configuration (Case-I), with the successive addition of the BTO layer (Case-II), sensitivity was improved but at the cost of poor FOM, as already reported in the literature. In the proposed Al-based multi-layered plasmonic device with MDM configuration (Case-III), an enhancement in FOM or resolution was observed due to a reduction in the FWHM of the SP curve at 1550nm.

TABLE 6.3: Effect of different layers on the performance parameters of the proposed device

Configurations	S_θ[°/RIU]	FWHM [°]	FOM [RIU^{-1}]
Case I	118	0.42	280.95
Case II	124	0.54	229.62
Case II	**119**	**0.22**	**540.9**

Finally, to demonstrate biosensing application for the proposed plasmonic device, a monolayer MoS_2 was considered on the proposed device (Fig. 6.1 (a)) as BRE to bind the biomolecules. The better absorptivity nature of this bio-analyte enables its extensive use for biosensing purposes. Since pure Al is not viable for biosensing applications, thus, the MoS_2 layer protects the Al metal layer from oxidation. Fig. 6.6 presents the reflection characteristics of different blood components in normal and infected stages as a bio-analyte on the proposed plasmonic device. The refractive index values for the different blood components were taken from Ref. [173]. For example, when a healthy/normal blood sample (n_a=1.35) is infected (n_a=1.33),the difference is reflected in their corresponding index values which shift the resonant location of

the SP curves. A blueshift in the SPR curves was observed for all the blood components due to a decrease in the refractive index in the infected stage as compared to the normal stage.
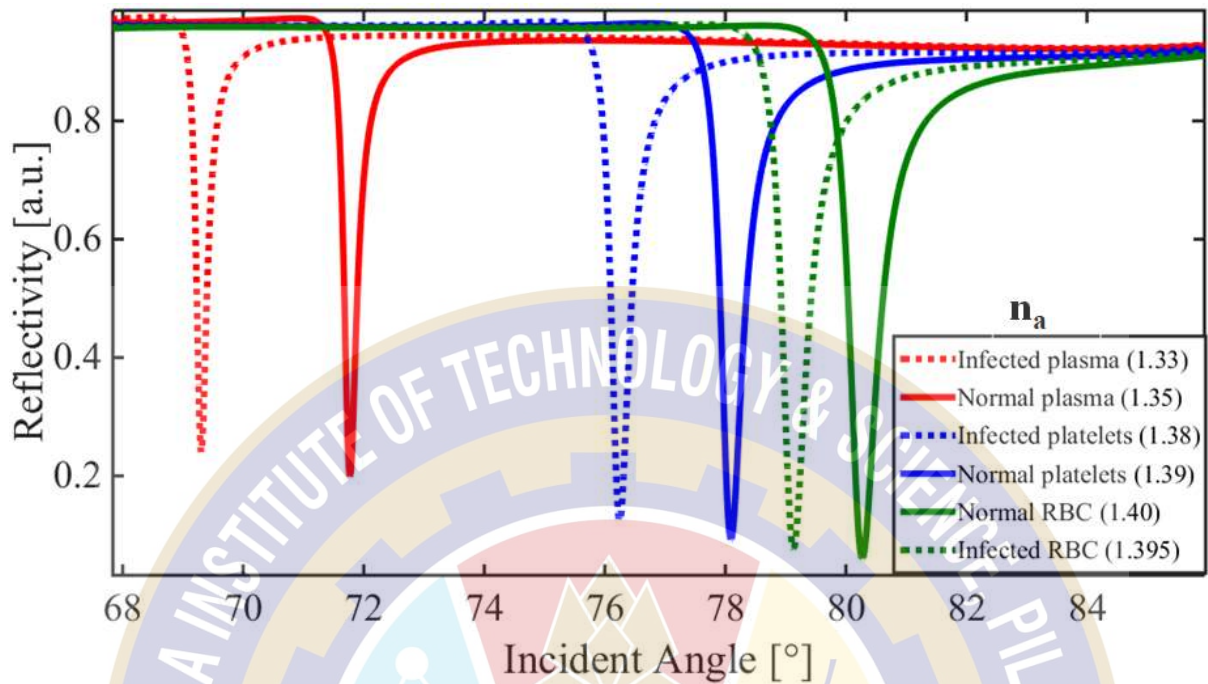
Fig. 6.6: Reflectivity characteristics of the proposed plasmonic device for different blood components in normal and infected stage.

At last, the results obtained from the proposed plasmonic device were compared with the previously published results as shown in Table 6.4. The obtained FOM is much higher than the recently published results which largely ignored this parameter. Utilizing the cost-effective Al for resolution/FOM enhancement with the proposed MDM configuration in the prism-based plasmonic device can be used as a promising SPR sensor for future applications in the NIR region.

TABLE 6.4: FOM comparison of the proposed plasmonic device with previously reported works

Ref. no.	Schematic	FOM [RIU^{-1}]
[167]	Cu + BTO + Cu+ BP	145
[164]	Ag + BTO + Gr	45.05
[174]	Ag+ Au+ BTO +Gr	42.13
[175]	Ag+ BTO+ Ag+ Gr	54
Proposed work	**Al +BTO+Al+MoS$_2$**	**540.9**

6.4 Conclusion

An Al-based multi-layered plasmonic device was proposed for enhanced resolution for sensing applications in the optical communication band. MDM configuration was introduced in the conventional prism-based plasmonic device to increase the FOM by decreasing the linewidth of SPR curves. The effect of each intermediate layer in the proposed Al-based multi-layered device was carried out by studying the performance parameter analysis from the reflection characteristics. An improved value of FOM with a decent sensitivity was obtained for the proposed plasmonic device, leading to the resolution enhancement. The engineered plasmonic device was then used to demonstrate the bio-sensing application at the optical wavelength of 1550nm. The different blood components were considered in normal and infected stages on the proposed plasmonic device for detecting the chikungunya virus. The proposed plasmonic device can serve many bio-sensing applications for resolution enhancement in the near-infrared region.

Chapter 7

Aluminum-based engineered plasmonic nanostructures for sensing applications in the near-infrared region

Besides the prism-based configuration, it is also possible to excite SPs with normal incident TM-polarized light using periodic nanostructures [176]–[182] – a technique that is gaining popularity due to availability and relative ease of fabrication techniques, particularly interference and nanoimprint lithography techniques [183], [184]. The sensitivity of these nanostructure-based SPR sensors, while slightly lesser than that of prism-based designs, have several other advantages in terms of integration and compactness. Sensors designed to work with the normal incidence of light are advantageous from the perspective of noise reduction [178] and are also integrable with optical fibers, which can be used for both excitation of SPs and the interrogation of reflectivity spectra [185]. The resonance characteristics of these sensors can be easily controlled by tuning the physical parameters of the nanostructures such as period, width, height, etc. We have divided this chapter into two major sections, i.e., 1D and 2D periodic nanostructure-based plasmonic devices.

7.1 Introduction

Increasing the sensitivity of periodic nanostructure-based sensors while taking into account the feasibility of fabrication, is still a challenge. Recently, Au-based periodic nanostructure-based Kretschmann configuration has been reported for quality factor enhancement via dispersion engineering [186]. But, a wide linewidth of the SPR curve is the major drawback associated with the Au-based structure.

In this chapter, we proposed highly-sensitive plasmonic devices with Al-based periodic nanostructures to capture the minute changes in the refractive index and thickness of an analyte in the NIR region. The nanostructures were engineered for high sensitivity and low FWHM, using a custom-made RCWA simulator. The high sensitivity and FOM obtained in the optical communication band and the possibility of self- referencing which avoids the measurement error due to optomechanical shift and temperature fluctuations are the novelty of the proposed device. Since the proposed plasmonic device work in the communication band, the device will be advantageous from the biosensing point of view, as it causes very small photodamage to bio-samples.

In this chapter, we started by observing the reflectivity spectra for a 1D Al nanostructures-based plasmonic device using wavelength interrogation for different refractive indices of the analyte. The proposed work with optimized parameters ends up with higher sensitivity as well as FOM. Since light is incident from the bottom of the glass substrate, the constraints associated with the analyte won't be a point of concern. Next, we proposed 2D Al nanostructures-based plasmonic device with two different periodicities in two different directions to capture the multiwavelength SP excitation for two different wavelength regions.

7.2 1D Al nanostructure-based plasmonic device

In our proposed 1D nanostructure arrangement, the normal incidence operation from the bottom of the device eases the integration of the proposed plasmonic device with optical fibers. Such an arrangement acts as an advantage since the proposed configuration can be used both to excite the SP and to interrogate the spectral reflectance. The proposed nanostructures can easily be fabricated using conventional semiconductor processing techniques involving electron beam lithography, a metal evaporation step followed by a liftoff process. The geometrical parameters of the proposed device were systematically varied to optimize the performance parameters (sensitivity, FOM, and spectral linewidth) while taking the feasibility of the fabrication into account.

7.2.1 Design parameters

The schematic for the proposed plasmonic device is shown in Fig. 7.1(a). It includes Al-based periodic nanostructures on the top of the thin homogeneous Al-coated glass substrate integrated with one end of the optical fiber. The geometric parameters for the proposed structures were engineered for their sensitivity to an analyte with different refractive indices and thicknesses using the RCWA method [187], implemented on a custom-made MATLAB program. The different geometrical parameters considered were the thickness of the metal layer 't_m', the thickness of the nanostructure 't_{ns}', and the fill factor of the nanostructure's 'f'. The period 'P' of the nanostructures will certainly influence the wavelengths at which resonances will occur, allowing us to design a sensor that exhibits resonance at desired wavelength ranges.

A thin homogeneous layer of Al was assumed between the periodic nanostructures and the glass substrate. When light is incident normally, much of it is reflected back by this metal layer which behaves as a mirror. However, some of the wavelengths couple with the nanostructures to excite SPs by the phase-matching condition. The wavelength-dependent dielectric constant

values of Al are taken from [188].
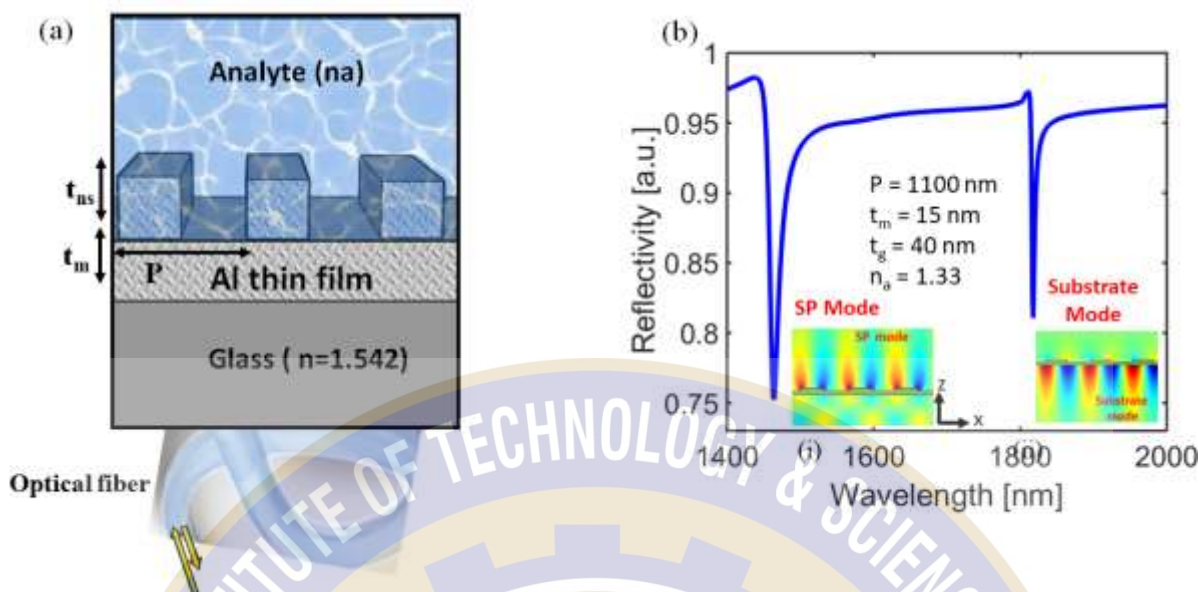
Fig. 7.1 (a) Schematic diagram of the proposed Al-based nanostructure integrated with the one end of the optical fiber (b) Reflectivity spectrum for the nanostructure of period = 1100 nm indicating the regions where resonance occurs (i) at the nanostructures-analyte interface (SP mode) and (ii) At thin metal-substrate interface (Substrate mode). Insets (i) and (ii) show the electric field distribution for SP mode and substrate mode respectively.

7.2.2 Numerical Analysis

The reflectivity spectra obtained under TM polarization for plasmonic nanostructure of period P = 1100 nm, t_m = 15 nm, and t_{ns} = 40 nm, is shown in Fig 7.1(b). The structures exhibited two distinct reflection dips corresponding to two different interactions with the plasmonic device at the wavelengths 1464 nm and 1818 nm respectively as shown in Fig. 7.1(b). The reflection dips occur when, instead of being reflected, the light generates SPs (resonance condition) on either the nanostructure-analyte interface or the thin Al metal-glass substrate interface. The electric field (E_z) distributions for this geometry at wavelengths 1464 nm and 1818 nm are shown in the inset (i) & (ii) of Fig. 7.1(b) respectively. It was observed that the resonance dip at a wavelength of 1464 nm is due to the SP excitation at the nanostructures-analyte interface (inset (i)) where the electric field distribution shows a strongly confined mode at the nanostructure-analyte interface. The resonance dip at the wavelength of 1818 nm is attributed to the SP excitation on a thin Al metal-glass substrate interface as shown in the inset (ii) of Fig. 7.1(b) which is named as substrate mode.
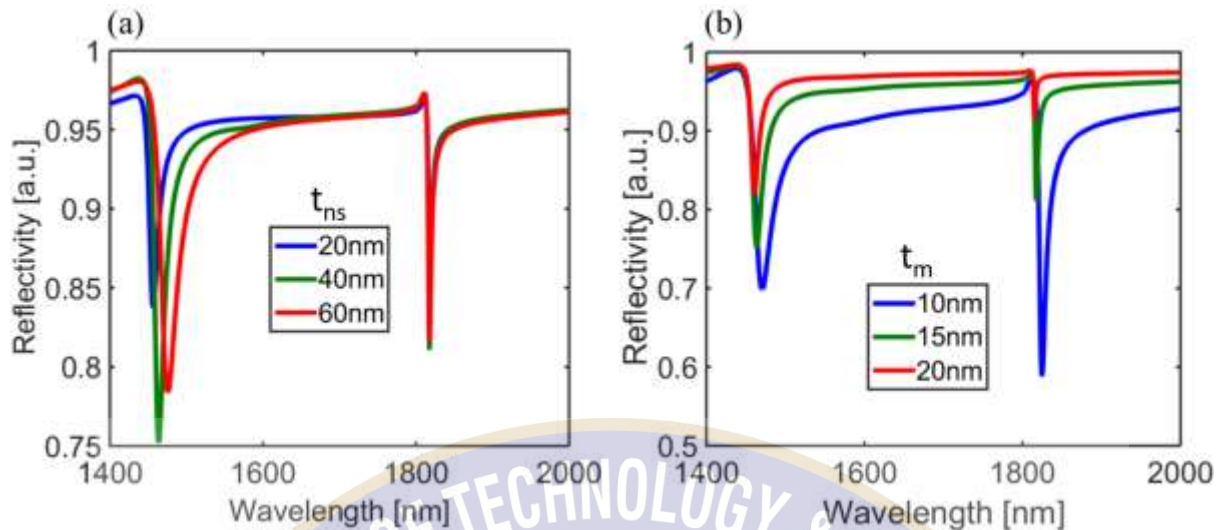
Fig. 7.2 Reflectivity spectra as a function of wavelength for plasmonic nanostructures (a) of t_m = 15nm and with variation in nanostructure height (t_{ns}) (b) of t_{ns} = 40nm and with the variation in thin metal height (t_m).

Fig. 7.2(a) shows the obtained reflectivity spectra for different thicknesses of nanostructure height (t_{ns}) which was changed systematically and Fig. 7.2(b) shows the reflectivity spectra for a systematic variation of thin homogeneous metal height (t_m). The optimal value was selected based on two factors – the depth of the dip (which is a measure of signal contrast) and the FWHM. A narrower FWHM implies better sensing capabilities (resolution, in particular) of the sensor. The spectrum which showed a dip of reasonable signal contrast and less FWHM was selected as the optimum – higher contrast usually led to a greater FWHM, so a reasonable trade-off was considered. It was found that a t_{ns} of 40 nm and a t_m of 15 nm gave the best results. Since t_{ns} is a parameter related to only periodic nanostructures, the dip corresponding to substrate mode (right side dip) remains unchanged, and only the wavelength at which SP mode occurs will change. As the thickness of the metal layer 't_m' increases, the light of different wavelengths gets reflected back, and consequently, the dips show lesser contrast. At lower thicknesses, more light passes through, which leads to better signal contrast but at the cost of increased FWHM.
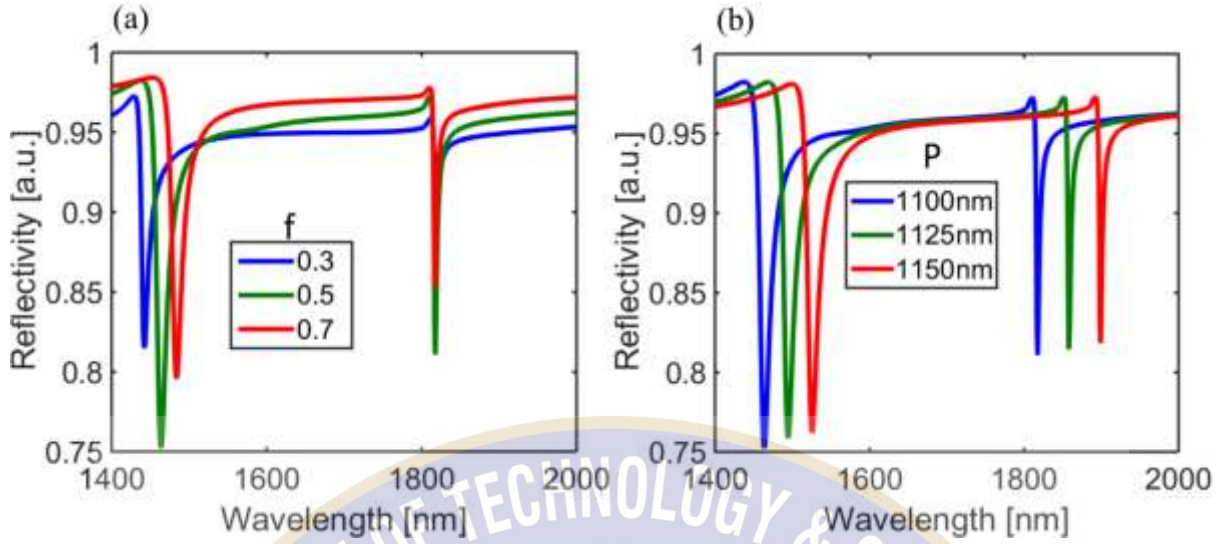
Fig. 7.3 (a) Reflectivity spectra plotted against wavelength for systematic variation of fill factor (f), and (b) illustrates the shift in the position of the dip corresponding to SP mode and Substrate mode with the variation in the Period (P).

Fig. 7.3(a) shows how the fill factor affects the reflectivity spectrum. It was found that a fill factor of 0.5 gave the best signal contrast and FWHM. Fig. 7.3(b) illustrates how the SP mode dip and Substrate mode dip positions can be tuned in the desired region by changing the period of the periodic nanostructures. The resonance wavelength (λ_{SP}) for plasmonic nanostructures is given by:

$$\lambda_{SP} = \frac{P}{m}(\pm \mathrm{Re}(\sqrt{\frac{\varepsilon_m n_a^2}{\varepsilon_m + n_a^2}})) \tag{7.1}$$

From equation (7.1), we find that λ_{SP} or the wavelength at which SPR occurs is close to $P \times n_a$, if the first-order diffraction order is present, an observation corroborated by Fig. 7.3(b).

Fig. 7.4 illustrates the sensor in operation, showing reflectivity characteristics for different analytes of differing refractive indices, with P = 1100 nm, t_{ns}= 40 nm, and t_m=15 nm. The substrate mode occurs at a wavelength of 1818 nm. It is evident from this graph why a narrow FWHM and signal contrast are desired parameters; the better those parameters are, the more sensitive the device is to changes in the analyte refractive index. We also observed that the signal corresponding to the substrate refractive index remains perfectly unchanged, which suggests that it can be used as a reference for the SP mode signal.
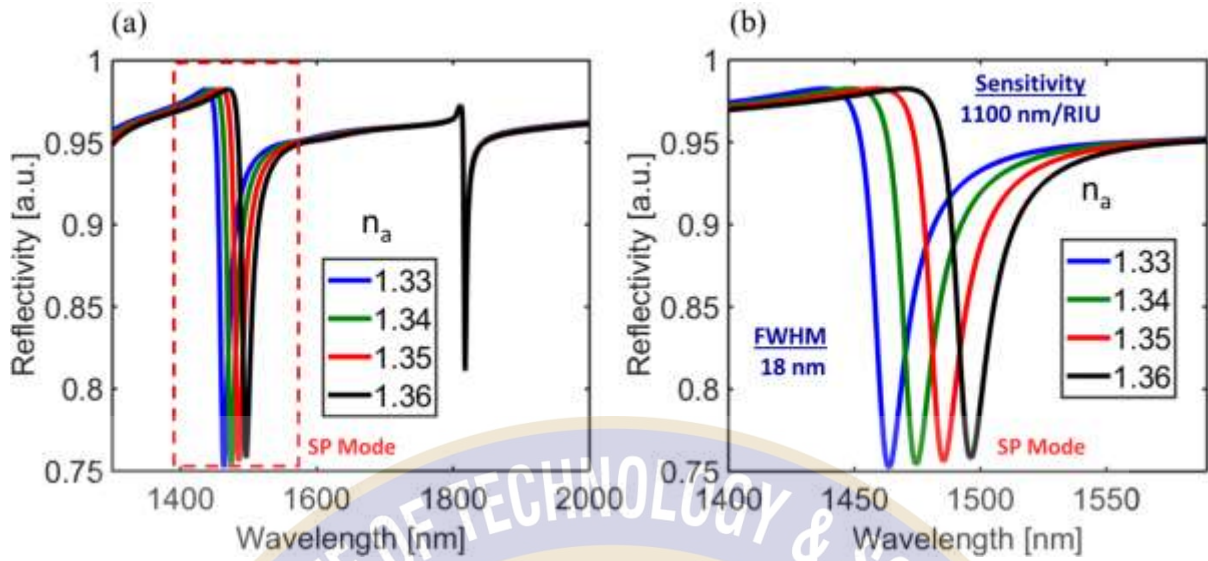
Fig. 7.4 (a) Reflectivity spectra obtained with optimized parameters of P = 1100 nm, t_{ns}= 40 nm, and t_m=15 nm when analytes of different refractive indices were examined (b) The zoom-in picture of the shift in the position of SP mode with the variation in the refractive index of the analyte.

To utilize these plasmonic nanostructures as a refractive index sensor, the refractive index of the analyte (n_a) was varied by 0.01RIU, and reflectivity spectra for plasmonic nanostructures were calculated as shown in Fig. 7.4(a). The right shift in the resonance wavelength, corresponding to SP excitation at the nanostructure-analyte interface, with the increase in the analyte's refractive index was observed as shown in Fig. 7.4(b). The FWHM for the SP resonance dip was extracted as 18 nm, the sensitivity of this mode to a change in refractive index was 1100 nm/RIU and FOM value was found to be 61.11 RIU^{-1}. From equation 7.1, the refractive index sensitivity is determined by the diffraction order and the periodicity of the nanostructures which is sensitivity = $\Delta\lambda_{SPR}/\Delta n_a \approx$ P/m. A low diffraction order and a larger grating period are desirable to achieve higher sensitivity. In our case, we used the same approach by using the Period (P) = 1100 nm and m = 1 which resulted in a sensitivity of 1100nm/RIU. Table 7.1 represents the sensitivity and FWHM comparison for the proposed work with earlier reported plasmonic nanostructure-based optical sensors. The proposed work offers high sensitivity and FOM in the communication band compared to other work. This is not the first time a large sensitivity is reported with plasmonic nanostructures or plasmonic gratings. Recently, a study presented the performance analysis of a grating-based SPR sensor [180] with a large sensitivity (1200 nm/RIU). However, the overall FOM was very less owing to a large SPR line width (FWHM). Moreover, the incident light is operated at a fixed incidence angle (20°), which is bound to cause errors in measurement because it is very difficult to

maintain a specific oblique angle. This work was not added to the table because the idea was to compare the performance of the normal incident light-based devices.

Table 7.1. Performance parameters for different plasmonic nanostructure-based optical sensors

Ref. no	Schematic	Sensitivity [nm/RIU]	FOM [RIU^{-1}]	λ [nm]
[189]	Meta-surface-based biosensor	192	64	400-700nm
[190]	Plasmonic bio sensor on Blu-ray disc	425	35	500-800nm
[191]	Semi-circle groove-based sensor	428.7	24	500-850nm
[178]	Metal oxide grating-based sensor	461.5	31.18	1400-1540nm
Proposed work	**Al-based plasmonic nanostructure**	**1100**	**61.11**	**NIR**
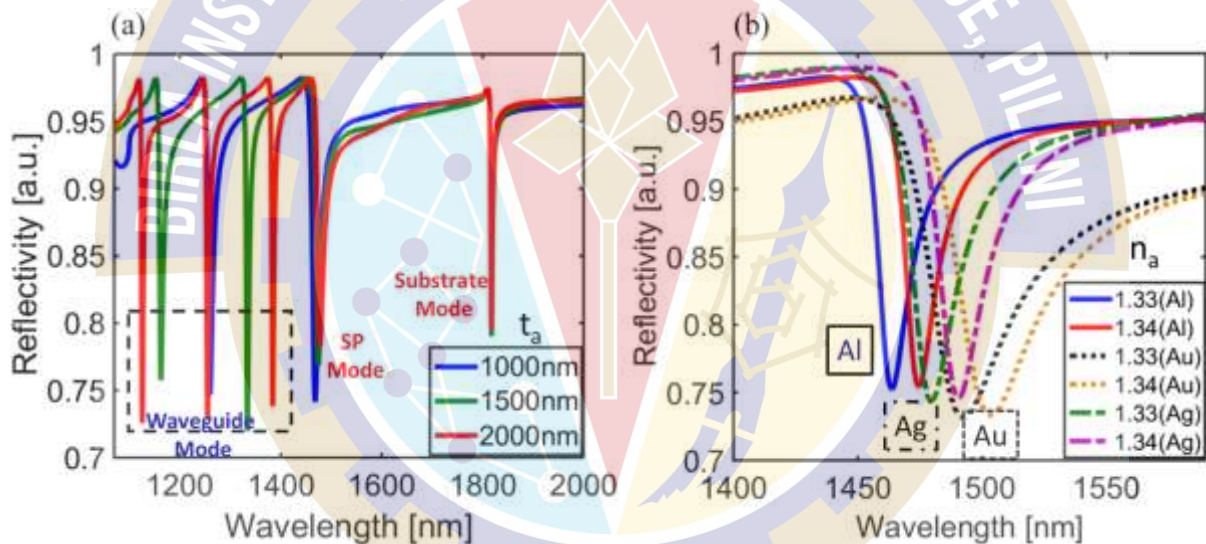
Fig. 7.5 (a) Reflectivity spectra obtained with optimized parameters of P = 1100 nm, t_{ns}= 40 nm, and t_m=15 nm with varying thickness of the analyte (b) Comparison in the reflectivity spectra of Al-based, Ag-based, and Au-based periodic plasmonic nanostructures of period P = 1100 nm.

To use this proposed plasmonic device for the thickness sensor, the thickness of the analyte (t_a) was varied for the nanostructures of period P = 1100 nm, t_{ns}= 40 nm, and t_m=15 nm as shown in Fig. 7.5(a). In addition to the occurrence of SP mode and substrate mode, the presence of the third mode named as 'dielectric waveguide' was observed in the reflectivity spectra. It was observed that the number of dips corresponding to these higher-order waveguide modes increased as the thickness of the analyte increased. This suggests that the waveguide mode can

be used as a coarse estimator for the thickness of the analyte, once the refractive index is determined from the SP mode.

Fig. 7.5(b) shows the comparison of refractive index variation for three different plasmonic metals namely Al, Ag, and Au assumed in the proposed plasmonic device. Al-based plasmonic nanostructures offered a narrow linewidth (FWHM {Al} = 18nm) compared to Ag and Au based plasmonic nanostructures (FWHM {Ag} = 25nm, FWHM {Au} = 54nm) as shown in Fig. 7.5(b). The increase in the FWHM value leads to a decrease in the FOM value. Therefore, Al is considered as the plasmonic metal in the proposed plasmonic device.
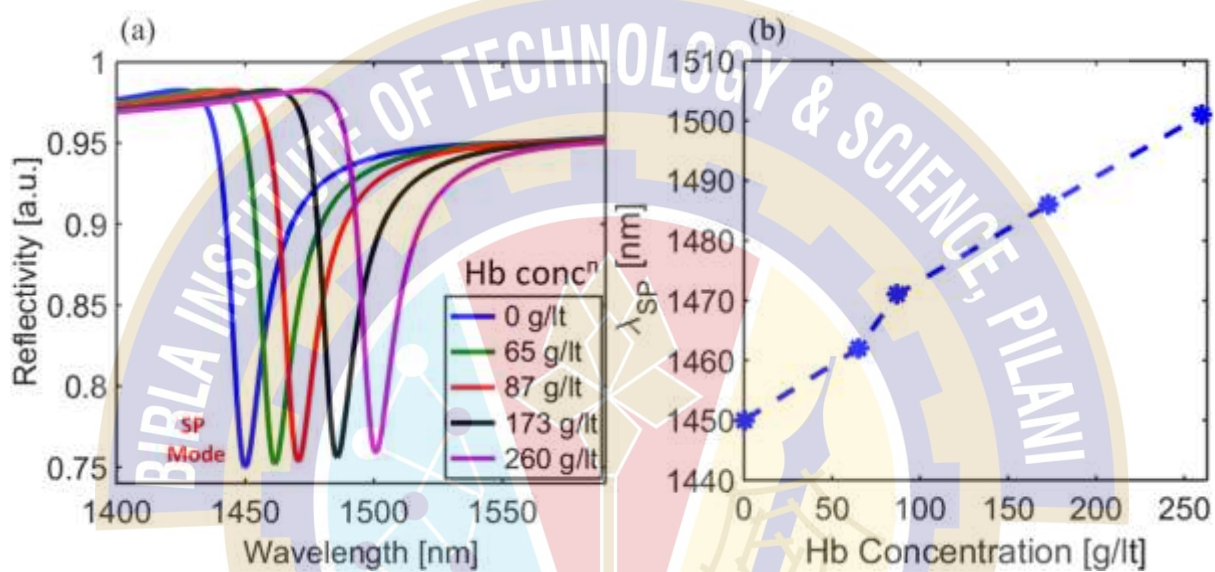
Fig. 7.6 (a) Simulated reflectivity spectra obtained with optimized parameters of P = 1100 nm, t_{ns}= 40 nm, and t_m=15 nm for different concentrations of the Hemoglobin (Hb Conc^n) considering that nanostructures are filled with the analyte (Hb). (b) The corresponding shift in the SP mode wavelength with the variation in the Hemoglobin concentration.

Fig. 7.6 (a) shows the simulated reflectivity spectra for the optimized proposed nanostructures for the different Hemoglobin concentrations (Hb Conc^n) in the optical communication band and Fig. 7.6 (b) shows the corresponding shift in the SP mode wavelength. The selected optical communication band will be advantageous in terms of integration with the existing optical fiber system, which makes it possible to apply the proposed structure in on-chip sensing applications. The values of the corresponding refractive indices for the different Hb concentrations are taken from Ref. [192]. Table 7.2 shows the corresponding values of sensitivity, FWHM, and FOM for the different concentrations of Hemoglobin considering 0g/lt as a reference. It was noticed that the values of sensitivity and FOM increase for larger Hb concentrations.

Table 7.2. Calculated parameter values for different values of Hb concentrations

Hb Conc^n (g/lt)	λ_{SP}[nm]	n_a (at λ_{SP})	FWHM [nm]	S [nm/RIU]	FOM [RIU^{-1}]
0	1450.00	1.3174	16.50	Reference	---------
65	1462.00	1.3280	18.00	1037.77	57.6
87	1471.00	1.3364	19.00	1071.42	56.39
173	1486.00	1.3503	14.00	1079.13	77.08
260	1501.00	1.3642	17.00	1079.13	63.47

7.3 2D Al nanostructure-based plasmonic device

Various designs that have been proposed in the previous chapters are exclusive to a particular wavelength regime. However, real-time sensing applications necessitate such a configuration/methodology that can be compatible with a spectrum large enoughsuch that the wavelength no longer serves to be a bottleneck during the fabrication process. Additionally, when it comes to biomolecular level detection, the frequencies associated with electromagnetic radiation in the biomolecules (DNA) are estimated to be within the IR, visible, as well as partially UV regions [193].

We already witnessed in chapter 2 (literature review) that Al-based plasmonic devices work exclusively well either in the deep UV or in the visible region. Similarly, employing Al in the IR region provides minimal photodamage to the bio-sample in the respective regions [194]. These works show Al working extremely well in a particular wavelength region. As of now, there are limited reports on the use of the plasmonic response of Al-based nanostructures in the entire visible–IR band for such applications. For example, González-Campuzano et al. discussed how Al-based nano-domes can become a popular alternative by expanding towards the entire UV-Vis-IR region of the electromagnetic spectrum [18]. Along similar lines, our approach in this section is to come up with such a plasmonic device that can be employed in multiwavelength regions.

In this section, we demonstrate the 2D Al-nanostructure-based plasmonic device supporting multispectral SP resonances. This allows the evaluation of unknown bio-analytes at different wavelengths in a single experiment.

7.3.1 Design parameters

A schematic for the proposed plasmonic device has been shown in Fig. 7.7. Thin Al film was deposited over the top of the glass substrate, followed by Al-based periodic nanostructures. The analyte covers the Al nanostructures where the SP excitation takes place. A shift in the resonance wavelength is expected to be observed with the subsequent changes in the analyte's refractive index, hence demonstrating its biosensing capability. Fig. 7.7(a) shows the 3-D view of the 1D Al-nanostructure-based plasmonic device. Fig. 7.7(b) shows the 3-D view of the 2D Al-nanostructure-based plasmonic device where the period along the x and y direction decides the region of plasmonic sensing operation. To get the optimized geometrical parameters for the proposed 2D nanostructures, firstly, a 1D nanostructure-based plasmonic device was taken into consideration for engineering the different layers of the device. An analyte thickness of 50nm was assumed to fill the nanostructures of period along the x-direction, $P_x = 1000$ nm, and period along the y-direction, $P_y = 500$ nm with the analyte ($n_a=1.33$) as shown in Fig. 7.7(b). All the simulations were performed at a 50% duty cycle. In the proposed plasmonic device, under the normal incidence condition for a TM polarized light, when most of the light gets reflected from the thin homogeneous Al metal layer, SP transmission peaks are observed in the transmitted spectra due to the momentum matching condition at the nanostructure and analyte interface. The corresponding transmission peaks due to SP excitation can be captured from the bottom of the substrate.
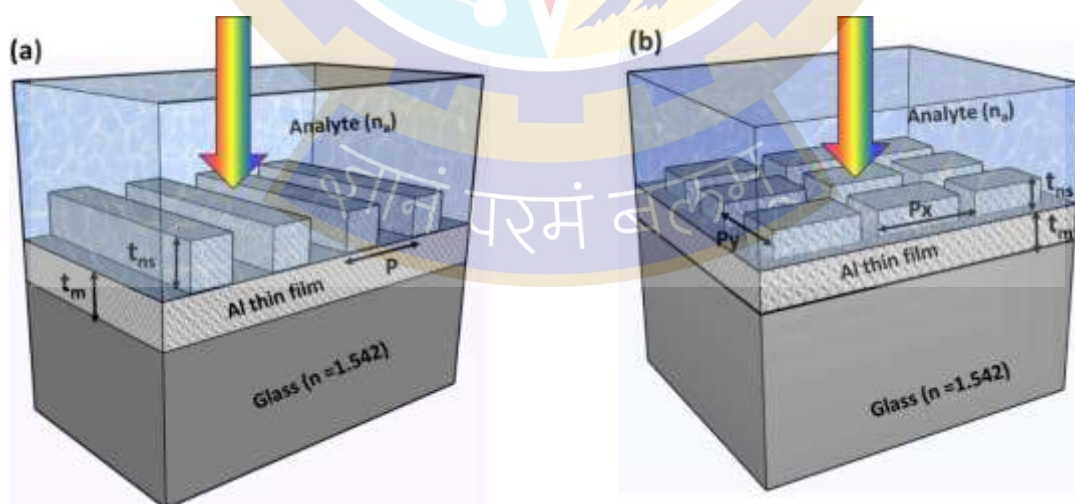
Fig. 7.7 (a) Schematic of the 1D Al-nanostructure based plasmonic device- {3D view} (b) Schematic of the 2D Al-nanostructure based plasmonic device- {3D view}.

7.3.2 Numerical Analysis

Fig. 7.8(a) & 7.8(b) show the simulated transmittivity spectra using RCWA with the variation in the t_m and t_{ns} respectively. Fig. 7.8(a) shows that $t_m = 20$ nm is the optimal choice, keeping the narrow line-width of SP peaks and high signal contrast as the key parameters. Similarly, the highest transmission peak was observed for $t_{ns} = 20$ nm as shown in Fig. 7.8(b).
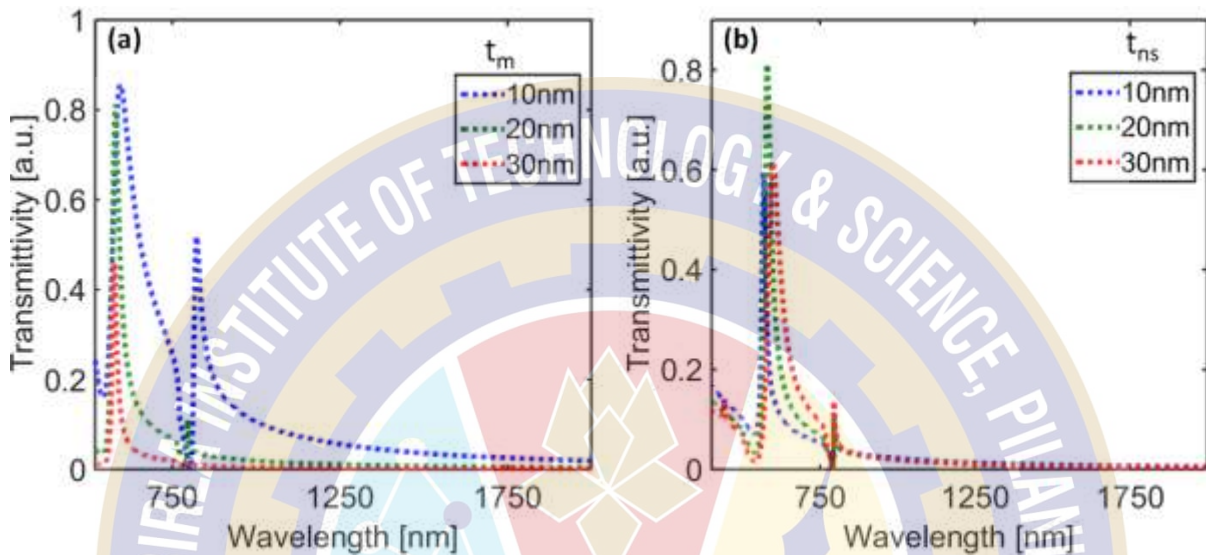
Fig. 7.8 Transmittivity spectra for the proposed 1D Al-nanostructure-based plasmonic device of period P = 500 nm with (a) variation in thin Al metal film thickness (t_m) (b) variation in the nanostructure thickness (t_{ns}) respectively.

Subsequently, the plasmonic response in the form of SP transmission peaks was analyzed for the optimized 1D Al-nanostructure-based plasmonic device with P = 500 nm, and $t_m = t_{ns} = 20$ nm as shown in Fig. 7.9(a). The presence of two transmission peaks corresponding to SP mode and Substrate mode was observed in the transmitted spectra at the wavelength of 580 nm and 795 nm respectively. The occurrence of these modes was confirmed by calculating the electric field distributions (shown as inset (i) & (ii)) for the above-mentioned wavelengths.

To study the effect of the period for the proposed Al-based nanostructures on the plasmonic response, the transmittivity spectra were calculated for $t_m = t_{ns} = 20$ nm with the variation in the period 'P' as shown in Fig. 7.9(b). It is clear that the SP resonance wavelength can be easily tuned according to the period of the nanostructures. Varying the period from 500 nm to 1200 nm shows that variation in the periodicity of nanostructures can tune the plasmonic response to a specific wavelength regime.
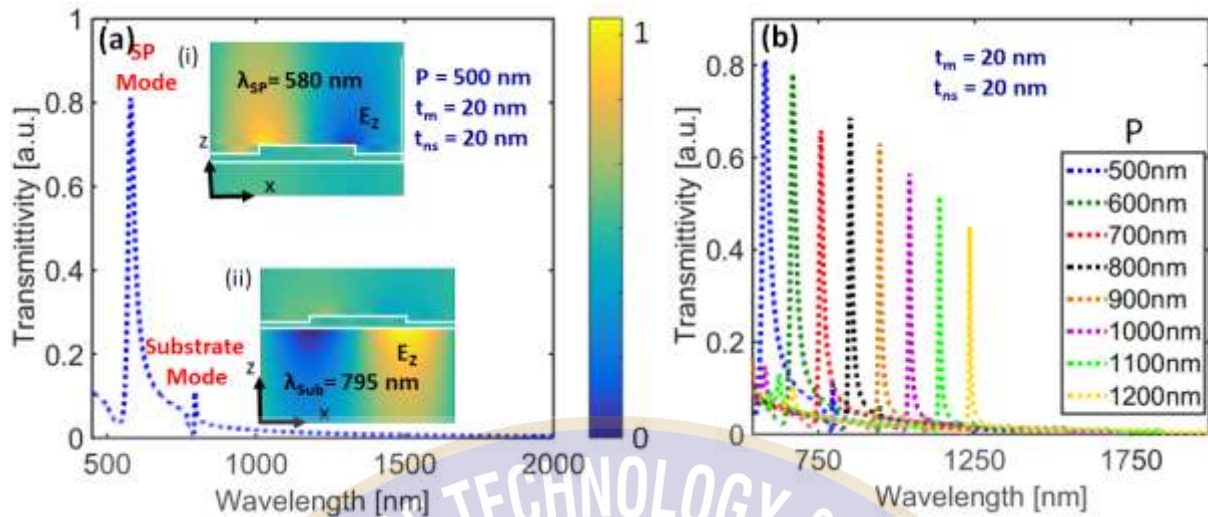
Fig. 7.9 (a) Transmittivity spectra for the optimized 1D plasmonic nanostructures of period P = 500 nm, and $t_m = t_{ns} = 20$ nm along with the electric field distributions for SP mode and Substrate mode shown as the insets (i) & (ii) respectively (b) Transmittivity spectra for the engineered 1D Al-nanostructure based plasmonic device with the variation in the period.

From Fig. 7.9(b), we selected the second period to 1000 nm to observe the plasmonic response in the near IR wavelength region. Fig. 7.10(a) shows the transmittivity spectra for 1D plasmonic nanostructure of period P = 1000 nm, and $t_m = t_{ns} = 20$ nm. The observation of two transmission peaks at the wavelength of 1041 nm and 1553 nm corresponding to SP and substrate mode was verified by the electric field distributions shown as inset (i) & (ii) of Fig. 7.10(a).

After observing the SP resonances in the Visible region for 1D nanostructure of period P = 500 nm and in the near IR region for 1D nanostructure of period P = 1000 nm separately, we proposed a 2D Al-nanostructure-based plasmonic device with period P_X = 1000 nm (in the x-direction) and P_Y = 500 nm (in the y-direction) as shown in Fig. 7.7(b). Fig. 7.10(b) shows the simulated transmittivity spectra for the proposed 2D Al-nanostructure-based plasmonic device where the transmission peaks are located at the wavelength of 580 nm and 1040 nm corresponding to SP modes for the period 500 nm and 1000 nm along y and x-direction respectively.
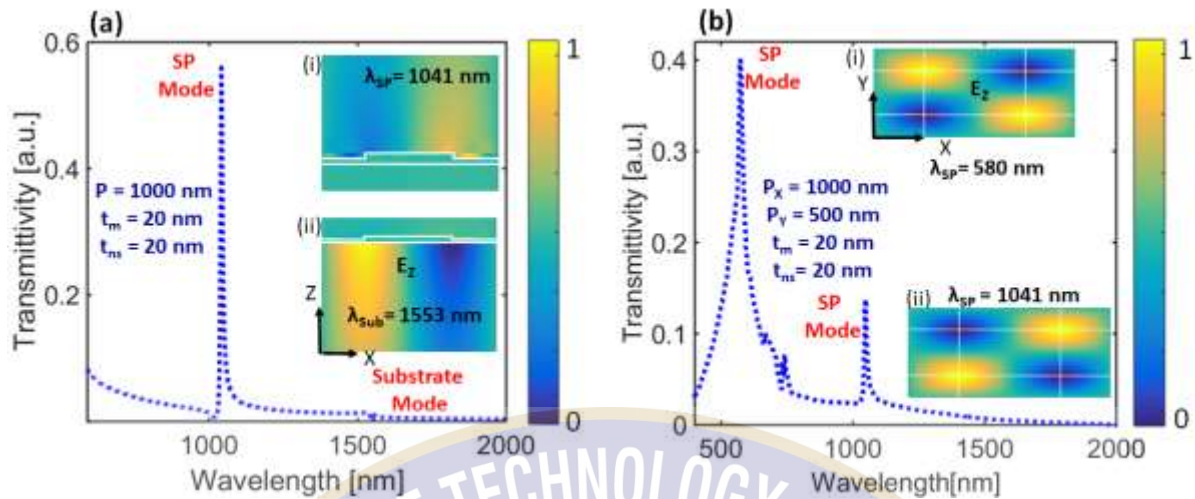
Fig. 7.10 (a) Transmittivity spectra for the optimized 1D plasmonic nanostructures of period P = 1000 nm, and $t_m = t_{ns} = 20$ nm along with the electric field distributions for SP mode and Substrate mode shown in the insets (i) & (ii) respectively (b) Transmittivity spectra for the proposed 2D Al-nanostructure based plasmonic device with P_x= 1000 nm, P_y = 500 nm, and $t_m = t_{ns} = 20$ nm along with the electric field distributions for SP modes in the visible and near-infrared region as shown in the insets (i) & (ii) respectively.

The simulated electric field distributions for the excited SP modes in visible and near IR regions can be seen in the inset (i) and (ii) of Fig. 7.10(b) which show strong confinement of the field at the corners of 2D nanostructures. For 2D nanostructures, the light was incident normally for the polarization angle of 45° (both TE+TM). As a result of which SP modes are excited in both x and y directions with the opposite polarity of the electromagnetic field as shown in the field distribution. The magnitude of the peaks corresponding to SP modes in the transmittivity spectra of 2D nanostructures (Fig. 7.10(b)) reduced to almost 50% compared to 1D plasmonic nanostructures due to 50% distributions of the total incident light into TE and TM polarization components. The presence of SP modes in two different wavelength regions in a single experiment opens a new door to demonstrate the biosensing applications in both visible and NIR regions with the same plasmonic substrate.

Finally, to demonstrate the sensitivity analysis, the refractive index of the analyte 'n_a' on the top of the proposed 2D-nanostructure-based plasmonic device was varied and the transmittivity spectra were calculated as shown in Fig. 7.11(a). Subsequent redshift was observed by varying the refractive index of the analyte 'n_a' in steps of 0.01. Fig. 7.11(b) & (c) show the zoomed-in picture for the shift in the transmittivity peaks corresponding to excited SP modes in the visible and near-infrared regions respectively. A sensitivity of 500 nm/RIU was observed for the visible region while 1000 nm/RIU was observed for the NIR region. This observation shows that the device is sensitive enough to be implemented in bio-sensing and chemical-sensing applications. Table 7.3 shows the comparison of our final results with the previously reported

works. It can be inferred that our work has achieved decent sensitivity for both the visible and NIR regions with the added advantage of the wide wavelength difference (visible and near-infrared), self-reference capability, and wavelength tunability of SP modes by changing the period in the x and y direction.
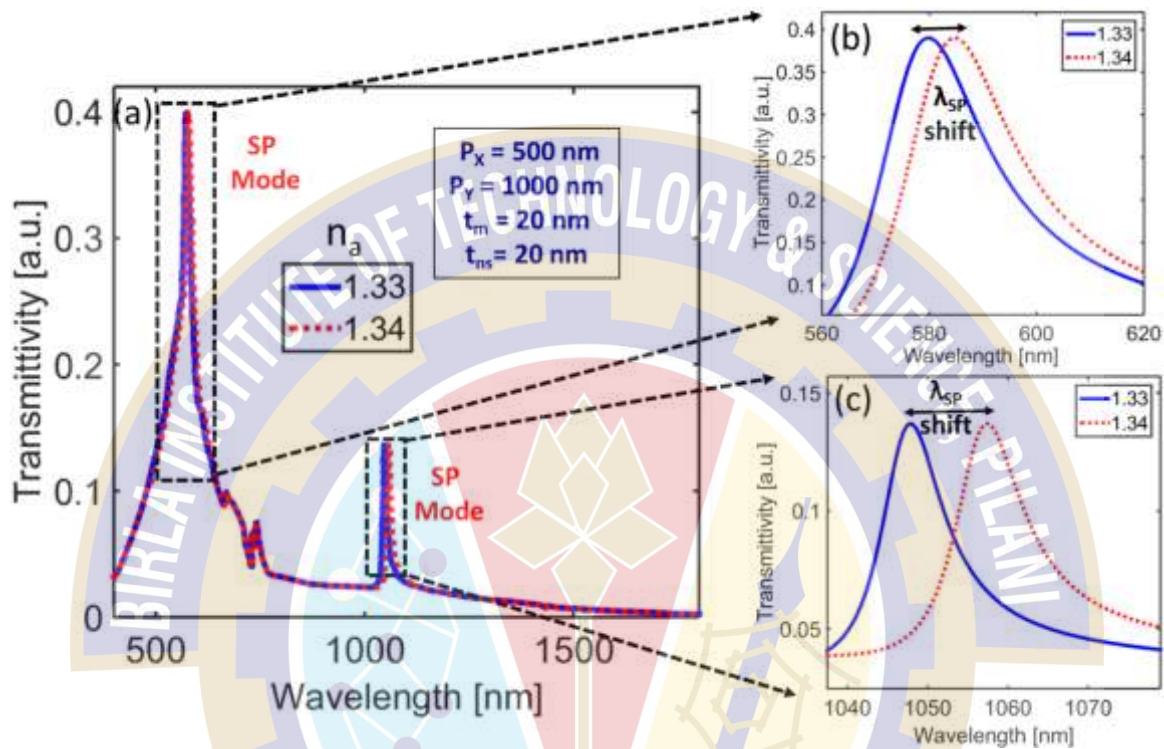
Fig. 7.11 (a) Transmittivity spectra for the proposed Al-based 2D nanostructures with P_X= 1000 nm, P_y = 500 nm, t_m=t_{ns}=20 nm with variation in the refractive index of the analyte 'n_a' (b) zoomed-in picture for the variation of the 'n_a' in SP mode for the visible region (c) zoomed-in picture for the variation of the 'n_a' in SP mode for the near-infrared region.

TABLE 7.3: Comparison of the proposed work with previous results reported in the literature

Ref. no	Schematic	S [nm/RIU]	λ [nm]
[178]	Ag+Si+Al$_2$O$_3$ grating	477.02	1440-1540nm
[195]	Au-covered titania gratings	938.7	1040-1100nm
[180]	Al-based grating sensor	~700	500-1000nm
[189]	GaN gratings+SiO$_2$	192	400nm-800nm
[179]	Si$_3$N$_4$ gratings +Ag+SiO$_2$	580	1400nm-1700nm
Our work	**Glass +Al film +Al nanostructures**	**1000 nm/RIU (NIR)** **500nm/RIU (Visible)**	**500-1500nm**

7.4 Conclusion

This chapter broadly examined 1D and 2D nanostructure-based arrangements. Both configurations are feasible enough to be implemented for real-time sensing applications since all the performance parameters are equally taken care of. Firstly, a self-referenced plasmonic device with 1D Al-based periodic nanostructures was proposed. The normal incidence operation from the bottom of the device eases the integration of the proposed plasmonic device with optical fiber. Moreover, shining the light from the bottom of the device would not add any constraints such as the analyte or flow cell needed to be optically transparent, which is the main novelty of the work. The proposed device offered a competitive sensitivity (1100 nm/RIU) in the optical communication band.

In the proceeding section, we evaluated the possibility of using Al-based 2D nanostructures for the multiwavelength plasmonic activity from the visible to the NIR region. Here, after confirming the presence of the SP modes in both the wavelength regimes independently, the multiwavelength plasmonic behavior of the proposed device was studied with different periods in the x and y directions. Al-based 2D nanostructures with different periods in different directions can be exploited in multiple applications such as imaging sensors or sensing spectroscopy wherein the analyte characteristics corresponding to different wavelengths can easily be extracted in a single experiment.

Chapter 8

Aluminum-nanostructure-based plasmonic device with enhanced sensitivity and figure of merit using both wavelength and angle interrogation

Even the most simplified prismatic structure still accounts for limited dynamic range detection. Thus, the flexible and controllable geometry of nanostructures has become an interesting alternative for improved miniaturization and a large dynamic range. Of late, sine and rectangular nanostructures have gained popular perspective due to ease in the fabrication process flow. This chapter focuses on Al-based nanostructures and the proposed geometry that can enable both modes of interrogation i.e., angle and wavelength-based analysis of the plasmonic design.

A detailed analysis using RCWA is carried out to prove the feasibility of the proposed plasmonic device with the same designed parameters to operate in two interrogation modes, which is impossible in a conventional prism configuration. The performance parameters, sensitivity, and FOM are found to be 1000nm/RIU and 333.33RIU^{-1} during wavelength interrogation and 119°/RIU and 318.91RIU^{-1} for the angle interrogation respectively. Finally, the biosensing application is carried out by demonstrating the glucose concentration detection in the urine samples. The proposed Al-based plasmonic device decorated with a Gr layer has the advantages of being cost-effective and possessing real-time sensing capability, paving the way for biomedical applications in the near-infrared region.

8.1 Introduction

Nanostructure-coupled SPR sensors are also known to show modest sensitivity and narrow linewidth which makes them widely compatible with sensor chip mass production [12]. Even Al-based plasmonic nanostructures have demonstrated appreciable refractive index and thickness sensing [13], [14]. Nanostructures such as Al-based nanohole arrays have shown negligible signs of degradation on oxygen plasma and are 25,000 times cheaper than noble metallic arrays [8]. To assist the functionalization of the Al-thin films, research on Gr-based photonic devices has accelerated among the various BRE available [15], [16]. Over the years, researchers have established exemplary results in a quest to enhance the performance parameters of sensing in a typical SPR sensor. Kong et al. recently presented reflectivity spectra for Gr-coated sub-wavelength Ag nanostructures at the wavelength of 633 nm. The angular interrogation performed in a multilayered Gr nano-device resulted in

maximum sensitivity of about 220.67°/RIU, however, a broader linewidth of almost 7° led to a poor FOM [17]. Likewise, at 1550 nm, the MXene-based sensor aided by Gr for biomolecular binding produced a FOM of 559.24 RIU^{-1} and low sensitivity of about 39.12°/RIU [18]. Parallelly, for an SPR sensor under wavelength interrogation, Au-covered titania nanostructures showed high sensitivity (938.7 nm/RIU) but degraded FOM (39.7 RIU^{-1}) respectively [19]. With Gr being deposited over the nanostructure ridges, a sensitivity of 2780 nm/RIU was achieved but again with a very broader linewidth of around 150 nm, thus resulting in a poor FOM of almost 18.5 RIU^{-1} [20]. As per our knowledge, works reported on wavelength interrogation have considered sensitivity as an important parameter without considering the effect of the broader linewidth of the SPR curve in the spectra. Overall, the advantages offered by plasmonic devices have been examined exhaustively in the recent past but only with either of the interrogation e.g., wavelength interrogation or angle interrogation. Moreover, it is difficult to realize SPR sensing simultaneously with large sensitivity and FOM in a conventional prism coupling structure.

In this chapter, we have proposed a Gr-decorated Al nanostructure-based plasmonic device for sensing in the NIR region where the same engineered device can be used under both angular as well as wavelength interrogation with high sensitivity and FOM simultaneously. It should be noticed that a larger value of FOM mainly originates from the narrow SPR linewidth which is favorable to realizing high-resolution detection and improving the detection limit considerably. Al-based engineered periodic nanostructures with characteristics of coupling of plasmonic modes have been utilized in the plasmonic device to shrink the linewidth. Our proposed plasmonic device does not need any complex fabrication processes which manifests itself as a feasible way to show the promising sensing application for biomedical purposes, employing Gr for functionalization purposes on an Al-based plasmonic device. In the proposed device, Al nanostructures can easily be fabricated using conventional semiconductor processing techniques involving electron beam lithography, a metal evaporation step followed by a lift-off process. Thereafter, the dielectric buffer layer (PMMA) can be spin-coated to fill the nanostructures resulting in a planar surface. Later, a thin Al film can be deposited on top of the buffer layer. Finally, the Gr monolayer can be directly transferred on top of the Al film by either simple use of the scotch tape method, glow discharge method, or CVD process. To experiment under wavelength interrogation, the fabricated substrate can be

integrated with the tip of the optical fiber, which can be used for both excitation of SPs and the interrogation of reflectivity spectra under normal incidence conditions.

For angle interrogation, the fabricated plasmonic glass substrate can be integrated into the prism with index-matched (NOA-142) optical adhesive, and the reflectivity measurements can be taken for the angle interrogation for a wavelength of 1550 nm.

8.2 Design parameters for the proposed device
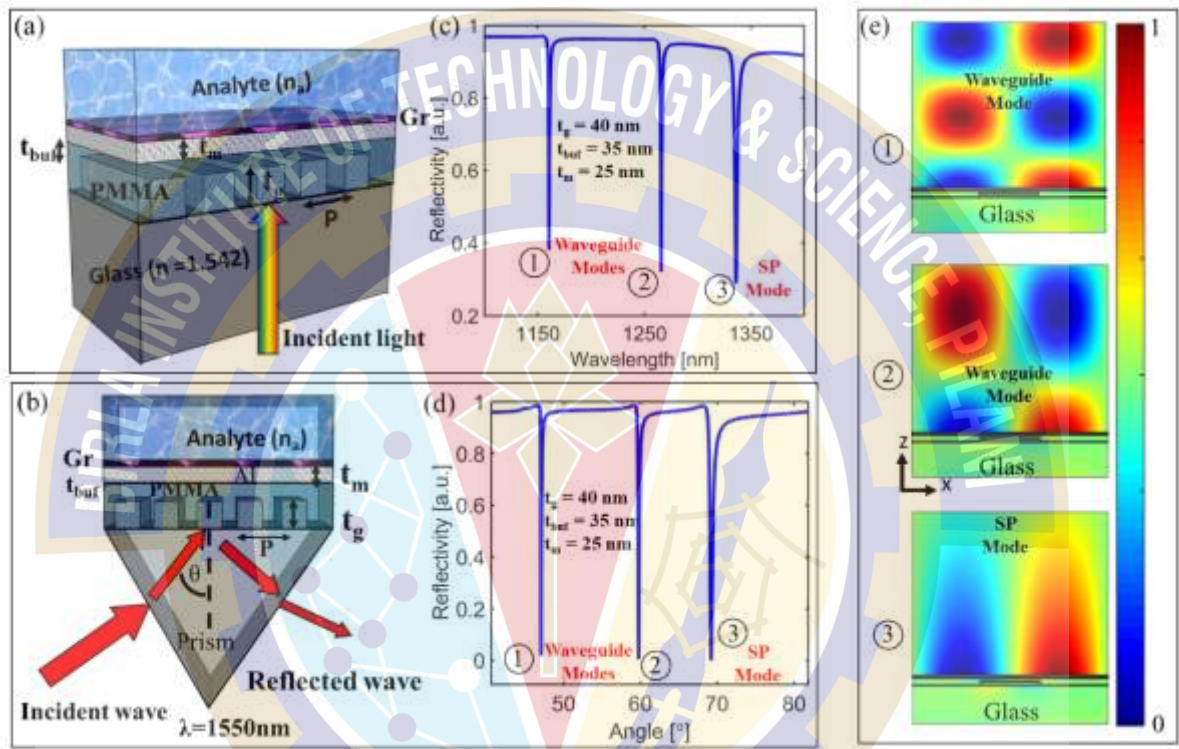
Fig. 8.1. (a) Schematic for the proposed Gr decorated plasmonic device under wavelength interrogation (b) Schematic for the proposed design under angle interrogation with the addition of prism; Reflectivity curves for the proposed design (c) under wavelength interrogation (d) under angle interrogation respectively. (e) The electric field distribution corresponding to reflectivity dips appeared in the reflectivity curves.

The schematic shown in Fig. 8.1(a) represents the proposed Gr-decorated plasmonic device and Fig. 8.1(b) represents the same proposed device integrated with a glass prism. The glass material used for both schematics is CaF_2. In both schematics, the proposed device involves Al as the plasmonic metal. The dielectric layer (PMMA) acts as a buffer layer over the nanostructures which makes the resulting surface planar for further Al thin film deposition. The analyte, under test, is in contact with a Gr monolayer of thickness 0.34 nm [16] where the SPR propagates and interacts with the analyte. The use of the Gr layer not only protects the Al metal from oxidation but also acts like a BRE for the bio-

functionalization of the Al film. The pie bonding of Gr helps with a better attachment of carbon-based biomolecules. Also, the impermeability towards gases is among the many advantages because of which Gr has been decorated over the proposed plasmonic device for biosensing applications. In the proposed plasmonic device, the use of Al nanostructure is to scatter the incoming light which propagates towards thin Al film to excite SPs. A broadband TM-polarized wavelength source under normal incidence conditions was considered for the case of wavelength interrogation (Fig. 8.1(a)) and a single wavelength source of 1550 nm was considered for the case of angle interrogation (Fig. 8.1(b)). All the geometrical parameters were then optimized for low reflectivity amplitude, better signal contrast, and narrow linewidth of SP curves for an analyte of refractive index (n_a = 1.33) using RCWA. The other existing methods in the literature for the same analysis are the FDTD method (Lumerical), the Finite element Method (COMSOL Multiphysics), etc. We have verified our results with Comsol Multiphysics software using the RF module. The parameters sensitivity and FOM were used as the performance parameters for both wavelength interrogation and angle interrogation.

8.3 Numerical Analysis

Fig. 8.1(c) shows the reflectivity curves corresponding to the device shown in Fig. 8.1(a) with a period (P) =1000nm, nanostructure thickness (t_{ns}) = 45nm, buffer layer (PMMA) thickness (t_{buff}) = 35nm, and thin Al metal thickness (t_m) = 25nm. For wavelength interrogation, a broadband source under normal incident conditions was used to excite SPs. In the reflectivity spectra (Fig. 8.1(c)), three distinct dips were observed at 1161 nm, 1266nm, and 1336nm respectively.

Fig. 8.1(d) shows the simulated reflectivity curves corresponding to the plasmonic device shown in Fig. 8.1(b) where the light source of wavelength 1550 nm was incident on the device under angle interrogation. Similarly, three distinct dips at 47.32°, 59.23°, and 69.18° in the reflectivity curves were observed for the same geometrical parameters, when angular interrogation was performed.

The electric field distributions corresponding to these three dips that appeared in both wavelength and angle interrogation were calculated as shown in Fig. 8.1(e). The first two dips were found to correspond to waveguide modes whereas the existence of strong electric field confinement at the Gr-analyte interface, corresponding to the third dip position,

ensured the presence of SP mode. Since SP mode is very sensitive to the refractive index of the surrounding medium, the third dip in the reflectivity curves had been considered for sensing purposes throughout this work.

8.3.1 Wavelength Interrogation

Under the wavelength interrogation, the normal incidence of the incoming light makes the proposed device easily integrable to the end of the optical fiber. For the proposed Gr-decorated Al-nanostructure-based plasmonic device shown in Fig. 8.1(a), firstly, all the geometrical parameters were engineered by varying one parameter at a time using RCWA, and reflectivity spectra were calculated as shown in Fig. 8.2. The reflectivity spectra with the variation in Al-nanostructure height (t_{ns}) from 30 nm to 50 nm, keeping all other parameters constant is shown in Fig. 8.2 (a). 40 nm height resulted in minimum reflectivity amplitude and narrow linewidth so it was considered to be the optimized thickness for the nanostructures. Fig. 8.2 (b) shows the reflected spectra with the variation in the fill factor (f) which is defined as 'nanostructure width'/ 'period' (w/P). The width (w) of the nanostructures determines the angular pattern of the scattered light which propagates toward the thin Al metal. A value of 0.3 for the fill factor resulted in minimum reflectivity which ensures the SP excitation with higher efficiency. Fig. 8.2(c) shows the reflectivity spectra with the variation in buffer layer height (t_{buf}). The planar surface provided by the buffer layer makes the operation of the device easier. From Fig. 8.2 (c), a thickness of 35 nm for the buffer layer was found to be the optimized one resulting in high signal contrast. Fig. 8.2 (d) represents the reflectivity spectra with the variation in thin Al metal height (t_m) where the thinner layer resulted in the shallower reflectivity minima, and the thicker layers provided the broader linewidth. A thickness of 25 nm for the thin Al metal layer was found to be the optimized value from the spectra.

After meticulously varying each parameter, t_m was found to be 25 nm, t_{buff} =35 nm, and t_{ns}= 40 nm for a period of P =1000 nm with a fill factor of 0.3. The effect of the period on the reflectivity spectra was also studied by varying the period (not shown here) and a right shift in the wavelength was noticed when the period varied from 950 nm to 1050 nm in steps of 50 nm. This shows that the characteristics of a particular plasmonic device can be tuned to the desired wavelength range by varying the period.
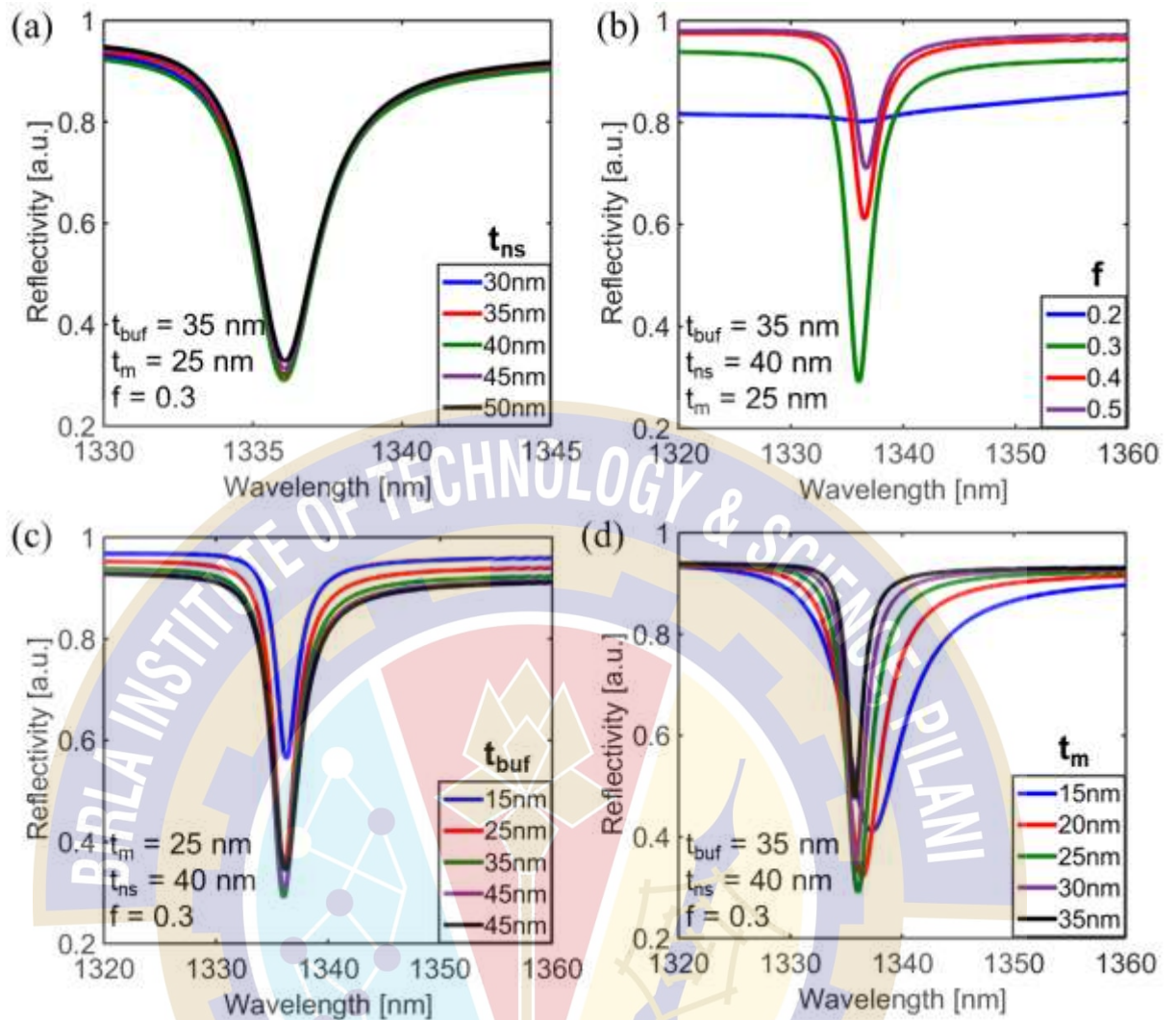
Fig. 8.2. Reflectivity spectra with the variation in (a) nanostructure height (t_{ns}) (b) fill factor of nanostructures which is defined as width/period (c) buffer layer (PMMA) height (t_{buf}) and (d) thin Al metal height (t_m) of the proposed plasmonic device under wavelength interrogation.

8.3.2 Angular Interrogation

After the optimization of the proposed device under wavelength interrogation, a glass prism integrated with Al nanostructure-based plasmonic device, shown in Fig. 8.1(b), was taken into consideration to carry out the angle interrogation. The source of wavelength 1550 nm was used for the angle interrogation. To narrow down the discrete optimal values for all the in-between layers, the reflectivity curves were plotted and a similar approach was used based on reflection minima points as done during wavelength interrogation. To begin with, nanostructure height (t_{ns}) was varied in the range of 30-50 nm, and the reflectivity curves with respect to incident angles were plotted as shown in Fig. 8.3(a). Similarly, Fig. 8.3(b) shows the variation of buffer layer height (t_{buf}) in the range of 25-45 nm. Fig. 8.3(c) and (d) show the zoomed-in image of reflectivity dips for SP mode

corresponding to Fig. 8.3(a) and (b) respectively.
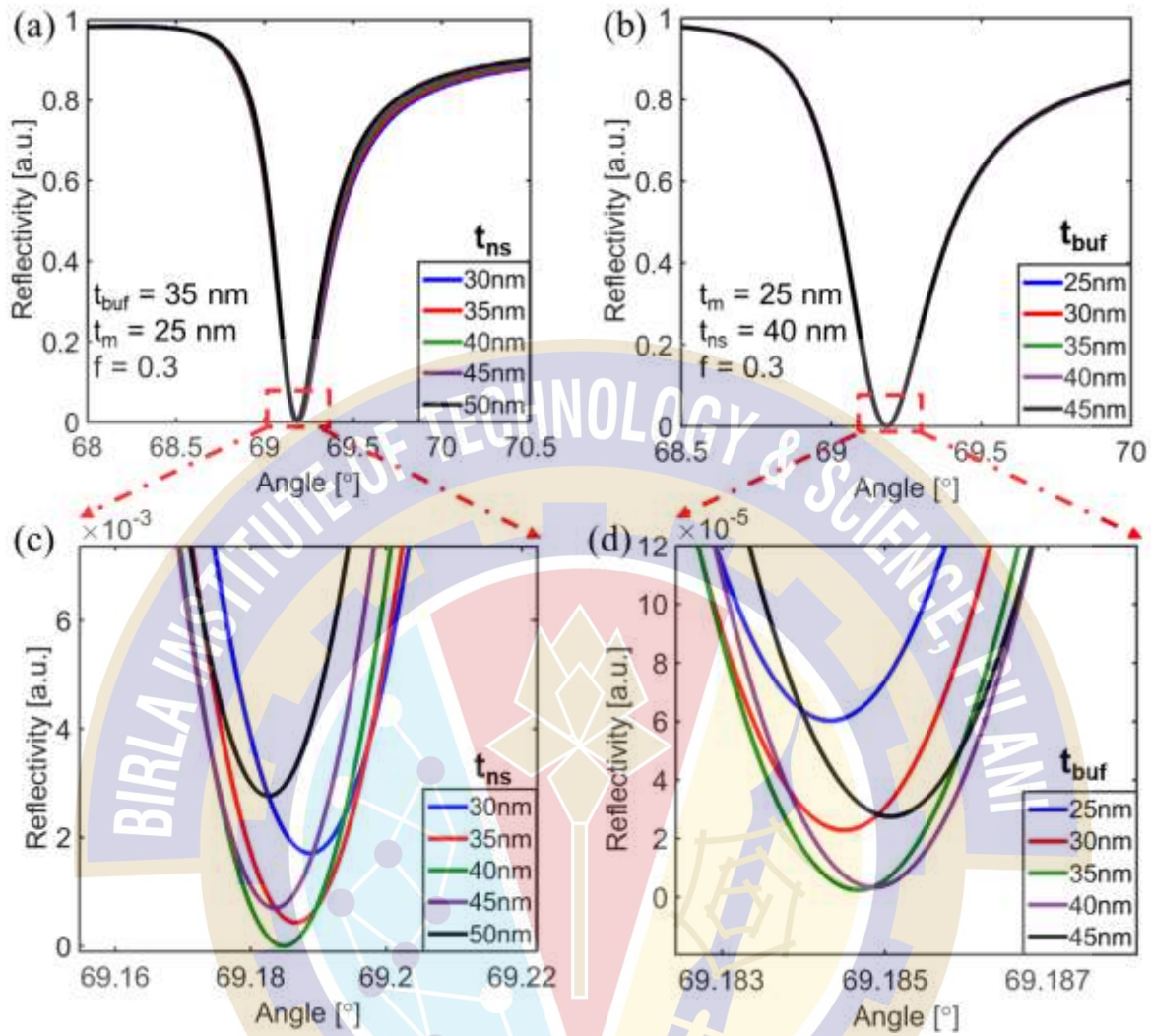
Fig. 8.3. Reflectivity curves with the variation in (a) nanostructure height (t_{ns}) (b) buffer layer (PMMA) height (t_{buf}) of the proposed plasmonic device under angle interrogation (c)-(d) The zoomed-in picture of the reflectivity dip for the SP mode corresponding to (a) and (b) respectively.

Just like in wavelength interrogation, a thickness of 40 nm for (t_{ns}) and 35 nm for (t_{buf}) were found to be the engineered values with minimum reflectivity for the SP curve. Fig. 8.4 (a) shows the reflectivity with the variation in thin Al metal height (t_m). The SPR curve approached near-zero reflectance till 25 nm, beyond which the curves offered low signal contrast. Therefore, 25 nm was chosen to achieve the maximum resonant activity. After a series of optimizations, it was observed that the geometrical parameters achieved in angle interrogation are the same as in wavelength interrogation. To show the significance of the presence of nanostructures in prism configuration, the reflectivity curves were compared with the conventional Kretschmann configuration, where the nanostructures are absent as shown in Fig. 8.4(b). An improved reflection minimum and

reduced linewidth in the proposed device are the resulting advantages that give us an edge over conventional configuration.
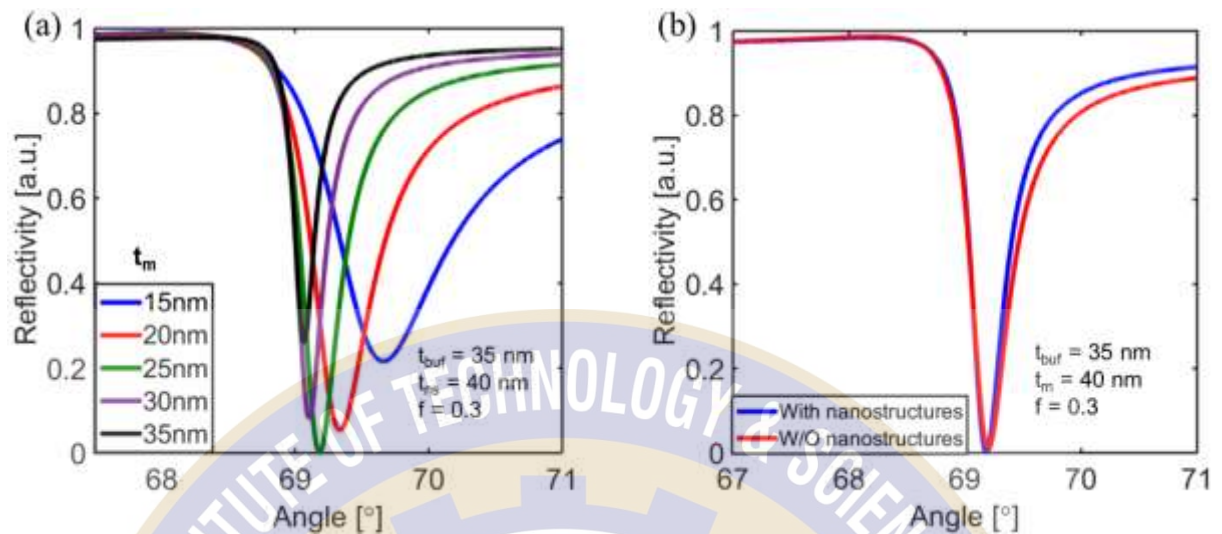
Fig.8.4. (a) Reflectivity curve for the proposed plasmonic device with the variation in thin Al metal height (t_m) under angle interrogation. (b) Reflectivity curve with and without the presence of nanostructures in the proposed plasmonic device.

Finally, the refractive index sensing was performed over the proposed engineered design under wavelength and angle interrogation as shown in Fig. 8.5. The refractive index (n_a) of the analyte varied from 1.33 to 1.37 and the values for sensitivity and FOM were calculated for both cases. From Fig. 8.5(a), the value of sensitivity and FOM were calculated as 1000 nm/RIU and 333.33 RIU^{-1} respectively for the case of the wavelength interrogation, and a value of 119°/RIU and 318.91 RIU^{-1} were found for angle interrogation (Fig. 8.5(b)). Minute changes in the concentration of the analyte cause the refractive index to vary which in turn shifts the SP resonance curves. Therefore, the proposed plasmonic device can easily be delved into the biosensing arena. Traces of glucose in the urine/blood samples can be detected in diabetic patients when the effective refractive index of the urine sample (analyte) deviates from the normal sample.
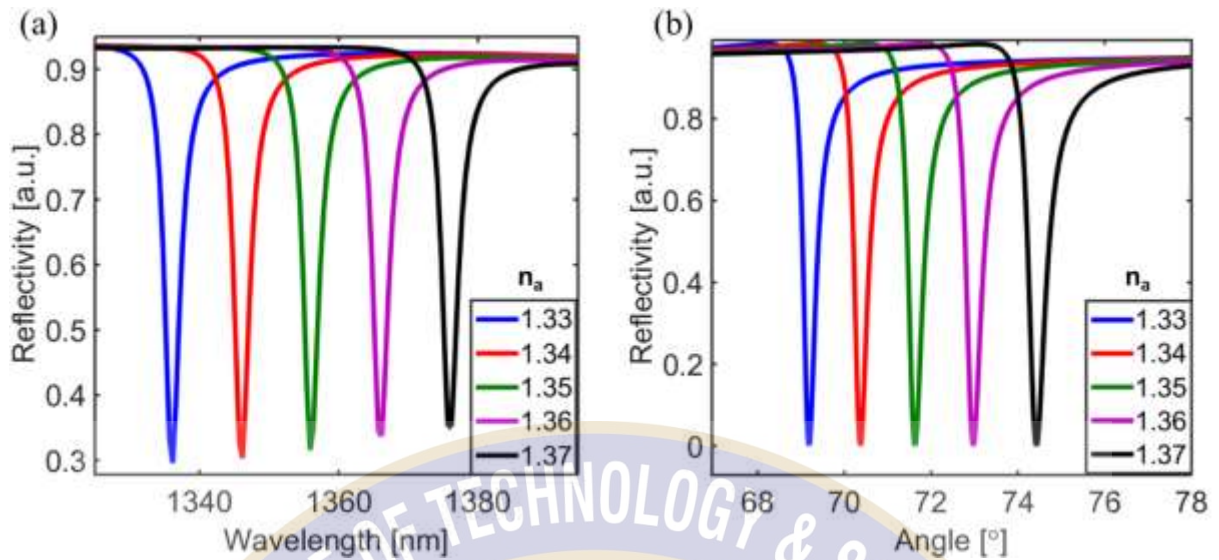
Fig. 8.5. Reflectivity curves for the engineered plasmonic device with variation in the refractive index of the analyte under (a) wavelength interrogation and (b) angle interrogation.

Fig. 8.6(a) illustrates the output spectra for glucose concentration in the urine samples varying from 0 mg/dl to 5 mg/dl. The refractive index increases with increased glucose concentration [23], thereby demonstrating the real-time application of the proposed device. Similarly, under angle interrogation, sensing application was carried out as depicted in Fig. 8.6(b) for different glucose concentrations. Therefore, the proposed design for the sensor can easily be assimilated into medical applications.
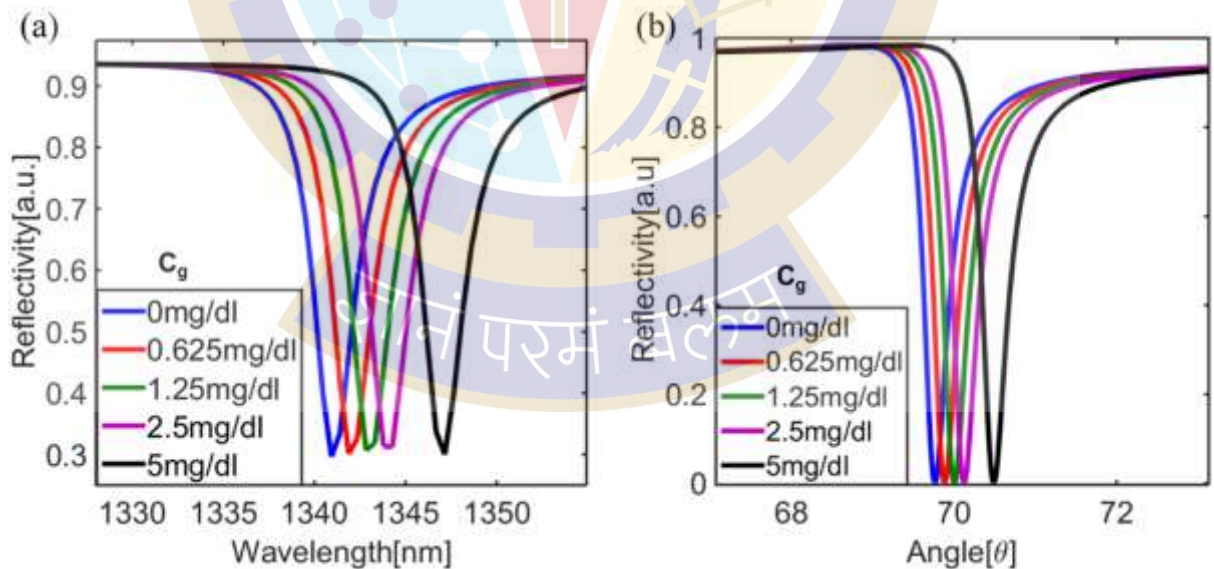
Fig. 8.6. Reflectivity curves for the engineered plasmonic device with the variation in the glucose concentration for (a) wavelength interrogation and (b) angle interrogation.

Finally, Table 8.1 compares the present work with the previously reported results in terms of sensitivity and FOM for both the angle and wavelength interrogation mode. While a couple

of them have shown considerable improvement in sensitivity, the same cannot be said about FOM. Similarly, a few of them have reported higher FOM but at the cost of poor sensitivity. Unlike the present work, none of the reported plasmonic devices are seen to exhibit both high sensitivity and FOM simultaneously for both modes of interrogation.

TABLE 8.1: Comparison of the proposed work with the previously reported results

REFERENCES	SCHEMATIC	ANGLE INTERROGATION		WAVELENGTH INTERROGATION	
		SENSITIVITY [°/RIU]	FOM[RIU^{-1}]	SENSITIVITY [nm/RIU]	FOM[RIU^{-1}]
[106]	BK$_7$ prism+ Ag + Gr	300.26	33.25	--	--
[141]	BK$_7$ prism+Dielectric+ MXene+ Gr	39.12	559.24	--	--
[162]	BK$_7$ Prism + TiO$_2$ + Ag+MoSe$_2$+ Gr	194	54.03	--	--
[110]	SF$_{10}$ prism +Au+ WS$_2$+ Gr	95.71	25.19	--	--
[180]	Al-based grating sensor	--	--	700	~35 to 45
[178]	Ag+Si+Al$_2$O$_3$ grating	--	--	477.02	38.16
[195]	Au-covered titania gratings	--	--	938.7	39.7
[196]	Au mirror+MgF$_2$+Au film	--	--	~600	55
Proposed Work	**Al nanostructures + PMMA +Al film + Gr**	**119**	**318.91**	**1000**	**333.33**

8.4 Conclusion

Investigation of Al-based plasmonic nanostructures decorated with Gr monolayer was performed in the NIR region. From the spectrum analysis, the optimized values showed sensitivity and FOM of about 1000 nm/RIU and 333.33RIU^{-1} respectively. Further, it was seen that the set of design parameters used for wavelength interrogation can also be used for angle interrogation with enhanced sensitivity and FOM simultaneously. This illustrates the fact that an engineered plasmonic device can be used for both wavelength and angle interrogation-based sensing. Overall, the sensitivity and FOM were found to be 119°/RIU and 318.91RIU^{-1} respectively under the angle interrogation. The significance of the presence of nanostructures in the proposed design was explained by the fact that it provides better signal contrast and narrower linewidth. Finally, the bio-sensing application was demonstrated via glucose concentration sensing in the urine samples on the proposed plasmonic device for both wavelength and angle-interrogation. The present work highlighted the robustness of the plasmonic device for both interrogation methods, plus the application of the Gr layer in the bio-sensing arena in the vicinity of nanostructures with Al being used to control the plasmonic activity.

Conclusions and Future Scope

This thesis can be summarised as a comprehensive investigation of Al-based plasmonic devices; to utilize their plasmonic properties for sensing applications in the near-infrared region.

- **Chapter 1** gave a brief account of the basics of the SPR phenomenon and explained that the optical output parameters are a result of examining reflectivity or transmittivity characteristics as a function of incident angles or wavelengths.

- Al-based plasmonic devices in three different forms i.e., nanoapertures, thin films, and periodic nanostructures were elaborately discussed in **chapter 2** which gathers all the work done so far using Al as the plasmonic material. The methods of numerical analysis i.e. TMM and RCWA, used for engineering the plasmonic devices, were discussed at the end of the chapter.

- The previous chapter motivated us to work towards Al-based thin films and nanostructures in the NIR region which have been briefly explored by researchers till now. Thus, in **chapter 3**, we started with studying the effect of high dielectric constant material (Silicon) over an Al thin film-coated glass prism for intermediate Si-Gr stacks. The use of Si-Gr stacks in the proposed plasmonic device helped to increase the sensitivity value up to 200°/RIU with a decent value of FOM.

- Thereafter, moving beyond Gr, TMDCs (MoS_2) were explored for enhanced sensitivity as well as FOM in the absence and presence of the Si dielectric layer in **chapter 4**. Due to the negligible value of the imaginary part of the dielectric constant for MoS_2 in the NIR region, the presence of MoS_2 enhanced the FOM as compared to the previous chapter. Out of the four proposed Al-MoS_2-based configurations, ASMG based plasmonic device offered the highest sensitivity and AM based plasmonic device offered the largest value of FOM.

- As observed in the previous chapters, the BRE layers assist the bio-functionalization of Al film, we further went along exploring the carbides-based 2D nanomaterials (Ti_3C_2Tx) in **chapter 5**, for enhanced interaction with biomolecules at longer wavelengths. Heterogeneous composites over Al-MXene-based Kretschmann configuration led to a stable and oxidation-resistant combination along with improved FOM. The presence of FG and MoS_2 (2D material) over the Al-MXene-based plasmonic devices can be utilized to ease the precise control of

the number of layers during the fabrication process since the sensing parameters were merely affected by the increase in the number of MoS_2 and FG layers on Al-MXene based plasmonic devices.

- Later on, we observed that enhancing sensitivity was one way to improve FOM, another approach can be to reduce SPR linewidth and thus obtain improved FOM or resolution. Therefore, in **chapter 6**, we utilized the MDM configuration in a multi-layered Al-based plasmonic device that involves $BaTiO_3$ as a dielectric material sandwiched between two thin Al metal layers. This MDM configuration offered large field confinement at the metal-analyte interface leading to a narrow linewidth of the SPR curve which results in high resolution/FOM.

- **Chapter 7** introduced the Al-nanostructures-based plasmonic devices, where the output characteristics were manipulated with parameters such as period, width, and height of the nanostructures. For the proposed 1D Al nanostructure-based plasmonic device, the obtained reflectivity curves under normal incidence excitation from the bottom of the device make it integrable to the end of the optical fiber. We also proposed a 2D Al-nanostructures-based plasmonic device where the multiwavelength SP excitation in two different wavelength regions can be utilized to investigate the analyte's characteristics at different wavelengths in a single experiment itself.

- Lastly, in **chapter 8**, the robustness of the Al-based plasmonic device was illustrated by employing such an engineered design that can be used for both angle and wavelength interrogation. The proposed plasmonic device utilizes both prism and nanostructure-based configurations, where the same designed parameters for the device offered both high sensitivity and FOM in both modes of interrogation.

Future Scope of the research

- The thesis is concluded with high-performance sensing parameters, though there is still scope for enhancing the efficiency by working on different geometries/shapes and exploring the device properties thereafter. As of now, Al-based rectangular nanostructures have been our prime focus that can be switched to trapezoidal nanostructures or Swastik shape nanostructures, etc. in the future.

- Different alloys of Al (e.g., Al-doped ZnO, Mg-Al alloy Ag-Al alloy, etc) can be worked around, to observe how the performance sensing parameters are different

from Al-rich plasmonic configurations in the optical communication window. Additionally, we can always explore other bimetallic designs with Al as one of the thin films. Apart from gold and silver which are the conventional plasmonic metals used, nickel is one other plasmonic metal like Al that is low in cost and at the same time provides higher sensitivity. Thus, such a bimetallic design can provide an interesting insight into the enhanced plasmonic activity at the metal-analyte boundary surface.

- SiO_2-TiO_2 nanosheets have been used in the visible region aiding high plasmonic effects and thus higher sensitivity. It will be interesting to explore their effect on the performance parameters in the NIR region with Al as the plasmonic material.

- Other 2D nanomaterials can also be explored with Al-based plasmonic devices such as 2D Franckeite nanosheets, Antimonnene layers, etc., that are already gaining momentum for sensing applications in the visible region with the noble metals. Apart from 2D nanomaterials, other materials like polymers have also been employed in fiber-optic-based sensors. However, these polymers are used as an alternative approach to enhance sensitivity in the visible region. To come up with a similar increment of performance parameters in the NIR region can be a prospect of research. We can try to formulate nanocomposites with such polymers that can either enhance the overall refractive index and thus increase sensitivity or increase the penetration depth to increase the detection accuracy.

- We have already observed that 2D Al-based plasmonic nanostructures can be utilized for multiwavelength SP sensing in different wavelength regions in a single device. This advantage can be extensively exploited for solar cell applications where larger bandwidth coverage will aim for maximum absorption in two different wavelength regions.

APPENDIX A

MATLAB Code for RCWA to Design Metal Grating Based Kretschmann Configuration
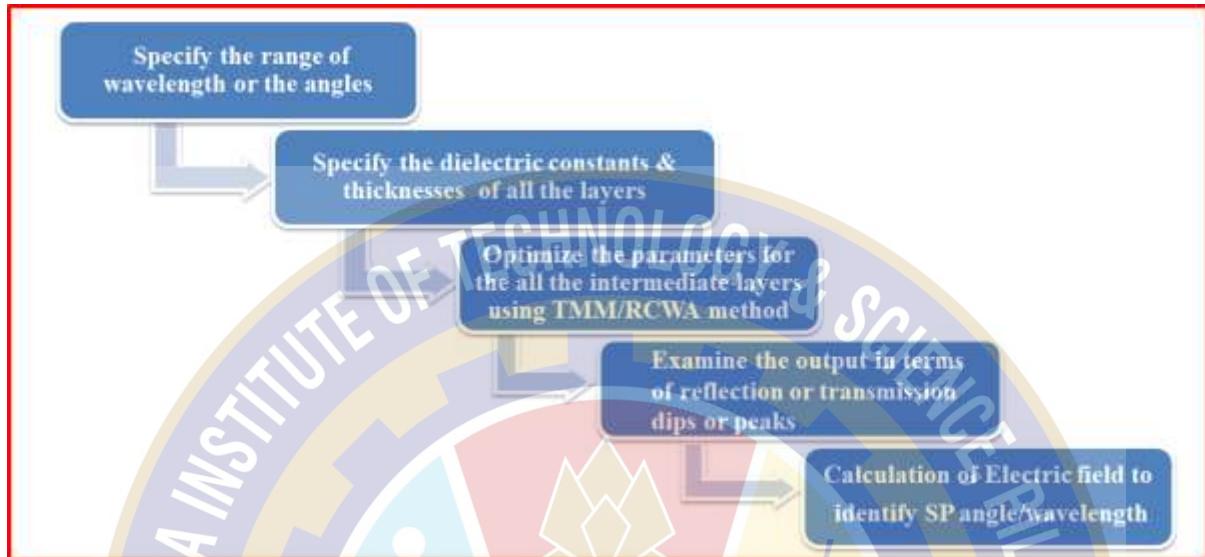
Fig. I Flowchart of the methodology used while engineering the geometrical parameters for proposed devices

The methodology used while engineering the geometrical parameters of the proposed plasmonic devices is shown in Fig. I.

1. To begin with, Drude-model is used to calculate the dielectric permittivity of Al for a particular wavelength using equation 2.1:

$$\varepsilon_m(\lambda) = 1 - \frac{\lambda^2 \lambda_c}{\lambda_p^2 (\lambda_c + j\lambda)} \tag{1}$$

wherein $\lambda_p = 1.0657e^{-7}$ m and $\lambda_c = 2.4511\ e^{-5}$ m denote the plasma wavelength and collision wavelength respectively [197].

2. Simultaneously, the dielectric constants as well as the thicknesses of the intermediate layers are specified so that the entire set of intermediate layers between the metal and analyte layer can be accounted for.

3. After mentioning all the required material parameters for all the layers, the geometrical parameters of the proposed devices are engineered for maximum sensitivity, narrow linewidth, and better signal contrast using either the Transfer matrix method (TMM) or Rigorous Coupled

Wave Analysis (RCWA) models (depending upon whether the proposed design includes the prism-based configuration or nanostructure-based configuration respectively).

Rigorous Coupled Wave Analysis
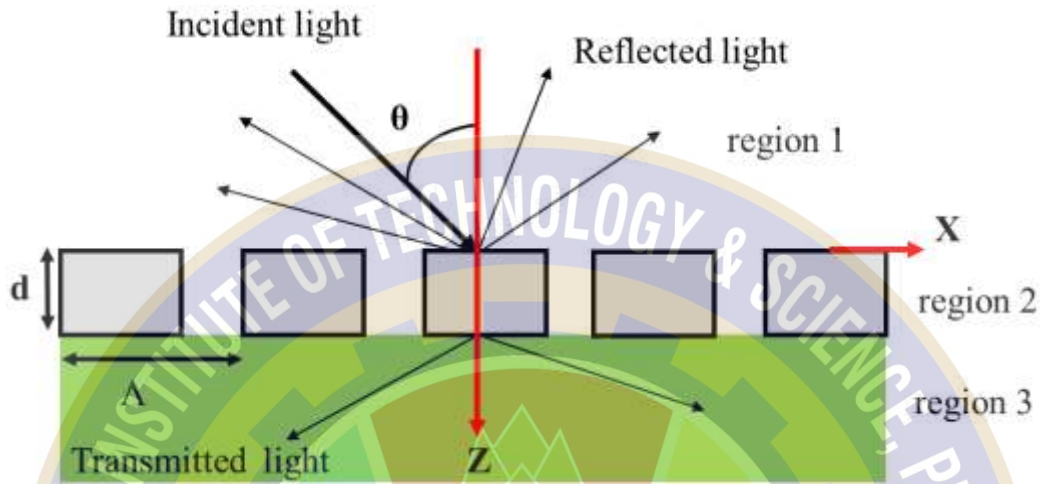
Fig. II Schematic of periodic nanostructure for RCWA modeling [187]

The program solves Maxwell's equations (without any approximation) based on fully vectorial calculations. Our RCWA consists of eliminating the y-dependency of the complex permittivity so that it is possible to write the solution inside the grooves as a Fourier expansion since only a dependency on the periodic coordinate x is present. The way RCWA accomplishes this is by slicing up the periodic nanostructure domain so that inside each slice, the permittivity only depends on x.

In the periodic nanostructure domain (region1), the relative permittivity is given by [187]:

$$\varepsilon(x) = \sum_h \varepsilon_h \, exp(j\frac{2\Pi h}{\Lambda}) \qquad (6)$$

where ε_h is the h_{th} Fourier component of relative permittivity in the periodic region and Λ is the period of the nanostructure. For alternating regions of refractive indices of n_{rd} (ridge) and n_{gr} (groove), the average value of relative permittivity (ε_o) can be expressed as:

$$\varepsilon_0 = n_{rd}^2 f + n_{gr}^2(1 - f) \text{ and } \varepsilon_h = (n_{rd}^2 - n_{gr}^2)\frac{sin(\Pi hf)}{\Pi h} \qquad (7)$$

Where f is the fraction of the period. Using the computed values of permittivity, we find the solutions to satisfy Maxwell's equations in all three regions. The field normalized to the plane of incidence is represented as:

$$E_{inc,y} = exp[-jk_0 n_1(sin\theta\, x + cos\theta\, z)] \qquad (8)$$

104

where $k_o = 2\pi/\lambda$, θ is the angle of incidence, and n_1 is the refractive index of region 1. The normalized solution in the region $1(0 < z)$ and $3(z > d)$ are:

$$E_{1,y} = E_{inc,y} + \sum_i R_i \, exp[\, - j(k_{xi} \, x - k_{1,zi} z)] \tag{9}$$

$$E_{3,y} = \sum_i T_i \, exp[\, - j(k_{xi} \, x - k_{3,zi}(z - d))] \tag{10}$$

Where K_{xi} and K_{zi} are the wave vectors along x and z directions respectively and R_i and T_i are the normalized electric field of the i_{th} reflected and transmitted wave in regions 1 and 3 respectively.

Similarly, the magnetic field in regions 1 and 3 can be obtained from Maxwell's equation:

$$H = \left(\frac{j}{\omega\mu}\right) \nabla XE \tag{11}$$

In the periodic region, the tangential electric field (E_y) and Magnetic field (H_X) components are continuous and expressed as:

$$E_{gy} = \sum_i S_{yi}(z) \, exp(\, - jk_{xi}x) \tag{12}$$

$$H_{gx} = -j(\tfrac{\varepsilon_0}{\mu_0})^{1/2} \sum_i U_{xi}(z) \, exp(\, - jk_{xi}x) \tag{13}$$

Where $S_{yi}(z)$ and $U_{xi}(z)$ are the normalized components of the ith space harmonic fields such that

$$\frac{\partial E_{gy}}{\partial z} = j\omega\mu_0 H_{gx} \tag{14}$$

$$\frac{\partial H_{gx}}{\partial z} = j\omega\varepsilon_0\varepsilon(x)E_{gy} + \frac{\partial H_{gz}}{\partial x} \tag{15}$$

After substituting (12) & (13) into (14) & (15) and eliminating H_{gz} coupled wave equation, the obtained differential equations are converted to matrix form and reduced to

$$[\frac{\partial^2 S_y}{(\partial z')^2}] = [A][Sy] \tag{16}$$

Where $A = K_x^2 - E$, E is the matrix formed by permittivity harmonic components with i, p elements equal to $\mathcal{E}_{(i-p)}$; k_X is the diagonal matrix and I is the identity matrix. The solution of the coupled wave equation is obtained by calculating the eigen vector and eigen values of A. It is these eigen values that provide us with the respective diffraction-related efficiencies of reflection and transmission that are calculated as:

$$DE_{ri} = R_i R_i^* \, Re(\frac{k_{1,zi}}{k_o n_1 \cos\theta}) \tag{17}$$

$$DE_{ti} = T_i T_i^* \, Re(\frac{k_{3,zi}}{k_o n_1 \cos\theta}) \tag{18}$$

This way, the unknown reflection and transmission coefficients of the upper and lower half-space were determined by summing up the diffraction efficiencies for all orders. Sufficient

space harmonic orders (201) were used to accomplish convergence and to improve calculation accuracy.

4. Thereafter, the optical output is obtained by plotting the reflectivity/transmittivity curves with respect to angle/wavelength for the proposed devices

5. The last step involves calculating the electric field distribution for the particular dips/peaks observed in the reflectivity/transmittivity curves.
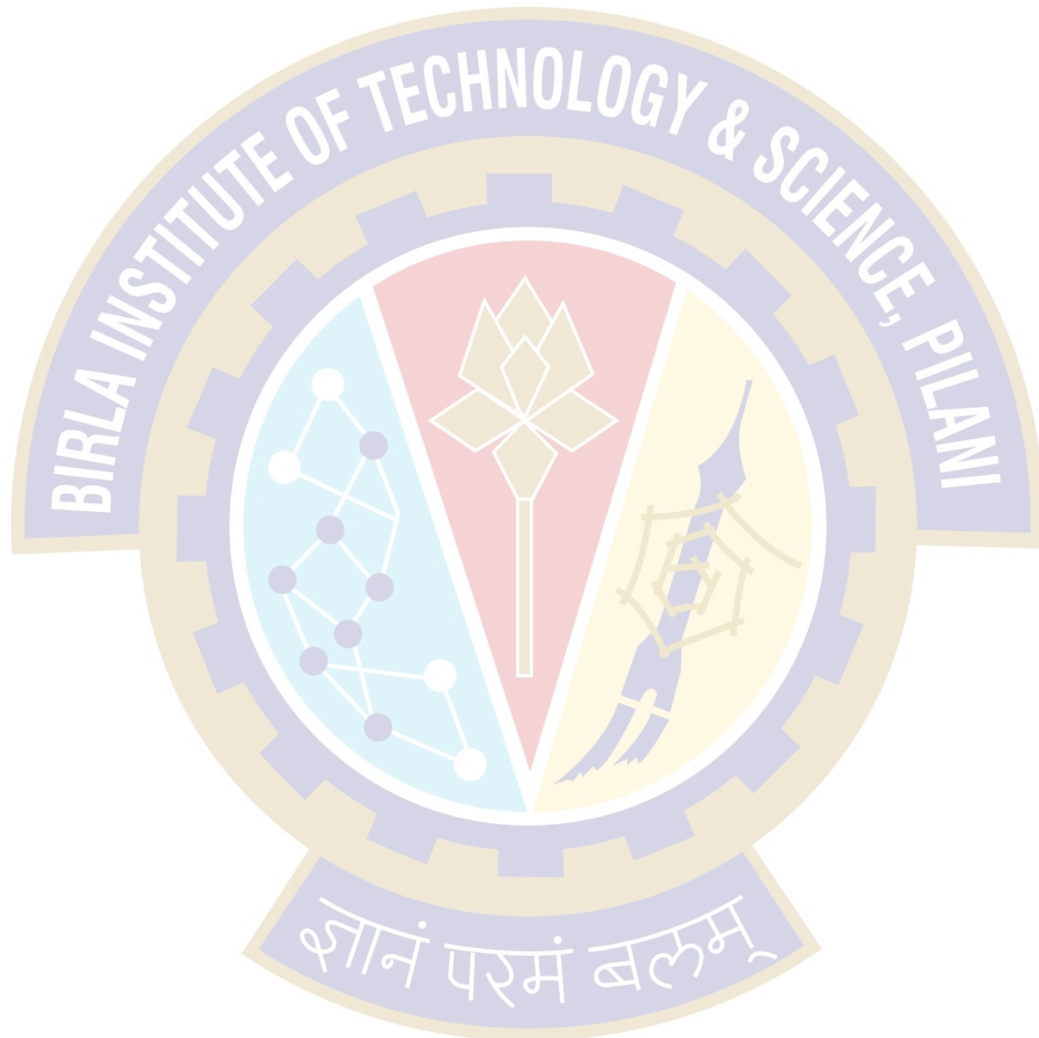
APPENDIX B

MATLAB Code for Transfer Matrix Method (TMM) to Design Metal Dielectric Based Kretschmann Configuration
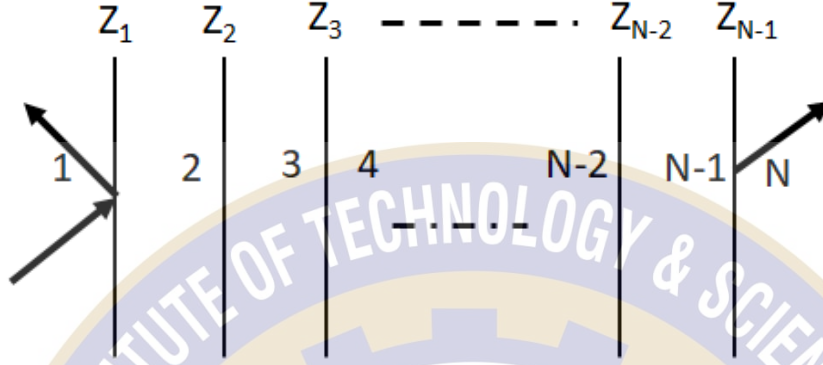
Fig. III N-layer model considered for Transfer Matrix Method [TMM] [198]

For the N-layer TMM model as shown in Fig. III, each layer was considered along the z-direction having the dielectric constant ε_k and refractive index n_k for the kth layer respectively. The relationship between the tangential field components at the final boundary and the first boundary was defined using characteristic matrix M given as [199]:

$$\begin{bmatrix} V_1 \\ W_1 \end{bmatrix} = M \begin{bmatrix} V_{n-1} \\ W_{n-1} \end{bmatrix} \tag{2.2}$$

where V_1 and W_1 represent the tangential components of electric and magnetic fields respectively at the boundary of the first layer and V_{n-1} and W_{n-1} are the corresponding fields for the boundary at the nth layer. Finally, the reflection coefficient (r_p) for p polarized wave was calculated from the characteristic matrix of the combined structure, given by M_{ij} [199], where

$$M_{ij} = \left(\prod_{k=2}^{n-1} M_k \right)_{ij} = \begin{bmatrix} M_{11} & M_{12} \\ M_{21} & M_{22} \end{bmatrix} \tag{2.3}$$

$$\text{with } \mathbf{M}_k = \begin{pmatrix} \cos\beta_k & -i\sin\beta_k / s_k \\ -is_k \sin\beta_k & \cos\beta_k \end{pmatrix}$$

$$\text{where } s_k = \left(\frac{\mu_k}{\varepsilon_k} \right)^{1/2} \cos\theta_k = \frac{(\varepsilon_k - n_1^2 \sin^2\theta_1)^{1/2}}{\varepsilon_k}$$

$$\beta_k = \frac{2\pi}{\lambda} n_k \cos\theta_k (z_k - z_{k-1}) = \frac{2\pi t_k}{\lambda} (\varepsilon_k - n_1^2 \sin^2\theta_1)^{1/2}$$

$$r_p = \frac{(M_{11} + M_{12}s_n)s_1 - (M_{21} + M_{22}s_n)}{(M_{11} + M_{12}s_n)s_1 + (M_{21} + M_{22}s_n)} \tag{2.4}$$

And the corresponding reflection intensity of the p-polarised light was expressed as [199]:

$$Rp = |r_p|^2 \tag{2.5}$$
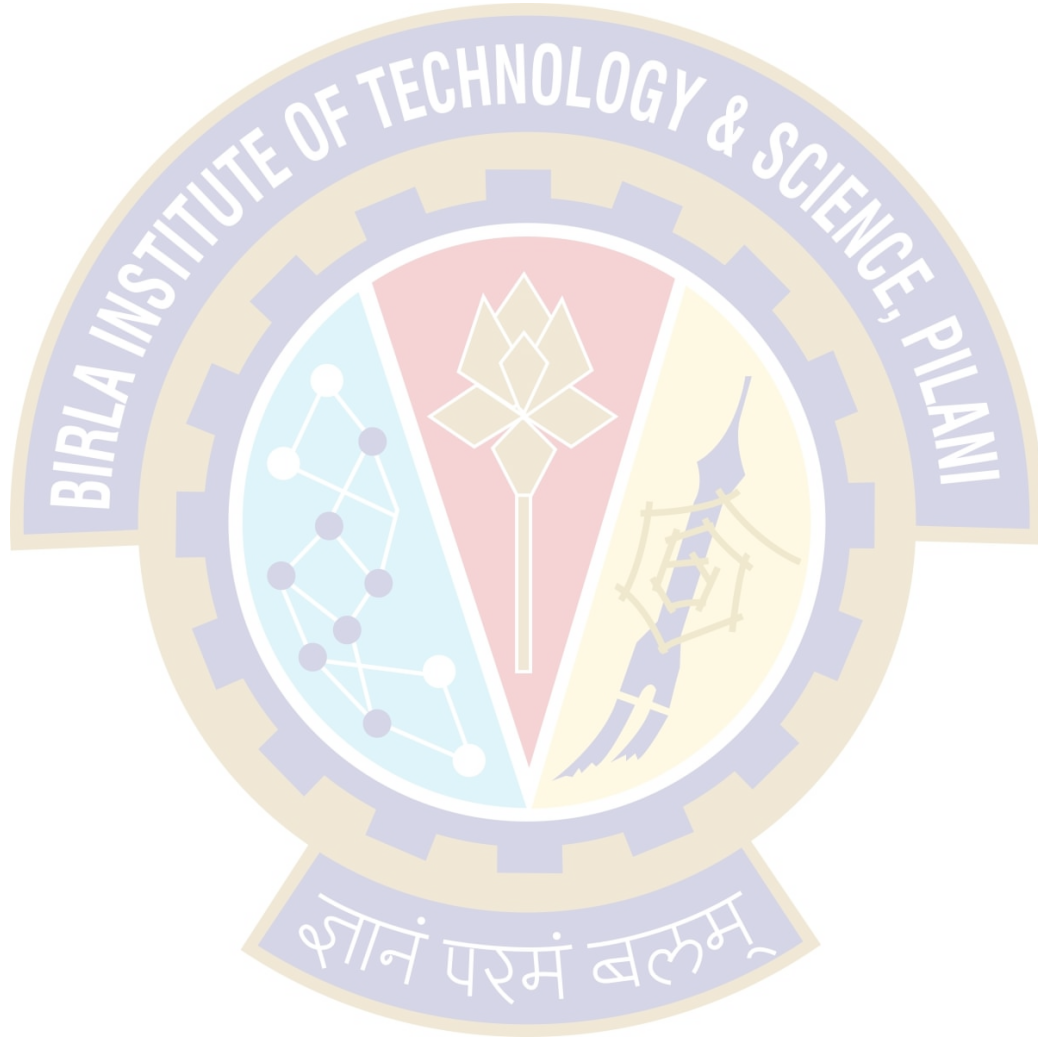
References

[1]   S. Tian *et al.*, "Aluminum nanocrystals: A sustainable substrate for quantitative SERS-Based DNA Detection," *Nano Lett.*, vol. 17, no. 8, pp. 5071–5077, 2017, doi: 10.1021/acs.nanolett.7b02338.

[2]   W. Li *et al.*, "Aluminum nanopyramid array with tunable ultraviolet-visible-infrared wavelength plasmon resonances for rapid detection of carbohydrate antigen 199," *Biosens. Bioelectron.*, vol. 79, pp. 500–507, 2016, doi: 10.1016/j.bios.2015.12.038.

[3]   X. Fu *et al.*, "High-sensitivity nanostructured aluminium ultrathin film sensors with spectral response from ultraviolet to near-infrared," *Phys. Scr.*, vol. 94, no. 5, 2019, doi: 10.1088/1402-4896/ab0a12.

[4]   W. Su, G. Zheng, and X. Li, "Design of a highly sensitive surface plasmon resonance sensor using aluminum-based diffraction grating," *Opt. Commun.*, vol. 285, no. 21–22, pp. 4603–4607, 2012, doi: 10.1016/j.optcom.2012.07.026.

[5]   P. Yang, H. Ye, and Z. M. Zhang, "Experimental Demonstration of the Effect of Magnetic Polaritons on the Radiative Properties of Deep Aluminum Gratings," *J. Heat Transfer*, vol. 141, no. 5, pp. 1–8, 2019, doi: 10.1115/1.4042698.

[6]   B. Y. Zheng, Y. Wang, P. Nordlander, and N. J. Halas, "Color-Selective and CMOS-Compatible Photodetection Based on Aluminum Plasmonics," *Adv. Mater.*, vol. 26, no. 36, pp. 6318–6323, 2014, doi: 10.1002/adma.201401168.

[7]   H. Xu, L. Wu, X. Dai, Y. Gao, and Y. Xiang, "An ultra-high sensitivity surface plasmon resonance sensor based on graphene-aluminum-graphene sandwich-like structure," *J. Appl. Phys.*, vol. 120, no. 5, pp. 1–6, 2016, doi: 10.1063/1.4959982.

[8]   K. B. Mogensen *et al.*, "Surface-enhanced Raman scattering on aluminum using near infrared and visible excitation," *Chem. Commun.*, vol. 50, no. 28, pp. 3744–3746, 2014, doi: 10.1039/c4cc00010b.

[9]   A. S. Lambert, S. N. Valiulis, A. S. Malinick, I. Tanabe, and Q. Cheng, "Plasmonic Biosensing with Aluminum Thin Films under the Kretschmann Configuration," *Anal. Chem.*, vol. 92, no. 13, pp. 8654–8659, 2020, doi: 10.1021/acs.analchem.0c01631.

[10]   E. Kretschmann and H. Raether, "Radiative Decay of Non Radiative Surface Plasmons Excited by Light," *Zeitschrift fur Naturforsch. - Sect. A J. Phys. Sci.*, vol. 23, no. 12, pp. 2135–2136, 1968, doi: 10.1515/zna-1968-1247.

[11]   N. Khansili, G. Rattu, and P. M. Krishna, "Label-free optical biosensors for food and biological sensor applications," *Sensors Actuators, B Chem.*, vol. 265, pp. 35–49, 2018, doi: 10.1016/j.snb.2018.03.004.

[12]   M. Minunni and A. R. Bilia, "SPR in drug discovery: searching bioactive compounds in plant extracts.," *Methods Mol. Biol.*, vol. 572, pp. 203–218, 2009, doi: 10.1007/978-1-60761-244-5_13.

[13]   H. Emami Nejad, A. Mir, and A. Farmani, "Supersensitive and Tunable Nano-Biosensor for Cancer Detection," *IEEE Sens. J.*, vol. 19, no. 13, pp. 4874–4881, 2019, doi: 10.1109/JSEN.2019.2899886.

[14]   P. Arora and D. O. F. Philosophy, "Colorimetric Sensors Using Hybrid Mode Plasmon Imaging for Refractive Index and Thickness Sensing," 2016.

[15]   N. K. Chaki and K. Vijayamohanan, "Self-assembled monolayers as a tunable platform for biosensor applications," *Biosens. Bioelectron.*, vol. 17, no. 1–2, pp. 1–12, 2002, doi: 10.1016/S0956-5663(01)00277-9.

[16]   D. T. Nurrohman, Y. Wang, and N. Chiu, "Exploring Graphene and MoS2 Chips Based Surface Plasmon Resonance Biosensors for Diagnostic Applications," *Front. Nanosci.*, vol. 8, pp. 1–17, 2020, doi: 10.3389/fchem.2020.00728.

[17]   B. D. Gupta, A. Pathak, and V. Semwal, "Carbon-based Nanomaterials for Plasmonic Sensors: A review," *Sensors*, vol. 19, no. 16, 2019, doi: 10.3390/s19163536.

[18]   R. González-Campuzano, J. M. Saniger, and D. Mendoza, "Plasmonic resonances in hybrid systems of aluminum nanostructured arrays and few layer graphene within the UV-IR spectral range," *Nanotechnology*, vol. 28, no. 46, 2017, doi: 10.1088/1361-6528/aa8ce4.

[19]   F. Siebert, "Infrared spectroscopy applied to biochemical and biological problems," *Methods Enzymol.*, vol. 246, no. C, pp. 501–526, 1995, doi: 10.1016/0076-6879(95)46022-5.

[20]   K. G. Chernov, T. A. Redchuk, E. S. Omelina, and V. V. Verkhusha, "Near-Infrared Fluorescent Proteins, Biosensors, and Optogenetic Tools Engineered from Phytochromes," *Chem. Rev.*, vol. 117, no. 9, pp. 6423–6446, 2017, doi: 10.1021/acs.chemrev.6b00700.

[21]   C. J. Powell and J. B. Swan, "Origin of the Characteristic Electron Energy Losses in Aluminum," *Phys. Rev.*, vol. 115, no. 4, pp. 869–875, 1959, doi: 10.1103/PhysRev.115.869.

[22]   R. D. Araguillin, L. C. Brazzano, L. I. Perez, and F. E. Veiras, "Design of reflectivity-based surface plasmon resonance optical sensors for ultrasound detection," *J. Mod. Opt.*, vol. 68, no. 13, pp. 689–698, 2021, doi: 10.1080/09500340.2021.1939898.

[23]   M. W. Knight, N. S. King, L. Liu, H. O. Everitt, P. Nordlander, and N. J. Halas, "Aluminum for plasmonics," *ACS Nano*, vol. 8, no. 1, pp. 834–840, 2014, doi: 10.1021/nn405495q.

[24]   R. Kumar, S. Pal, Y. K. Prajapati, S. Kumar, and J. P. Saini, "Sensitivity Improvement of a MXene-immobilized SPR Sensor with Ga-doped-ZnO for Biomolecules Detection," *IEEE Sens. J.*, 2022, doi: 10.1109/jsen.2022.3154099.

[25]   S. Ayas, A. E. Topal, A. Cupallari, H. Güner, G. Bakan, and A. Dana, "Exploiting Native Al2O3 for Multispectral Aluminum Plasmonics," *ACS Photonics*, vol. 1, no. 12, pp. 1313–1321, 2014, doi: 10.1021/ph500330x.

[26]   N. Zhao et al., "Wafer-scale 3D cloud-like aluminum hierarchical nanostructure for NIR SERS," *Opt. Mater. Express*, vol. 9, no. 8, p. 3546, 2019, doi: 10.1364/ome.9.003546.

[27]   J. Spettel et al., "Aluminium, gold-tin and titanium-tungsten alloys for mid-infrared plasmonic gratings," *Opt. Mater. Express*, vol. 11, no. 4, p. 1058, 2021, doi: 10.1364/ome.417877.

[28]   J. Martin, M. Kociak, Z. Mahfoud, J. Proust, D. Gérard, and J. Plain, "High-resolution imaging and spectroscopy of multipolar plasmonic resonances in aluminum nanoantennas," *Nano Lett.*, vol. 14, no. 10, pp. 5517–5523, 2014, doi: 10.1021/nl501850m.

[29]   J. Zhou, Y. Wang, L. Zhang, and X. Li, "Plasmonic biosensing based on non-noble-metal materials," *Chinese Chem. Lett.*, vol. 29, no. 1, pp. 54–60, 2018, doi: 10.1016/j.cclet.2017.09.003.

[30]   H. W. Liu et al., "Single-Crystalline Aluminum Nanostructures on a Semiconducting GaAs Substrate for Ultraviolet to Near-Infrared Plasmonics," *ACS Nano*, vol. 9, no. 4, pp. 3875–3886, 2015, doi: 10.1021/nn5070887.

[31]   W. Li, K. Ren, and J. Zhou, "Aluminum-based localized surface plasmon resonance for biosensing," *TrAC - Trends Anal. Chem.*, vol. 80, pp. 486–494, 2016, doi: 10.1016/j.trac.2015.08.013.

[32]   D. Gerard and S. K. Gray, "Aluminium plasmonics," *J. Phys. D. Appl. Phys.*, vol. 48, no. 18, p. 184001, 2015, doi: 10.1088/0022-3727/48/18/184001.

[33]   Y. Gutiérrez, R. A. de la Osa, D. Ortiz, J. M. Saiz, F. González, and F. Moreno, "Plasmonics in the Ultraviolet with Aluminum, Gallium, Magnesium and Rhodium," *Appl. Sci.*, vol. 8, pp. 1–14, 2018, doi: 10.3390/app8010064.

[34]   C. W. Cheng et al., "Epitaxial aluminum plasmonics covering full visible spectrum," *Nanophotonics*, vol. 10, no. 1, pp. 627–637, 2020, doi: 10.1515/nanoph-2020-0402.

[35]   M. W. Knight, N. S. King, L. Liu, H. O. Everitt, P. Nordlander, and N. J. Halas, "Aluminum for Plasmonics," no. 1, pp. 834–840, 2014.

[36]   R. Ziblat, V. Lirtsman, D. Davidov, and B. Aroeti, "Infrared Surface Plasmon Resonance: A Novel Tool for Real Time Sensing of Variations in Living Cells," *Biophys. J.*, vol. 90, no. 7, pp. 2592–2599, 2006, doi: 10.1529/biophysj.105.072090.

[37]   M. Salemizadeh, F. F. Mahani, and A. Mokhtari, "Design of aluminum-based nanoring arrays for realizing efficient plasmonic sensors," *J. Opt. Soc. Am. B*, vol. 36, no. 3, pp. 786–793, 2019, doi: 10.1364/josab.36.000786.

[38]   J. Proust, S. Schuermans, J. Martin, D. Gérard, T. Maurer, and J. Plain, "Synthesis of aluminum nanoparticles for UV plasmonics," in *Conference on Lasers and Electro-Optics, CLEO 2013*, 2013, pp. 11–12, doi: 10.1364/cleo_at.2013.jtu4a.58.

[39]   Z. Yan et al., "Multipolar Plasmonic Resonances of Aluminum Nanoantenna Tuned by Graphene," *Nanomaterials*, vol. 11, no. 1, pp. 1–9, 2021, doi: 10.3390/nano11010185.

110

[40] J. Hu *et al.*, "Deep-ultraviolet-blue-light surface plasmon resonance of Al and Al core/Al 2O 3shell in spherical and cylindrical nanostructures," *J. Phys. Chem. C*, vol. 116, no. 29, pp. 15584–15590, 2012, doi: 10.1021/jp305844g.

[41] M. B. Ross and G. C. Schatz, "Aluminum and Indium Plasmonic Nanoantennas in the Ultraviolet," *J. Phys. Chem. C*, vol. 118, no. 23, pp. 12506–12514, 2014, doi: 10.1021/jp503323u.

[42] G. Maidecchi *et al.*, "Deep Ultraviolet Plasmon Resonance in Aluminum Nanoparticle Arrays," *ACS Nano*, vol. 7, no. 7, pp. 5834–5841, 2013, doi: 10.1021/nn400918n.

[43] H. D. Robinson, L. Neely, C. Y. Jao, and V. Kochergin, "Enhanced absorption in organic semiconductors with embedded aluminum nanoparticles," *IEEE Photonic Soc. 24th Annu. Meet. PHO 2011*, vol. 2, pp. 863–864, 2011, doi: 10.1109/PHO.2011.6110831.

[44] J. Katyal and V. Badoni, "Localized surface plasmon resonance and field enhancement of Au, Ag, Al and Cu nanoparticles having isotropic and anisotropic nanostructure," *Mater. Today Proc.*, vol. 44, pp. 5012–5017, 2020, doi: 10.1016/j.matpr.2021.01.027.

[45] J. Zhu, J. J. Li, and J. W. Zhao, "A computational study of the double-bands plasmonic light scattering of Al2O3 coated Al nanoshells in the deep-ultraviolet range," *Appl. Surf. Sci.*, vol. 314, pp. 145–150, 2014, doi: 10.1016/j.apsusc.2014.06.129.

[46] T. F. Villesen, C. Uhrenfeldt, B. Johansen, J. L. Hansen, H. U. Ulriksen, and A. N. Larsen, "Aluminum nanoparticles for plasmon-improved coupling of light into silicon," *Nanotechnology*, vol. 23, no. 8, 2012, doi: 10.1088/0957-4484/23/8/085202.

[47] Y. Yang, R. G. Hobbs, P. D. Keathley, and K. K. Berggren, "Electron energy loss of ultraviolet plasmonic modes in aluminum nanodisks," *Opt. Express*, vol. 28, no. 19, pp. 27405–27409, 2020, doi: 10.1364/oe.401835.

[48] J. Katyal and R. K. Soni, "Size- and shape-dependent plasmonic properties of aluminum nanoparticles for nanosensing applications," *J. Mod. Opt.*, vol. 60, no. 20, pp. 1717–1728, 2013, doi: 10.1080/09500340.2013.856483.

[49] J. Katyal and R. K. Soni, "Field Enhancement Around Al Nanostructures in the DUV – Visible Region," pp. 1729–1740, 2015, doi: 10.1007/s11468-015-9991-5.

[50] Q. Chen and D. R. S. Cumming, "High transmission and low color cross-talk plasmonic color filters using triangular-lattice hole arrays in aluminum films," *Opt. Express*, vol. 18, no. 13, p. 14056, 2010, doi: 10.1364/oe.18.014056.

[51] V. Kulkarni, E. Prodan, and P. Nordlander, "Quantum Plasmonics: Optical Properties of a Nanomatryushka," *Nano Lett.*, vol. 13, no. 12, pp. 5873–5879, 2013, doi: 10.1021/nl402662e.

[52] S. Ramadurgam, T. G. Lin, and C. Yang, "Aluminum plasmonics for enhanced visible light absorption and high efficiency water splitting in core-multishell nanowire photoelectrodes with ultrathin hematite shells," *Nano Lett.*, vol. 14, no. 8, pp. 4517–4522, 2014, doi: 10.1021/nl501541s.

[53] D. Lehr *et al.*, "Plasmonic properties of aluminum nanorings generated by double patterning," *Opt. Lett.*, vol. 37, no. 2, p. 157, 2012, doi: 10.1364/ol.37.000157.

[54] A. Ziashahabi and R. Poursalehi, "Optical Properties of Al@Al2O3 Nanorod as a UV and Visible Wavelengths Plasmonic Nanostructure," *Procedia Mater. Sci.*, vol. 11, pp. 743–748, 2015, doi: 10.1016/j.mspro.2015.11.066.

[55] B. D. Clark *et al.*, "Aluminum Nanorods," *Nano Lett.*, vol. 18, no. 2, pp. 1234–1240, 2018, doi: 10.1021/acs.nanolett.7b04820.

[56] R. Gillibert, F. Colas, R. Yasukuni, G. Picardi, and M. L. De La Chapelle, "Plasmonic Properties of Aluminum Nanocylinders in the Visible Range," *J. Phys. Chem. C*, vol. 121, no. 4, pp. 2402–2409, 2017, doi: 10.1021/acs.jpcc.6b11779.

[57] F. Zhang, J. Martin, and J. Plain, "Long-term stability of plasmonic resonances sustained by evaporated aluminum nanostructures," *Opt. Mater. Express*, vol. 9, no. 1, pp. 85–93, 2019, doi: 10.1364/ome.9.000085.

[58] F. Fouladi Mahani, A. Mokhtari, and M. Mehran, "Design and development of aluminum nanoring arrays for realization of dual-mode operation plasmonic color filters," *J. Opt. Soc. Am. B*, vol. 35, no. 8, p. 1764, 2018, doi: 10.1364/josab.35.001764.

[59]   F. A. Said *et al.*, "FDTD analysis of structured metallic nanohole films for LSPR-based biosensor," in *RSM 2015 - 2015 IEEE Regional Symposium on Micro and Nano Electronics, Proceedings*, 2015, pp. 0–3, doi: 10.1109/RSM.2015.7355024.

[60]   M. G. Blaber, M. D. Arnold, N. Harris, M. J. Ford, and M. B. Cortie, "Plasmon absorption in nanospheres: A comparison of sodium, potassium, aluminium, silver and gold," *Phys. B Condens. Matter*, vol. 394, no. 2, pp. 184–187, 2007, doi: 10.1016/j.physb.2006.12.011.

[61]   N. K. Pathak, Parthasarathi, P. S. Kumar, and R. P. Sharma, "Tuning of the surface plasmon resonance of aluminum nanoshell near-infrared regimes," *Phys. Chem. Chem. Phys.*, vol. 21, no. 18, pp. 9441–9449, 2019, doi: 10.1039/c9cp01115c.

[62]   S. Bhardwaj, R. Uma, and R. P. Sharma, "A Study of Metal@Graphene Core–Shell Spherical Nano-Geometry to Enhance the SPR Tunability: Influence of Graphene Monolayer Shell Thickness," *Plasmonics*, vol. 12, no. 4, pp. 961–969, 2017, doi: 10.1007/s11468-016-0347-6.

[63]   J. Liu, B. Cankurtaran, G. McCredie, M. J. Ford, L. Wieczorek, and M. B. Cortie, "Investigation of the optical properties of hollow aluminium 'nano-caps,'" *Nanotechnology*, vol. 16, no. 12, pp. 3023–3028, 2005, doi: 10.1088/0957-4484/16/12/049.

[64]   B. Wang, S. C. Singh, H. Lu, and C. Guo, "Design of Aluminum Bowtie Nanoantenna Array with Geometrical Control to Tune LSPR from UV to Near-IR for Optical Sensing," *Plasmonics*, vol. 15, no. 3, pp. 609–621, 2020, doi: 10.1007/s11468-019-01071-z.

[65]   C. Langhammer, M. Schwind, B. Kasemo, and I. Zorić, "Localized surface plasmon resonances in aluminum nanodisks," *Nano Lett.*, vol. 8, no. 5, pp. 1461–1471, 2008, doi: 10.1021/nl080453i.

[66]   G. Jia and C. Guo, "Interband-transition-modified third-order nonlinear optical properties of Al nanoshells in carbon disulfide," *RSC Adv.*, vol. 6, no. 12, pp. 10038–10043, 2016, doi: 10.1039/c5ra25981a.

[67]   S. Ambardar, D. Nguyen, G. Binder, Z. W. Withers, and D. V. Voronine, "Quantum leap from gold and silver to aluminum nanoplasmonics for enhanced biomedical applications," *Appl. Sci.*, vol. 10, no. 12, pp. 1–28, 2020, doi: 10.3390/APP10124210.

[68]   M. H. Chowdhury, K. Ray, and J. R. Lakowicz, "Use of aluminum films as substrates for enhanced fluorescence in the ultraviolet-blue spectral region.," *Plasmon. Biol. Med. V*, vol. 6869, p. 68690E, 2008, doi: 10.1117/12.760724.

[69]   I. Tanabe *et al.*, "Far- and deep-ultraviolet surface plasmon resonance sensors working in aqueous solutions using aluminum thin films," *Sci. Rep.*, vol. 7, no. 1, pp. 1–7, 2017, doi: 10.1038/s41598-017-06403-9.

[70]   D. V. Nesterenko and Z. Sekkat, "Resolution Estimation of the Au, Ag, Cu, and Al Single- and Double-Layer Surface Plasmon Sensors in the Ultraviolet, Visible, and Infrared Regions," *Plasmonics*, vol. 8, no. 4, pp. 1585–1595, 2013, doi: 10.1007/s11468-013-9575-1.

[71]   K. M. McPeak *et al.*, "Plasmonic films can easily be better: Rules and recipes," *ACS Photonics*, vol. 2, no. 3, pp. 326–333, 2015, doi: 10.1021/ph5004237.

[72]   A. V. Krasavin, K. F. MacDonald, A. S. Schwanecke, and N. I. Zheludev, "Gallium/aluminum nanocomposite material for nonlinear optics and nonlinear plasmonics," *Appl. Phys. Lett.*, vol. 89, no. 3, pp. 2004–2007, 2006, doi: 10.1063/1.2234276.

[73]   A. Sobhani *et al.*, "Pronounced Linewidth Narrowing of an Aluminum Nanoparticle Plasmon Resonance by Interaction with an Aluminum Metallic Film," *Nano Lett.*, vol. 15, no. 10, pp. 6946–6951, 2015, doi: 10.1021/acs.nanolett.5b02883.

[74]   M. Kumar, K. B. Thapa, and P. Singh, " Long-range surface plasmon resonance biosensors with cytop/Al/Perovskite and cytop/Al/MoS 2 configurations ," *Phys. Scr.*, vol. 97, no. 5, p. 055501, 2022, doi: 10.1088/1402-4896/ac5e5b.

[75]   S. R. K. Rodriguez, M. C. Schaafsma, A. Berrier, and J. Gmez Rivas, "Collective resonances in plasmonic crystals: Size matters," *Phys. B Condens. Matter*, vol. 407, no. 20, pp. 4081–4085, 2012, doi: 10.1016/j.physb.2012.03.053.

[76]   P. K. Maharana, T. Srivastava, and R. Jha, "On the Performance of Highly Sensitive and Accurate Graphene-on-Aluminum and Silicon-Based SPR Biosensor for Visible and Near Infrared," *Plasmonics*, vol. 9, no. 5, pp. 1113–1120, 2014, doi: 10.1007/s11468-014-9721-4.

[77]   A. Bijalwan and V. Rastogi, "Gold–aluminum-based surface plasmon resonance sensor with a high quality factor and figure of merit for the detection of hemoglobin," *Appl. Opt.*, vol. 57, no. 31, pp. 9230–9237, 2018, doi: 10.1364/ao.57.009230.

[78]   A. Bijalwan and V. Rastogi, "Design and Simulation of a Palladium-Aluminum Nanostructure-Based Hydrogen Sensor With Improved Figure of Merit," *IEEE Sens. J.*, vol. 19, no. 15, pp. 6112–6118, 2019, doi: 10.1109/JSEN.2019.2909349.

[79]   L. C. Oliveira, A. Herbster, C. S. Moreira, H. F. Neff, and A. M. N. Lima, "Surface Plasmon Resonance Sensing Characteristics of Thin Aluminum Films in Aqueous Solution," *IEEE Sens. J.*, vol. 17, no. 19, pp. 6258–6267, 2017, doi: 10.1109/JSEN.2020.2980388.

[80]   G. Albrecht, M. Ubl, S. Kaiser, H. Giessen, and M. Hentschel, "Comprehensive Study of Plasmonic Materials in the Visible and Near-Infrared: Linear, Refractory, and Nonlinear Optical Properties," *ACS Photonics*, vol. 5, no. 3, pp. 1058–1067, 2018, doi: 10.1021/acsphotonics.7b01346.

[81]   K. L. Lee *et al.*, "Highly Sensitive Aluminum-Based Biosensors using Tailorable Fano Resonances in Capped Nanostructures," *Sci. Rep.*, vol. 7, pp. 1–14, 2017, doi: 10.1038/srep44104.

[82]   J. Martin *et al.*, "Aluminum nanostructures for ultraviolet plasmonics," in *Proceedings of SPIE*, 2017, no. August, p. 12, doi: 10.1117/12.2274970.

[83]   Y. H. Chou *et al.*, "Metal for Plasmonic Ultraviolet Laser: Al or Ag?," *IEEE J. Sel. Top. Quantum Electron.*, vol. 23, no. 6, 2017, doi: 10.1109/JSTQE.2017.2748521.

[84]   C. L. Lay *et al.*, "Aluminum nanostructures with strong visible-range SERS activity for versatile micropatterning of molecular security labels," *Nanoscale*, vol. 10, no. 2, pp. 575–581, 2018, doi: 10.1039/c7nr07793a.

[85]   M. L. Tseng, J. Yang, M. Semmlinger, C. Zhang, P. Nordlander, and N. J. Halas, "Two-Dimensional Active Tuning of an Aluminum Plasmonic Array for Full-Spectrum Response," *Nano Lett.*, vol. 17, no. 10, pp. 6034–6039, 2017, doi: 10.1021/acs.nanolett.7b02350.

[86]   D. Franklin, M. George, J. Fraser, and D. Chanda, "Atomic Layer Deposition Tuning of Subwavelength Aluminum Grating for Angle-Insensitive Plasmonic Color," *ACS Appl. Nano Mater.*, vol. 1, no. 9, pp. 5210–5216, 2018, doi: 10.1021/acsanm.8b01147.

[87]   P. N. Melentiev *et al.*, "Single nano-hole as a new effective nonlinear element for third-harmonic generation," *Laser Phys. Lett.*, vol. 10, no. 7, 2013, doi: 10.1088/1612-2011/10/7/075901.

[88]   A. J. Hughes, D. Jones, and A. H. Lettington, "Calculation of the optical properties of aluminium," *J. Phys. C Solid State Phys.*, vol. 2, no. 1, pp. 102–103, 1969, doi: 10.1088/0022-3719/2/1/313.

[89]   R. Audhkhasi and M. L. Povinelli, "Design of aluminum-based hybrid gratings with predefined infrared spectral response," *Opt. InfoBase Conf. Pap.*, no. c, pp. 8–9, 2020, doi: 10.1364/FIO.2020.FTh5C.2.

[90]   L. Wu *et al.*, "Sensitivity Improved SPR Biosensor Based on the MoS2/Graphene-Aluminum Hybrid Structure," *J. Light. Technol.*, vol. 35, no. 1, pp. 82–87, 2017, doi: 10.1109/JLT.2016.2624982.

[91]   A. Bijalwan and V. Rastogi, "Design Analysis of Refractive Index Sensor with High Quality Factor Using Au-Al2O3 Grating on Aluminum," *Plasmonics*, vol. 13, no. 6, pp. 1995–2000, 2018, doi: 10.1007/s11468-018-0715-5.

[92]   C. Hu and D. Liu, "High-performance Grating Coupled Surface Plasmon Resonance Sensor Based on Al-Au Bimetallic Layer," *Mod. Appl. Sci.*, vol. 4, no. 6, pp. 8–13, 2010, doi: 10.5539/mas.v4n6p8.

[93]   S. Shukla and P. Arora, "Design and Analysis of Aluminum-Silicon-Graphene Based Plasmonic Device for Biosensing Applications in the Optical Communication Band," *Silicon*, 2021, doi: 10.1007/s12633-021-00953-4.

[94]   A. K. Pandey and A. K. Sharma, "Simulation and analysis of plasmonic sensor in NIR with fluoride glass and graphene layer," *Photonics Nanostructures - Fundam. Appl.*, vol. 28, pp. 94–99, 2018, doi: 10.1016/j.photonics.2017.12.003.

[95]   S. Shukla, V. Venkatesh, and P. Arora, "Highly sensitive self-referenced plasmonic devices based on engineered periodic nanostructures for sensing in the communication band," *J. Opt. Eng.*, vol. 59, no. 6, pp. 65101–65108, 2020, doi: 10.1117/1.OE.59.6.065101.

113

[96] P. K. Maharana and R. Jha, "Chalcogenide prism and graphene multilayer based surface plasmon resonance affinity biosensor for high performance," *Sensors Actuators B. Chem.*, vol. 169, pp. 161–166, 2012.

[97] I. H. Malitson, "A Redetermination of Some Optical Properties of Calcium Fluoride," *Appl. Opt.*, vol. 2, no. 11, pp. 1103–1107, 1963.

[98] Y. Kim and M. Kwon, "Electroabsorption modulator based on inverted-rib-type silicon waveguide including double graphene layers," *J. Opt.*, vol. 19, no. 045804, pp. 1–9, 2017.

[99] L. Zhang, L. Tang, W. Wei, X. Cheng, W. Wang, and H. Zhang, "Enhanced near-infrared absorption in graphene with multilayer metal-dielectric -metal nanostructure," *Opt. Express*, vol. 24, no. 18, pp. 1–8, 2016.

[100] M. Mohsin *et al.*, "Experimental verification of electro-refractive phase modulation in graphene," *Sci. Rep.*, vol. 5, pp. 1–7, 2015, doi: 10.1038/srep10967.

[101] H. Shu *et al.*, "Significantly High Modulation Efficiency of Compact Graphene Modulator Based on Silicon Waveguide," *Sci. Rep.*, vol. 8, no. 1, pp. 1–8, 2018, doi: 10.1038/s41598-018-19171-x.

[102] L. Wu, H. S. Chu, W. S. Koh, and E. P. Li, "Highly sensitive graphene biosensors based on surface plasmon resonance," *Opt. Express*, vol. 18, no. 14, pp. 14395–14400, 2010, doi: 10.1364/oe.18.014395.

[103] P. Bhatia and B. D. Gupta, "Surface plasmon resonance based fiber optic refractive index sensor : sensitivity enhancement," *Appl. Opt.*, vol. 50, no. 14, pp. 2032–2036, 2011.

[104] A. Panda, P. Devi, and P. Gerd, "Performance analysis of graphene - based surface plasmon resonance biosensor for blood glucose and gas detection," *Appl. Phys. A*, vol. 126, no. 3, pp. 1–12, 2020, doi: 10.1007/s00339-020-3328-8.

[105] A. Shalabney and I. Abdulhalim, "Electromagnetic fields distribution in multilayer thin film structures and the origin of sensitivity enhancement in surface plasmon resonance sensors," *Sensors Actuators, A Phys.*, vol. 159, no. 1, pp. 24–32, 2010, doi: 10.1016/j.sna.2010.02.005.

[106] S. Chen and C. Lin, "Sensitivity comparison of graphene based surface plasmon resonance biosensor with Au , Ag and Cu in the visible region," *Mater. Res. Express*, vol. 6, no. 056503, pp. 1–8, 2019.

[107] P. K. Maharana, R. Jha, and S. Palei, "Sensitivity enhancement by air mediated graphene multilayer based surface plasmon resonance biosensor for near infrared," *Sensors Actuators, B Chem.*, vol. 190, pp. 494–501, 2014, doi: 10.1016/j.snb.2013.08.089.

[108] A. Lahav, A. Shalabaney, and I. Abdulhalim, "Surface plasmon sensor with enhanced sensitivity using top nano dielectric layer," *J. Nanophotonics*, vol. 3, no. 031501, pp. 1–14, 2009, doi: 10.1117/1.3079803.

[109] H. Fu, S. Zhang, H. Chen, and J. Weng, "Graphene Enhances the Sensitivity of Fiber-Optic Surface Plasmon Resonance Biosensor," *IEEE Sens. J.*, vol. 15, no. 10, pp. 5478–5482, 2015.

[110] M. S. Rahman, M. R. Hasan, K. A. Rikta, and M. S. Anower, "A novel graphene coated surface plasmon resonance biosensor with tungsten disulfide (WS2) for sensing DNA hybridization," *Opt. Mater. (Amst).*, vol. 75, pp. 567–573, 2018, doi: 10.1016/j.optmat.2017.11.013.

[111] C. H. Gan, "Analysis of surface plasmon excitation at terahertz frequencies with highly doped graphene sheets via attenuated total reflection," *Appl. Phys. Lett.*, vol. 101, no. 111609, pp. 1–4, 2012.

[112] F. J. Bezares *et al.*, "Intrinsic Plasmon − Phonon Interactions in Highly Doped Graphene: A Near-Field Imaging Study," *Nano Lett.*, vol. 17, pp. 5908–5913, 2017, doi: 10.1021/acs.nanolett.7b01603.

[113] A. Hoggard *et al.*, "Using the Plasmon Linewidth To Calculate the Time and Efficiency of Electron Transfer between Gold Nanorods and Graphene," *ACS Nano*, vol. 7, no. 12, pp. 11209–11217, 2013, doi: 10.1021/nn404985h.

[114] T. M. Wijesinghe, M. Permarante, and G. P. Agarwal, "Low-loss dielectric-loaded graphene surface plasmon polariton waveguide based biochemical sensor," *J. Appl. Phys.*, vol. 117, no. 213105, pp. 1–10, 2015, doi: 10.1063/1.4922124.

[115] S. Raikwar, Y. K. Prajapati, D. K. Srivastava, J. B. Maurya, and J. P. Saini, "Detection of Leptospirosis Bacteria in Rodent Urine by Surface Plasmon Resonance Sensor Using Graphene," *Photonics Sensors*, vol. 11, no. 3, pp. 305–313, 2021, doi: 10.1007/s13320-020-0587-2.

[116]   Y. F. Kitagawa, T. Takahashi, and H. Hayashi, "Relationship between the refractive index and specific gravity of the rat urine," *Exp. Anim.*, vol. 30, no. 3, pp. 307–311, 1981.

[117]   J. Li *et al.*, "Revisiting the surface sensitivity of nanoplasmonic biosensors," *ACS Photonics*, vol. 2, no. 3, pp. 425–431, 2015, doi: 10.1021/ph5004779.

[118]   R. Verma, B. D. Gupta, and R. Jha, "Sensitivity enhancement of a surface plasmon resonance based biomolecules sensor using graphene and silicon layers," *Sensors Actuators, B Chem.*, vol. 160, no. 1, pp. 623–631, 2011, doi: 10.1016/j.snb.2011.08.039.

[119]   A. Verma, A. Prakash, and R. Tripathi, "Performance analysis of graphene based surface plasmon resonance biosensors for detection of pseudomonas-like bacteria," *Opt. Quant Electron.*, vol. 47, no. 5, pp. 1197–1205, 2015, doi: 10.1007/s11082-014-9976-1.

[120]   A. Verma, A. Prakash, and R. Tripathi, "Sensitivity enhancement of surface plasmon resonance biosensor using graphene and air gap," *Opt. Commun.*, vol. 357, pp. 106–112, 2015, doi: 10.1016/j.optcom.2015.08.076.

[121]   G. A. Ermolaev *et al.*, "Broadband optical properties of monolayer and bulk MoS2," *npj 2D Mater. Appl.*, vol. 4, no. 1, pp. 1–6, 2020, doi: 10.1038/s41699-020-0155-x.

[122]   A. K. Sharma and A. K. Pandey, "Blue Phosphorene / MoS 2 Heterostructure Based SPR Sensor With Enhanced Sensitivity," *IEEE Photonics Technol. Lett.*, vol. 30, no. 7, pp. 595–598, 2018.

[123]   J. B. Maurya and Y. K. Prajapati, "A comparative study of different metal and prism in the surface plasmon resonance biosensor having MoS2-graphene," *Opt. Quantum Electron.*, vol. 48, no. 5, pp. 1–12, 2016, doi: 10.1007/s11082-016-0562-6.

[124]   A. K. Sharma and B. Kaur, "Simulation and analysis of 2D material (MoS2 / MoSe2) based plasmonic sensor for measurement of organic compounds in infrared," *Optik (Stuttg).*, vol. 157, pp. 161–169, 2018, doi: 10.1016/j.ijleo.2017.11.067.

[125]   J. B. Maurya, Y. K. Prajapati, V. Singh, J. P. Saini, and R. Tripathi, "Improved performance of the surface plasmon resonance biosensor based on graphene or MoS 2 using silicon," *Opt. Commun.*, vol. 359, pp. 426–434, 2016, doi: 10.1016/j.optcom.2015.10.010.

[126]   X. Zhu, Y. Zhang, M. Liu, and Y. Liu, "2D titanium carbide MXenes as emerging optical biosensing platforms," *Biosens. Bioelectron.*, vol. 171, 2021, doi: 10.1016/j.bios.2020.112730.

[127]   D. Zhang, D. Shah, A. Boltasseva, and Y. Gogotsi, "MXenes for Photonics," *ACS Photonics*, vol. 9, no. 4, pp. 1108–1116, 2022, doi: 10.1021/acsphotonics.2c00040.

[128]   R. Kumar, S. Pal, A. Verma, Y. K. Prajapati, and J. P. Saini, "Effect of silicon on sensitivity of SPR biosensor using hybrid nanostructure of black phosphorus and MXene," *Superlattices Microstruct.*, vol. 145, 2020, doi: 10.1016/j.spmi.2020.106591.

[129]   R. Kumar, S. Pal, Y. K. Prajapati, S. Kumar, and J. P. Saini, "Sensitivity Improvement of a MXene- Immobilized SPR Sensor With Ga-Doped-ZnO for Biomolecules Detection," *IEEE Sens. J.*, vol. 22, no. 7, pp. 6536–6543, 2022, doi: 10.1109/JSEN.2022.3154099.

[130]   L. Wu, Q. You, Y. Shan, S. Gan, Y. Zhao, and X. Dai, "Few-layer Ti3C2Tx MXene : A promising surface plasmon resonance biosensing material to enhance the sensitivity," *Sensors Actuators B. Chem.*, vol. 277, pp. 210–215, 2018, doi: 10.1016/j.snb.2018.08.154.

[131]   S. Pal, A. Verma, and Y. K. P. J. P. Saini, "Sensitive detection using heterostructure of black phosphorus , transition metal di - chalcogenides and MXene in SPR sensor," *Appl. Phys. A*, vol. 126, no. 809, pp. 1–10, 2020, doi: 10.1007/s00339-020-03998-1.

[132]   P. Zhang, J. Wang, G. Chen, J. Shen, C. Li, and T. Tang, "A high-sensitivity SPR sensor with Bimetal/Silicon/Two-Dimensional Material Structure: A Theoretical Analysis," *Photonics*, vol. 8, no. 7, 2021, doi: 10.3390/photonics8070270.

[133]   A. Srivastava, A. Verma, R. Das, and Y. K. Prajapati, "A theoretical approach to improve the performance of SPR biosensor using MXene and black phosphorus," *Opt. - Int. J. Light Electron Opt.*, vol. 203, 2020, doi: 10.1016/j.ijleo.2019.163430.

115

[134] Vikas and R. K. Verma, "On the application of few layer Ti 3C 2 MXene on fiber optic SPR sensor for performance enhancement," *Eur. Phys. J. D*, vol. 75, no. 5, pp. 1–11, 2021, doi: 10.1140/epjd/s10053-020-00020-4.

[135] X. Wu, F. Tan, S. Cheng, Y. Chang, X. Wang, and L. Chen, "Investigation of interaction between MXene nanosheets and human plasma and protein corona composition," *Nanoscale*, vol. 14, no. 10, pp. 3777–3787, 2022, doi: 10.1039/d1nr08548d.

[136] S. Asgari, N. Granpayeh, and T. Fabritius, "Controllable terahertz cross-shaped three-dimensional graphene intrinsically chiral metastructure and its biosensing application," *Opt. Commun.*, vol. 474, no. February, p. 126080, 2020, doi: 10.1016/j.optcom.2020.126080.

[137] X. Chen *et al.*, "Recent Advances in Fluorinated Graphene from Synthesis to Applications: Critical Review on Functional Chemistry and Structure Engineering," *Adv. Mater.*, vol. 34, no. 1, pp. 1–44, 2022, doi: 10.1002/adma.202101665.

[138] P. S. Pandey, Y. Singh, and S. K. Raghuwanshi, "Theoretical analysis of the LRSPR sensor with Enhance FOM for Low Refractive Index Detection using MXene and Fluorinated Graphene," *IEEE Sens. J.*, vol. 21, no. 21, pp. 23979–23986, 2021, doi: 10.1109/JSEN.2021.3112530.

[139] J. Zou *et al.*, "Plasmonic MXene Nanoparticle-Enabled High-Performance Two-Dimensional MoS(2) Photodetectors.," *ACS Appl. Mater. Interfaces*, vol. 14, no. 6, pp. 8243–8250, Feb. 2022, doi: 10.1021/acsami.1c22074.

[140] T. Srivastava and R. Jha, "Black Phosphorus: A New Platform for Gaseous Sensing Based on Surface Plasmon Resonance," *IEEE Photonics Technol. Lett.*, vol. 30, no. 4, pp. 319–322, 2018, doi: 10.1109/LPT.2017.2787057.

[141] R. Kumar, S. Pal, N. Pal, A. Verma, J. P. Saini, and Y. K. Prajapati, "Figure of merit enhancement of Ti3C2Tx-graphene based long-range surface plasmon sensor at telecommunication wavelength," *Opt. Quantum Electron.*, vol. 53, pp. 1–15, 2021, doi: 10.1007/s11082-021-02862-7.

[142] X. Dai, C. Song, C. Qiu, L. Wu, and Y. Xiang, "Theoretical Investigation of Multilayer Ti3C2Tx MXene as the Plasmonic Material for Surface Plasmon Resonance Sensors in Near Infrared Region," *IEEE Sens. J.*, vol. 19, no. 24, pp. 11834–11838, 2019, doi: 10.1109/JSEN.2019.2937843.

[143] G. R. Berdiyorov, "Optical properties of functionalized Ti3C2T2 (T = F, O, OH) MXene: First-principles calculations," *AIP Adv.*, vol. 6, no. 5, 2016, doi: 10.1063/1.4948799.

[144] S. J. Kim *et al.*, "Metallic Ti3C2Tx MXene Gas Sensors with Ultrahigh Signal-to-Noise Ratio," *ACS Nano*, vol. 12, no. 2, pp. 986–993, 2018, doi: 10.1021/acsnano.7b07460.

[145] A. M. Ross, G. M. Paternò, S. Dal Conte, F. Scotognella, and E. Cinquanta, "Anisotropic Complex Refractive Indices of Atomically Thin Materials: Determination of the optical constants of Few-Layer Black Phosphorus," *Materials (Basel).*, vol. 13, no. 24, pp. 1–12, 2020, doi: 10.3390/ma13245736.

[146] S. Shukla and P. Arora, "Design and comparative analysis of aluminum-MoS2 based plasmonic devices with enhanced sensitivity and Figure of Merit for biosensing applications in the near-infrared region," *Optik (Stuttg).*, vol. 228, 2021, doi: 10.1016/j.ijleo.2020.166196.

[147] L. Zhao *et al.*, "Highly-stable polymer-crosslinked 2D MXene-based flexible biocompatible electronic skins for in vivo biomonitoring," *Nano Energy*, vol. 84, no. December 2020, 2021, doi: 10.1016/j.nanoen.2021.105921.

[148] H. Riazi, G. Taghizadeh, and M. Soroush, "MXene-Based Nanocomposite Sensors," *ACS Omega*, vol. 6, no. 17, pp. 11103–11112, 2021, doi: 10.1021/acsomega.0c05828.

[149] Y. Chae *et al.*, "An investigation into the factors governing the oxidation of two-dimensional Ti3C2 MXene," *Nanoscale*, vol. 11, no. 17, pp. 8387–8393, 2019, doi: 10.1039/c9nr00084d.

[150] Y. Jinho, S. Minkyu, L. Joungpyo, L. Ji-Young, and C. Jeong-Woo, "Recent Advances in MXene," *Biosensors*, vol. 10, no. 11, 2020.

[151] A. K. Pandey, "Graphene–Ti3C2Tx MXene hybrid nanostructure: a promising material for sensitivity enhancement in plasmonic sensor," *Appl. Phys. A Mater. Sci. Process.*, vol. 127, no. 2, pp. 1–6, 2021, doi: 10.1007/s00339-020-04235-5.

[152] H. Li, P. Lian, Q. Lu, J. Chen, R. Hou, and Y. Mei, "Excellent air and water stability of two-dimensional black phosphorene/MXene heterostructure," *Mater. Res. Express*, vol. 6, no. 6, 2019, doi: 10.1088/2053-1591/ab0b84.

[153] S. Ganorkar, J. Kim, Y. H. Kim, and S. Il Kim, "Effect of precursor on growth and morphology of MoS2 monolayer and multilayer," *J. Phys. Chem. Solids*, vol. 87, pp. 32–37, 2015, doi: 10.1016/j.jpcs.2015.07.016.

[154] Y. Ahmad, N. Batisse, X. Chen, and M. Dubois, "Preparation and Applications of Fluorinated Graphenes," *C*, vol. 7, no. 1, p. 20, 2021, doi: 10.3390/c7010020.

[155] M. I. Kairi, M. Khavarian, S. A. Bakar, B. Vigolo, and A. R. Mohamed, "Recent trends in graphene materials synthesized by CVD with various carbon precursors," *J. Mater. Sci.*, vol. 53, no. 2, pp. 851–879, 2018, doi: 10.1007/s10853-017-1694-1.

[156] O. A. Abd El-Aziz, H. A. Elsayed, and M. I. Sayed, "One-dimensional defective photonic crystals for the sensing and detection of protein," *Appl. Opt.*, vol. 58, no. 30, p. 8309, 2019, doi: 10.1364/ao.58.008309.

[157] R. Kumar, S. Pal, Y. K. Prajapati, and J. P. Saini, "Sensitivity Enhancement of MXene Based SPR Sensor Using Silicon: Theoretical Analysis." *Silicon*, vol. 13, no. 6, pp. 1887–1894, 2021, doi: 10.1007/s12633-020-00558-3.

[158] R. Kumar, S. Pal, N. Pal, V. Mishra, and Y. K. Prajapati, "High-performance bimetallic surface plasmon resonance biochemical sensor using a black phosphorus–MXene hybrid structure," *Appl. Phys. A Mater. Sci. Process.*, vol. 127, no. 259, pp. 1–12, 2021, doi: 10.1007/s00339-021-04408-w.

[159] M. Q. Zhao, N. Trainor, C. E. Ren, M. Torelli, B. Anasori, and Y. Gogotsi, "Scalable Manufacturing of Large and Flexible Sheets of MXene/Graphene Heterostructures," *Adv. Mater. Technol.*, vol. 4, no. 5, pp. 1–7, 2019, doi: 10.1002/admt.201800639.

[160] B. Tan, T. Lu, W. Luo, Z. Chao, R. Dong, and J. Fan, "A Novel MoS2-MXene Composite Cathode for Aluminum-Ion Batteries," *Energy and Fuels*, vol. 35, no. 15, pp. 12666–12670, 2021, doi: 10.1021/acs.energyfuels.1c01461.

[161] Z. Pan *et al.*, "Black Phosphorus@Ti3C2TxMXene Composites with Engineered Chemical Bonds for Commercial-Level Capacitive Energy Storage," *ACS Nano*, vol. 15, no. 8, pp. 12975–12987, 2021, doi: 10.1021/acsnano.1c01817.

[162] M. Moznuzzaman, I. Khan, and M. R. Islam, "Nano-layered surface plasmon resonance-based highly sensitive biosensor for virus detection: A theoretical approach to detect SARS-CoV-2," *AIP Adv.*, vol. 11, no. 6, pp. 065023-1-065023–10, 2021, doi: 10.1063/5.0046574.

[163] M. Zekriti, D. V. Nesterenko, and Z. Sekkat, "Long-range surface plasmons supported by a bilayer metallic structure for sensing applications," *Appl. Opt.*, vol. 54, no. 8, pp. 2151–2157, 2015, doi: 10.1364/ao.54.002151.

[164] P. Sun *et al.*, "Sensitivity enhancement of surface plasmon resonance biosensor based on graphene and barium titanate layers," *Appl. Surf. Sci.*, vol. 475, pp. 342–347, 2019, doi: 10.1016/j.apsusc.2018.12.283.

[165] Y. Vasimalla, H. S. Pradhan, and R. J. Pandya, "Sensitivity enhancement of the SPR biosensor for Pseudomonas bacterial detection employing a silicon-barium titanate structure," *Appl. Opt.*, vol. 60, no. 19, 2021, doi: 10.1364/ao.427499.

[166] S. Mostufa *et al.*, "Numerical approach to design the graphene-based multilayered surface plasmon resonance biosensor for the rapid detection of the novel coronavirus," *Opt. Contin.*, vol. 1, no. 3, p. 494, 2022, doi: 10.1364/optcon.445255.

[167] B. Karki, A. Pal, Y. Singh, and S. Sharma, "Sensitivity enhancement of surface plasmon resonance sensor using 2D material barium titanate and black phosphorus over the bimetallic layer of Au, Ag, and Cu," *Opt. Commun.*, vol. 508, p. 127616, 2022, doi: 10.1016/j.optcom.2021.127616.

[168] Z. Liang, Y. Wen, Z. Zhang, Z. Liang, Z. Xu, and Y. S. Lin, "Plasmonic metamaterial using metal-insulator-metal nanogratings for high-sensitive refraction index sensor," *Results Phys.*, vol. 15, p. 102602, 2019, doi: 10.1016/j.rinp.2019.102602.

[169] S. W. Brighton, "Chikungunya Virus Infections," *South African Med. J.*, vol. 59, no. 16, p. 552, 1981, doi: 10.1056/NEJMc1505501.

[170] S. Ramesh, B. A. Shutzberg, C. C. Huang, J. Gao, and E. P. Giannelis, "Dielectric Nanocomposites for Integral Thin Film Capacitors: Materials design, Fabrication and Integration issues," *IEEE Trans. Adv. Packag.*, vol. 26, no. 1, pp.

17–24, 2003, doi: 10.1109/TADVP.2003.811365.

[171]   M. Cardona, "Optical properties and band structure of SrTiO3 and BaTiO3," *Phys. Rev.*, vol. 140, no. 2A, 1965, doi: 10.1103/PhysRev.140.A651.

[172]   P. Arora and A. Krishnan, "Analysis of transmission characteristics and multiple resonances in plasmonic gratings coated with homogeneous dielectrics," in *Progress in Electromagnetics Research Symposium*, 2013, pp. 927–931.

[173]   S. Sharma, A. Kumar, K. S. Singh, and H. K. Tyagi, "2D photonic crystal based biosensor for the detection of chikungunya virus," *Optik (Stuttg).*, vol. 237, p. 166575, 2021, doi: 10.1016/j.ijleo.2021.166575.

[174]   B. Karki, A. Uniyal, B. Chauhan, and A. Pal, "Sensitivity enhancement of a graphene, zinc sulfide-based surface plasmon resonance biosensor with an Ag metal configuration in the visible region," *J. Comput. Electron.*, vol. 36, no. 4, pp. 1108–1116, 2022, doi: 10.1007/s10825-022-01854-4.

[175]   A. Pal and A. Jha, "A theoretical analysis on sensitivity improvement of an SPR refractive index sensor with graphene and barium titanate nanosheets," *Optik (Stuttg).*, vol. 231, p. 166378, 2021, doi: 10.1016/j.ijleo.2021.166378.

[176]   A. K. Sharma and A. K. Pandey, "Design and analysis of plasmonic sensor in communication band with gold grating on nitride substrate," *Superlattices Microstruct.*, vol. 130, pp. 369–376, 2019.

[177]   T. Iqbal and S. Afsheen, "One Dimensional Plasmonic Grating : High Sensitive Biosensor," *Plasmonics*, vol. 12, pp. 19–25, 2017, doi: 10.1007/s11468-016-0223-4.

[178]   A. K. Sharma and A. K. Pandey, "Metal Oxide Grating Based Plasmonic Refractive Index Sensor with Si Layer in Optical Communication Band," *IEEE Sens. J.*, vol. 20, no. 3, pp. 1275–1282, 2020, doi: 10.1109/JSEN.2019.2947627.

[179]   M. Abutoama and I. Abdulhalim, "Self-referenced biosensor based on thin dielectric grating combined with thin metal film," *Opt. Express*, vol. 23, no. 22, p. 28667, 2015, doi: 10.1364/oe.23.028667.

[180]   J. Cao, Y. Sun, Y. Kong, and W. Qian, "The Sensitivity of Grating-Based SPR Sensors with Wavelength Interrogation," *Sensors*, vol. 19, no. 405, pp. 1–9, 2019, doi: 10.3390/s19020405.

[181]   M. SEO, J. Lee, and M. Lee, "Grating-coupled surface plasmon resonance on bulk stainless steel," *Opt. Express*, vol. 25, no. 22, pp. 26939–26949, 2017.

[182]   P. Arora and A. Krishnan, "Fourier plane colorimetric sensing using broadband imaging of surface plasmons and application to biosensing," *J. Appl. Phys.*, vol. 118, no. 23, 2015, doi: 10.1063/1.4937567.

[183]   C. Valsecchi and A. G. Brolo, "Periodic metallic nanostructures as plasmonic chemical sensors," *Langmuir*, vol. 29, no. 19, pp. 5638–5649, 2013, doi: 10.1021/la400085r.

[184]   N. Tucher *et al.*, "Interference and nanoimprint lithography for the patterning of large areas," in *Proceedings of SPIE*, 2017, vol. 10115, no. 02, pp. 1–7, doi: 10.1117/12.2249605.

[185]   M. H. Elshorbagy, A. Cuadrado, and J. Alda, "High-sensitivity integrated devices based on surface plasmon resonance for sensing applications," *Photonics Res.*, vol. 5, no. 6, pp. 654–661, 2017.

[186]   P. Arora, E. Talker, N. Mazurski, and U. Levy, "Dispersion engineering with plasmonic nano structures for enhanced surface plasmon resonance sensing," *Sci. Rep.*, vol. 8, no. 1, pp. 1–9, 2018, doi: 10.1038/s41598-018-27023-x.

[187]   M. G. Moharam, T. K. Gaylord, E. B. Grann, and D. A. Pommet, "Formulation for stable and efficient implementation of the rigorous coupled-wave analysis of binary gratings," *J. Opt. Soc. Am. A*, vol. 12, no. 5, p. 1068, 1995, doi: 10.1364/josaa.12.001068.

[188]   P. Arora and H. V. Awasthi, "Aluminum-based engineered plasmonic nanostructures for the enhanced refractive index and thickness sensing in ultraviolet-visible-near infrared spectral range," in *Progress In Electromagnetics Research M*, 2019, vol. 79, pp. 167–174, doi: 10.2528/PIERM19012401.

[189]   K. He, Y. Liu, and Y. Fu, "Transmit-array, metasurface-based tunable polarizer and high-performance biosensor in the visible regime," *Nanomaterials*, vol. 9, no. 4, pp. 1–9, 2019, doi: 10.3390/nano9040603.

[190]   G. A. L. Munoz *et al.*, "A label fee nanostructured plasmonic biosensor based on Blu-ray discs with integrated

microfluidics for sensitive Bio detection," *Biosens. Bioelectron.*, vol. 96, pp. 260–267, 2017.

[191] M. Shen, M. Wang, J. Zhou, L. Du, and C. Deng, "Nanostructured Plasmonic Interferometers for Compact Sensing," *Plasmonics*, vol. 12, no. 3, pp. 691–697, 2017, doi: 10.1007/s11468-016-0315-1.

[192] E. N. Lazareva and V. V Tuchin, "Measurement of refractive index of hemoglobin in the visible / NIR spectral range," *J. Biomed. Opt.*, vol. 23, no. 3, pp. 1–9, 2018, doi: 10.1117/1.JBO.

[193] I. Costic, E. Pirogova, V. Vojisavljevic, and Q. Fang, "Electromagnetic Properties of Biomolecules," *FME Trans.*, vol. 34, p. 71, 2006, [Online]. Available: http://scindeks.ceon.rs/article.aspx?artid=1450-82300602071C.

[194] Y. Yang, J. Aw, and B. Xing, "Nanostructures for NIR light-controlled therapies," *Nanoscale*, vol. 9, no. 11, pp. 3698–3718, 2017, doi: 10.1039/c6nr09177f.

[195] B. Choi, X. Dou, Y. Fang, B. M. Phillips, and P. Jiang, "Outstanding surface plasmon resonance performance enabled by templated oxide gratings," *Phys. Chem. Chem. Phys.*, vol. 18, no. 37, pp. 26078–26087, 2016, doi: 10.1039/c6cp04977j.

[196] F. Cheng, X. Yang, and J. Gao, "Enhancing refractive index sensing capability with infrared plasmonic perfect absorbers," *Opt. InfoBase Conf. Pap.*, vol. 39, no. 11, pp. 3185–3188, 2014, doi: 10.1364/cleo_at.2014.jw2a.94.

[197] R. Jha and A. K. Sharma, "High-performance sensor based on surface plasmon resonance with chalcogenide prism and aluminum for detection in infrared," vol. 34, no. 6, pp. 749–751, 2009.

[198] H. Oraizi and M. Afsahi, "Analysis of Planar Dielectric Multilayers as FSS by Transmission Line Transfer Matrix Method (TLTMM)," in *Progress In Electromagnetics Research*, 2007, pp. 217–240.

[199] M. S. Rahman, M. S. Anower, M. R. Hasan, M. B. Hossain, and M. I. Haque, "Design and numerical analysis of highly sensitive Au-MoS2-graphene based hybrid surface plasmon resonance biosensor," *Opt. Commun.*, vol. 396, pp. 36–43, 2017, doi: 10.1016/j.optcom.2017.03.035.
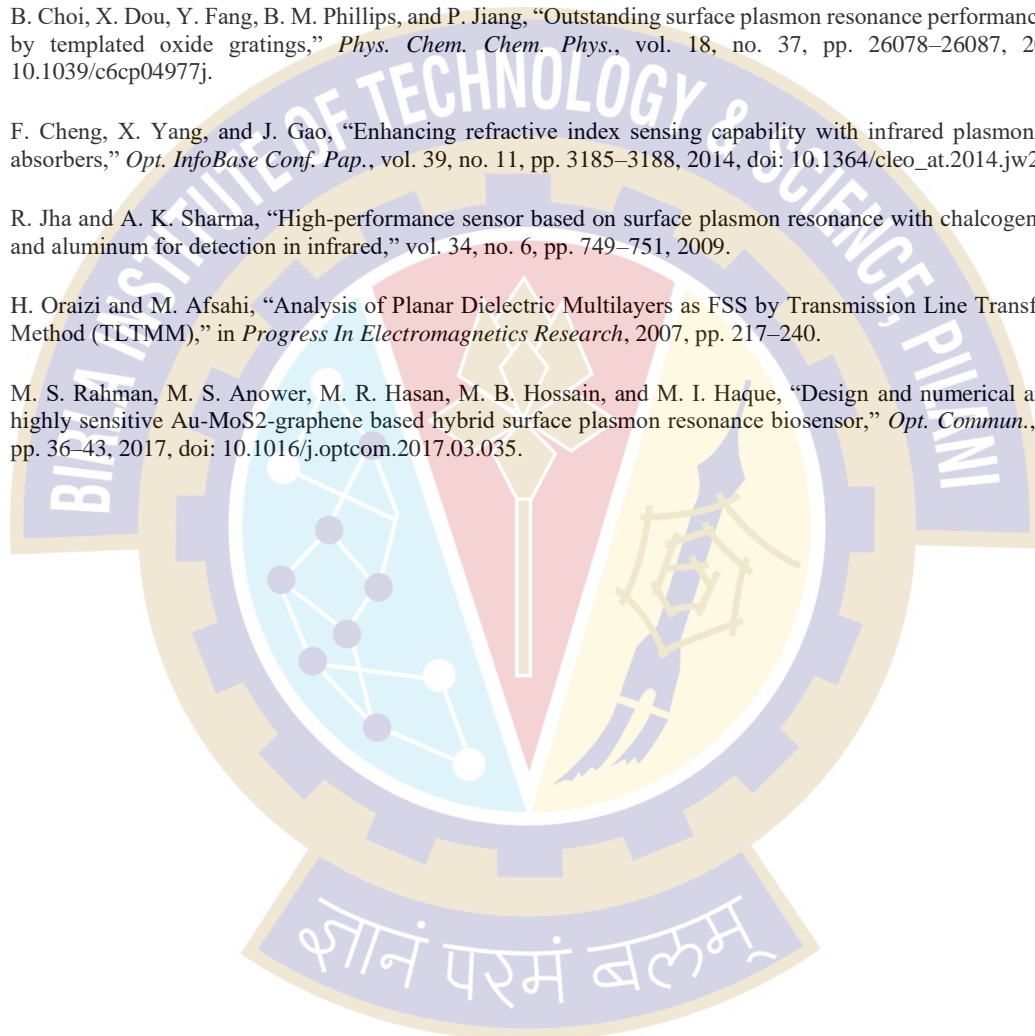
List of Publications

Peer Reviewed Journal

1. **S. Shukla**, and P. Arora, "Design and analysis of aluminum-graphene based plasmonic device for biosensing applications in the optical communication band," **Silicon 13, no. 10 (2021): 3703-3711 https://doi.org/10.1007/s12633-021-00953-4** .

2. **S. Shukla**, and P. Arora, "Design and comparative analysis of aluminum-MoS_2 based plasmonic devices with enhanced sensitivity and Figure of Merit for biosensing applications in the near-infrared region," **Optik, 228, p.166196, 2021 https://doi.org/10.1016/j.ijleo.2020.166196 {Best Researcher Award}**

3. **S. Shukla,** V. Venkatesh, and P. Arora, "Highly sensitive self-referenced plasmonic devices based on periodic nanostructures for sensing in the communication band," **Optical Engineering, 59, 6 (065101), 2020 https://doi.org/10.1117/12.2544582** .

4. **S. Shukla,** and P. Arora, "Multiwavelength Plasmonic activity in aluminum-based 2D nanostructures for biosensing applications in the near-infrared region," **Journal of Computational Electronics, 1-7, 2022, https://doi.org/10.1007/s10825-022-01879. {Selected for the cover art of issue June 2022}**

5. **S. Shukla**, and P. Arora, "Graphene decorated aluminum-nanostructure based plasmonic device with enhanced sensitivity and Figure of Merit using both wavelength and angle interrogation" **Optik, 261 (169177), 2022 https://doi.org/10.1016/j.ijleo.2022.169177**

6. **S. Shukla,** and P. Arora, "Investigation of 2D nanomaterials on MXene ($Ti_3C_2T_X$)-based aluminum-plasmonic devices for biosensing in the near-infrared region" **Appl. Phys. A 128, 785 (2022) https://doi.org/10.1007/s00339-022-05947-6**

7. **S. Shukla**, and P. Arora, "Resolution enhancement using a multi-layered aluminum-based plasmonic device for chikungunya virus detection" **Optical and Quantum Electronics, 55, 274 (2023) https://doi.org/10.1007/s11082-022-04485-y**

8. **S. Shukla**, and P. Arora, "A review on Aluminum-based plasmonic devices for sensing in UV-Vis-near-IR region" **Applied Optics (under review).**

Conference Proceedings

1 **S. Shukla,** and P. Arora, "Multiwavelength Plasmonic Activity in Aluminum-based 2D Nanostructures for Biosensing Applications," **44th International Conference PIERS 2021 held at Hangzhou (China) from November 21-25, 2021.**

2. **S. Shukla,** A. R. Harkishankaa, A. Baranwal, and P. Arora, "Engineered Al-based Plasmonic Devices working under both angle and wavelength interrogation with high sensitivity and figure of merit," **International Conference OSA Advanced Photonics Congress 2021 held at the USA from July 26-30, 2021.**

3. **S. Shukla,** and P. Arora, "Analysis of engineered aluminum-based plasmonic devices decorated with graphene/2D nanomaterials for enhanced biosensing applications in the near-infrared region," **International Conference CLEO/Europe 2021 held at Munich (Germany) from June 20-24, 2021.**

4. S. Shukla, J. Yadav, S. Jain, and P. Arora, "Engineered Graphene decorated Aluminum-based plasmonic nanostructures for biosensing applications in the optical Communication band," **6th International Conference Nanotech France 2021 held at Paris (France) from June 23-25, 2021.**

5. S. Shukla, and P. Arora, "Analysis of Aluminum-graphene based plasmonic sensor for biosensing applications in the communication band," **SPIE Photonics West-2021, San Francisco, California (USA).**

6. S. Shukla, and P. Arora, "Design and comparative analysis of aluminum-MoS2 based plasmonic devices with enhanced sensitivity and Figure of Merit for biosensing applications in the near-infrared region," **9th International Conference on Photonics, Optics and Laser Technology, Photo-Optics (NanoPlasMeta-2021), Spain.**

7. P. Arora, and **S. Shukla,** "Self-referenced integrated plasmonic device based on engineered periodic nanostructures for sensing applications," **SPIE Photonics West-2020, San Francisco, California (USA).**

8. S. Shukla, J. Kamat, and P. Arora, "Resolution enhancement with MDM configuration for plasmonics based optical sensors," was presented virtually at **"GEMN 2022", July14-16 2022, in Warwick, RI (USA).**

9. S. Shukla, and P. Arora, "Investigation of Graphene coated Aluminum based plasmonic devices for bio-sensing application in the near-infrared region," was presented virtually at **"International Workshop on Group IV Photonics from 15-20 March 2022, NIT Delhi" (India).**

10. S. Shukla, A. Verma, G. Karthiik, A. Sarkar, and P. Arora, "Effect of 2D nanomaterials on MXene based engineered Aluminum plasmonic devices for bio-sensing in the near-infrared region," **was presented virtually at "Nanotech France-2022" in Paris (France).**

11. A. Tyagi, **S. Shukla,** and P. Arora, "Graphene coated Aluminum-based 2D plasmonic nanostructures for perfect tunable absorber in the Visible and Infrared band," **44th International Conference PIERS 2021 held at Hangzhou (China) from November 21-25, 2021.**

12. S. Shukla, S.Galera, P. Shah, and P. Arora "Engineered core-shell nanoparticles-based absorber for the Visible-Near infrared regime" will be presented virtually at the International conference **"OPL 2022", during Nov 9-11 2022 in TX (USA).**

13. S. Shukla, and P. Arora "Nanoscale devices for low-power applications" **5th international conference ETMN 2021 held at Jaipur (India) during October 8-9 2021.**

14. S. Shukla, and P. Arora, **"**Investigation of 2D nanomaterials on Aluminum-based engineered plasmonic devices for sensing applications in the near-infrared region**" will be presented at the International Conference (IUMRS-ICA 2022) during Dec 19-23 in IIT Jodhpur (India).**

15. K. Sanghi, **Y.** Tripathy, **S. Shukla**, and P. Arora, "Comparative analysis of Indium Phosphide dielectric-based plasmonic sensors in the optical communication band" and the work was presented virtually at the international conference **"EPIC 2022", Dec 15-17 in SRM University (India).**

16. R. Shekhar, A. Lath, **S. Shukla**, and P. Arora, "Investigation of a highly sensitive plasmonic device utilizing antimonene for biosensing applications in the near infrared region" and the work was presented virtually at the international conference **"EPIC 2022", Dec 15-17 in SRM University (India).**

17. S. Mehta, P. Raghunath**, S. Shukla,** and P. Arora, "Design and comparative analysis of Aluminum-BiFeO3 based plasmonic sensor in the optical communication band" and the work was presented virtually at the international conference **"EPIC 2022", Dec 15-17 in SRM University (India). (Best Paper Award).**

18. S. Patria, A. Singh**, S. Shukla,** and P. Arora, "Highly sensitive surface plasmon-based refractive index sensor in the optical communication band using ZnS-PVP layers" and the work was presented virtually at the international conference **"EPIC 2022", Dec 15-17 in SRM University (India). (Best Paper Award).**

19. S. Shukla, K. Sanghi, Y. Tripathy, and P. Arora, "Investigation of 2D nanomaterials on Indium Phosphide based plasmonic devices for sensing application in optical communication band" and the work was presented virtually at the 5th International conference **"DevIC 2023", Apr 7-8 in Kalyani Government Engineering College (India). (Best Paper Award).**
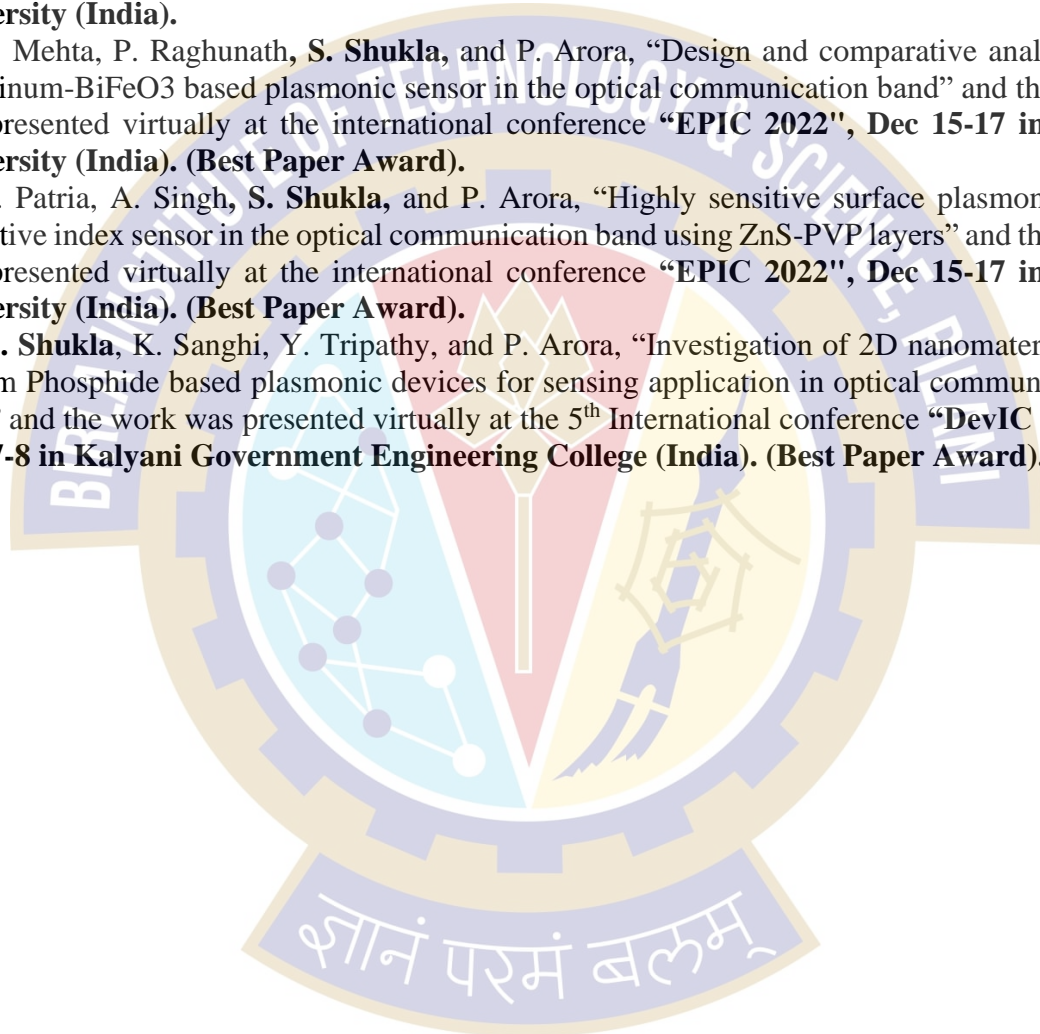
Brief Biography of the Candidate

Sambhavi Shukla received her B. Tech degree in Electronics and Communication engineering from M.D.U. Rohtak (Haryana) in 2015 and M.Tech. degree from J.C. Bose University of Science and Technology, YMCA, Faridabad in 2018. She is currently pursuing her Ph.D. degree in the area of nanoscale plasmonic devices with the Department of Electrical and Electronics Engineering, Birla Institute of Technology and Science at Pilani, Pilani campus, India. Her current research includes plasmonics, photonics, and biosensors.
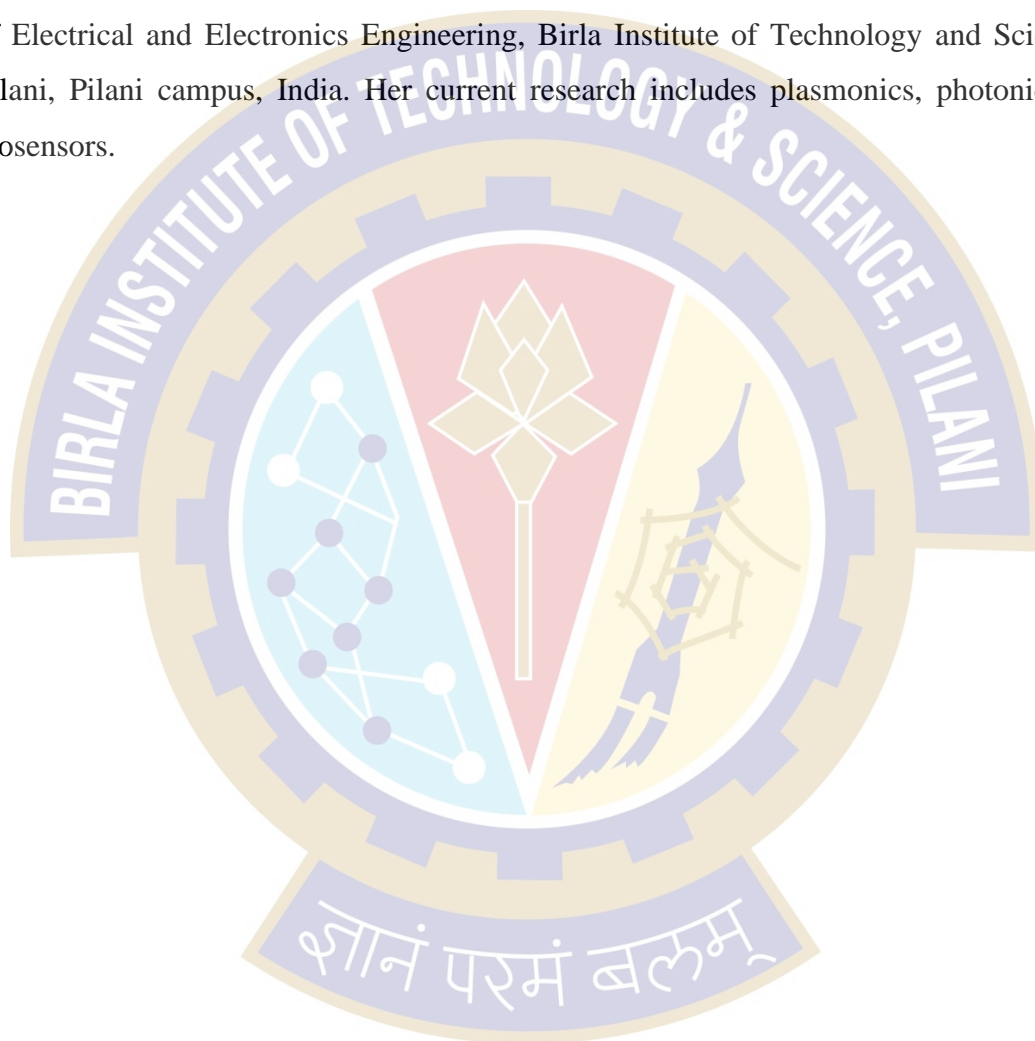
Brief Biography of the Supervisor

Dr. Pankaj Arora received his M.S. and Ph.D. dual degree in Electrical Engineering from IIT Madras, Chennai, India, in 2016. From 2016 to 2018, he was a Post-Doctoral Researcher at the Faculty of Science, The Hebrew University, Jerusalem, Israel, where he was involved in studying the light-matter interaction at the nanoscale in photonic devices. He is currently working as an Assistant Professor with the Department of Electrical and Electronics Engineering, Birla Institute of Technology and Science at Pilani, Pilani, India. His current research interests include plasmonics, silicon photonics, optical sensors, 2D nanomaterials, Microfuildics, and imaging microscopy.